STUDY OF A BI-DIRECTIONAL AXIAL FLOW BLOOD PUMP

A thesis submitted for the degree of
Doctor of Philosophy

by
Marcel Johannes Petrus Swalen

School of Engineering & Design
Brunel University
February 2012

Abstract

A common treatment for circulatory disorders is the application of rotary blood pumps to locally increase blood flow to required levels. Existing devices tend to support flow from inlet to outlet and in that direction only. This thesis presents a bi-directional pump that may enable ventricle assist devices (VAD) to support blood flow to the organs during systole, when rotating in one direction, and to increase coronary perfusion during diastole, when rotating in the other.

For each flow direction blade profiles were designed and tested for performance. Both designs were merged to obtain a symmetric profile to provide flow support in both directions. This initial bi-directional design was optimised using computational fluid dynamics modelling. The model was set to accelerate to a maximum forward rotational speed of 8,000 rpm, change rotational direction after 300 ms and accelerate to 2,400 rpm whilst rotating backwards. Experimental testing was carried out to validate the computational results.

In the forward direction, the pump was predicted to deliver 39 cm^3 compared to 19 cm^3 in the backward direction. Pressure heads reached maxima of 2.2 kPa in forward and 0.16 kPa in backward direction. Analysis of wall shear stress profiles at the blades' surface showed that the maximum was 140 Pa lasting less than 300 ms in the forward direction, whilst in the backward direction this was approximately 23 Pa lasting for 700 ms.

A design for the bi-directional blades is established and characterised computationally and experimentally. Analysis of the blade pressure profiles confirmed generation of pressure rise in both directions. The computational results for wall shear stress were predicted to be below the accepted limits of haemolysis. Recirculation zones were found at the outlet in the backward rotating direction. Future work may reduce those by using guide vanes at either side of the rotor.

List of Contents

LIST OF FIGURES

LIST OF TABLES

Nomenclature

Greek
α [°] = angle of absolute velocity
β [°] = blade angle
θ [°] = camber angle
μ [Pa·s] = dynamic viscosity
ν [m^2/s] = kinematic viscosity
ρ [kg/m^3] = density
σ [Pa] = average stress
τ [N/m^2] = shear stress
φ [-] = flow coefficient
ψ [-] = head coefficient
ω [rad/s] = angular velocity

Latin
A [m^2] = area of flow
c [m/s] = absolute velocity of flow
c_m [m/s] = meridional velocity
d [m] = diameter
d_r [-] = hub ratio
g [m/s^2] = gravitational acceleration
H [Pa] = head
I [$kg \cdot m^2$] = mass momentum of inertia
K_m [-] = capacity constant
K_u [-] = velocity constant
L [kgm^2s^{-1}] = angular momentum
l [m] = chord
N_v [-] = number of vanes
n [rpm] = rotational speed
N_s [-] = specific speed
Q [m^3/s] = flow
r [m] = radius
t [m] = pitch
T [N·m] = torque
u [m/s] = peripheral velocity of impeller
U [m/s] = velocity
w [m/s] = velocity *c* of flow, relative to the blade

Subscripts
$_1$ = inlet
$_2$ = outlet
$_c$ = chord
$_h$ = hub
$_t$ = tip
$_u$ = tangential component of velocity

1 Introduction

1.1 Background

Cardiovascular diseases (CVD) are globally the most common cause of death today. Each year CVD causes over 4.3 million deaths in Europe, 48% of all deaths. In the UK, around 2.6 million people are currently diagnosed with coronary heart disease (CHD). Though mortality from CHD is falling rapidly in the UK, the prevalence of CHD and other circulatory disease appears to be rising, especially for men in older age groups. Since the late 1980s, it has risen by 52% in men aged 75 and older. United States statistics show that despite the significant progress made over the last 30 years and a decrease in death rate from all cardiovascular disease of 45%, treatment of the 5 million people suffering from chronic heart failure is not deemed satisfactory; for the 50,000 patients awaiting heart transplant only 2,500 donor hearts become available each year (DeBakey, 2000; Mathers & Loncar, 2006; Allender et al., 2008; BHF, 2010).

1.2 Physiology of the heart

The structure of the human heart enables it to function as a mechanical double pump. It consists of two sides, left and right, separated by the septum wall (figure 1.1a). The right side is responsible for collecting de-oxygenated blood from the body via the superior and inferior vena cava and delivering it to the lungs through the pulmonary trunk. The left side then collects the oxygenated blood from the lungs via the pulmonary veins to deliver it to the body through the aorta, closing the circulatory circle.

The left and right side have each two chambers, an atria and a ventricle. The ventricles have a one-way valve at the inlet and outlet, to ensure blood to flow in a single direction (figure 1.1b). On the right side, the tricuspid valve separates atrium and ventricle and the pulmonary valve separates ventricle and pulmonary trunk. On the left side, the mitral valve separates atrium and ventricle and the aortic valve ensures blood to flow from ventricle to aorta.

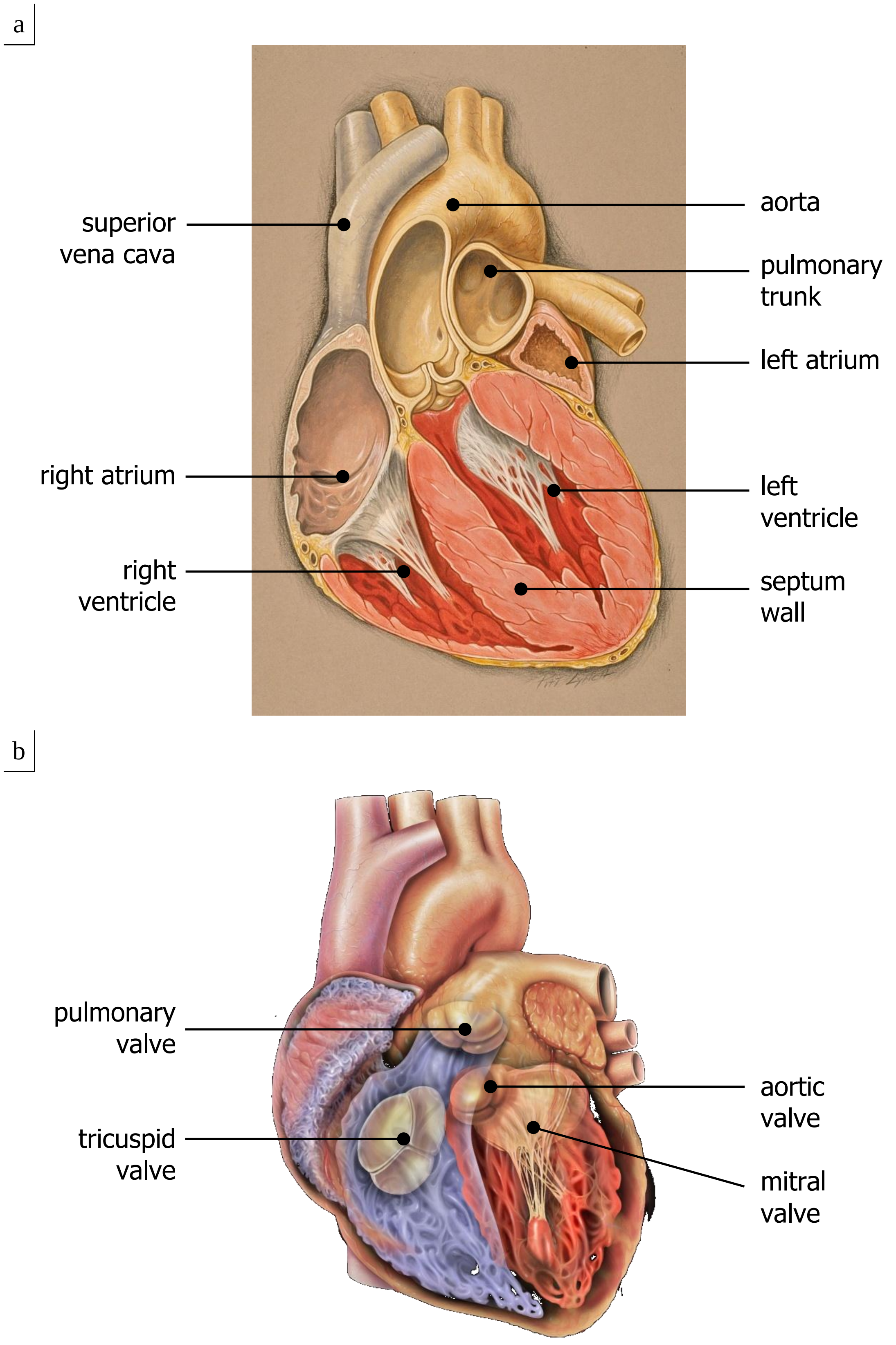

Figure 1.1: Structure of the human heart (a) and its double pumping mechanism (b). (CC Patrick J. Lynch and C. Carl Jaffe, Yale University, 2006)

The pumping action is triggered by the sinus node, located in the right atrium. The node produces an electrical potential to send an impulse to the myocardium, the middle layer of tissue the wall of the heart is composed of. The myocardium consists of muscle that will contract when receiving the electrical impulse and relax after the electrical energy has dissipated. Electrocardiography allows recording of this electrical energy to create a graphical representation of the heart's function, a.k.a. an electrocardiogram.

The electrocardiogram (ECG), plotted together with aortic, arterial, and ventricular pressure, ventricular volume and sound measurements (phonodiagram) establishes the Wiggers diagram (figure 1.2). The cardiac cycle is built up as follows: first the relaxed heart is allowing the ventricles to start filling with blood. The first wave (P) corresponds to the electrical discharge of the atria (atrial systole). Their simultaneous contraction forces the ventricles to be completely filled. The QRS-complex of the ECG indicates the isovolumetric contraction of the ventricles, marking the onset of the systolic stage of the cardiac cycle. The pulmonary and aortic valves open and the blood is ejected to the lungs and the body. Ventricular and aortic pressure rise sharply whereby aortic pressure lags behind ventricular because this point is located more distally. Up until the onset of the T-wave in the ECG is seen, after which aortic pressure starts lagging behind ventricular pressure. The T-wave represents the isovolumetric relaxation of the ventricles. Ventricular pressures decreases rapidly and the aortic valve closes. This marks the end of the systolic stage and the beginning of the diastolic stage, whereby the heart will start filling again with blood.

The aorta is the largest artery leaving the heart and through many branches it supplies all the organs with oxygenated blood. At the aortic root the diameter is 20-30 mm which gradually decreases distally. Two branches most close to the aortic root are the right and left coronary arteries. With a diameter of 2-3 mm, these arteries supply oxygenated blood to the myocardium. Their small size and being the only source of oxygen for the myocardium, makes the functioning of the coronary arteries critical.

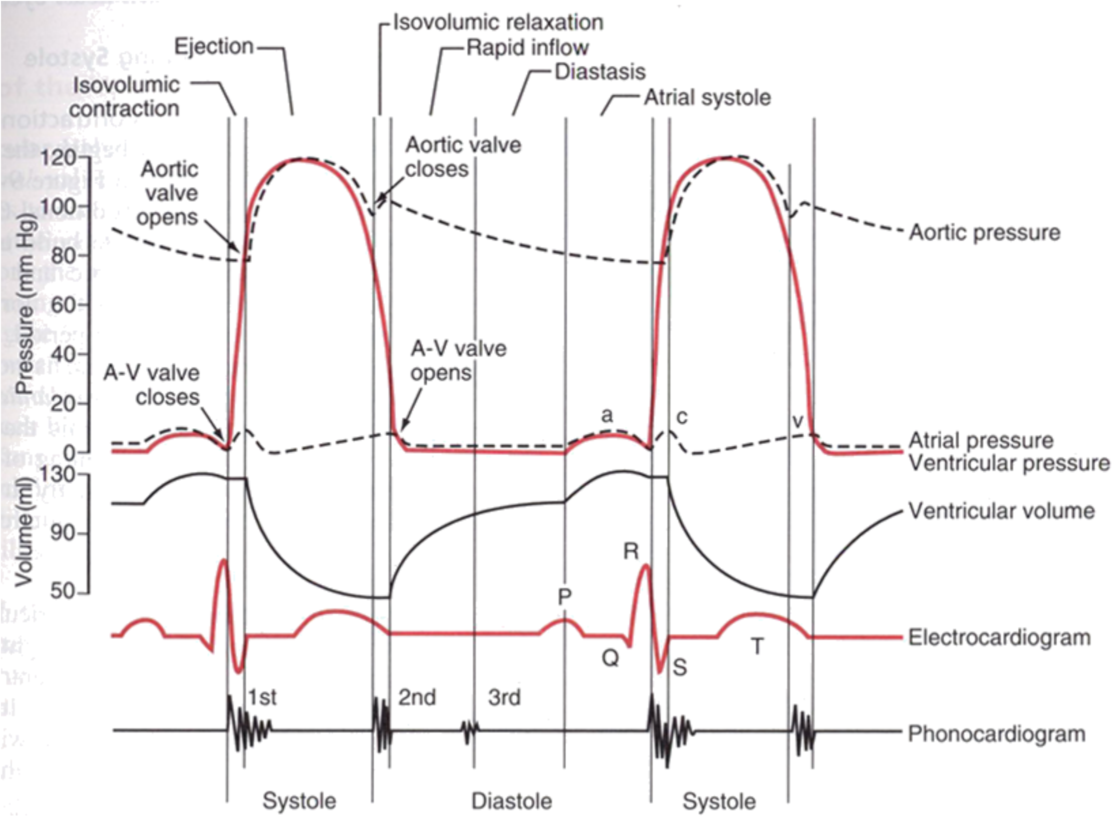

Figure 1.2: A representation of a Wiggers diagram of two subsequent heart cycles (figure 9.5 from Guyton's: “Textbook of Medical Physiology”, 10th Edition, 2000).

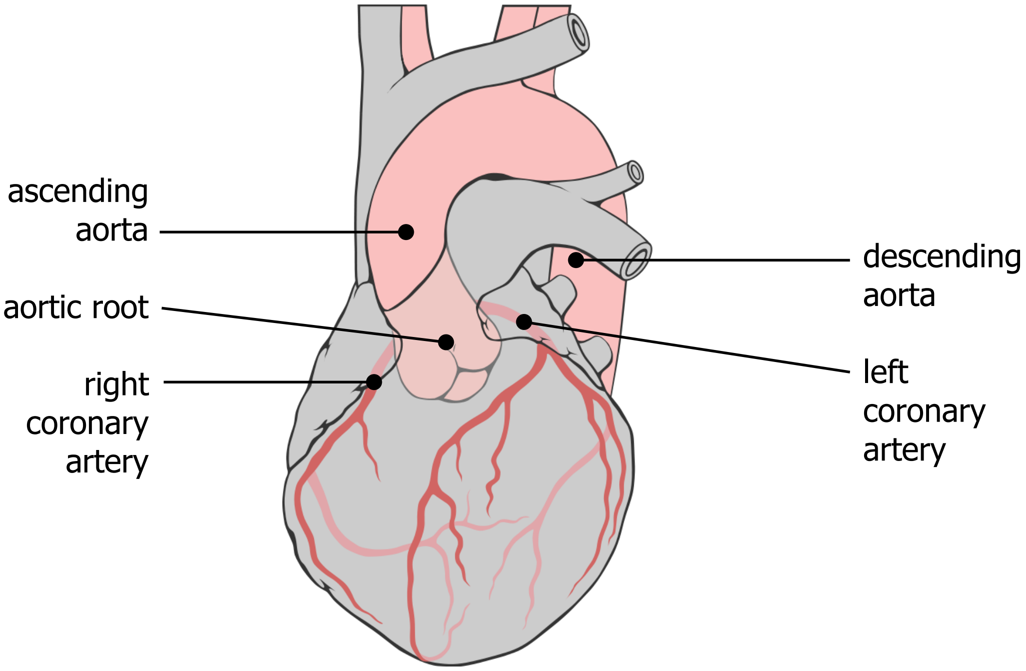

Figure 1.3: Coronary arteries, branches on the right and left side of the ascending aorta. (CC Patrick J. Lynch and C. Carl Jaffe, Yale University, 2006).

1.3 Heart failure

Although vascular disease may be present from birth, it is often the ageing process that leads to higher pressure levels and reduced elasticity of the vessels making the heart unable to provide the required flow rate to feed the body and its organs. The term of this overall deterioration process is congestive heart failure (CHF). Apart from the natural ageing process other factors may quicken the deterioration process, such as heart attacks, malfunctioning heart valves, lifestyle or diet.

1.3.1 Myocardial infarction

Myocardial infarction, or heart attack, is the damage of myocardium muscle tissue due to ischemia as a result of reduced blood supply. Commonly it is caused by the partial or total occlusion of one or more coronary arteries. As the heart itself is deprived from oxygen, the muscle weakens and tissue dies causing the heart to no longer beat as consistently. This will then lead to further oxygen deprivation of body and organs and possibly leading to life threatening levels.

Occlusion of the coronary arteries might be caused by blood cloths, consisting of platelets and fibrin, which are normally only formed to stop the blood loss caused by an injured vessel. Thrombosis is a coagulation disorder whereby formations of a blood clot are triggered by other situations, not related to an injured vessel. Such unintentionally formed blood clots may subsequently block blood vessels. Apart from blocking blood flow whilst the cloth is stuck to the vessel’s wall, it may also come loose from the vessel’s wall and start travelling along the circulatory system and block smaller arteries or veins. Thrombosis formation might be triggered by deviations of the blood’s composition, the vessel’s wall or flow disturbances or any combination of the aforementioned. It is important to avoid these circumstances from occurring whilst treating heart disease. Surgery might injure the vessels’ wall and the use of mechanical devices may disturb the flow with turbulence or stagnation areas. Subsequently such more invasive treatments have an increased risk of causing thrombosis.

Another condition that may occlude coronary arteries is atherosclerosis whereby the vessel’s wall is hardened and thickened by plaque. The formation of plaque is caused by the accumulation of white blood cells and fat material, such as cholesterol. As accumulation progresses over time, the blood flow is increasingly reduced. Also the fibrous cap of the plaque formation is likely to rupture causing thrombosis.

1.3.2 Valvular heart disease

A heart valve may consist of two or three flaps or cusps and is opened or closed by the pressure difference generated between either side. Its main purpose is to ensure blood flow will not change direction. Narrowing of deformation of heart valves prevent the heart from properly propelling blood flow or enable flow to unintentionally change direction. Subsequently such heart valve disorders may lead to a decreased flow rate to the body and its organs. Valvular disorders may be genetically acquired but typically occur as a result of natural ageing. However disorders such as deformed arteries in front or after the heart valve may also cause the valve not to function properly.

1.4 Treatment regimes

Treatments of low cardiac output involve the use of positive inotropic and vasoactive drugs. Patients with a left ventricular ejection fraction (LVEF) of 35% or less and a QRS-complex in the ECG of 120 ms or more may be further treated with cardiac resynchronization therapy by means of implanting a bi-ventricular artificial pacemaker. When the cardiac function further decreases, mainly due to cardiogenic shock or cardiac fibrillation, the above mentioned treatments will no longer suffice and more efficient cardiac support is required (Reul & Akdis, 2000).

1.4.1 Endarterectomy and angioplasty

If plaque formation is the underlying cause of reduced cardiac output, one possible treatment is endarterectomy. This procedure removes the plaque material from the vessel’s wall after which the vessel may be reconstructed. The stage of plaque formation or its location might also make other procedures, such as angioplasty, more suitable. Angioplasty is the restoration of the vessel’s to its original diameter, by filling a balloon at the location of the plaque (figure 1.4a). The plaque is not removed but thinned and forced towards the vessel’s wall, increasing the wall thickness to restore the original blood flow path. Depending on circumstances, a metal stent may be placed around the vessel’s wall (figure 1.4b). The procedure of coronary angioplasty is relatively non-invasive, by leading the balloon through a catheter inserted in a distal artery, not requiring the heart to be stopped during surgery.

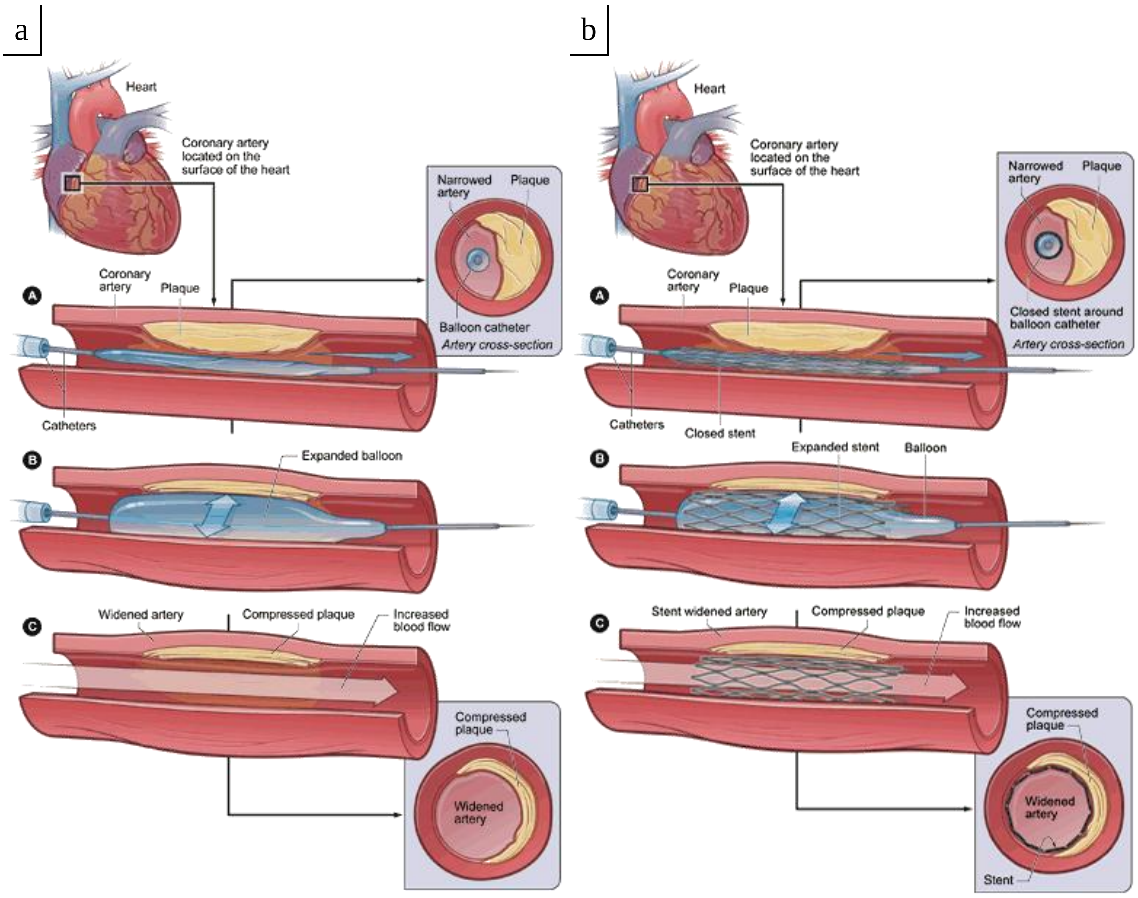

Figure 1.4: Angioplasty of the right coronary artery widening the artery by inflating a balloon without (a) or with (b) using a metal stent. (http://www.micc.com/services-angioplasty-miami-cardiology-florida.html).

1.4.2 Artery bypass grafting

Another possible treatment for plaque formation is bypass surgery. Hereby the occluded part of the artery is bypassed using a non-critical artery or vein from elsewhere in the body. The extra artery or vein is grafted at each side of the plaque formation to replace the flow function of the occluded vessel. This procedure is rather invasive and usually requires intervention of the beating heart.

1.4.3 Heart transplantation

One may expect the many problems that come with the invasive treatment of a heart transplant. Many criteria need to be respected to minimize the risk of rejection of the transplanted organ and, above all, the heart will never function as the patient’s own as part of the transplant involves the removal of nerves. Without these nerves the transplanted heart will not be able to respond to changes in physiological stimuli whereby a subsequent change in cardiac output would be required. Due to the development of heart failure diagnosis techniques, cardiac failure is now diagnosed in earlier stages further increasing the survival rate but also making the waiting list for a heart transplant longer. Due to the chronic shortage of donor hearts, a lot of research has been carried out to find alternative solutions and even today the field of research for alternative treatments remains a very active one. This led to the development of ventricular assist devices (VADs) that aim to support the circulatory system mechanically and supplement the output of a patient’s own left ventricle and not to completely replace its function but to work in parallel with the existing ventricle to provide adequate blood flow to the body (Wood et al., 2005). This is also known as “Bridge To Recovery” (BTR) therapy.

1.4.4 Ventricular assist devices

Application of VADs may often lead to recovery but when this is no longer deemed possible, the aim of recovery of the ventricle will no longer be viable and mechanical support will be exploited for bridging until a donor heart becomes available; also known as “Bridge To Transplant” (BTT) therapy. For bridging periods of a few days up to a few months, pneumatic displacement blood pumps have been developed and successfully applied to offer left and/or right ventricle support. Application of such a device may result in infection at the skin penetration sites and significantly reduces a patient’s mobility because of the large sized driving consoles. Therefore, when the bridging period goes up to several months or a few years, application of fully implantable electro-mechanical assist devices is considered. The two main systems currently available are the NOVACOR (Baxter Healthcare Corp., Deerfield, IL, USA) and the HeartMate (Thermo Cardiosystems Inc., Woburn, MA, USA) (Reul & Akdis, 2000).

When the bridging period further increases or when additional complications are present that cause the BTT not to suffice, long-term ventricular support is deemed necessary by either transplantation or as the only alternative to transplantation at this stage, a total artificial heart (TAH).

2 Literature Review

2.1 Historical review of ventricular assist devices

Over the last decade many cardiac assist devices have been developed and are widely accepted and used by clinicians as a tool to support a failing heart. A number of reviews about the many devices developed in recent years have been published (Reul & Akdis, 2000; Wheeldon, 2003; Wood et al., 2005). In the following a summary of all VADs, based on these reviews up until now is given below.

Figure 2.1 shows that blood pumps can be classified in (1) positive displacement, (2) rotary and (3) total artificial heart (TAH) pumps. The first two types aim to support the existing ventricle whereas the latter type replaces the function of the ventricle. Devices are classified according to four different criteria: application, power, function and position. Depending on the stage of the congestive heart failure a device might be applied to offer immediate short support (VAD), offer a mid-term bridge towards recovery or transplant (BTR/BTT), or fully replace the function of the heart (TAH). Note that some of the mid-term devices under the category BTR/BTT are also used for short term support. A ventricular support device might subsequently be powered pneumatically or electrically. Thirdly, the devices are classified according to the type of pump that can either be an axial, diagonal (mixed flow), radial (centrifugal) or pulsatile flow pump. Finally a ventricular assist device may either be positioned incorporeally or extracorporeally. Devices that have been in clinical use but have been found obsolete and are no longer in clinical use are not included in figure 2.1. Likewise, devices in preliminary stages of development where clinical trials have not yet commenced have not been included in this overview either. In line with the pump in this study the review will concentrate predominately on types 1 & 2.

2.1.1 Positive displacement pumps

The positive displacement pump is a machine whereby energy is transferred by volume change due to a moving boundary (figure 2.2a). This makes the flow pulsate. Many of the devices developed are still widely used but are limited to several hours only because of the resulting blood damage and spallation (Reul & Akdis, 2000).

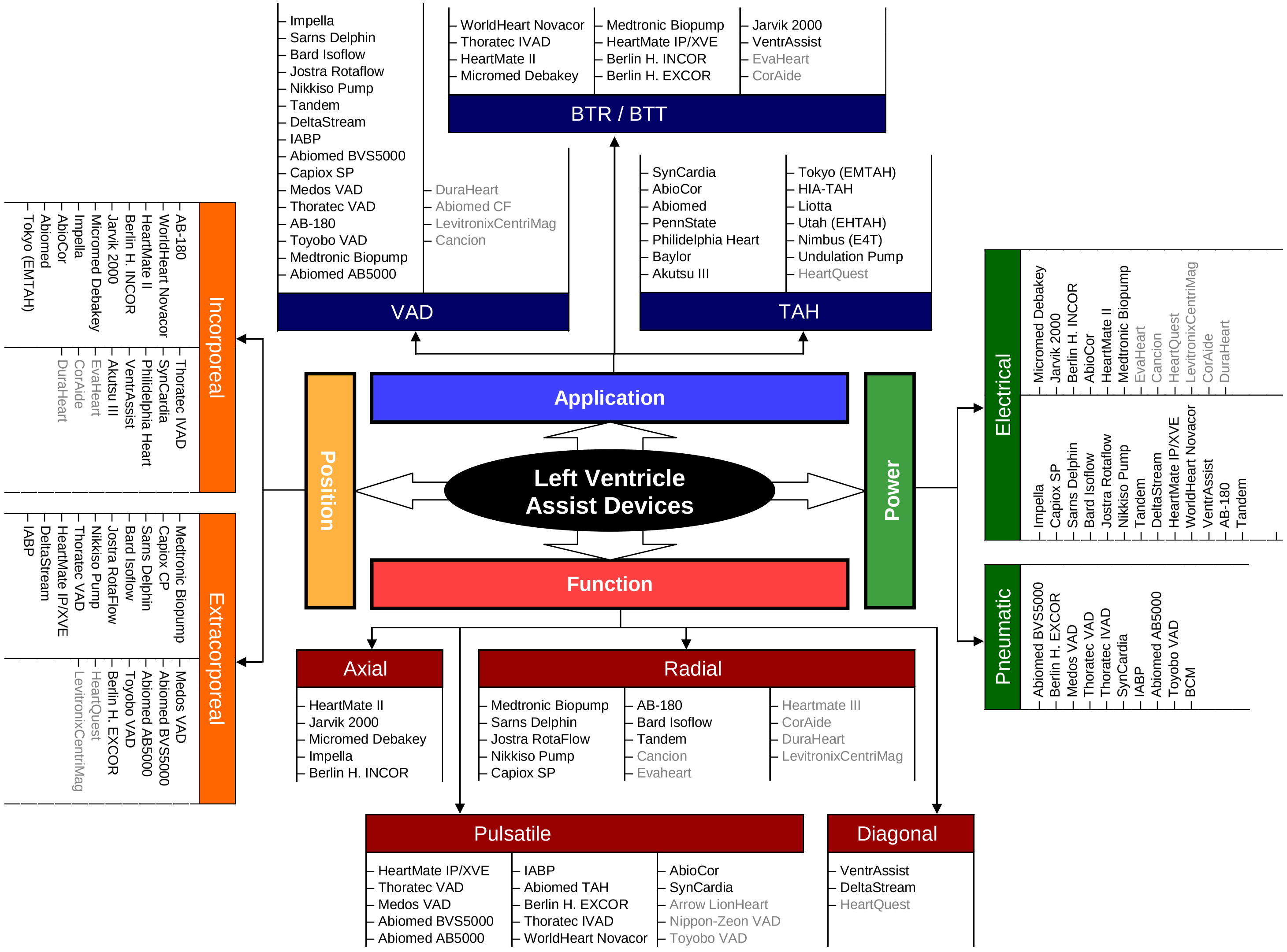

Figure 2.1: Overview of all existing assist devices on the market. Devices under development that are undergoing clinical trials have been printed in grey whereas devices printed in black are in clinical use and commonly have a FDA or CE approval.

Furthermore the use of many moving parts, mechanical failure of membranes and valves that are typically experienced and the large device size deems them satisfactory for short term use only (Goldstein & Oz, 2000). Notable displacement pumps like the HeartMate IP / VE, Thoratec and Novacor are able to deliver flow rates up to 115-200 cm^3/s at a maximum heart rate of 120-140 bpm and have a well-established clinical history of up to 20 years. More recent developments include the Novacor II, HeartSaver and LionHeart. Most designs of positive displacement pumps consist of one or more chambers with a pusher plate mechanism to create the pulsatile flow. One pump that does not meet that design but still provides pulsatile flow is the Intra-Aortic Balloon Pump (figure 2.2b). In this case the pulsatile flow is generated by inflation and deflation of a balloon sitting in the descending aorta, inserted through the femoral arteries.

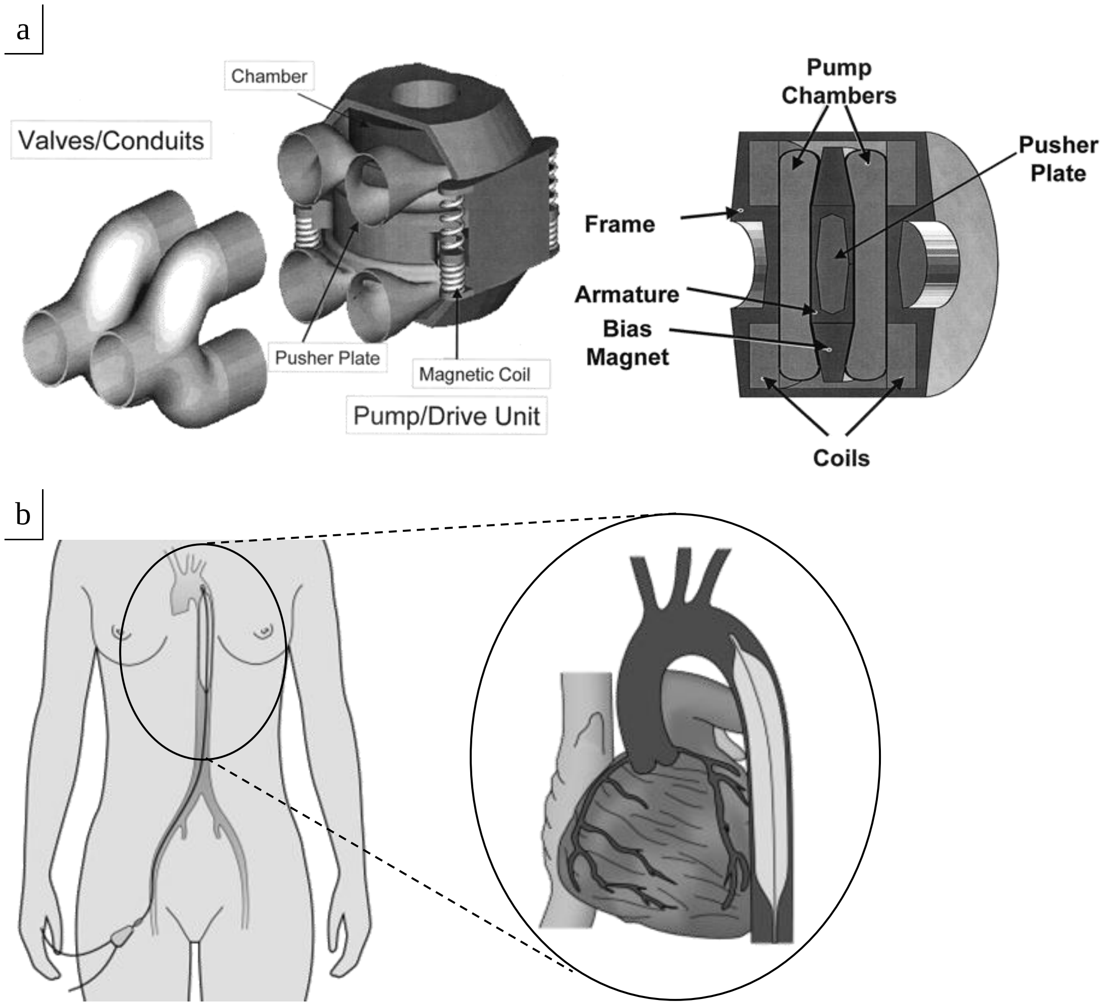

Figure 2.2: Examples of positive displacement pumps, such as the Novacor II (a) and the Intra-aortic balloon pump (b) (Robbins et al., 2001; Ducas et al., 2003).

2.1.2 Rotary pumps

In contrast to positive displacement pumps, rotary blood pumps do not have a closed volume. All work is done by the dynamic effects between rotor and the fluid flow. Typically they are smaller in size, have lower filling volume, no spallation and therefore less blood damage and better portability. First generation devices are characterized by various types of mechanical bearings that generate local heating. This problem was solved for the second generation devices by applying magnetic or hydraulic bearings instead that allow fewer parts to be in contact with blood therefore lowering the blood damage. Rotary blood pumps are further classified by the nature of the rotation; (a) axially, (b) diagonally (mixed flow) and (c) radially (centrifugal flow); see figure 2.4. Each type is characterised by a specific speed coefficient, the more radial pumps are associated with lower specific speeds and the more axial with higher speeds (figure 2.3). The radial pump is capable of producing a high pressure head at a low flow whereas the axial pump generates high flow at a low pressure head (figure 2.5). The diagonal pump produces both a high pressure head at a high flow. This design classification is reflected in the device size: axial flow pumps that may have diameters as small as 6 mm tend to be more compact making them less invasive and easier to implant than the centrifugal pump (diameter up to 60mm). The latter on the other hand is capable of pumping more fluid at a higher pressure head. The centrifugal and mixed flow pumps are therefore more suitable for extracorporeal circulation and the axial flow pump is appropriate for intracorporeal circulation and best suits the needs to assist the heart or perfuse other organs locally.

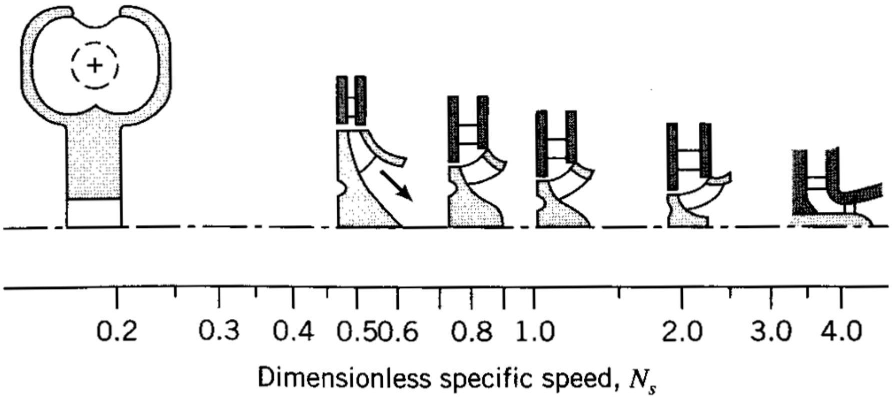

Figure 2.3: Range of the characteristic specific speed and the corresponding impeller design. Radial impellers are characterised having a lower specific speed, The more axial an impeller design is, the higher the specific speed. Copy of figure 10.16 from “Introduction to Fluid Mechanics” (Fox et al., 2011).

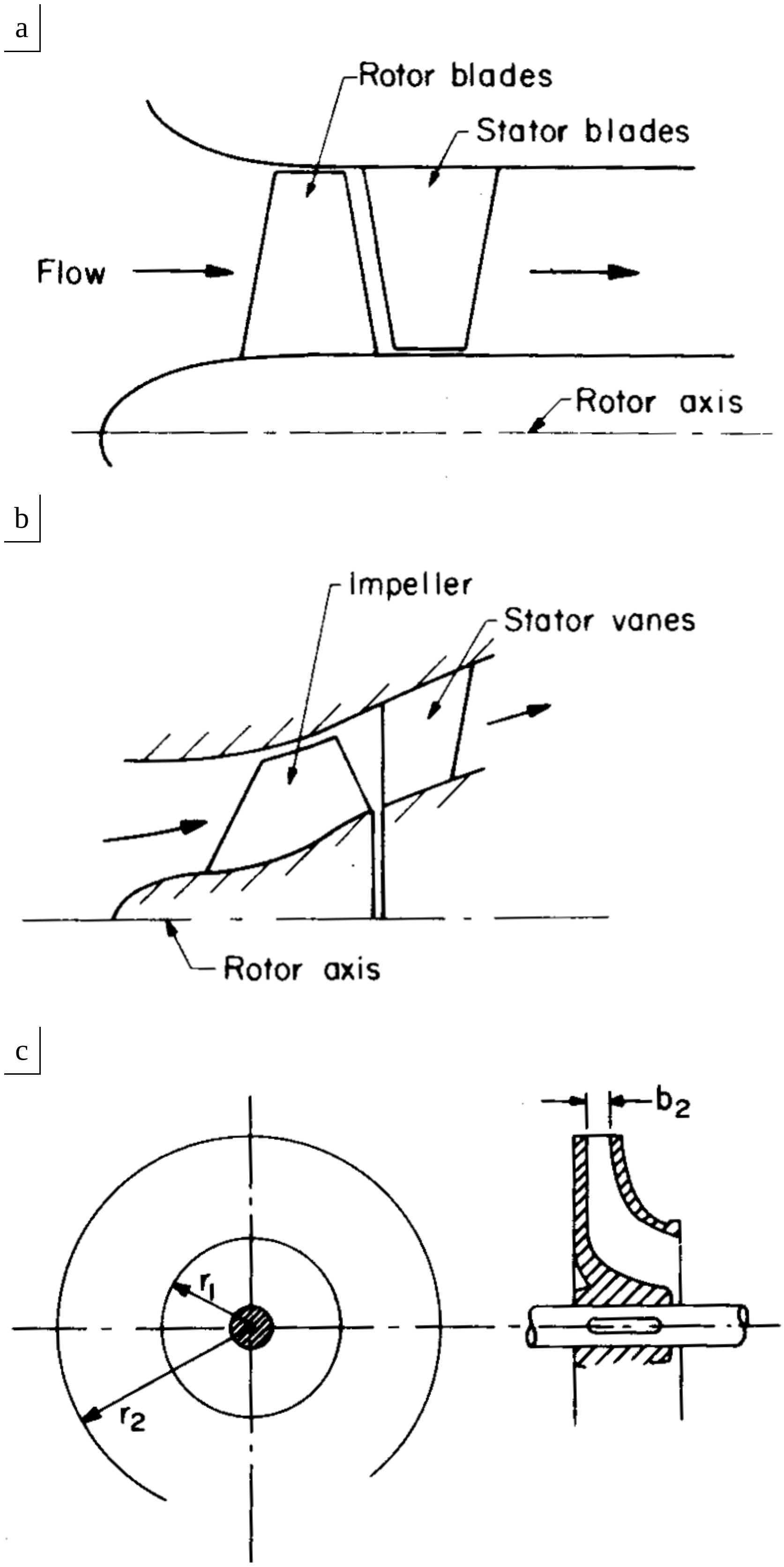

Figure 2.4: Schematic of an axial (a), diagonal (b) and radial (c) flow impeller. Copy of figures 1.10, 1.11 and 1.5 from “Turbomachinery: basic theory and applications” (Logan, 1993).

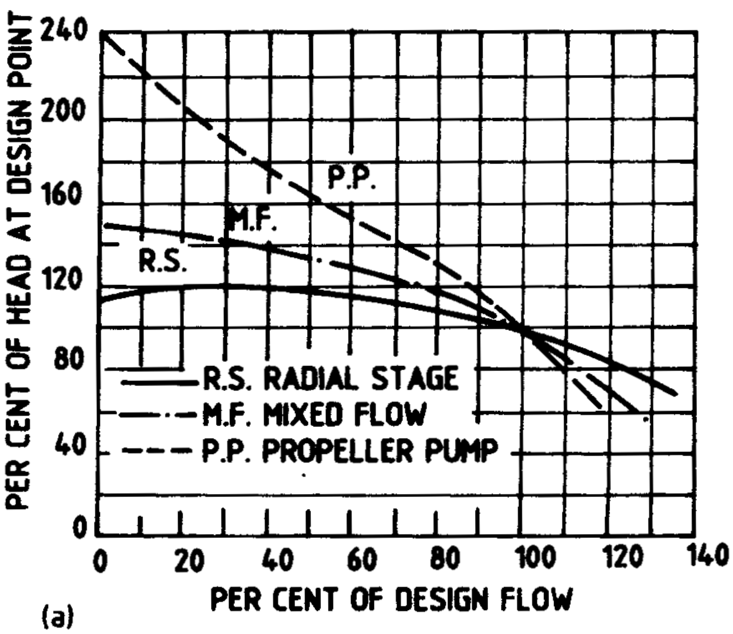

Figure 2.5: Characteristic HQ curve for an axial, radial and mixed flow impeller. Copy from "Principles of Turbomachinery" (Turton, 1995).

Clinical experience of the centrifugal pump goes as far back as 20 years ago. Centrifugal flow pumps like the Biopump, Capiox, Sarns Delphin, Isoflow, RotaFlow, Nikkiso, AB-180, Evaheart and Abiomed CF typically have a rotational speed of 2,000-5,000 rpm allowing for a flow rate ranging 80-160 cm^3/s. Exceptions are the Nikkiso and Gyro that with a rotational speed of 36,000 and 26,000 rpm, respectively, both support a flow rate of 160 cm^3/s. Like the axial pumps of group A, centrifugal flow pumps, are more invasive and more difficult to implant. They also require an inflow cannula from the ventricle and outflow cannula to the ascending or descending aorta to be connected to the pump.

Mixed flow pumps like the VentrAssist, HeartQuest and DeltaStream appear not to have reached clinical trials yet.

2.2 Review of axial flow pump design

Another type of rotary pump is the axial flow pump. Devices such as the Jarvik 2000, DeBakey, HeartMate II and INCOR (group A) deliver flow rates up to 115 cm^3/s at rotational speeds 7,000-13,000 rpm. These pumps tend to consist of an inducer, an impeller and a diffuser (figure 2.6). The static diffuser's function is to decrease the high tangential velocity of the blood exiting from the impeller and transferring this energy into an increase in pressure. These pumps are positioned outside the ventricle and a graft is applied between the ventricle and the ascending or descending aorta whereby the pump is positioned in between (figure 2.7).

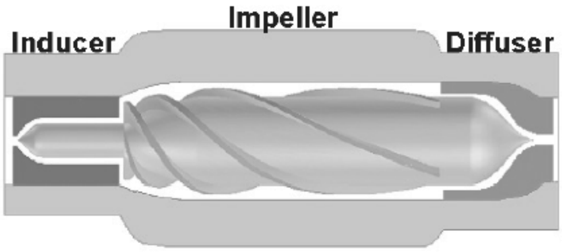

Figure 2.6: Schematic of the three main components an axial flow pump is typically composed of: the inducer, impeller and diffuser (Wood et al., 2005).

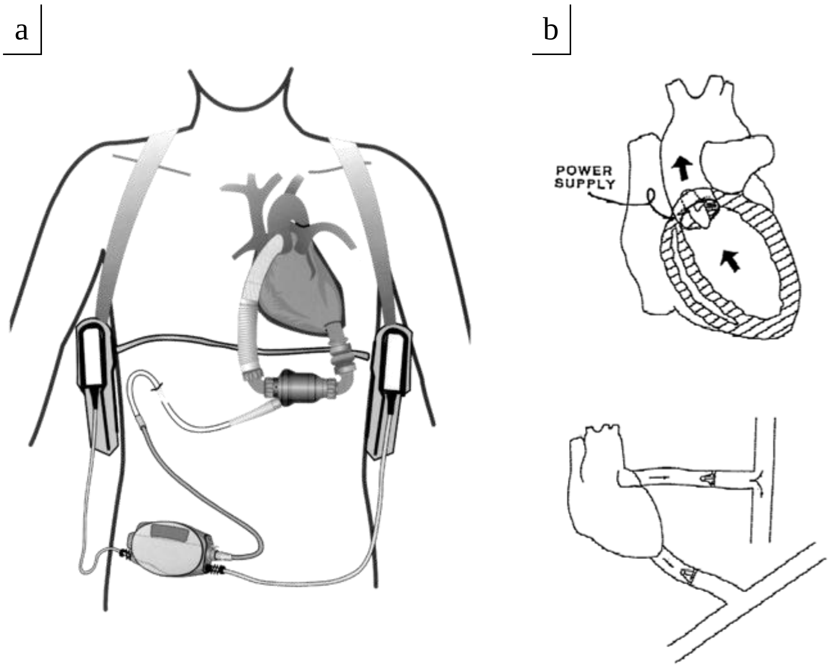

Figure 2.7: The HeartMate II LVAD System, an extracorporeal device, and the Valvo Pump, an incorporeal device. (Griffith et al., 2001; Mitamura et al., 1999).

The designs of the Hemopump and Impella axial flow pumps (group B) are quite different from the above by being small sized (diameter range of 6-8 mm in contrast to the 25-40 mm diameter of group A) and by operating at higher rotational speeds, 17,000-30,000 rpm instead of the 7,500-12,500 rpm of group A. Whereas the pumps of group A are positioned inside the body, but outside the ventricle and the circulatory system (figure 2.7), the Hemopump and Impella actually sit inside the ventricle and/or ascending aorta and are therefore easier to implant, namely through the femoral arteries, and are less invasive. With a delivery of approximately 75 cm^3/s the flow rate of these devices tends to be slightly lower than those of group A. Note has been made of the published developments of the Streamliner, Valvo Pump, IVAP and the INTEC that all seem to correspond with the characteristic design of axial flow pump group B. However, no evidence could be found that these devices have reached clinical trials.

Apart from the very first axial flow pump, the Hemopump, that started clinical trials in 1988, axial flow pumps that are currently used in clinic typically have up to 10 years of clinical history.

2.3 Turbomachinery fluid mechanics

The conventional design of an axial flow pump starts by applying the second law of Newton which states that, as the fluid is passing a rotating impeller, the change of angular momentum is equal to the torque (Stepanoff, 1957). In order to calculate flow rate, pressure rise, torque or power a finite control volume analysis may be used. Angular momentum given to an impeller makes the impeller rotate and torque is exerted on the fluid. Within this fluid region, a steady state control volume is defined at t_0 (figure 2.8a). The angular momentum principle states that the total torque, T, exerted on the control volume for a period Δt is defined by the rate of change of angular momentum, L:

$$\vec{T} = \frac{d\vec{L}}{dt} \tag{2.1}$$

Torque is produced by three elements: (1) the surface force, F, with force vector, r; (2) the sum of all body forces; (3) shafts crossing the control volume:

$$\vec{T} = \overbrace{\vec{r} \times \vec{F}}^{(1)} + \overbrace{\int_{\text{CV}} \vec{r} \times \vec{g} \rho dV}^{(2)} + \overbrace{\vec{T}_{\text{shaft}}}^{(3)} \tag{2.2}$$

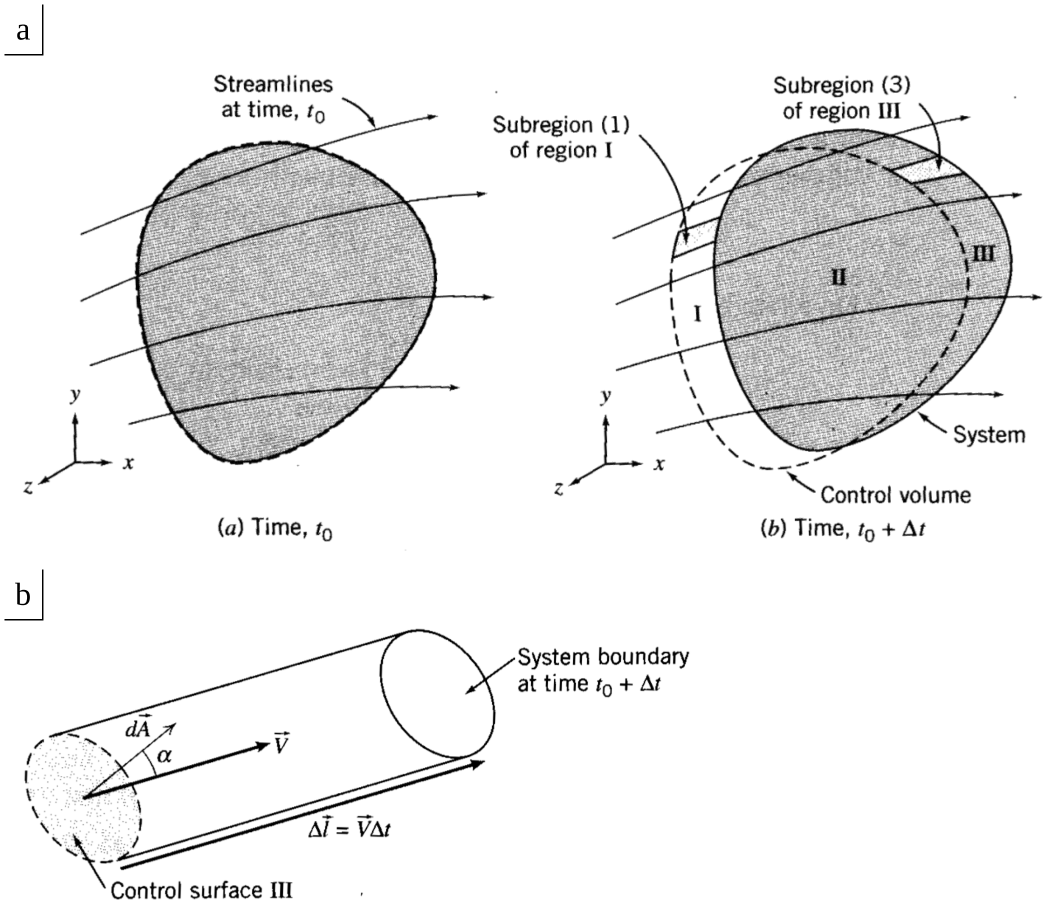

Figure 2.8: Definition of the control volume (a) and enlarged views of subregions 1 and 3. Copy of figure 4.1 from “Introduction to Fluid Mechanics” (Fox et al, 2011).

The period Δt is considered infinitely small, so the rate of change of angular momentum can be written as a derivative (2.3). The control volume at t_0+Δt consists of three regions; regions I and II consecute the state of the control volume at t_0 and regions II and III at t_0+Δt. Within regions I and III the angular momentum L_{I} and L_{III} are written in terms of a sum of absolute velocity vectors, c, of the flow working on a control surface, dA (figure 2.8b). This allows the derivative to be shortened to an equation that is also known as Reynold’s Transport Theorem (2.4).

$$\frac{d\vec{L}}{dt} \equiv \lim_{\Delta t \to 0} \frac{\vec{L}_{t_0+\Delta t} - \vec{L}_{t_0}}{\Delta t} \tag{2.3}$$

$$= \lim_{\Delta t \to 0} \frac{\left(\vec{L}_{\mathrm{CV}} - \vec{L}_{\mathrm{I}} + \vec{L}_{\mathrm{III}}\right)_{t_0+\Delta t} - \left(\vec{L}_{\mathrm{CV}}\right)_{t_0}}{\Delta t} \tag{2.3a}$$

$$= \lim_{\Delta t \to 0} \frac{\left(\vec{L}_{\mathrm{CV}}\right)_{t_0+\Delta t} - \left(\vec{L}_{\mathrm{CV}}\right)_{t_0}}{\Delta t} + \lim_{\Delta t \to 0} \frac{(L_{III})_{t_0+\Delta t}}{\Delta t} - \lim_{\Delta t \to 0} \frac{\left(\vec{L}_{I}\right)_{t_0+\Delta t}}{\Delta t} \tag{2.3b}$$

$$= \frac{\partial}{\partial t}\int_{\mathrm{CV}} \vec{r} \times \vec{c}\rho dV + \frac{\partial}{\partial t}\int_{\mathrm{CS_I}} \vec{r} \times \vec{c}\rho\vec{c} \cdot dA + \frac{\partial}{\partial t}\int_{\mathrm{CS_{III}}} \vec{r} \times \vec{c}\rho\vec{c} \cdot dA \tag{2.3c}$$

$$= \frac{\partial}{\partial t}\int_{\mathrm{CV}} \vec{r} \times \vec{c}\rho dV + \frac{\partial}{\partial t}\int_{\mathrm{CS}} \vec{r} \times \vec{c}\rho\vec{c} \cdot dA \tag{2.4}$$

Equations (2.1), (2.2) and (2.4) may be combined, leading to equation (2.5). For turbomachinery applications a control volume is chosen to enclose the rotor. Shaft torqueses are expected to dominate and therefore, as a first approximation, the surface forces are considered insignificant. Furthermore body forces are neglected due to symmetry (2.5a), shortening the equation to (2.6):

$$\vec{r} \times \vec{F} + \int_{\mathrm{CV}} \vec{r} \times \vec{g}\rho dV + \vec{T}_{\mathrm{shaft}} = \frac{\partial}{\partial t}\int_{\mathrm{CV}} \vec{r} \times \vec{c}\rho dV + \frac{\partial}{\partial t}\int_{\mathrm{CS}} \vec{r} \times \vec{c}\rho\vec{c} \cdot dA \tag{2.5}$$

$$\cancel{\vec{r} \times \vec{F} + \int_{\mathrm{CV}} \vec{r} \times \vec{g}\rho dV} + \vec{T}_{\mathrm{shaft}} = \cancel{\frac{\partial}{\partial t}\int_{\mathrm{CV}} \vec{r} \times \vec{c}\rho dV} + \frac{\partial}{\partial t}\int_{\mathrm{CS}} \vec{r} \times \vec{c}\rho\vec{c} \cdot dA \tag{2.5a}$$

$$\vec{T}_{\mathrm{shaft}} = \frac{\partial}{\partial t}\int_{CS} \vec{r} \times \vec{c}\rho\vec{c} \cdot dA \tag{2.6}$$

In its scalar form, equation (2.6) is also referred to as Euler's turbomachine equation (2.7):

$$T_{\mathrm{shaft}} = \left(r_2 c_{u_2} - r_1 c_{u_1}\right)\dot{m} \tag{2.7}$$

Hereby c_u is the tangential component of the absolute velocity, c, defined at inlet (1) and outlet (2) of the rotor (figure 2.9). In the figure the rotational direction of the blade is vertical and the flow will be passing horizontally. At the leading (left hand side) and trailing (right hand side) edge triangles are drawn to define the components of velocity.

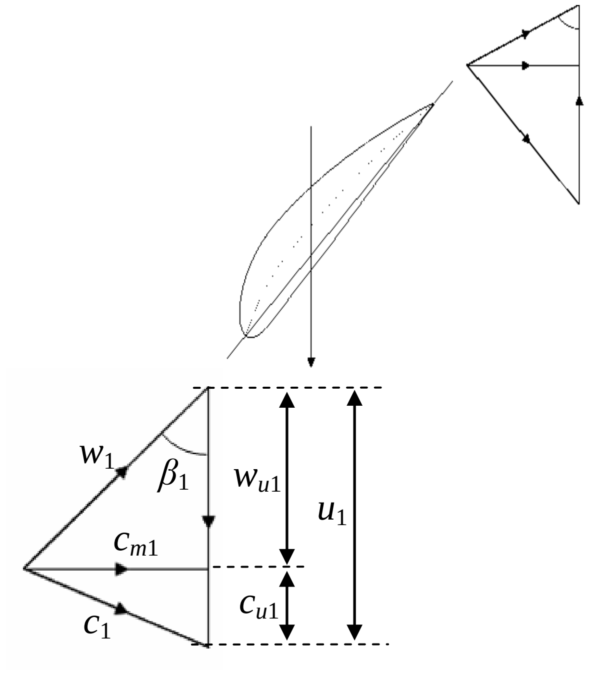

Figure 2.9: Definition of Euler's velocity triangles.

Equations (2.7) forms the fundament for all turbomachines. It may be rewritten in terms of work:

$$W = \omega T_{\text{shaft}}$$

$$W = \left(u_2 c_{u_2} - u_1 c_{u_1}\right)\dot{m} \tag{2.8}$$

where $u = r\omega$.

Further dividing equation (2.8) by $\dot{m}g$ an expression for the theoretical head is obtained:

$$H_t = \frac{W}{\dot{m}g} = \frac{1}{g}\left(u_2 c_{u_2} - u_1 c_{u_1}\right) \tag{2.9}$$

Specifically for axial flow pumps the following assumptions are made:

1. For any pump in general, angular momentum of the fluid is increased; the pump is doing work on the fluid (W>0).
2. Liquid is assumed to be entering the impeller axially, without secondary flows, hence c_{u1}=0.
3. Constant mean radius: $u_1 = u_2 = u = r\omega$.
4. Constant flow area, hence: $c_{m_1} = c_{m_2} = c_m$.

Considering these assumptions, equation (2.9) can be rewritten to be applied to axial flow pumps specifically:

$$H_t = \frac{uc_{u_2}}{g} \tag{2.10}$$

Equations (2.11) and (2.12) calculate the head and flow coefficient.

$$\varphi = \frac{c_m}{u_t} \tag{2.11}$$

$$\psi = \frac{H}{u_t^2/g} \tag{2.12}$$

2.4 Design aspects

The technique discussed in paragraph 2.3 offers a basic approach to estimate a pump's performance. However the underlying assumptions, neglecting surface forces and uniform inlet and exit flow, tangent to blade, make the theoretical calculations to always overestimate the actual performance. The technique is merely considering inertial forces and neglecting the dominating viscous flow conditions in VADs. The conventional design procedure is only used as a tool to obtain initial estimates and the main design is very much dependent on numerical and experimental work.

2.4.1 Blade geometry

Typically the blade angle is designed to vary across the blade span, to optimise the pressure difference between the two sides of the blade. These blade design changes influence the forces acting on the blade. At each location on the blade these forces may be different. When considering the sum of all forces, with an average overall blade angle (β_{ave}) and velocity (w_{ave}), the forces are composed of two components: lift and drag, respectively normal and parallel to the flow direction, with magnitude:

$$F_L = \tfrac{1}{2} C_L b l \rho w_{ave} \tag{2.13}$$

$$F_D = \tfrac{1}{2} C_D b l \rho w_{ave} \tag{2.14}$$

where C_L and C_D represent the lift and drag coefficient. Variations to blade geometry, such as width (b) and length (l) have a direct effect on the generated lift and drag forces and therefore the accompanied pressure difference. Other important design parameters are the blade angles relative to the entering (α) and exiting (β) flow, that influence velocity (w) and therefore also the lift and drag forces. The lift and drag coefficient, C_L and C_D, are obtained experimentally to characterise the performance for a specific blade shape.

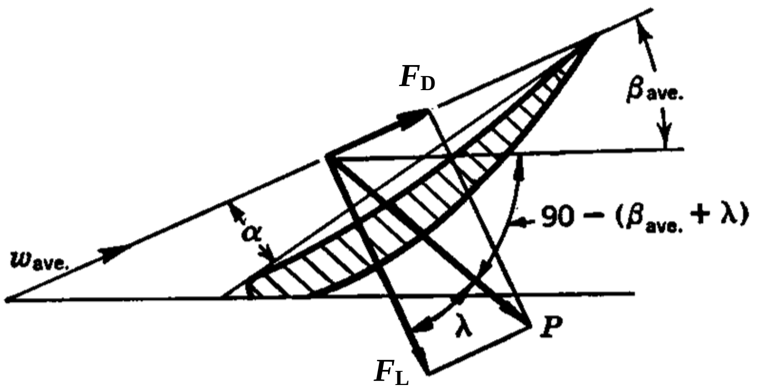

Figure 2.10: Lift and drag forces on an impeller (Stepanoff, 1957).

2.4.2 Blade clearance

As important it may be to have a rotor to propel the medium, it can also be important to define clearances. Especially the magnetic bearings associated with second generation pumping technology (paragraph 2.1.2), make designing such clearances possible. Traditional propulsion methods require physical contact between the rotating shaft and the blades. However, with magnetic propulsion the blades can “float” in the rotating magnetic field that is driving the blades, without physical contact at tip or hub.

Wu et al. investigated the effect of varying the clearance between the impeller and the housing in a numerical model of a centrifugal flow pump. The design of an unshrouded impeller (figure 2.11a) inherently has a leakage flow from the pressure to the suction side because of the clearance between the blade and the housing (figure 2.11b). This is making flow stagnate subsequently leading to reduced pressure rise. The work showed leakage flow increases as the gap is increased. With an increased gap, more pressure rise is required to reach the same flow rate (figure 2.11c). This may come as no surprise. More interestingly, calculations predicted an optimal point, with a gap of 100 µm, where blood damage is reduced (figure 2.11d) (Wu et al., 2009).

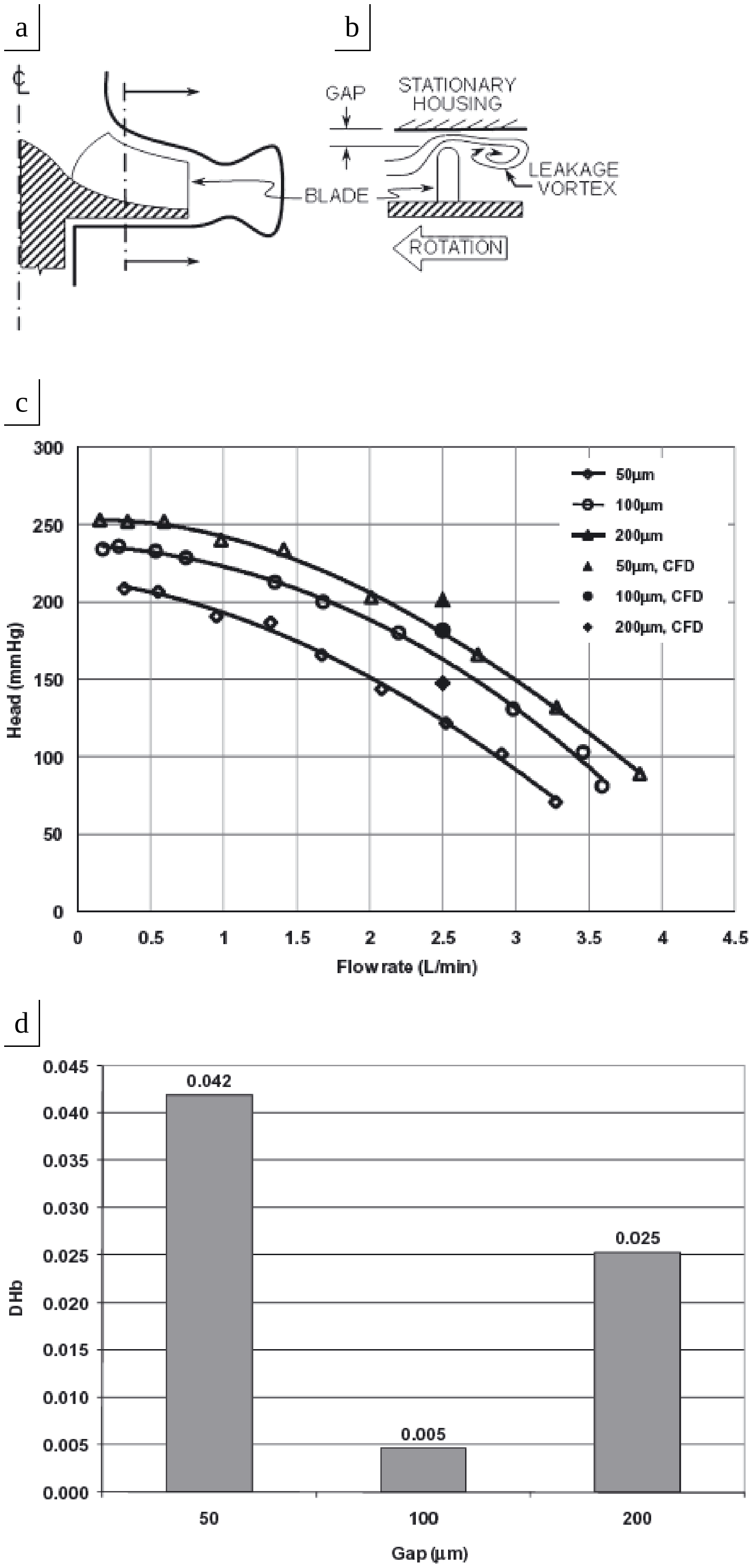

Figure 2.11: Design study of a centrifugal impeller, optimising blade clearance (a-b) by assessing HQ characteristics (c) and blood damage (d) (Wu et al, 2009).

Triep et al. investigated a similar gap, between rotor and stator, on an axial flow pump. Their work investigated the design of novel pump, the MicroVAD, equipped with magnetic bearings (figure 2.12a). The rotor, floating and held in place by a pivot ball, is driven by a rotating magnetic field. Due to the floating nature of the magnetic propulsion, the impeller is bound to have clearances. The design accommodates for this and to avoid flow stagnation, a washout channel is designed to increase flow circulation.

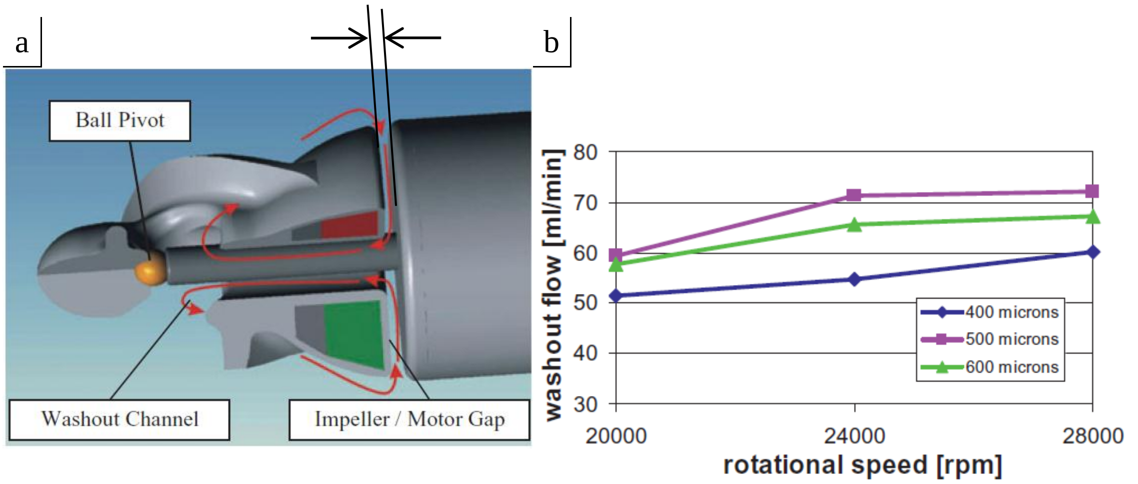

Figure 2.12: Design study of an axial impeller, optimising blade clearance (a) by assessing the flow rate through a washout channel (b) (Triep et al., 2008).

The design range of the clearance had an upper and lower limit due to mechanical constrictions. A clearance larger than 600 µm would no longer guarantee the impeller to be confined by the magnetic field. To ensure there is no physical contact (and damage) between rotor and stator, a minimum clearance was defined at 400 µm. The numerical work found an optimal clearance of 500 µm with maximum flow rate through the washout channel (figure 2.12b) (Triep et al., 2008).

2.4.3 Inducers and diffusers

The inducer and diffuser vanes are static and placed in the flow path, respectively prior to and after the impeller. Incoming flow will first pass the inducer to ensure flow approaches the impeller at the correct angle. Second, it reduces the secondary flows. The impeller itself generates pressure rise and increases tangential velocity of the blood. The diffuser can decrease the high tangential velocity exiting from the impeller and transfer this energy into additional pressure rise.

A typical axial flow blood pump will come with all three of these components. This is for example seen in the Debakey pump, inducer (2), impeller (3) and diffuser (4) as indicated in figure 2.13. In addition, this pump was also equipped with a flow straightener. More recent designs, such as the Impella (figure 2.12a), have a more integral design whereby some components are combined.

Figure 2.13: Design of the Debakey pump, consisting of a flow straightener (1), inducer (2), impeller (3) and diffuser (4) (Debakey, 1997).

A particular study by Song et al. investigated the disadvantages certain inlet and outlet devices may have (table 2.1). From the devices mentioned in table 2.1, only the inducer and diffuser specifically apply for axial flow pumps. The study concludes that for an inducer may lead to non-uniform flow distribution, high stress and whirl. Whilst a diffuser can lead to head pressure loss, flow separation and whirl (Song et al., 2004).

Table 2.1: Study of advantages and disadvantages of using specific inlet and outlet devices (Song et al., 2004).

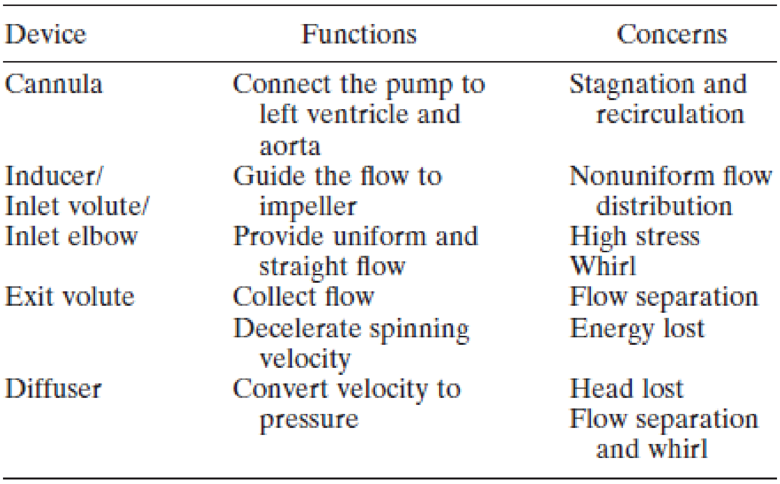

Device	Functions	Concerns
Cannula	Connect the pump to left ventricle and aorta	Stagnation and recirculation
Inducer/ Inlet volute/ Inlet elbow	Guide the flow to impeller Provide uniform and straight flow	Nonuniform flow distribution High stress Whirl
Exit volute	Collect flow Decelerate spinning velocity	Flow separation Energy lost
Diffuser	Convert velocity to pressure	Head lost Flow separation and whirl

Untaroiu et al. investigated specifically the function of the diffuser parametrically. For the specific axial flow pump design of this study it was concluded the use of a diffuser was important in order to have good hydraulic performance. The head pressure loss associated with the use of a diffuser was numerically found to be 12 mmHg. It was found this loss can be compensated for by increasing the rotational speed with 500rpm. Flow separation was kept to a minimum by setting the downstream diameter slightly larger than the inlet diameter. Whilst also setting the channel divergence angle to be less than 8 degrees in. By increasing the cross-sectional area (from d to D), the axial velocity of the blood flow leaving the pump is reduced. Finally shear stresses were retrieved from the numerical results and found too small to cause significant haemolysis (Untaroiu et al., 2005). This study shows the concerns a specific inlet or outlet device is inherently sensitive for, can be avoided by choosing specific design characteristics.

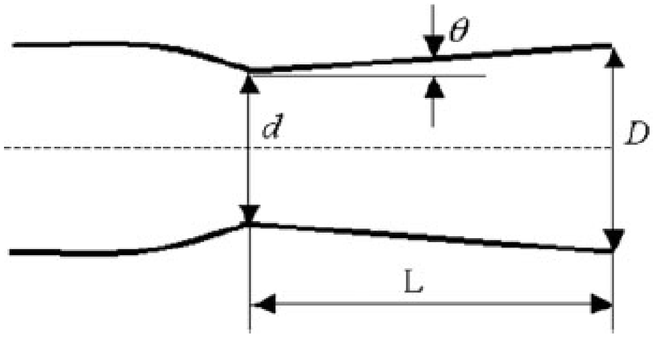

Figure 2.14: Designing the diffuser; inlet, d, and outlet, D, diameter, the divergence angle, θ, and the total length of expansion, L (Untaroiu et al., 2005).

2.4.4 Operational setting

The following operational requirements are considered in the design process of an axial blood flow pump (Wood et al., 2005). The following points relate to the operational setting of the pump and may only become more relevant in a later stage of the design process.

Implantibility

Constraining the pump diameter to be no more than 12 mm might enable the pump to be easily implanted in the ascending aorta through the femoral arteries. It is expected to apply a stent construction and use magnets to attach the pump to the stent. Deactivation of the magnets will enable easy removal of the pump from the patient.

Durability and portability

The aim is to exploit the pump for short-term treatment and therefore the criteria on durability and portability do not have to be very strict. The pump will have to be durable enough to last up to several weeks. A possible limited portability will not threaten the patient’s ability to live a comfortable life. Coils placed on the chest may be used to power the pump wirelessly making the system more portable.

Control feasibility and reliability

Based on the heart rate, the electronics of the pump are to change rotational speed accordingly, allowing the patient to do light physical activities. An ECG will be fed to the electronic controls of the pump.

2.4.5 Blood trauma

Haemolysis, the premature damage and/or destruction of red blood cells, may occur when blood is exposed to high levels and/or long durations of stress (Paul et al., 2003). As red blood cells carry oxygen to the body, a lack of red blood cells will result in reduced oxygen transport to the body. Further levels of shortage of red blood cells may also result in a state of haemolytic anemia. Several factors, pathological and external, play a role in the cause of haemolysis but the main cause for haemolysis in ventricle assist devices is deformation and fragmentation of red blood cells due to shearing (Arora, Behr & Pasquali, 2004). The level of haemolysis is hereby dependant on the amount of shear stress and the exposure time. Non-occluded arteries commonly have a shear stress in the range 3-50 Pa, depending on arterial properties. Another important factor is the surface roughness of the pump, that may results in blood damage.

Many studies have been carried out to obtain measurements of haemolysis by performing test-loop experiments using human or animal blood (Kawahito & Nosé, 1997; Takami et al., 1996; James et al., 2003). This type of experiment, however, does not allow for local estimation of haemolysis and only allows for collection of global averages. Use of flow visualization techniques (such as Particle Image Velocimetry, PIV) making it possible to obtain local estimates of haemolysis (Yamane et al., 1998). Whereas experimental haemolysis analysis can be time consuming and expensive, CFD analysis is less so and enables determination of pump performance during design modifications. In CFD haemolysis is dependent on a suitable blood damage model to calculate the haemolysis index based on the calculated shear flow data (Arora, Behr & Pasquali, 2004).

Another important factor is thrombosis. Usually a thrombus is formed to stop blood loss by repairing damaged vessels. Irregular flow patterns and inflammatory conditions within the vessels could, however, lead to unnecessary thrombosis formation, which will subsequently result in (partial) vessel occlusion. To avoid unnecessary thrombosis, low levels of shear stress should be avoided since that will result in recirculation (Wurzinger, Opitz & Eckstein, 1986). Other factors causing thrombosis are flow separation, narrow passages or clearances and flow stasis or stagnation. But apart from lysis to red blood cells, similarly platelets are also sensitive to shear. As detailed in paragraph 1.3.1, platelet activation can lead to coagulation problems.

2.5 Computational fluid dynamics

In 1996 Burgreen et al. demonstrated the use of computational fluid dynamics (CFD) as a design improvement strategy for axial flow pumps. CFD is a modelling technique whereby a fluid domain is defined and meshed. The software subsequently solves equations for conversation of mass and momentum. The numerical results allow for analysis of hydraulic performance, flow visualisation, shear stress and blood damage. Burgreen et al. carried out iterative CFD simulations on 4 different designs whereby the effect of geometrical changes to the guide vanes and the blade profile were investigated. This work showed how a blood pump may be designed by merely using CFD, without using conventional turbo machinery design theory. The authors do state the work is very dependent on intuitive “trail-and-error”.

Similar work was carried out by Untaroiu et al. in 2005 and by Triep et al. in 2006. In both cases the design underwent modifications iteratively and with these works the numerical measurements were validated. Untaroiu et al. carried out a bench experiment on a mock pump (in vitro) and performed animal experiments (in vivo). Triep et al. used particle image velocimetry to be able to compare velocity profiles obtained numerically and experimentally.

2.5.1 Turbulence model

Both of the aforementioned studies used a k-ε turbulence model with the CFD simulations. The k-ε turbulence model has successfully been used for several years and has become standard available in most CFD commercial software packages. The model is regarded the more conservative option for assessing pump performance. The first main disadvantage of the k-ε model is the low accuracy for modelling flow with low Reynolds numbers (table 2.2). Secondly, the model does not model flow separation along a boundary very well. The k-ω model performs better on those points, but is found rather sensitive to turbulence free-stream boundary conditions defined at the inlet. The SST k-ω model combines the functionalities of both these models.

More recently numerical work is carried out using the shear stress transport (SST) model (Throckmorton et al., 2007; Wu et al., 2010). These works choose the SST turbulence model over the common k-ε model as this model is more able to model turbulent flow of a low Reynolds number. The k-ε model is believed most suitable during the design phase, as it offers a more conservative calculation. The SST model is believed most suitable for more details optimisation studies and prototype manufacturing (Untaroiu, 2005).

Table 2.2: Comparing advantages and disadvantages of different turbulence models.

	k- ε model	k-ω model (generic)	k-ω model (SST)
Turbulent flow with low Re-number	–	+	+
Flow separation along boundary	–	+	+
Not sensitive for turbulence free-stream boundary conditions	+	–	+

2.5.2 Non-Newtonian modelling

Above shear rates of 100 s^{-1}, blood may be considered Newtonian (Berger and Jou, 2000). In transient studies when the flow stops, the shear rate can reach up to approximately 1000 s^{-1} in the larger arterial vessels (Cho and Kensey, 1991).

Kilpatrick et al. investigated non-Newtonian blood modelling in coronary arteries in steady state (2004) and transient (2006) conditions. Similarly to Ballyk et al. (1994) and Cho and Kensey (1991), different non-Newtonian models were compared and tested under which conditions non-Newtonian flow behaviour becomes apparent. These models are chosen because, even though there are many non-Newtonian blood flow models, no one model is universally accepted (Cole et al., 2002; Nget al., 2002; Misra and Ghosh, 2001). The Power Law model and Walburn–Schneck model predict decreasing viscosity at high strain. Cho and Kensey (1991) showed that the Power Law model can accommodate for the Newtonian behaviour above shear rates of 100 s^{-1}, by assuming constant viscosity at strains above 226.5 s^{-1}. This study also proposed modified parameters for the Power Law model and these values were tested in by Cole et al. (2002). The Walburn–Schneck model also includes haematocrit, H (the volume of red blood cells), but this merely moves the viscosity-strain curve vertically or changes the slope.

Like the Walburn-Schneck model, the Casson model can also accommodate for haematocrit. However, this model limits viscosity at high shear slightly above the usual Newtonian value. Nevertheless, Cho and Kensey (1991) found that this model compares well with the experimental data.

The Generalised Power Law model is considered the general model for non-Newtonian blood viscosity (Ballyk et al., 1994). It includes the Power Law model at low strain, the Newtonian model at medium and high strain and includes the Casson model under special circumstances (Ballyk et al., 1994).

2.5.3 Correlating Shear stress and Blood trauma

Typically the release of haemoglobin is used as an indicator for haemolysis and many studies have been carried out to define the relationship between amount and exposure time of shear stress and haemoglobin release (Bludszuweit, 1995; Wurzinger, Opitz & Eckstein, 1986; Paul et al., 1999). Heuser et al (1980) and Giersiepen et al (1990) used a two-dimensional regression analysis on their data to establish their empiric formula for the calculation of a haemolysis index (HI) in percent:

$$HI = C \cdot \tau^{\alpha} \cdot t^{\beta} \tag{2.15}$$

where t_{exp} is the exposure time (s) and τ (N/m^2) indicates the overall single scalar stress tensor. C, α and β are constants. Heuser et al defined these constants as $C = 1.8 \cdot 10^{-6}$, $\alpha = 1.991$, and $\beta = 0.765$. Giersiepen et al defined them as $C = 3.62 \cdot 10^{-5}$, $\alpha = 2.416$, and $\beta = 0.785$. Researchers who have applied this formula on their data confirm both models yield values close to values of hemolysis observed in blood pumps (Wu et al., 2010).

The above correlation is valid for steady shear only whilst the flow in the ventricle assist device is three-dimensional and unsteady. Bludszuweit (1995) therefore proposed to calculate τ, representing an instantaneous one-dimensional stress parameter in the above equation, by summing the components of the viscous and Reynolds stress tensor:

$$\tau = \left[\frac{1}{6}\sum\left(\tau_{ii} - \tau_{jj}\right)^2 + \sum \tau_{ij}^2\right]^{1/2} \tag{2.16}$$

More recently Arora et al (2004) proposed a tensor based blood damage model (opposed to the stress based models mentioned above) for CFD analysis. Time- and space dependent strain is hereby estimated for individual blood cells and correlated to data from steady shear flow experiments.

2.6 Rational for this study

Since the first clinical study of the axial blood flow pump “Hemopump” in 1988 several axial blood flow pumps have been developed and are clinically used to either provide bridge-to-transplant or destination therapy for cardiac failure patients. Apart from the axial flow pump, the centrifugal pump is also widely used in clinic. Axial and centrifugal pumps are both widely used clinically to provide continuous flow, in contrast to positive displacement flow pumps that provide pulsatile flow. Much research has been carried out to determine the effects of providing circulatory support by means of continuous or pulsatile flow. Even though arterial flow has a pulsatile character, several studies have shown that pulsatile flow does not affect the circulation and organ function (Allen, Murray & Olsen, 1997). However, the implications of long-term continuous flow conditions remain unclear, although hundreds of CHF patients have had continuous flow support exceeding thousands of hours (Allen, Murray & Olsen, 1997). Furthermore pulsatile heart pumps experience more mechanical failures than the continuous flow pumps due to failing membranes and valves (Goldstein & Oz, 2000). Components such as valves and air chambers are usually larger in pulsatile heart pumps than in continuous flow ones, resulting the latter to be significant smaller overall and thereby improving comfort and portability.

The axial flow pump has many benefits compared to the centrifugal pump which are mainly attributed to its small size (<10-15mm) and is therefore being minimally invasive which makes the axial flow pump unique. All flow pumps currently commercially available only support blood flow in one direction, either during systole or diastole. Currently an axial flow pump will either be used to support flow towards the organs during systole or to perfuse the coronary arteries in diastole to feed the heart muscle but none of the existing axial flow pumps are able to support flow during both parts of the heart cycle.

2.7 Aims and objectives

This work aims to design the blades of an axial flow pump that, synchronised with the heart cycle, will support flow bi-directionally. This is to be achieved by alternating the flow direction. By rotating the blades in one direction, blood flow is delivered towards the organs during systole, and by rotating in the opposite direction flow is supported towards the coronary arteries. For the pump to reach flow to the coronary arteries during diastole, the pump will need to be positioned in the ascending aorta. The aim is to deliver up to approximately half the cardiac output during systole, 35 cm^3, and 20 cm^3 (4x of the cardiac delivery to the coronary arteries) during diastole. This bi-directional axial flow pump may be used to support the circulatory system temporarily, for example during BTR therapy, but not to replace the function of the ventricle.

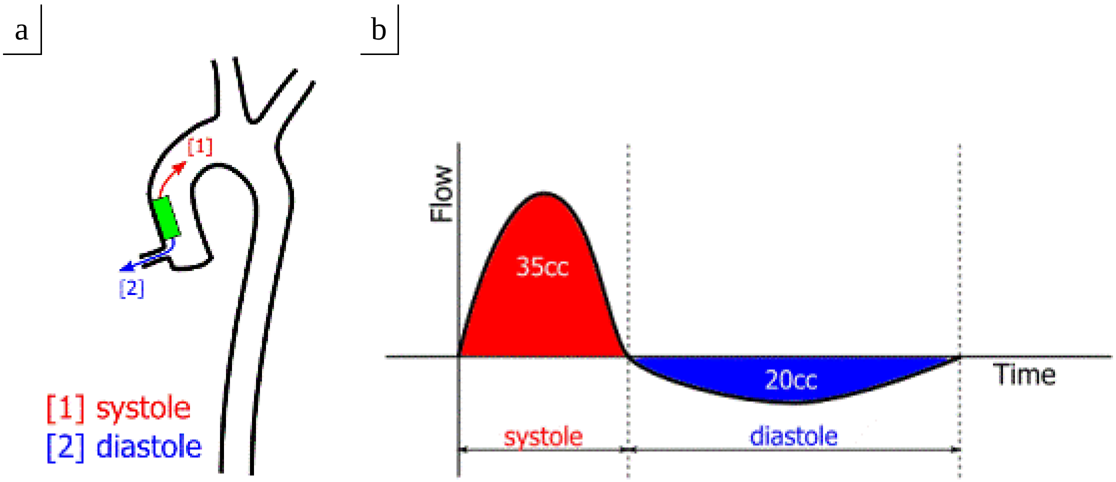

Figure 2.15: During systole the pump will support flow towards the body. At the end of systole the rotational direction is reversed to support flow towards the coronary arteries.

The main challenge is to develop a blade profile to support the flow bi-directionally. Traditional blade profiles, designed to rotate in a single direction, have a round leading edge and a sharp trailing edge to maximise the pressure difference between the pressure and suction side the blade (figure 2.16).

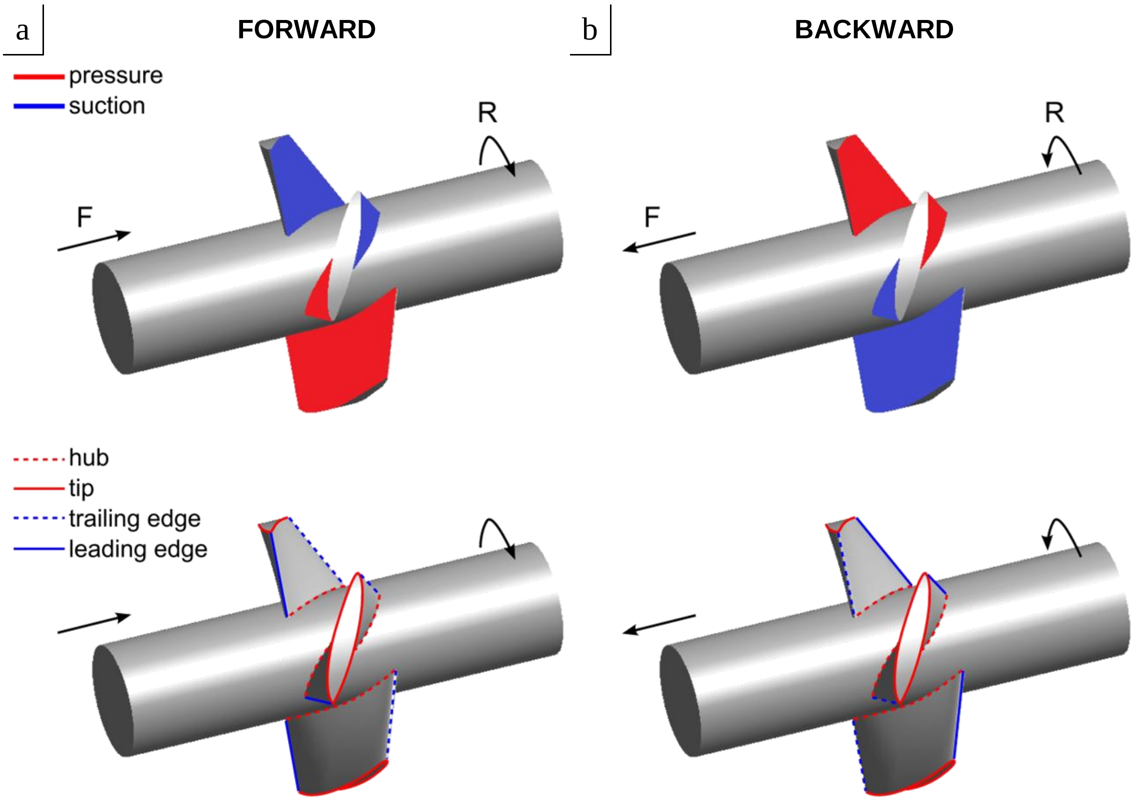

Figure 2.16: Definition of the flow direction (F), rotational direction (R) and the turbo machinery terminology in forward (a) and backward (b) direction.

The hydraulic performance will therefore be significantly reduced when the same profile is used to support flow in the opposite direction. Profile modifications designed to improve performance when rotating in the backward direction are likely to affect performance in the forward direction. The challenge is to find a compromise in between that leads to acceptable performance in both directions. This challenge is outlined as follows:

1. Blade design:
    a. Establish the uni-directional design characteristics of a forward and backward blade individually using zero-dimensional turbo machinery design theory.
    b. Investigate possibilities of using existing (aerofoil) blade profile designs.
    c. Propose a blade profile design that will perform in either rotational direction.
2. Numerical simulations:
    a. CFD simulations to verify uni-directional design characteristics (point 1a).

   b. Parametric CFD study during the bi-directional blade profile design process. To explore possibilities of design modifications and determine the effects these changes have on hydraulic performance in either rotational direction.
   c. Decide on a final bi-directional blade design on the basis of the parametric CFD design study (point 2b).
   d. CFD simulations to characterise the final blade design.
3. Experimental validation:
   a. Built a prototype of the final blade design.
   b. Design an experimental rig to measure pressure rise and flow characteristics.
   c. CFD simulation of final design, using the same conditions as the experiment, i.e. same fluid density and viscosity, same tip clearance.
   d. Take measurements to validate the numerical results.

2.8 Thesis outline

This thesis is comprised of the following chapters:

3. Methodology: First, the design criteria as stipulated by the clinical need are discussed, which is followed by defining design parameters and how these were calculated. Then the theoretical basis for calculating the profile of axial flow pumps is introduced. The initial blade design is tested and optimised using numerical models. This chapter also includes information on the experimental set up, which includes a specifically designed rig for testing the designed blades.
4. Results I: Numerical Simulations: This chapter lists the results of all numerical models that grow in complexity as the study progressed. Starting from a 2D model of a single blade passage, to a 3D model of the complete impeller. Finishing with a 3D model mimicking the environment of the impeller inside the ascending aorta.
5. Results II: Experimental Validation: This chapter lists the results of all measurements, both steady state and transient. Pressure and flow characteristics are presented.

6. Discussion: Both the numerically and experimentally obtained results are compared to test whether how well the numerical models mimic reality. The limitations associated with design simplifications are stipulated and discussed.
7. Conclusions and Future Work: Conclusions are drawn from the obtained results and compared against the aims and objectives from paragraph 2.7. To finalise, suggestions are made on what areas of this study future work can expand.

3 Methodology

The process steps involved to design the proposed bi-directional blood flow pump are visualised in figure 3.1. The first step is to define the design criteria against which the final design will be verified. Secondly, conventional turbomachinery design theory is used to calculate the blade angles. This, together with a proposed bi-directional blade profile design, establishes an initial pump design. By means of numerical parametric design iterations the initial design is optimised until the design is deemed optimal. Optimising the design for increased pressure rise in one direction will result in decreased pressure rise in the other direction. A design is deemed optimal when a good balance is found between generated pressure rise in forward and backward direction and all design criteria are met. Once the optimal design is finalised a prototype is built and a bench experiment is carried out. The numerical and experimental results are compared. If discrepancies are found, it may be necessary to verify the setup of the numerical model or the experiment. When the results are in good agreement, the numerical model is considered to be validated and the design may be finalised.

3.1 Design criteria

The pump is intended to be placed in the ascending aorta (figure 2.15a). It might be positioned against the wall or in the centre of the aorta. Therefore, the pump diameter is constrained to a maximum of 12 mm. When positioned in an ascending aorta of Ø25 mm, this implies the pump will occupy 23% ($=12^2/25^2$) of the cross-sectional area. A pump diameter of no more than 12 mm allows the pump to be easily implanted in the ascending aorta through the femoral arteries. It is expected to apply a stent construction (similar to as shown in figure 1.4) and use magnets to attach the pump to the stent. Deactivation of the magnets will enable easy removal of the pump from the patient. This operational setting implies the pump should not be used when the patient is suffering from a regurgitating aortic valve as a failing aortic valve will make the pump deliver flow back to the ventricle rather than to the coronaries during diastole.

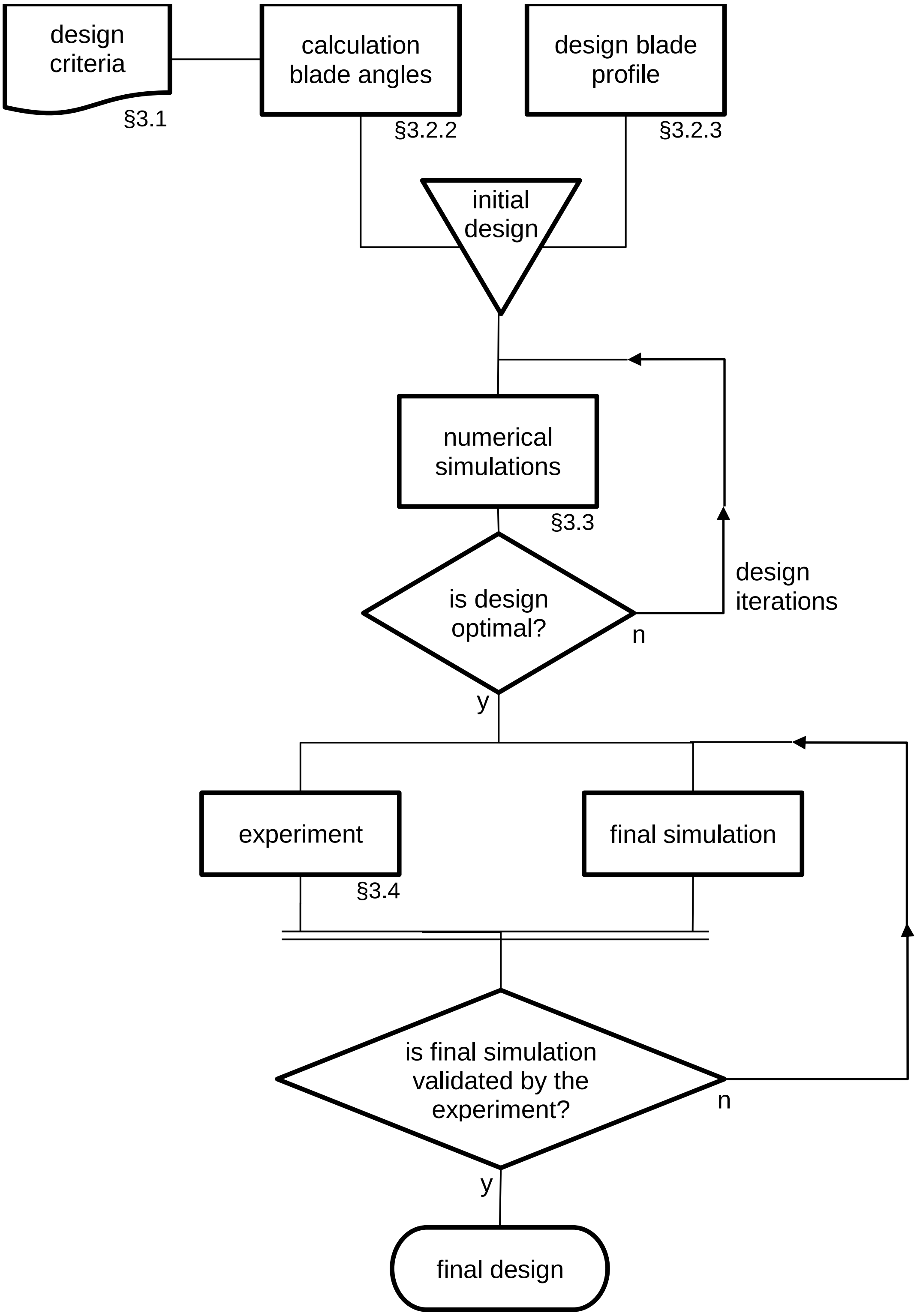

Figure 3.1: Flowchart of the design process (according to ISO 5807:1985).

The physiological systolic pressure difference between the ventricle and the ascending aorta is ~0.2 kPa. In each direction the pressure rise is aimed at 2 kPa, which is well above the 0.2 kPa to account for expected losses of pressure rise by guide vanes. During operation, the pump is to accelerate at the start of systole and deliver up to 35 cm^3, which approximates half of the cardiac output, towards the organs (figure 2.15b). The pump decelerates in the second half of systole to reach 0 rpm at the end of systole, also the start of diastole where the rotational direction changes. At the start of diastole, from 0 rpm, the pump will accelerate in the opposite direction and deliver up to 20 cm^3 towards the coronary arteries, corresponding to half the delivery of a 40 cm^3 intra-aortic balloon pump (IABP). The increased coronary flow will allow pressure rise to be generated and therefore the flow volume entering the coronary arteries is expected to be much smaller than 20 cm^3. The pump should decelerate and come to a full stop before the end of a full heart cycle. Flow delivery is adjusted by changing the rotational speed to make sure the total flow, generated by the weak ventricle and the pump, matches levels of that expected of a healthy ventricle.

3.2 Theoretical design

A well-established design method for the blades of unidirectional axial flow pumps was described in “Centrifugal and Axial Flow Pumps” (Stepanoff, 1957). This method allows for the theoretical calculation of the required design parameters, such as rotational speed, inlet/outlet blade angle, pitch and chord. The calculations require input parameters that need to be defined using characteristic data found in the literature. Some of the input parameters require design simplifications.

3.2.1 Design simplifications

In order to determine a flow rate, assumptions will need to be made about the time period during which 35 cm^3 systolic and 20 cm^3 diastolic flow is delivered. The duration of the systolic and diastolic phase depends on the length of the total duration of the heart beat and the duration ratio between the two phases. A healthy human heart rate ranges between 60 and 100 bpm. An average heart rate is considered of 60 bpm, implying an average heart beat period of 1 s. The systole/diastole-ratio of a human heart may vary between 0.5 and 1.0. A systole/diastole ratio of 0.5 is more likely to occur at lower heart rates (60 bpm) and the 1.0 ratio is associated with higher heart rates. This research considers a heart rate of 60 bpm and a systole/diastole ratio of 0.5. An average systolic flow rate may now be calculated, for 35 cm^3 to be delivered in 1/3 s, leading to 105 cm^3/s. Likewise, for a 2/3 s long diastolic phase, for 20 cm^3, an average flow rate is calculated of 30 cm^3/s. Physiological flow velocity in the ascending aorta ranges between 0 en 1.0 m/s. The flow velocity inside the pump, U, should therefore also not exceed the upper boundary of 1.0 m/s.

$$U = \int_h^t c_m dA \tag{3.1}$$

As introduced in paragraph 2.1.2, specific speed is a characteristic value of how radial or axial the blade of a pump is. The higher specific speeds, between 3.5 and 5.5 are associated with axial flow pumps (figure 1.4). For the theoretical design calculations, specific speed is therefore used as an input parameter, with an average value for specific speed of 4.0. Summarising the design criteria from paragraph 3.1 and the above design simplifications, the following input parameters have now been defined:

flow rate (Q):	105 cm^3/s for systole 30 cm^3/s for diastole
head pressure (H):	2 kPa
tip diameter (d_t):	12 mm
specific speed (N_s):	4.0
flow velocity (U):	1.0 m/s

3.2.2 Calculation of blade angles

The process behind the theoretical design of a uni-directional axial flow pump is visualised in figure 3.2. As the methodology accommodates for uni-directional designs, two sets of theoretical designs parameters are calculated, for forward, systolic and backward, diastolic flow. Two flowcharts of calculations need to be followed. Flowchart 1 (figure 3.3) is repeated two times, for systole and diastole. Flowchart 2 (figure 3.5) is repeated four times, for systole and diastole both at tip and hub location. The design method for the blades of unidirectional axial flow pumps relies on industrial charts, as shown in figure 3.4. This standardised design methodology may not be accurate as these industrial charts have been developed for larger applications so further verification is necessary. The purpose of this process is, however, to get a preliminary design and further design alterations are made through CFD analysis.

The main outcomes, as shown in the two tables at the bottom of figure 3.2, suggest a maximum rotational speed of 5,800 rpm during systole and 11,000 rpm during diastole. With a tip diameter of 15 mm, the hub diameter follows to be in the range of 6 (systole) -13 (diastole) mm. The theory suggests a recommended number of 4 vanes, with a chord length of 4-8 mm.

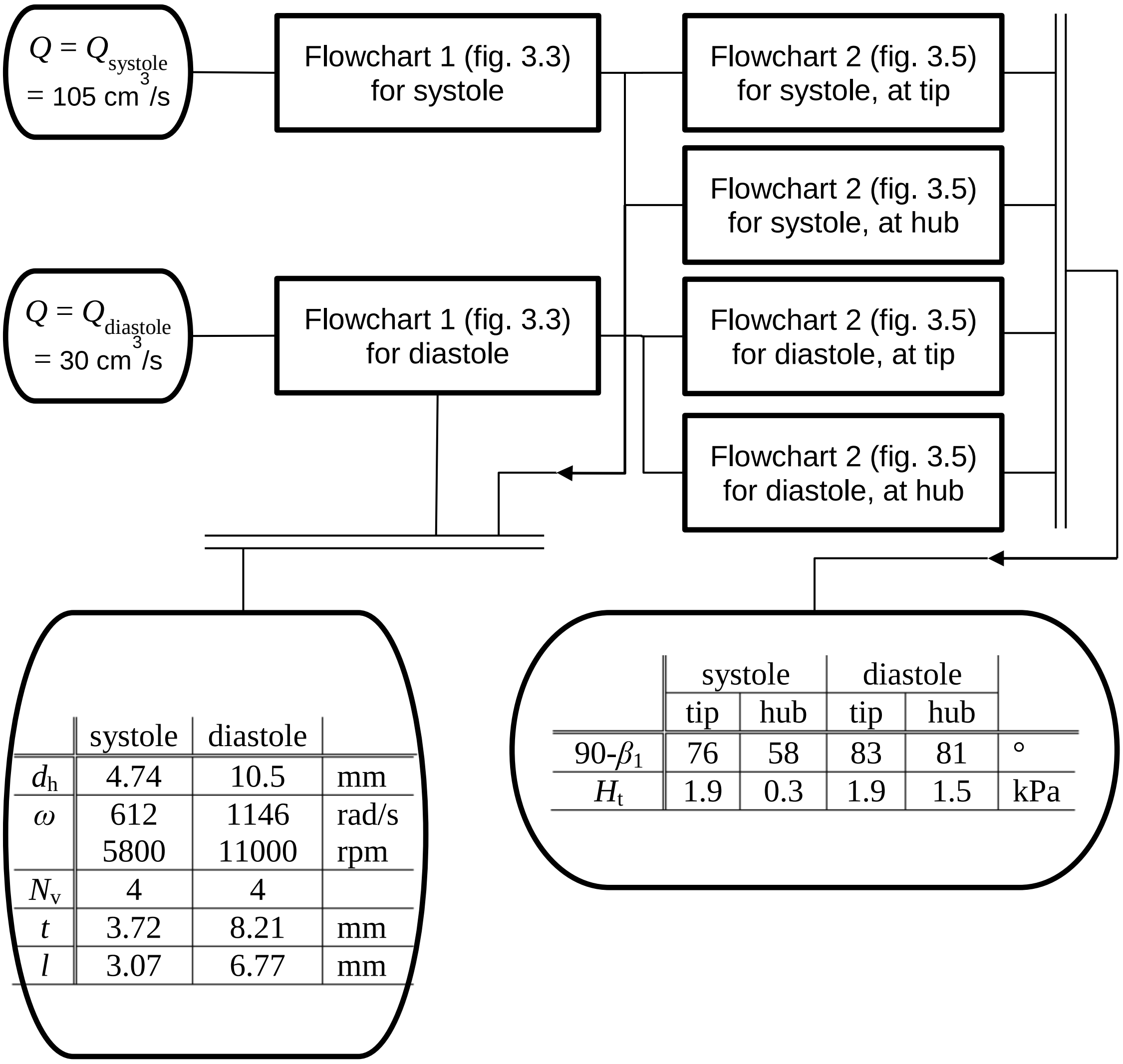

	systole	diastole	
d_h	4.74	10.5	mm
ω	612 5800	1146 11000	rad/s rpm
N_v	4	4	
t	3.72	8.21	mm
l	3.07	6.77	mm

	systole		diastole		
	tip	hub	tip	hub	
$90\text{-}\beta_1$	76	58	83	81	°
H_t	1.9	0.3	1.9	1.5	kPa

Figure 3.2: Flowchart for the calculation of blade angles (according to ISO 5807:1985).

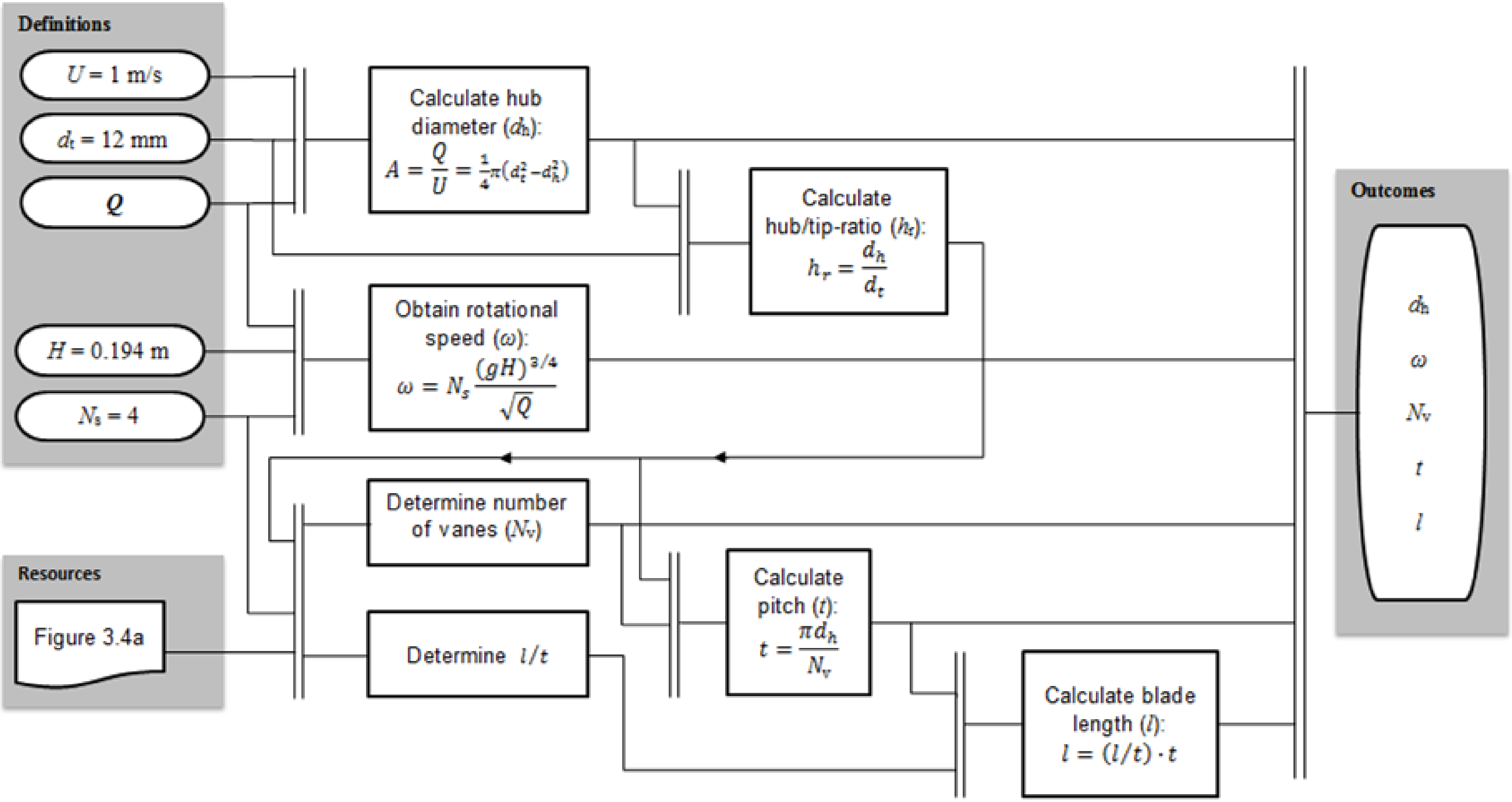

Figure 3.3: Flowchart 1 of 2, for the calculation of blade angles (according to ISO 5807:1985).

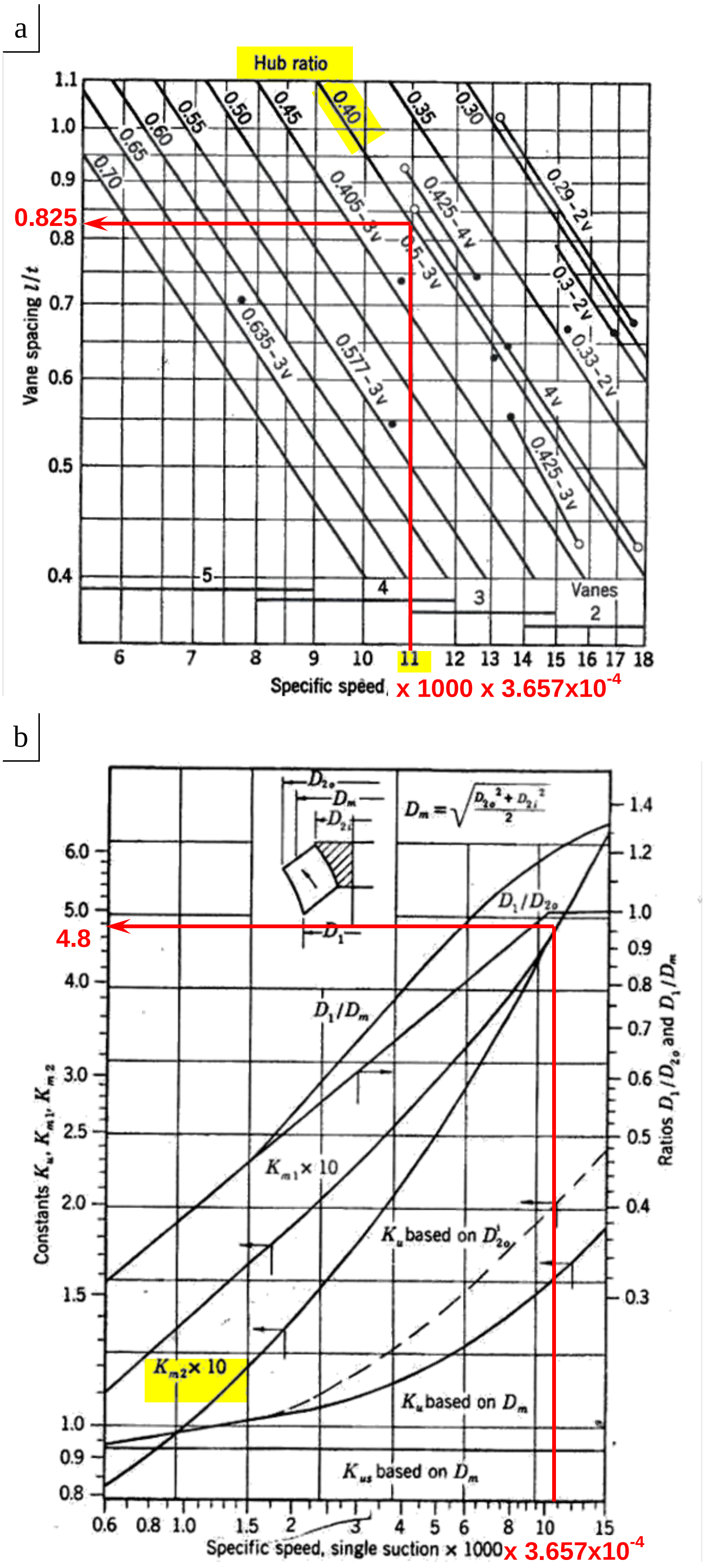

Figure 3.4: Based on specific speed the hub ratio, number of vanes, l/t ratio (a) and impeller constants (b) are derived. The specific speed is shown in United States customary units and is multiplied with 3.657×10^{-4} to convert to metric units.
Copy of figures 5.2 and 8.7 from "Centrifugal and Axial flow pump" (Stepanoff, 1957).

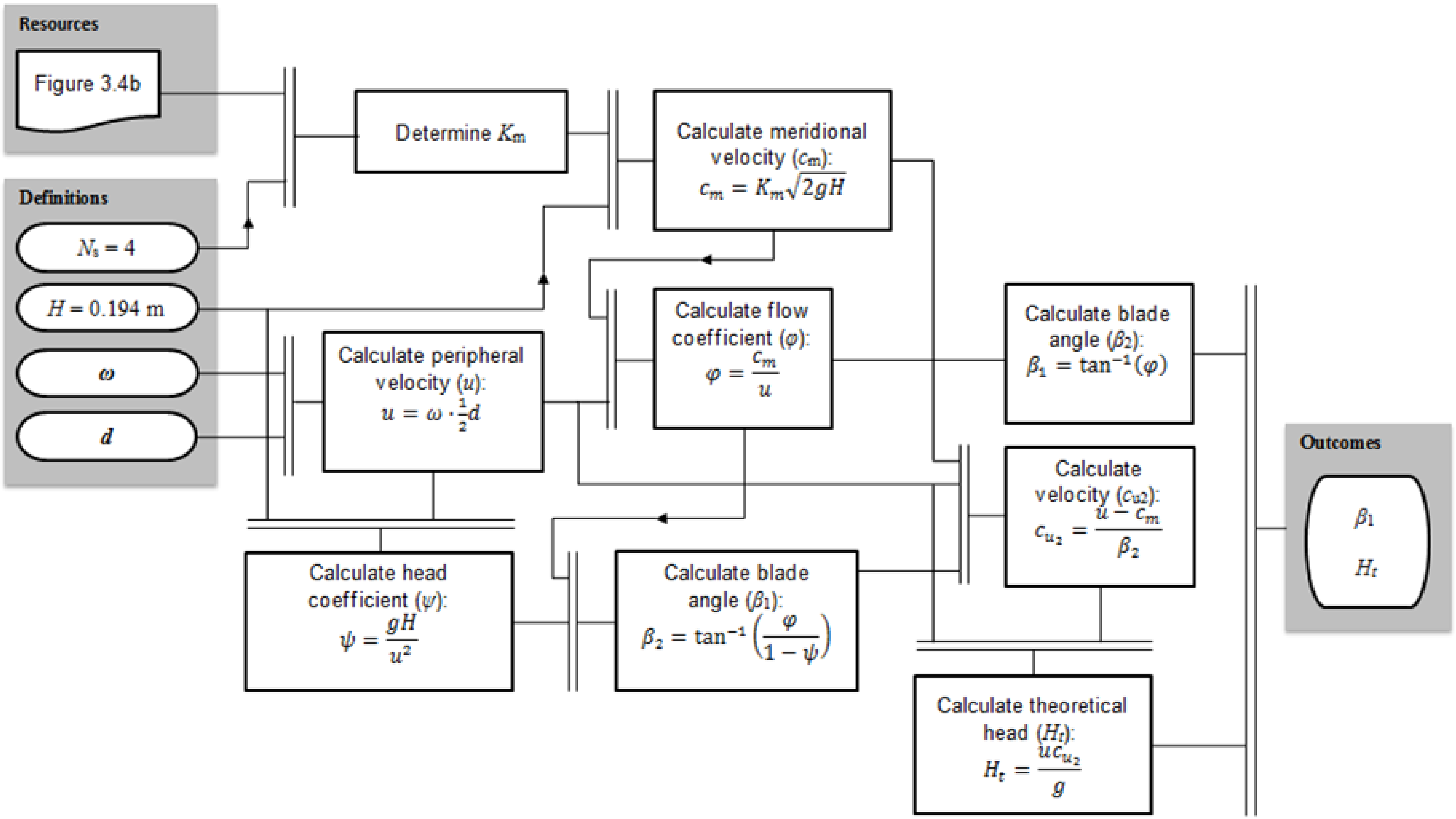

Figure 3.5: Flowchart 2 of 2, for the calculation of blade angles (according to ISO 5807:1985).

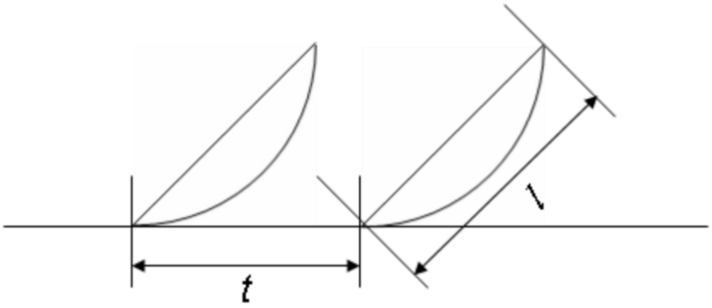

Figure 3.6: Definition of the distance between the vanes, pitch (*t*), and the length of the vanes, chord (*l*).

3.2.3 Designing the blade profile

From the preliminary uni-directional design, predefined by target pressure ratio and flow rate, a bi-directional design was developed and subsequently enhanced iteratively using CFD analysis. Due to the application and bi-directional feature, no existing impeller designs will suffice for this study and a unique profile needs to be designed to meet the criteria listed in the Introduction chapter.

Uni-directional blade profile

In order to obtain a bi-directional blade design, firstly a uni-directional design was established (figure 3.7a). The theoretically optimal parameters (blade angles, rotational speed and blade length) were tested and optimised by means of a numerical parametric study for systolic and diastolic conditions. Whilst keeping other parameters constant, each parameter was varied. For each case the geometry and mesh were updated accordingly and the numerical simulation was repeated. The optimisation was performed by analysing the effect of the varied parameters on hydraulic performance. A subsequent second numerical study was used to investigate the effect of rotating the uni-directional blade profile in the backward direction to identify sections of the profile that required modification in order for the blade to perform in the backward direction as well.

The uni-directional profile used for the above studies was a NACA-4312 airfoil standard (Jacobs, Ward & Pinkerton, 1933). A specific feature of this profile is that the suction side (which, in the backward direction, becomes the pressure side) does not have much camber and is relatively straight. Due to this, the loss in performance caused by rotating the uni-directional blade backwards will be small.

The characteristics of this profile (figure 3.7b) indicate the stalling attack angle is at ~14°,at which maximum lift is seen. Maximum lift-drag ratio occurs at ~2°, at which angle most lift is generated with the least drag. The amount of lift generated at a zero angle of attack, is an indicator for the symmetry of the profile. Asymmetric profiles can generate lift at a zero angle of attack. The more symmetric a profile gets, the less lift it will generate. This specific profile, NACA 4312 has a small lift coefficient at a zero angle of attack of ~0.26.

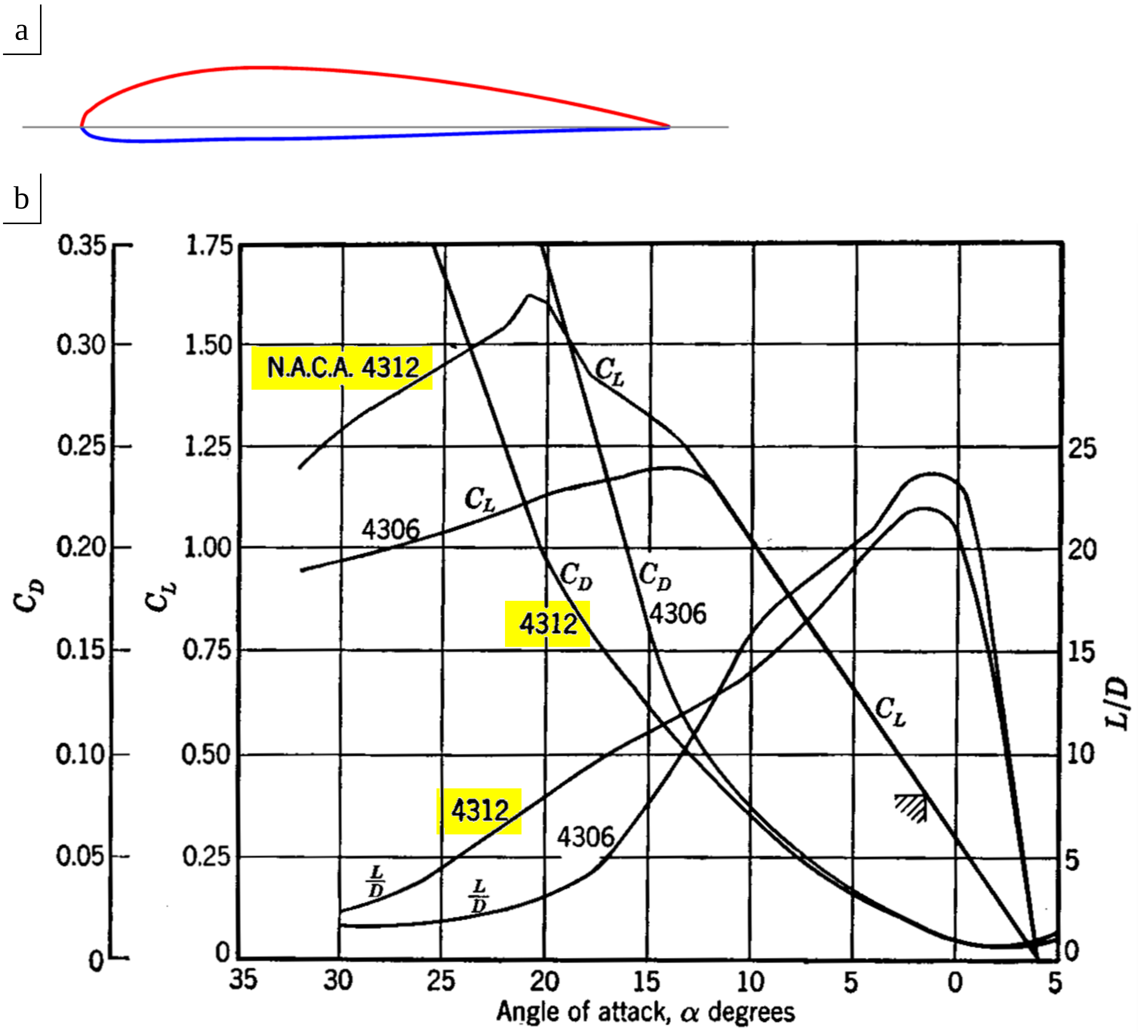

Figure 3.7: Profile of the NACA-4312 airfoil (a) and its lift and drag characteristics (b).

Bi-directional blade profile

The second design stage is to establish a bi-directional profile that will support flow in the forward direction whilst rotating one way and support flow in the backward direction when rotating in the opposite direction. Inherently this requires the blade profile to be rotationally symmetric or near symmetric as the pressure side in one direction becomes the suction side in the opposite rotational direction.

By amalgamating two uni-directional NACA 4312 profiles (figure 3.8a), one rotated 180° from the other, an initial rotationally symmetric bi-directional profile was established (figure 3.8b). Geometry points of areas where the profiles meet were modified to ensure a smooth profile. When the rotational direction changes, the profile of the pressure and suction side will remain the same.

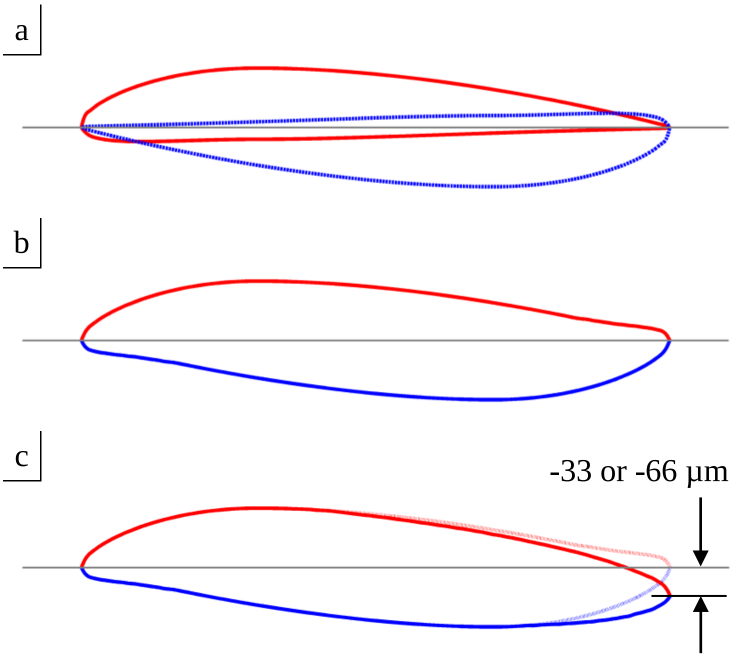

Figure 3.8: Development of the blade profile. Two uni-directional profiles (a) were combined to establish a bi-directional profile (b). This initial bi-directional profile (b) was further modified (c).

The parametric study to find optimum blade angles, rotational speed and blade length carried out for the uni-directional profile was repeated for the bi-directional profile. Furthermore the bi-directional functionality was optimised by investigating the best balance of performance in forward and backward direction. The bi-directional blade has hereby undergone design modifications, as shown in figure 3.8c, whereby the trailing edge was lowered by 33 and 66µm.

The 3D design was performed using Pro/ENGINEER (PTC, Needham, United States) by setting the 2D cross-section of the blade at the tip at an angle that was found suitable for peak systolic conditions. The 2D cross-section of the blade at the hub was set at an angle suitable for peak diastolic conditions. The two cross-sections at tip and hub were interpolated to establish the 3D design for the bi-directional blade. The main reason for setting the cross-section at the tip at an angle suitable for systolic conditions rather than diastolic ones, was that the blade performance is known to be higher at the tip than at the hub and the systolic conditions are more demanding than the diastolic conditions (McDonald 1974). For that same reason, design modifications of the 3D model focussed on the profile towards the tip. The pump is aimed to deliver 35 cm^3 in 1/3 second during systole and 20 cm^3 in 2/3 second during diastole, thus systole requires higher flow rates.

3.3 Numerical simulations

3.3.1 Computational Fluid Dynamics

Hydraulic performance of the 3D design was tested by steady-state and transient numerical simulations. With the steady-state simulations, the rotational speed of the pump was kept constant over the duration of each simulation. Whilst for the transient simulations, the pump was rotated with a variable speed; subsequently drive curves were defined. For all simulations, CFX software (Ansys Inc., Canonsburg, PA, USA) was used. Rather than considering the blades as solid bodies that rotate in the fluid, the blades were defined as a solid stationary wall. Instead of rotating the blades, the fluid domain is rotated. The Newtonian fluid modelled was given a density of 1050 kg/m^3 and a viscosity of 3.6 mPa·s to match those of blood (McDonald, 1974).

Turbulence modelling

An important indicator for choosing a turbulence model is the Reynolds number. Using the theoretical design parameters (paragraph 3.2.2) the Reynolds number can be estimated. At a rotational speed of 11,000 rpm, for a tip diameter of 12 mm, the tangential velocity, u, equals 6.91 m/s:

$$u = \pi \cdot d_t \cdot n/60 \tag{3.2}$$

$$= \pi \cdot 0.012 \cdot \frac{11{,}000}{60} = 6.91\ m/s$$

For a blade length of 6 mm and considering a blood density of 1050 kg/m^3 and a viscosity of 3.6 mPa·s, this would result in a Reynolds number of 12,000:

$$Re = \frac{\rho \cdot u \cdot l}{\mu} \tag{3.3}$$

$$Re = \frac{1050 \cdot 6.91 \cdot 0.06}{0.036} \cong 12{,}000$$

As this exceeds the critical Reynolds number of 3,400 at which transition to turbulent flow commences (Strackee & Westerhof, 1993), a turbulence transport model was used. Figure 3.9 shows the results of one steady state simulation in forward (a) and backward (b) direction whereby three different turbulence models were compared: k-ε, k-ω (generic) and k-ω SST. For reference, results of the laminar model are added as well. Maximum differences are seen of ~30%. The models start to differ from one another especially at increasing flow rate. The pressure rise calculated by the k-ε model, seems generally lower than the SST and k-ω models.

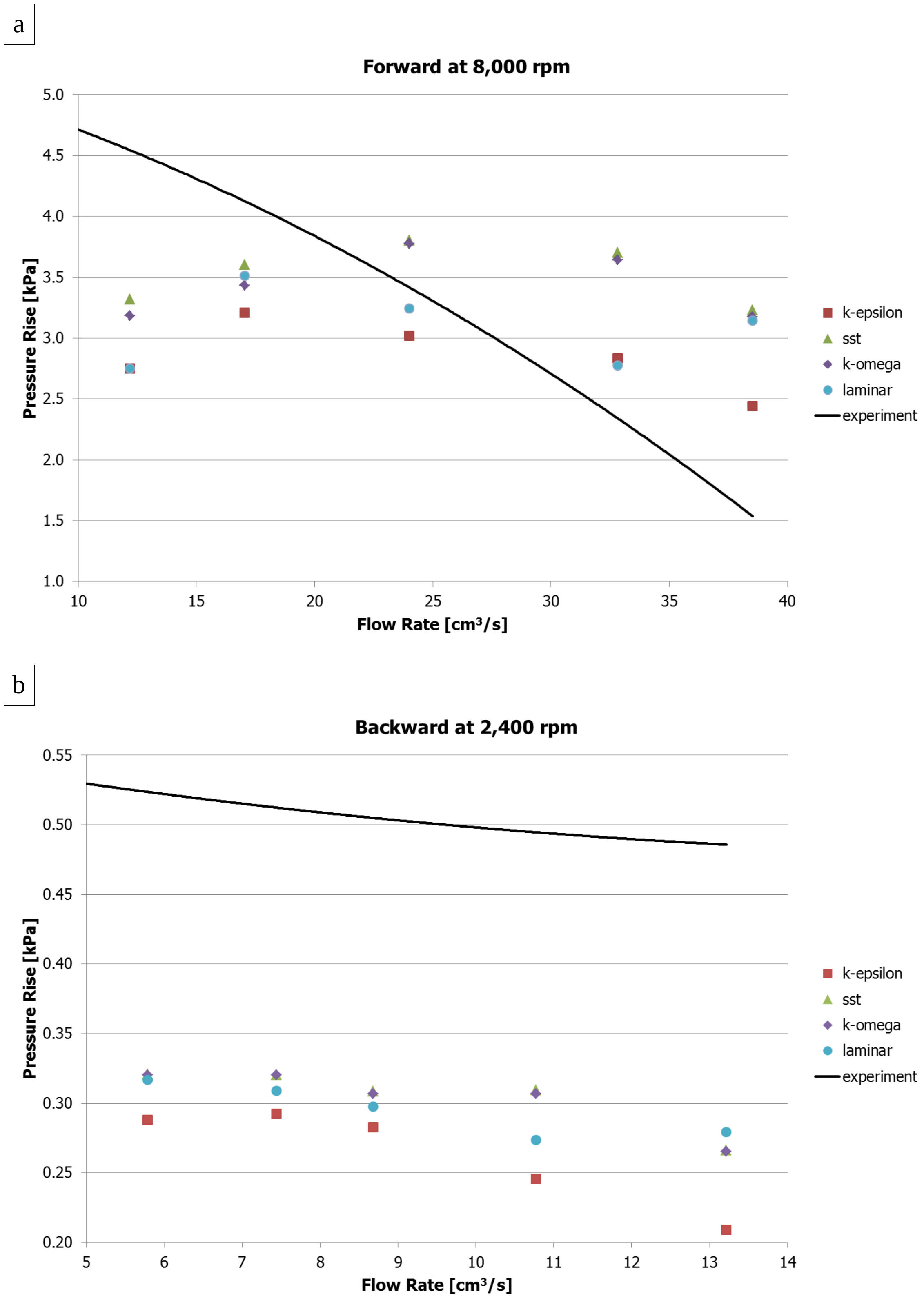

Figure 3.9: Steady state head-flow characteristics obtained using different turbulence models.

Non-Newtonian modelling

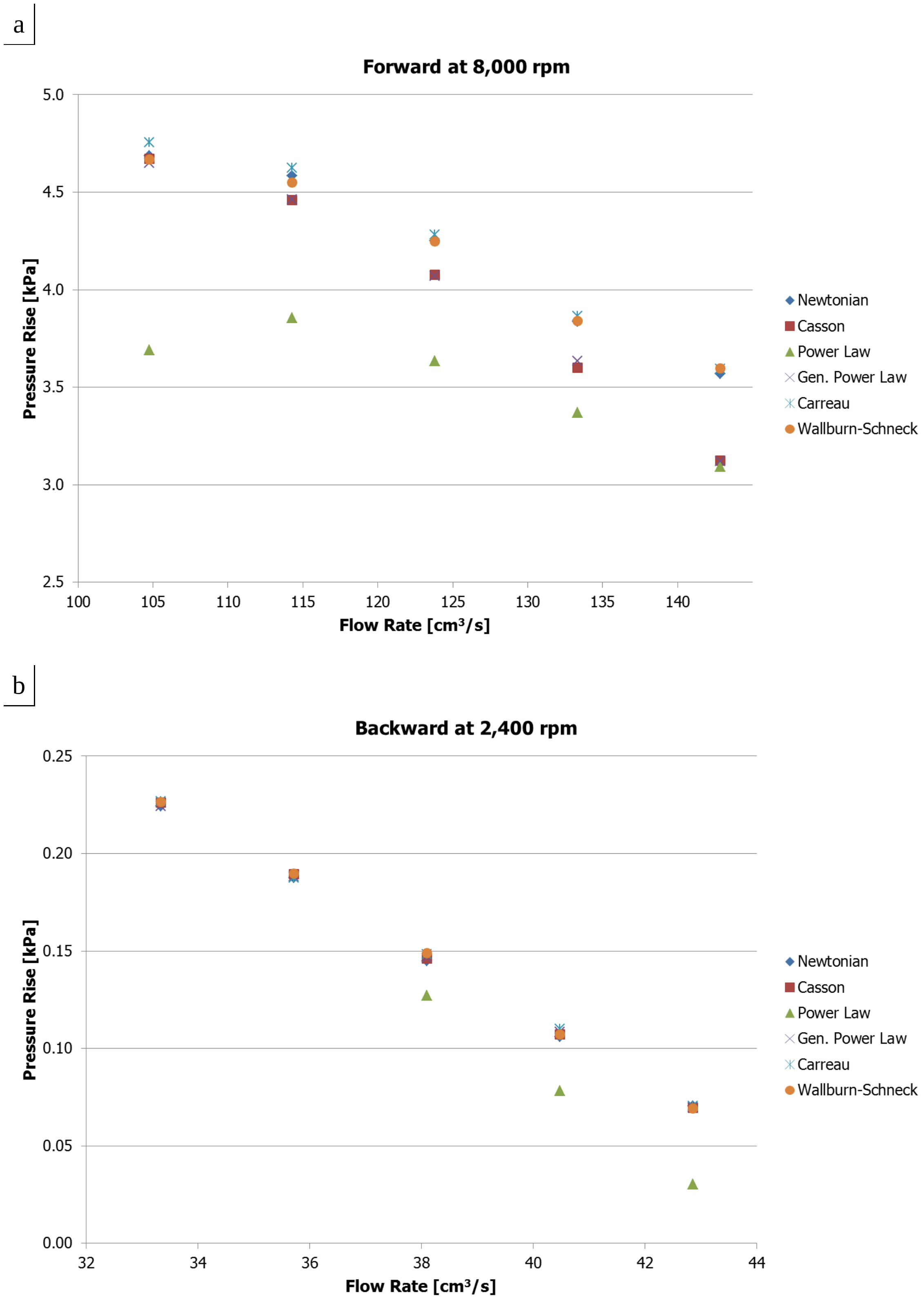

Figure 3.10: Steady state head-flow characteristics comparing the Newtonian fluid model with non-Newtonian fluid models.

As stated in paragraph 2.5.2, the non-Newtonian effects of blood are considered neglible for shear rates above 100 s^{-1}. For numerical models of a turbo machine, whilst the pump is rotating, shear rates are expected to be well above 100 s^{-1}. To assure the non-Newtonian effects are neglible for the numerical models of this study, five different non-Newtonian blood models were compared with the Newtonian model (figure 3.7). Except for the Power Law model, all other models show pressure-flow characteristics similar to that found with the Newtonian model.

3.3.2 Design of the computational models

2D model: a single blade passage

The 2D domain consists of a cylindrical cross sectional plane of the blades (figure 3.11a). Due to periodicity, only one blade passage needed to be simulated. At the inlet a flow rate was set of 105 cm^3/s for systolic and 30 cm^3/s for diastolic conditions. The outlet was defined as a pressure boundary with a constant average static pressure of 13 kPa (approx. 100 mmHg). The solution was obtained using a rotating frame of reference. For the 2D simulations this rotational force was mimicked by setting a translational velocity, perpendicular to the main flow. This velocity was recalculated for different rotational speeds and for different positions, hub and tip, at which the cylindrical cross sectional cut was taken.

Gambit (Ansys Inc., Canonsburg, PA, USA) was used to generate a 2D mesh with triangular shaped elements. The mesh was extruded and given a third dimension by giving it a thickness of a single cell to be compatible with CFX. The mesh of the model was regenerated for each modification of the blade profile. Sectional cuts taken at the tip typically consisted of 12,703 nodes and 13,160 cells, whilst those at the hub consisted of 12,212 nodes and 11,781 cells.

3D model: “pump only”

Figure 3.11b shows the boundary setup of the 3D models. The boundary conditions were defined consistently and were identical to those of the 2D models to allow for comparison. Where a translational velocity was applied on the 2D models, a rotational speed was used for the 3D models. The mesh consisted of 148,623 nodes that resulted in 755,495 tetrahedral cells.

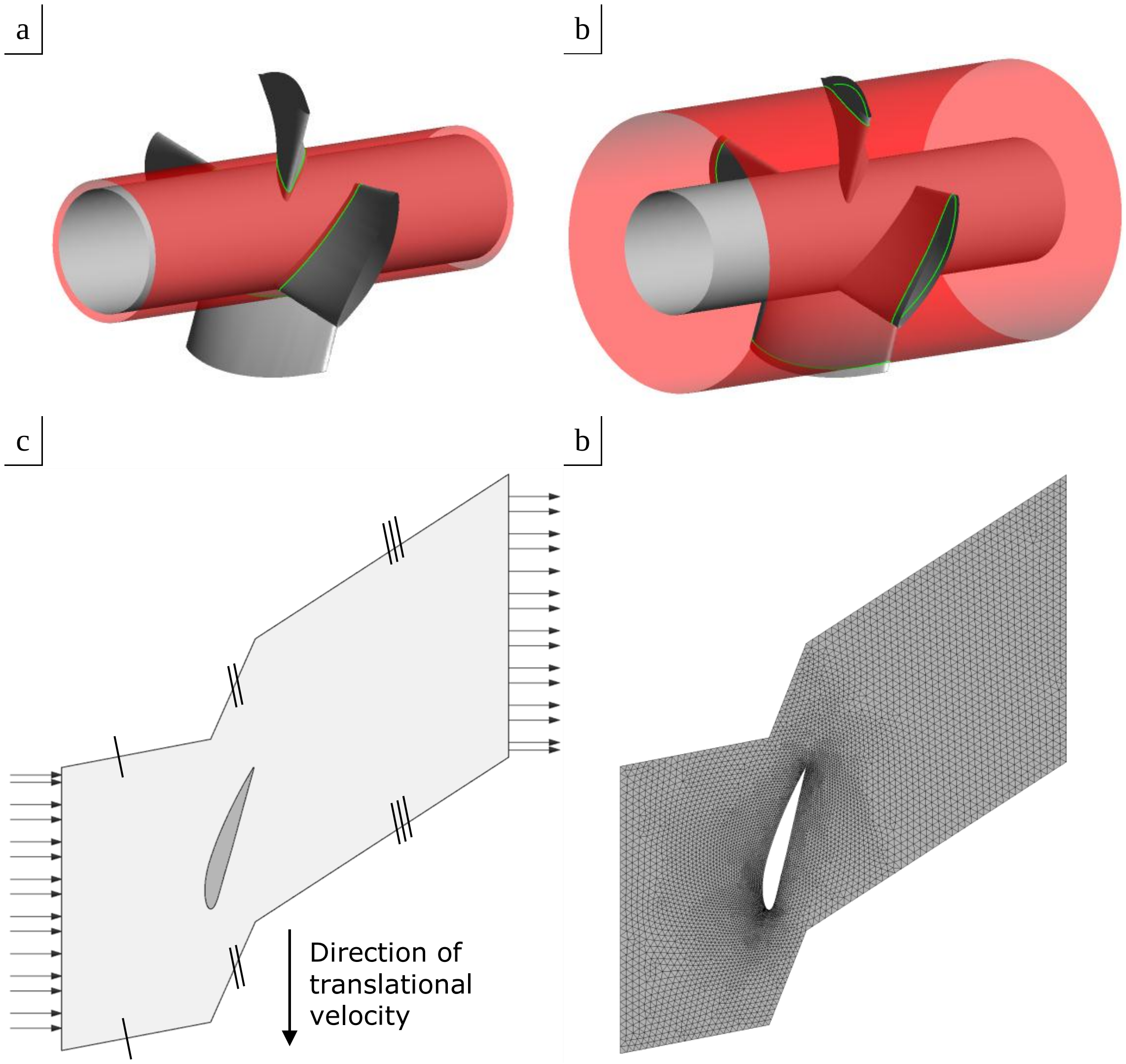

Figure 3.11: Boundary setup of the 2D numerical model.

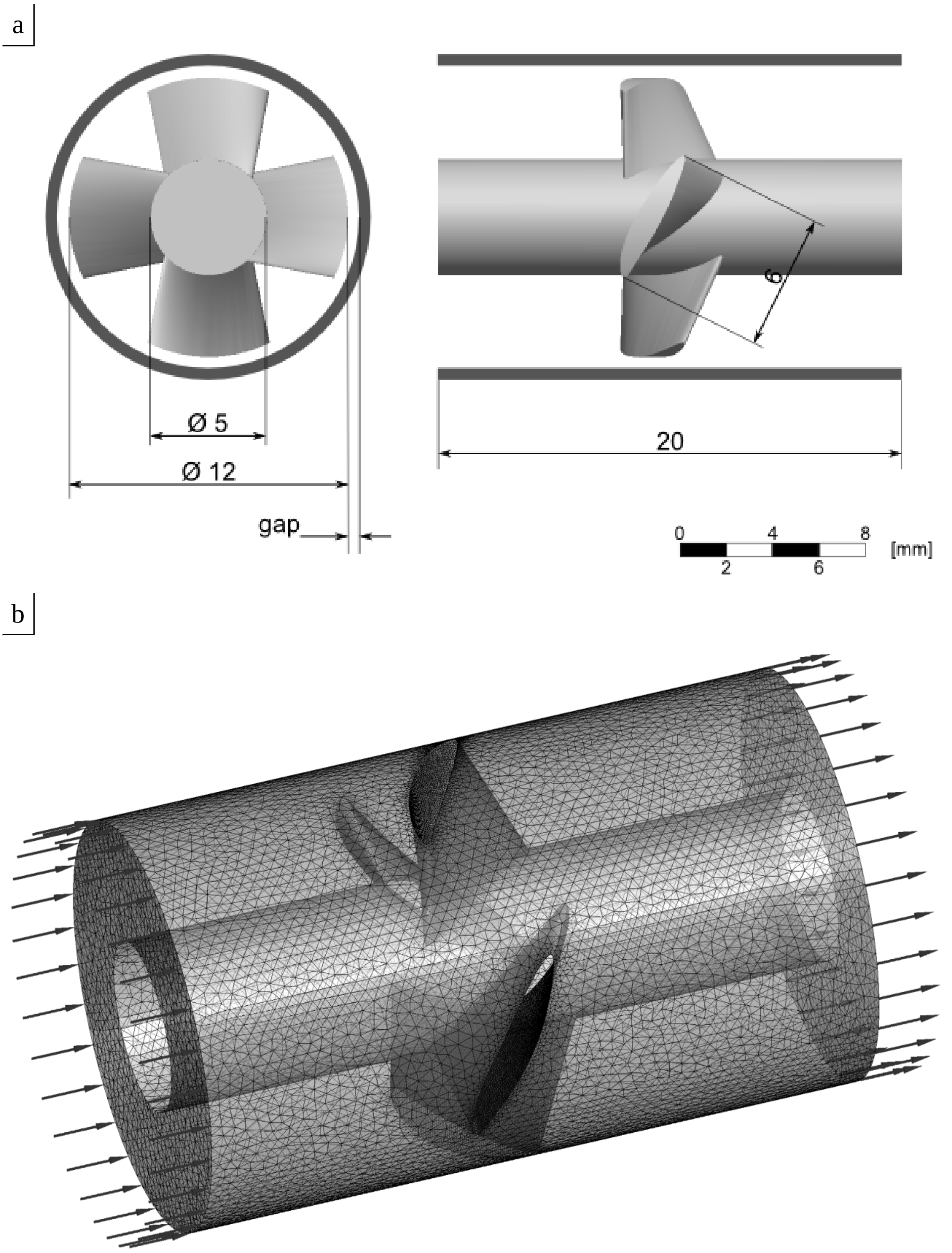

Figure 3.12: Boundary setup of the 3D numerical model: “pump only”.

3D model: “ascending aorta”

3D transient CFD simulations were carried out on each of the above steady state models with a time interval of 0.01 sec. The “pump only” domain consisted of 148,623 nodes and 755,495 tetrahedral cells. The meshes were then loaded into Ansys CFX software.

Following the aforementioned “pump only” model (figure 3.11b), the domain was extended and the pump was placed inside a fixed wall pipe to mimic the ascending aorta (figure 3.13a). The study of this model focuses on the effects of changing the direction of rotation, i.e. the flow distribution between the pump and ascending aorta domain at that instant. The ascending aorta domain consisted of 218,480 nodes and 1,143,676 tetrahedral cells. The simulations were repeated for three wall diameter (D_1) sizes, namely 20, 25 and 30 mm. The length of the pipe was varied and L_1-L_2 were defined as, 20-20, 20-40, 20-60, 20-80 and 40-40 mm respectively. Two sets of the aforementioned simulations were carried out to investigate the effect of the pump’s position inside the pipe. For one set the pump was placed at the pipe’s wall and for the second set the pump was placed in the centre of the pipe (figure 3.13b).

The blades domain was defined to initialise from the stationary position. At either side of the blades an opening boundary was defined, each of an opening pressure of 13 kPa. A variable rotational speed was given to the blades’ fluid domain defining an acceleration and deceleration phase in systole lasting 0.1 sec and in diastole of 0.2 sec (figure 3.14a). The acceleration and deceleration curves were given the shape of one quarter of a sinus. During the systolic phase the rotational speed accelerated up to a maximum of 8,000 rpm that was maintained for 0.1 sec. A maximum rotational speed of 2,400 rpm was maintained for 0.3 sec during diastole. The duration of the total cycle is 1 sec, 1/3 sec for systole and 2/3 sec for diastole, corresponding to a heart rate of 60 bpm.

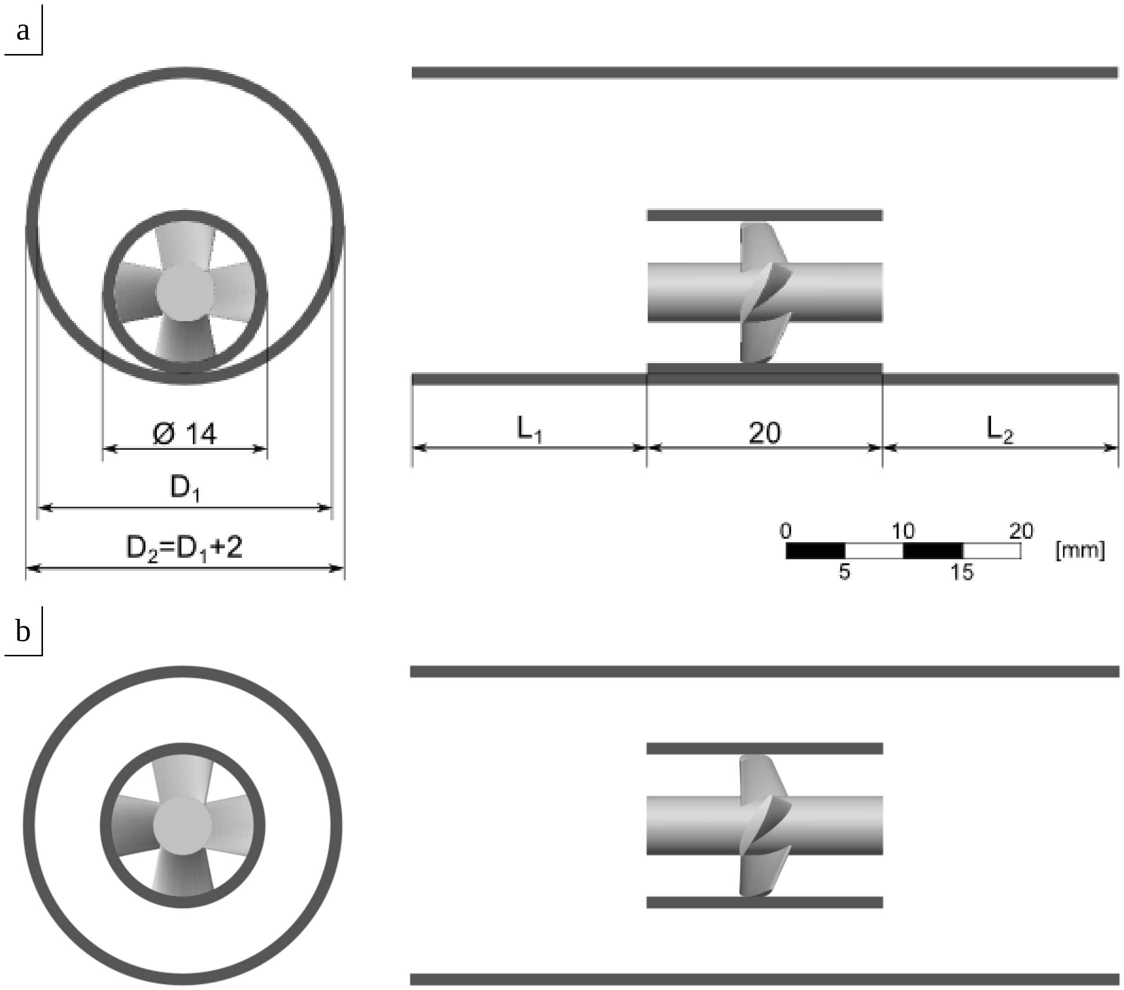

Figure 3.13: Boundary setup of the ascending aorta domain, with the pump either positioned at the aortic wall (a) or in the centre (b).

The simulations were repeated with four different drive curves. The first two drive curves rotate forward and backward, in one case starting with forward (figure 3.14a) and in the other case starting with backward (figure 3.14b). The latter two drive curves rotate either forward (figure 3.14c) or backward (figure 3.14d) to characterise the performance of the pump in both directions individually. Results obtained with these four different drive curves are compared to investigate the transition period when the rotational direction changes. It is expected that performance of the pump will be better when rotating in either forward or backward direction, without a transition to an opposite rotational direction. By comparing the results of the individual forward and backward driven simulation with the combined forward and backward simulations, possible pressure rise or flow losses will tell to what extend performance is compromised by changing rotational direction so rapidly. One possibility could be to rotate the pump in a single direction during one entire heart cycle and to rotate in the opposite direction in the following heart cycle. In that case, the acceleration and deceleration could be decreased. However, decreasing acceleration and deceleration will also lead to a reduced amount of time that the pump is rotating at its maximum/optimum rotational speed.

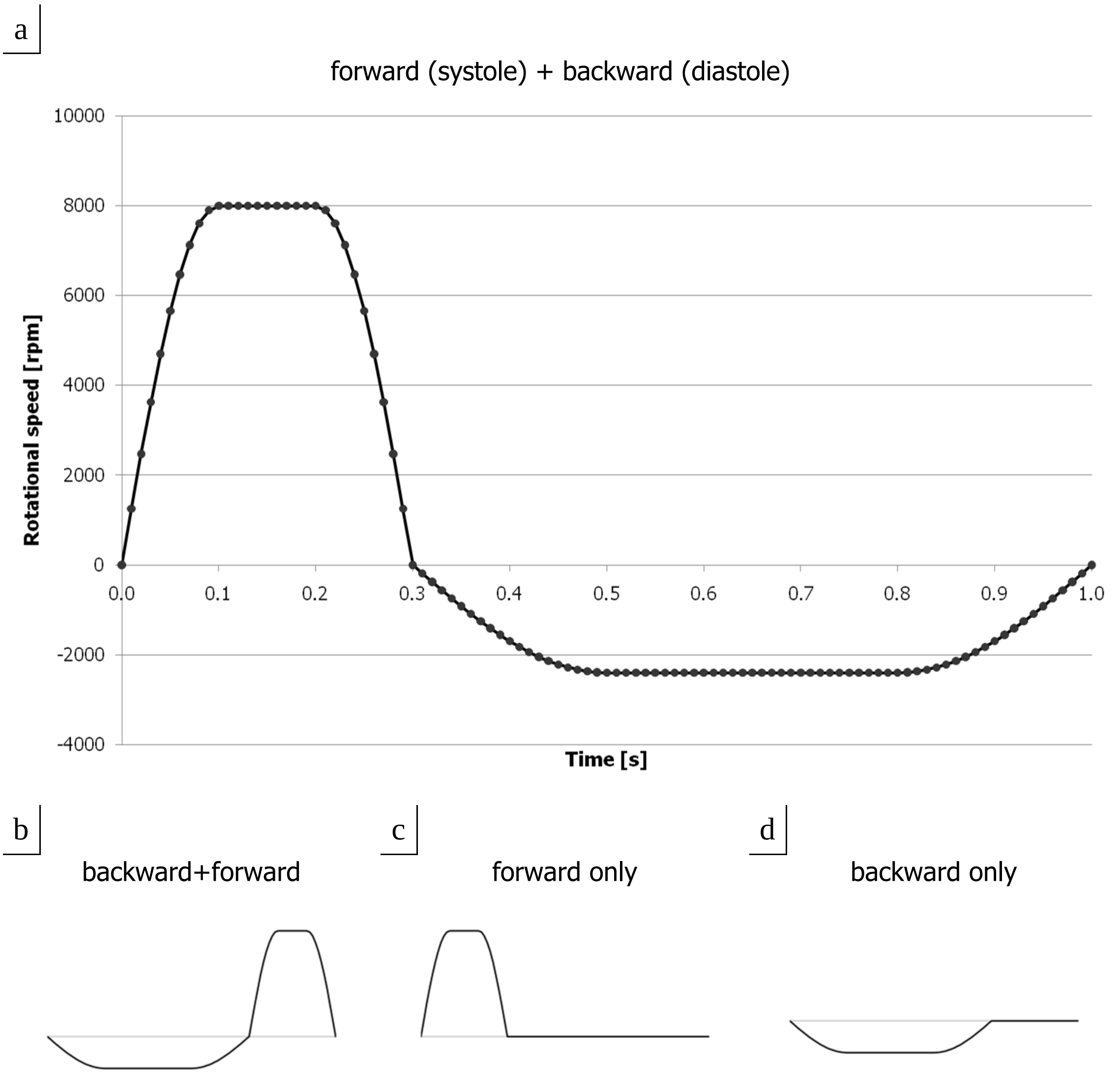

Figure 3.14: Sinusoidal drive curves for the transient simulations.

3.3.3 Repeatability and reproducibility

Apart from experimental validation, the following sanity checks were carried out to confirm reliability of the computational model:

- Grid independence study of the 2D model: a single blade passage
- Grid independence study of the 3D model: “pump only”
- Unsteadiness test / time step independence study

Grid independence study of the 2D model: a single blade passage

A grid independency study was carried out on the 2D grid of the pump, used in the “pump only” model and in the ascending aorta model. The grid used in the analysis has 14,338 elements and in order to confirm the results are independent on the grid, simulations were carried out on a finer and a coarser grid. Those consisted of 20,104 and 7,288 elements respectively.

Figure 3.15 shows the blade loading profile halfway between the hub and the tip for the three different grids. A small variation occurs with the coarse (dotted red) grid but the 14k and the finer grid correspond well. The 7k, 14k and 20k grids generated total pressure rises of 4.47, 4.43 and 3.99 kPa respectively. In figure 3.16 pressure is plotted against the normalised span. The normalised span ranges from 0-1 where 0 represents the inlet and 1 the outlet. All the three grids correspond well with one another.

In conclusion, the results obtained with the 14k are not dependent on the grid size and correspond well with those obtained from grids with increased/decrease density.

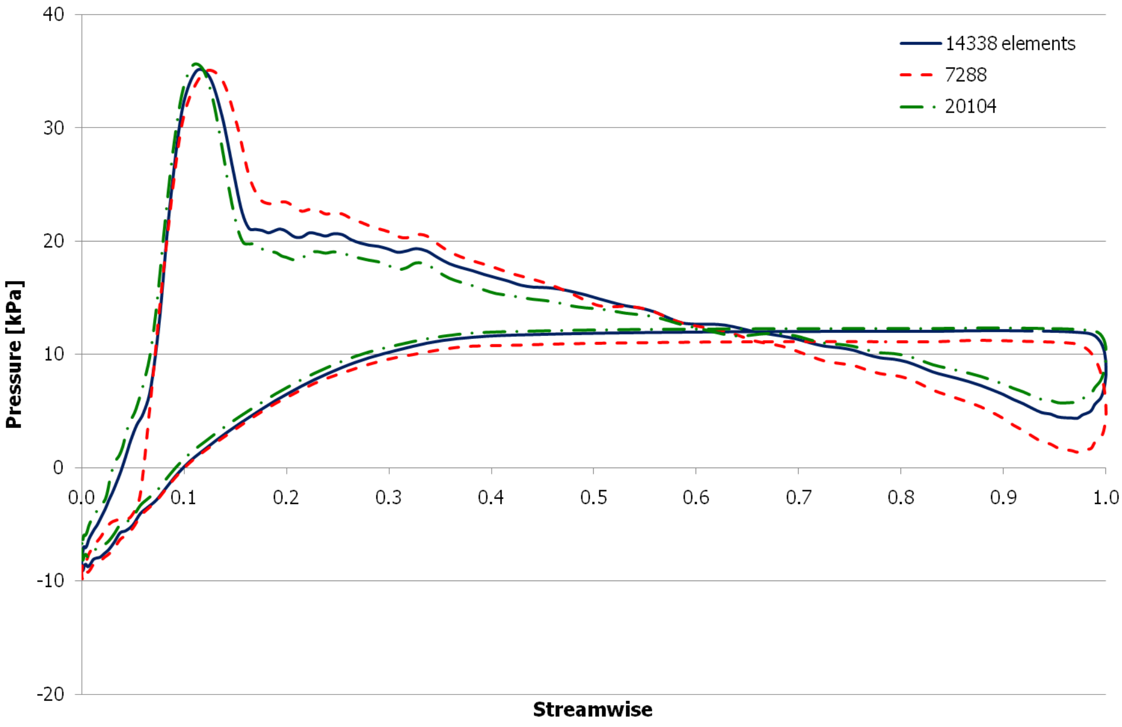

Figure 3.15: Pressure blade loading profiles of the bi-directional blade design.

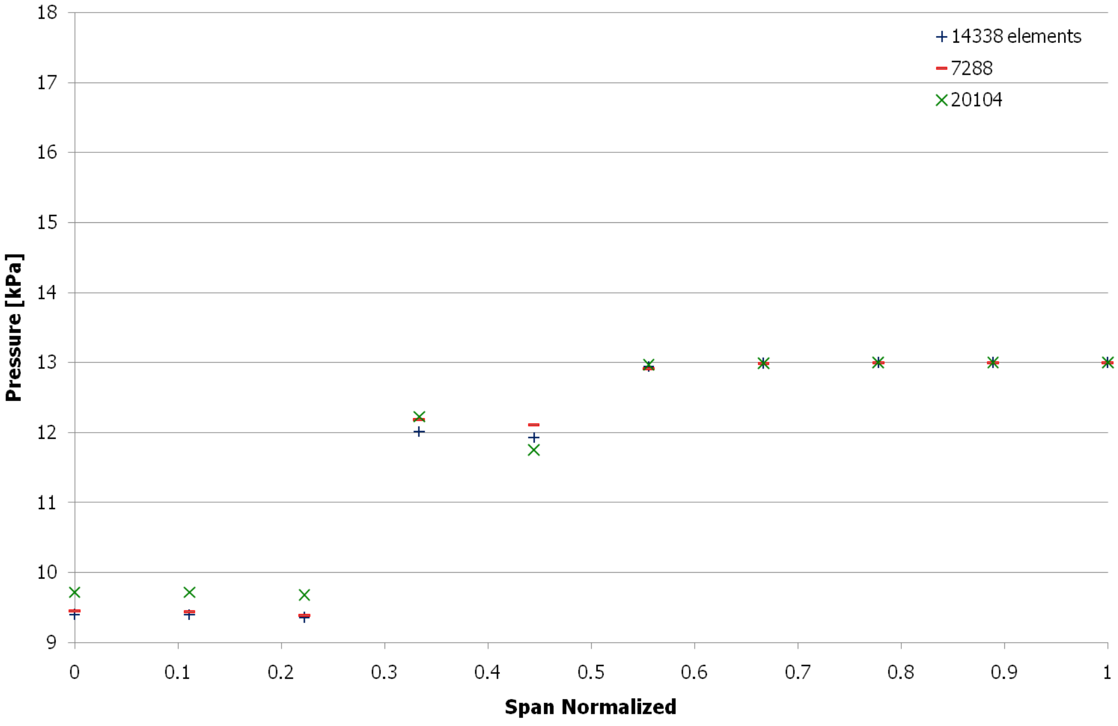

Figure 3.16: Pressure from inlet (span=0) to outlet (span=1).

Grid independence study of the 3D model: "pump only"

A grid independency study was carried out on the 3D grid of the pump, as per both the "pump only" model and the ascending aorta model. The grid used in the analysis has 753,620 elements and in order to confirm the results are independent on the grid, simulations were carried out on a finer and a coarser grid. Those consisted of 969,658 and 463,022 elements respectively.

Figure 3.17 shows the blade loading profile halfway between the hub and the tip for the three different grids. A small variation occurs with the coarse (dotted red) grid but the 753k and the finer grid correspond well. The 463k, 753k and 969k grids generated total pressure rises of 6.17, 6.38 and 6.43 kPa respectively. In figure 3.18 pressure is plotted against the normalised span. The normalised span ranges from 0-1 where 0 represents the blade's hub and 1 the tip. The solutions on all three grids correspond well with one another. To get an idea of the distance between the blades' wall and the nearest grid element, the y-plus values are plotted in figure 3.19. The maximum y-plus values are 12.5 (most coarse grid), 6.4 and 5.6 (most fine grid).

In conclusion, the results obtained with the 753k are not dependent on the grid size and correspond well with those obtained from grids with increased or decreased density.

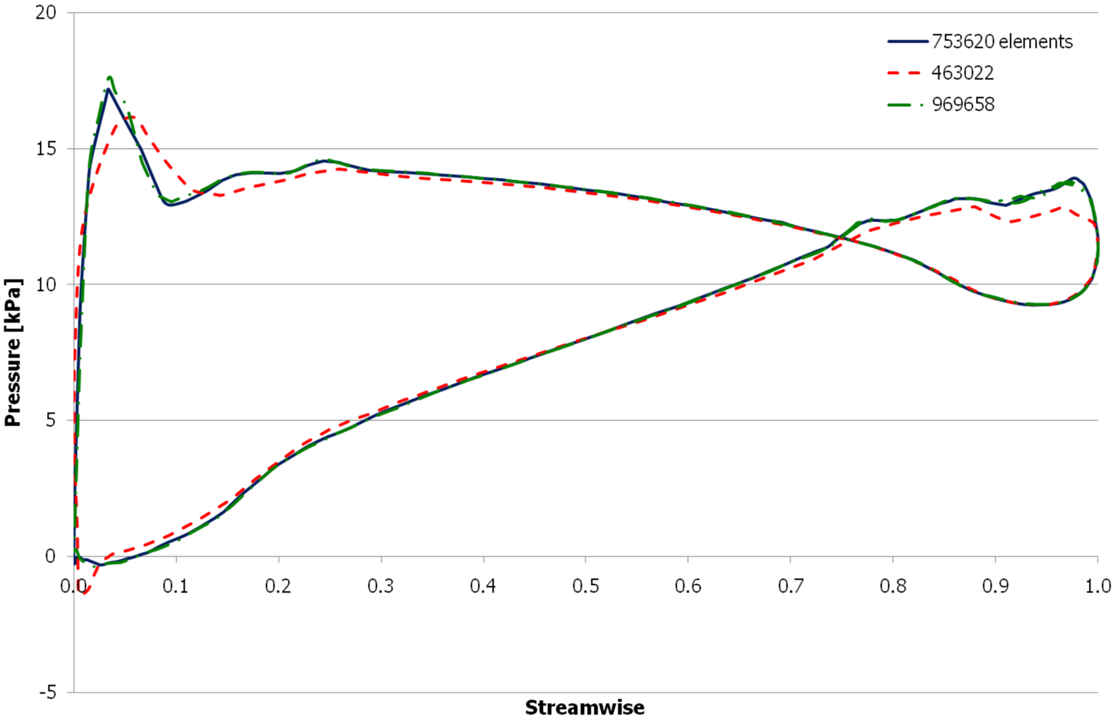

Figure 3.17: Pressure blade loading profiles of the bi-directional blade design, at a span of 0.5 (halfway between the hub and the tip).

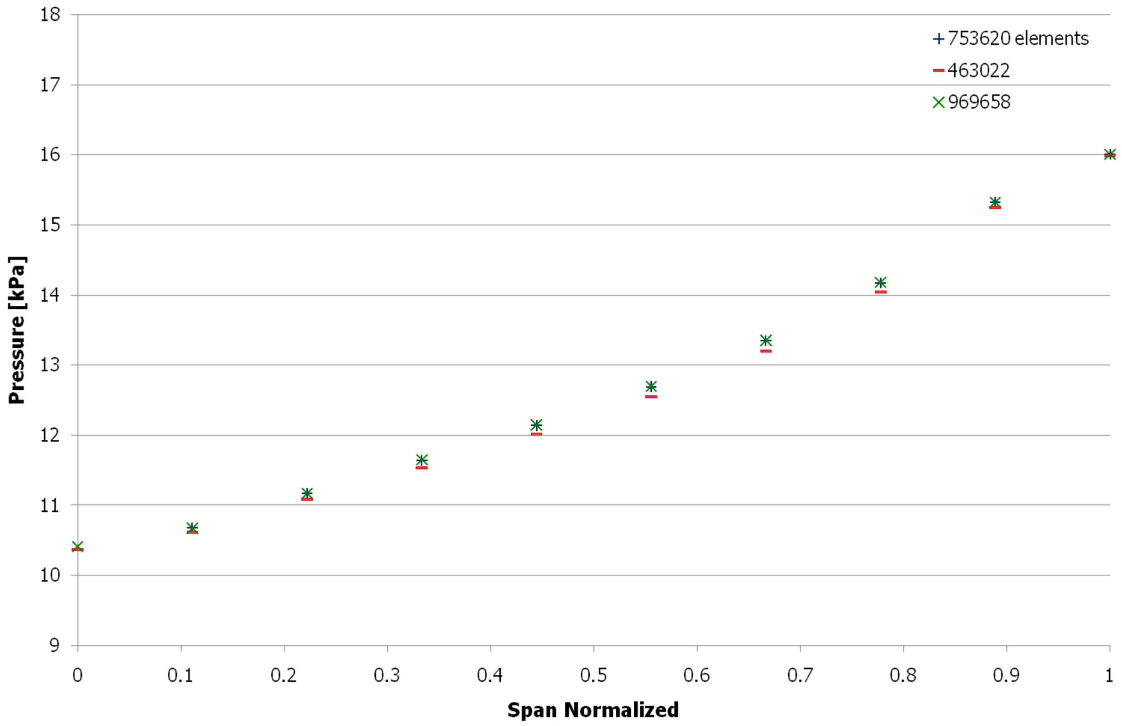

Figure 3.18: Pressure from hub (span=0) to tip (span=1).

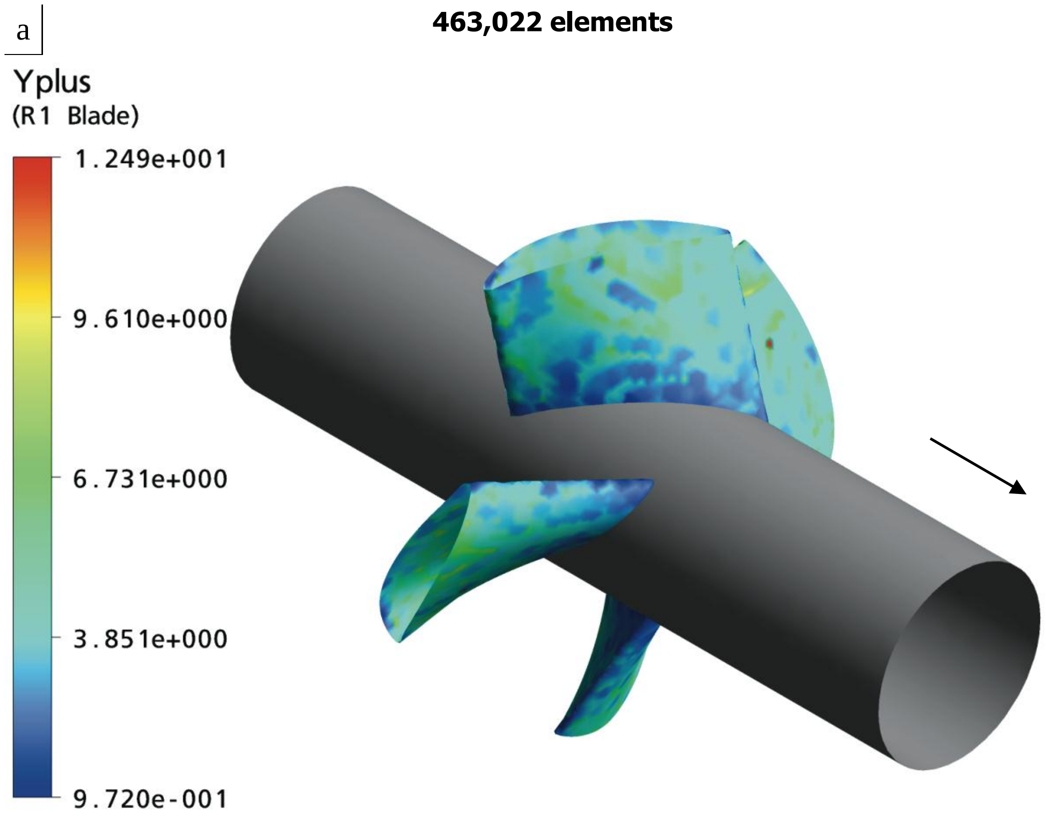

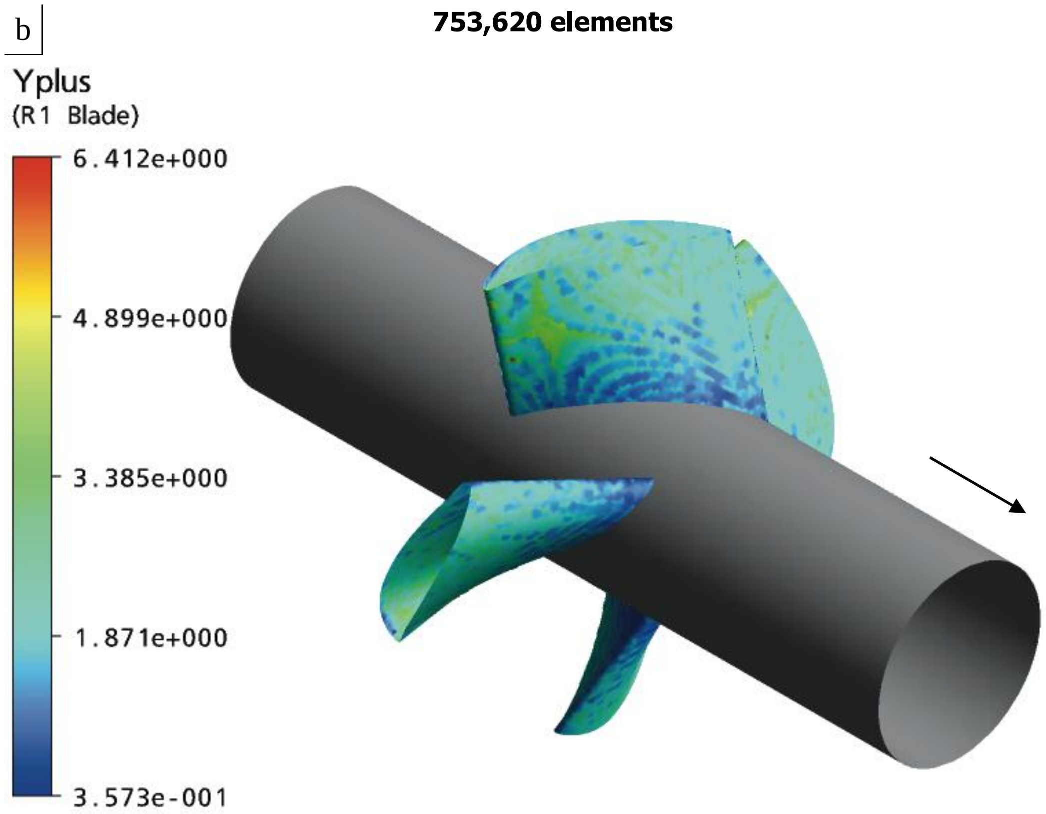

Figure 3.19: Comparison of the range of Y-plus values around the blades' wall for three different sized meshes.

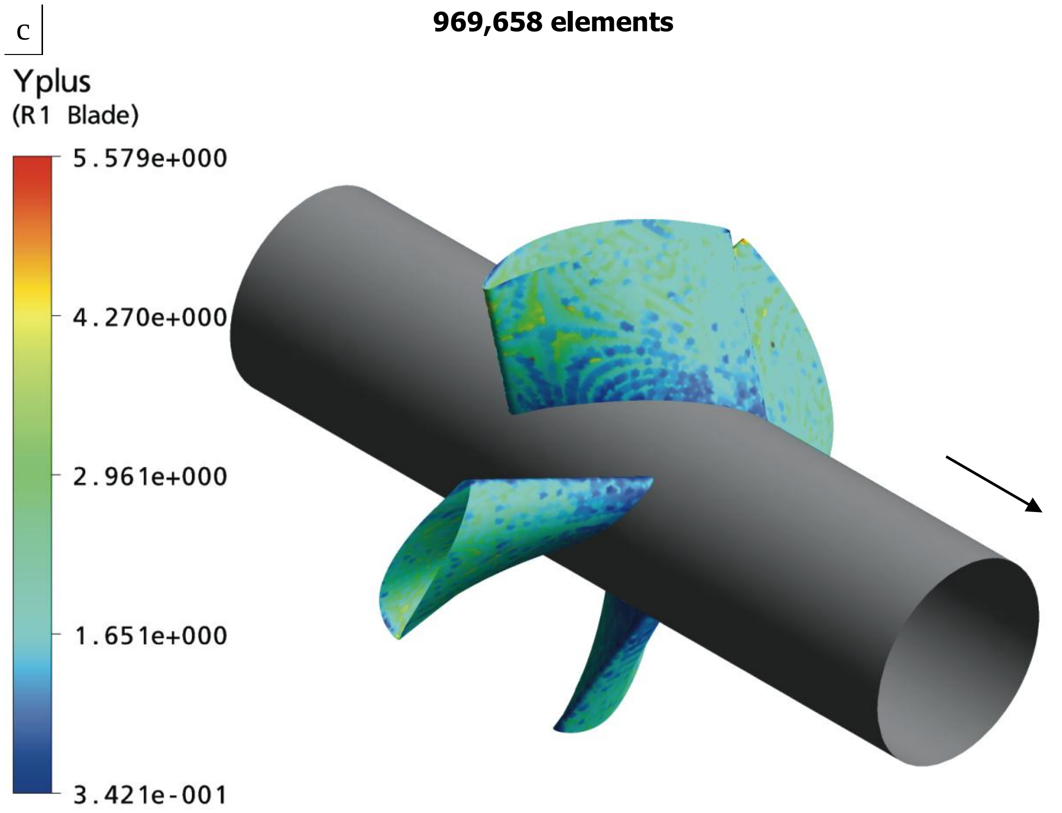

Figure 3.19 (continued)

Unsteadiness test

The sensitivity of unsteadiness was assessed by repeating the transient simulation for different time steps. The drive curve was fixed to rotate the "pump only" model forward and then backward. For each of the five time steps, maximum flow rate, maximum pressure rise and total flow delivery were determined from the results (table 3.1). Overall the results do not vary significantly with increasing or decreasing time step. The most sensitive parameter is found to be the total flow delivery. Comparing maximum and minimum values, in forward direction ~14% (41.3 vs. 36.3 cm^3) and in backward direction ~17% (22.2 vs. 19.0 cm^3).

Table 3.1: Results of the unsteadiness test.

Time step [ms]	Q_{max} [cm^3/s] fw	Q_{max} [cm^3/s] 6%bw	ΔP_{max} [kPa] fw	ΔP_{max} [kPa] bw	Q [cm^3] fw	Q [cm^3] bw
30	160	-38.4	2.26	-0.165	41.3	22.2
20	161	-38.1	2.23	-0.169	40.2	20.7
10	161	-36.6	2.26	-0.168	38.6	19.4
5.0	161	-36.2	2.29	-0.167	37.6	19.0
2.5	161	-36.5	2.32	-0.166	36.3	19.1

3.3.4 Protocol

For this study both 2D and 3D steady state CFD simulations were carried out, each for their own purpose. As simulations in 2D are less time demanding these were used as the starting point for testing a variety of design iterations performed to establish a bi-directional profile. Once the bi-directional profile was set, 3D simulations were carried out to test performance more realistically.

The first step was to establish a uni-directional design, study A, and find the best design parameters for systole and diastole conditions. The second numerical study, B, investigated the effect of rotating the uni-directional blade profile in the backward direction to identify those sections of the profile that required altering in order for the blade to perform in the backward direction as well.

The second design stage was to establish a symmetric two-dimensional profile. Similar to the uni-directional profile study, a parametric study, C, was carried out to see the effect of blade angles, rotational speed and blade length on hydraulic performance.

Table 3.2: Overview of numerical simulations.

		simulation		
	domain	model	state	main purpose
A	uni-dir. blade	2D	steady	- establish design parameters
				- rotated in backward direction
B	bi-dir. blade	2D	steady	- establish design parameters and optimise the blade profile
		3D	steady	- optimise profile
			transient	- model dynamic behaviour of acceleration, deceleration and the change of rotational direction and model the required torque/power
C	bi-dir. blade + fixed wall tube	3D	transient	- test under more physiological conditions

3.4 Experimental work

The numerical simulations were validated through a bench experiment. This was done by pressure and flow measurements on a true sized prototype of the bi-directional blades.

3.4.1 Materials

Figure 3.20 shows the operational setting of the experimental rig that consists of the following components:

a) Prototype pump: The pump design equipped with symmetric blades was externally commissioned and made of an aluminium alloy (L168) by 5-axis CNC machining (figure 3.21). The pump is fixed onto a Ø1.5 mm metal wire using Loctite 638. This type of Loctite ensures secure fixation of the pump with forces not exceeding 25-30 N/mm^2 and a temperature between -55 and +120°C.

b) Motor: The pump is driven by a brushless 12 W DC motor (Maxon Motor ag, Sachseln, Switzerland).

c) Housing: The pump was placed inside a housing made of aluminium and brass alloys. The aluminium components were anodised to prevent corrosion. The technical drawings are found in appendix C.

d) Motor interface, PC1: The interface with the motor was established by connecting the motor's EPOS controller to a PC running LabView software. This enabled rotational speed control and acquisition of the speed measured by the Hall sensors.

e) Reservoir: A reservoir, kept at a head of 13 kPa with respect to the pump, is providing the setup with fluid.

f) Tubes: Ø12 mm silicon flexible tubes carry water between the reservoir and the pump.

g) Valves: At both sides, the tubes between the reservoir and the housing are separated by valves. Whilst keeping the inlet valve fully open, the valve at the outlet may be partially shut to change the flow rate.

h) Y-connectors: Two y-connectors were placed at the inlet and outlet of the housing for the pressure catheters to be inserted in the system.

i) Pressure-measuring equipment: Two Ø2.0 mm pressure catheters with two sensors 5 cm apart (PCU 2000 control unit, Millar Instruments Inc, Houston, TX, USA) are introduced, one at either side of the blades to measure the pressure difference generated by the pumping action of the blades. Although each catheter is equipped with two sensors, only the signal of the distal sensors (at the catheters' tip) is acquired.

j) Flow-measuring equipment: An Ø12 mm ultrasonic perivascular flow probe (Transonic, Ithaca, NY, USA) is applied at one of the slanted tubes to measure the flow rate. The probe was connected to Transonic flow meters (T206 model). Ultrasonic gel was applied on the probe and the flexible tube (f) to ensure dry operation of the flow probe, without it needing to be submerged in a fluid.

k) Data acquisition, PC2 (not displayed in figure 3.20): pressure and flow signals are digitally stored using data acquisition hardware connected to a PC running Sonometrics data acquisition software (Sonometrics Corporation, London, Ontario, Canada).

l) Fluid: Tap water at room temperature (~22°C).

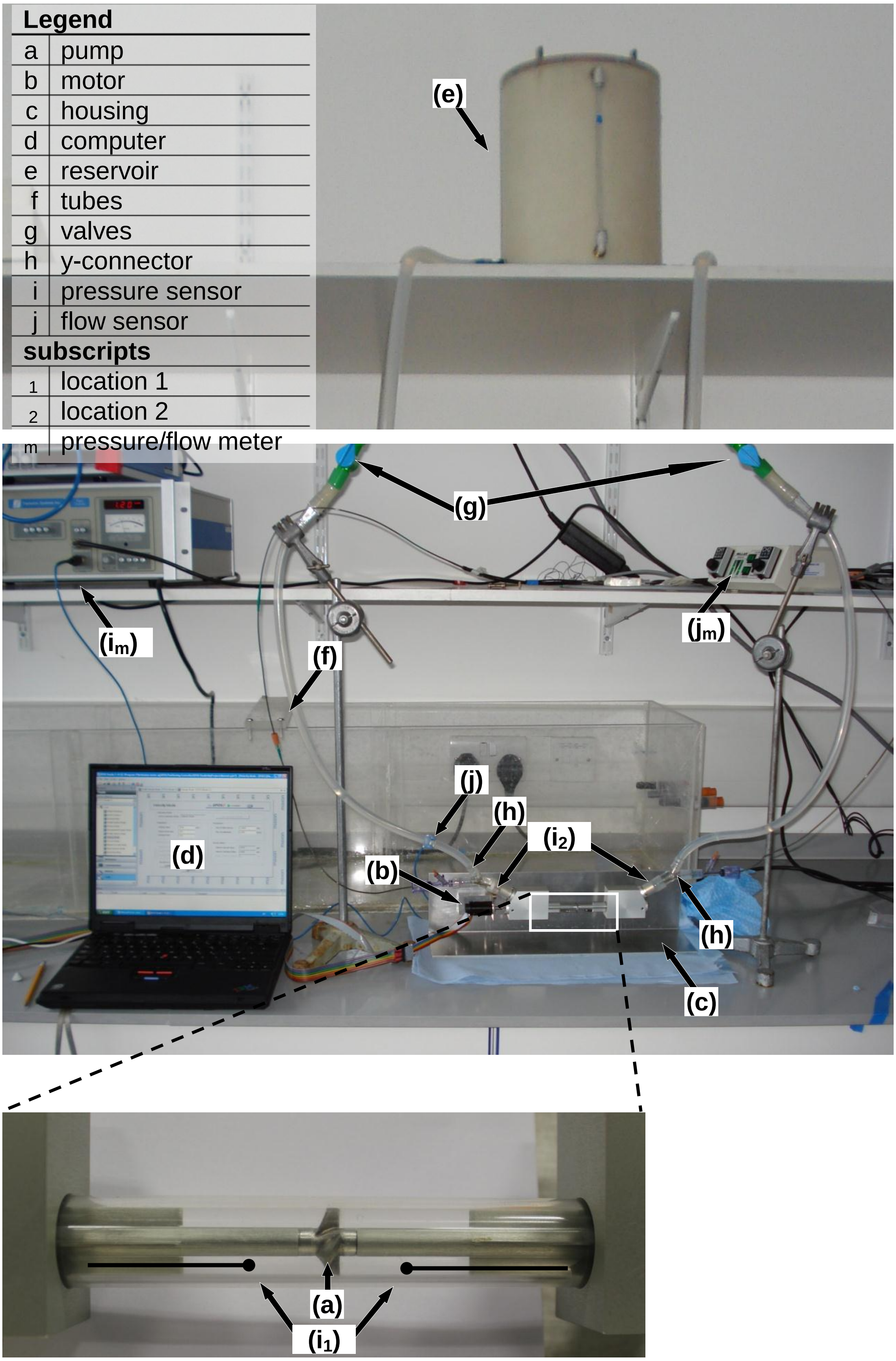

Figure 3.20: Photo of the experiment as set up on the bench.

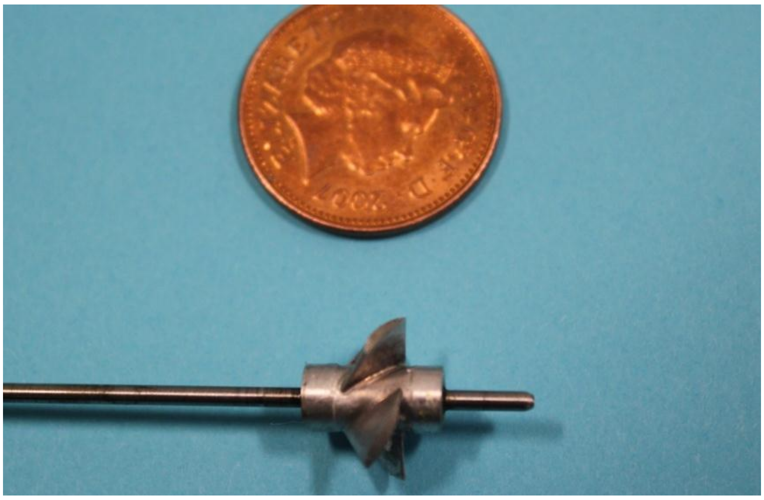

Figure 3.21: Picture of the aluminium prototype pump, with a two-penny coin placed next to it.

3.4.2 Design of the housing of the pump

Figure 3.22 shows the design concept of the housing of the pump, as previously marked with “c” in figure 3.20. The blades are placed in the centre of a 120 mm long perspex tube with an inner diameter of 12 mm (figure 3.22b). The clearance between the blade tip and the wall of the perspex tube was measured using two different methods, i.e. two values for tip clearance were obtained and compared. Both measurements were taken at the end of the experiments, after which wear of the perspex tube at the location of the blade was seen. For method 1 paper foil was used and wrapped around the blade section. Each time a layer of paper foil was added until a tight fit was found of the blades and the perspex tube. The tight fit was reached after two layers of foil, each 15µm thick, were wrapped around the blades. This leads to an estimated tip clearance of ~30µm. This first method is rather crude and the ~30µm is only considered an indication of order of magnitude and for reference to a more precise method. For method 2 the blade tip diameter was measured using an outer micrometer and was found to be 12.005±0.003mm. Using an inner micrometer the inside diameter of the perspex tube, at the location of the blade, was found at 12.060±0.003mm. This results in a tip clearance of 27.5±3µm (on each side).

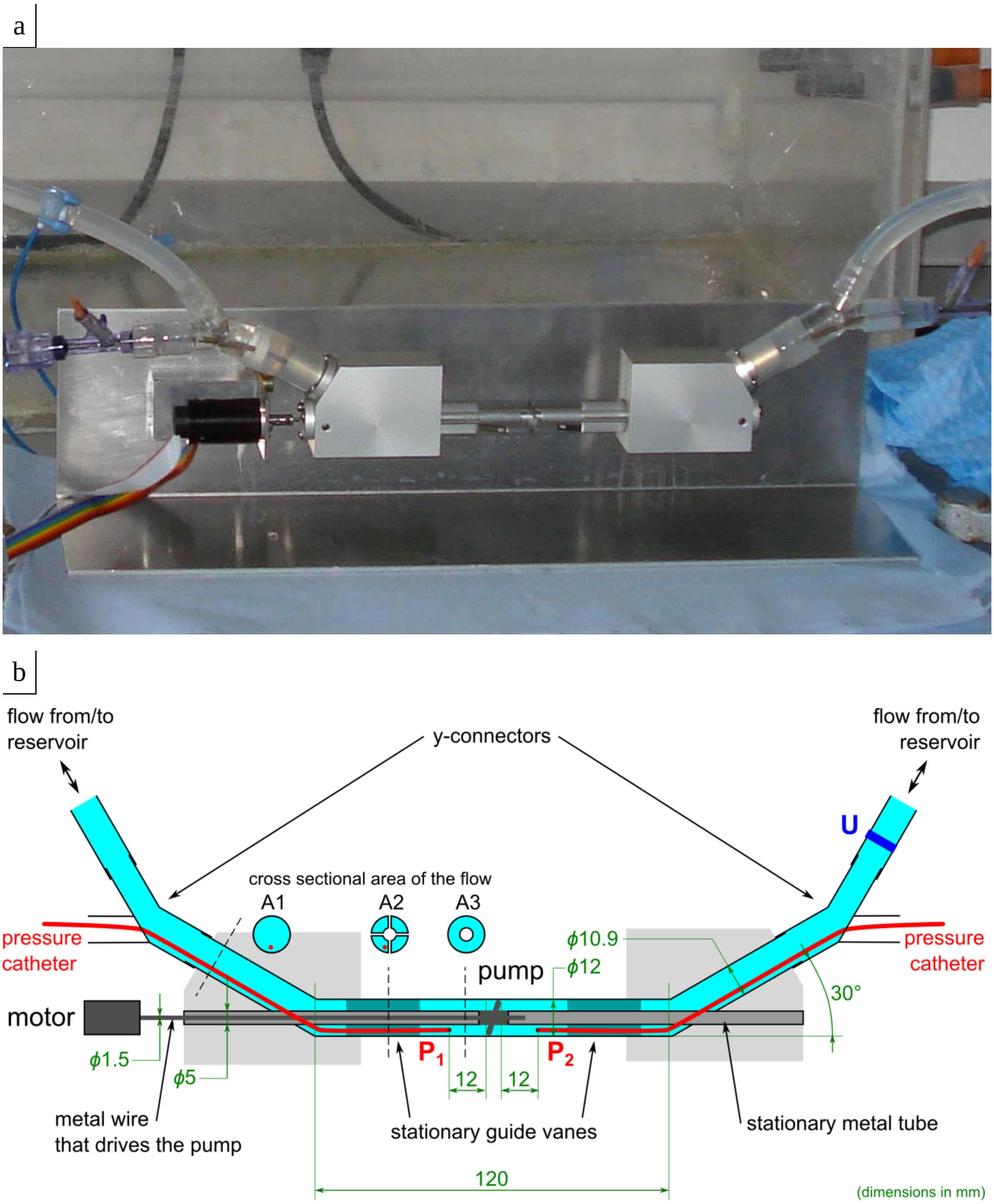

Figure 3.22: Picture (a) and schematic overview (b) of the housing of the pump.

Inlet and outlet tubes on either side are connecting the housing to the reservoir. In order to test the bi-directional functionality of the blades the inlet will serve as an outlet in the backward rotating direction. The pump, with hub diameter 5 mm and tip diameter 12 mm, is fixed onto a Ø1.5 mm steel wire that functions as a rotating axis. For the rotating axis not to be in contact with the fluid and subsequently affect velocity, it is placed inside a static Ø5 mm metal tube. The axis is supported by bearings at three locations, as shown in figure 3.23. The main purpose of the bearings is to compensate for misalignments and assure concentricity whilst the pump is rotating. The bearings as well as the axis are checked after each operation and replaced if significant wear or damage is found.

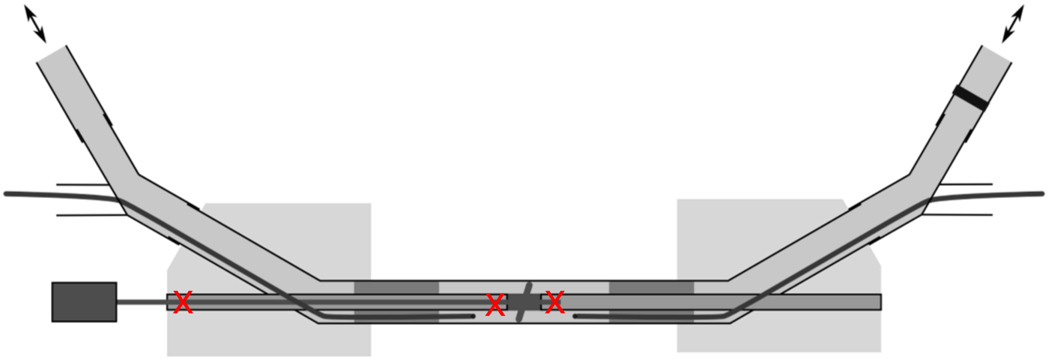

Figure 3.23: Location of the three bearings, marked by “x”, supporting the driving axis.

The inlet and outlet tubes are positioned at an angle of 30° (figure 3.22). This allows the motor to be connected to the rotating axis outside the setup, away from the fluid. Therefore the motor does not need to meet strict requirements on size and waterproof functionality. The slanted inlet and outlet tubes also ensure the distance between the blades inside the fluid domain and the pump outside the fluid domain is kept to a minimum. However, the slanted tubes will make the incoming fluid approach the blades under an angle that is not parallel to the rotating axis. This might subsequently lead to reduced pumping performance. To correct for this, stationary guide vanes are positioned at either side of the pump, as either side will function as an inlet. The assembly of one of the guide vanes is shown in figure 3.24. The Ø5 mm metal tube and the guide vanes are connected and placed onto the rotating axis. On the side where the pump will be positioned, on the right in figure 3.24, three items are placed inside the metal end of the guide vanes: a bearing to support the rotating axis, a rubber o-ring for sealing and a metal ring in between.

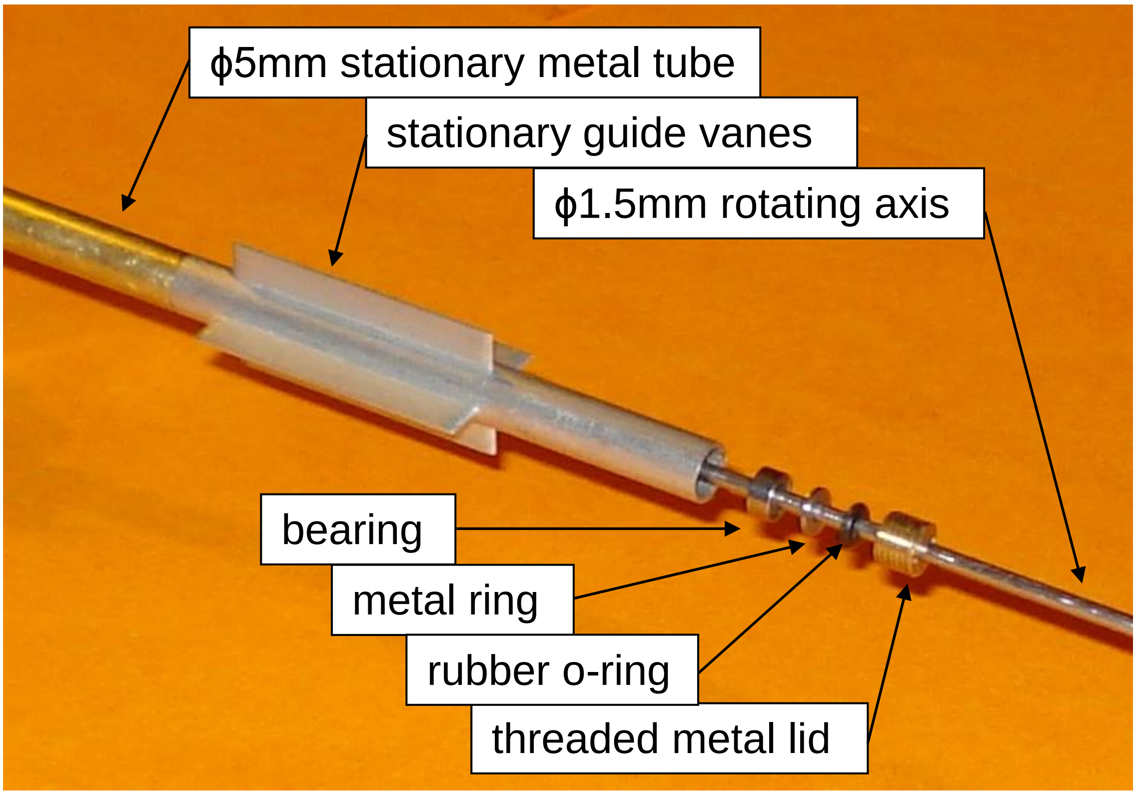

Figure 3.24: Photo of the assembly of the stationary guide vanes. Going from top to bottom and left to right. Onto the ϕ5mm tube, the guide vanes are connected. The ϕ5mm wire, on which the pump will be positioned, is passed through guide vanes and metal tube. Three items are placed inside the right end of the guide vanes: a bearing, a metal ring and a rubber o-ring. A metal lid is screwed into it for closure.

A threaded metal lid is screwed into the metal end of the guide vanes for closure and ensuring the three items keep in place. The thread of the lid is treated with Loctite 242 to ensure the lid remains secured when it is subjected to the rotating axis and associated vibrations. With this specific Loctite, disassembly is still possible with a normal amount of torque.

The Ø5 mm tube results in a 17% ($=5^2/12^2$) reduction of area A1 (figure 3.22). To minimise velocity changes inherited by the nature of the setup, rather than the blades themselves, the area A2 was given a diameter of 10.9 mm to ensure the cross-sectional area passed by the fluid is equal.

3.4.3 Calibrations

At the start of each day that measurements were taken the two pressure catheters and the flow probe were calibrated. The pressure catheters were calibrated with the “column-of-water” method (figure 3.25a). Since the pressure difference between the two catheters is especially important, both catheters were taped together and calibrated at the same time in the same column of water to ensure consistent calibrations.

The flow probes were calibrated using a continuous flow pump and a valve to control the flow rate. Timed collection of the water in a measuring cylinder started after the flow had settled and become steady.

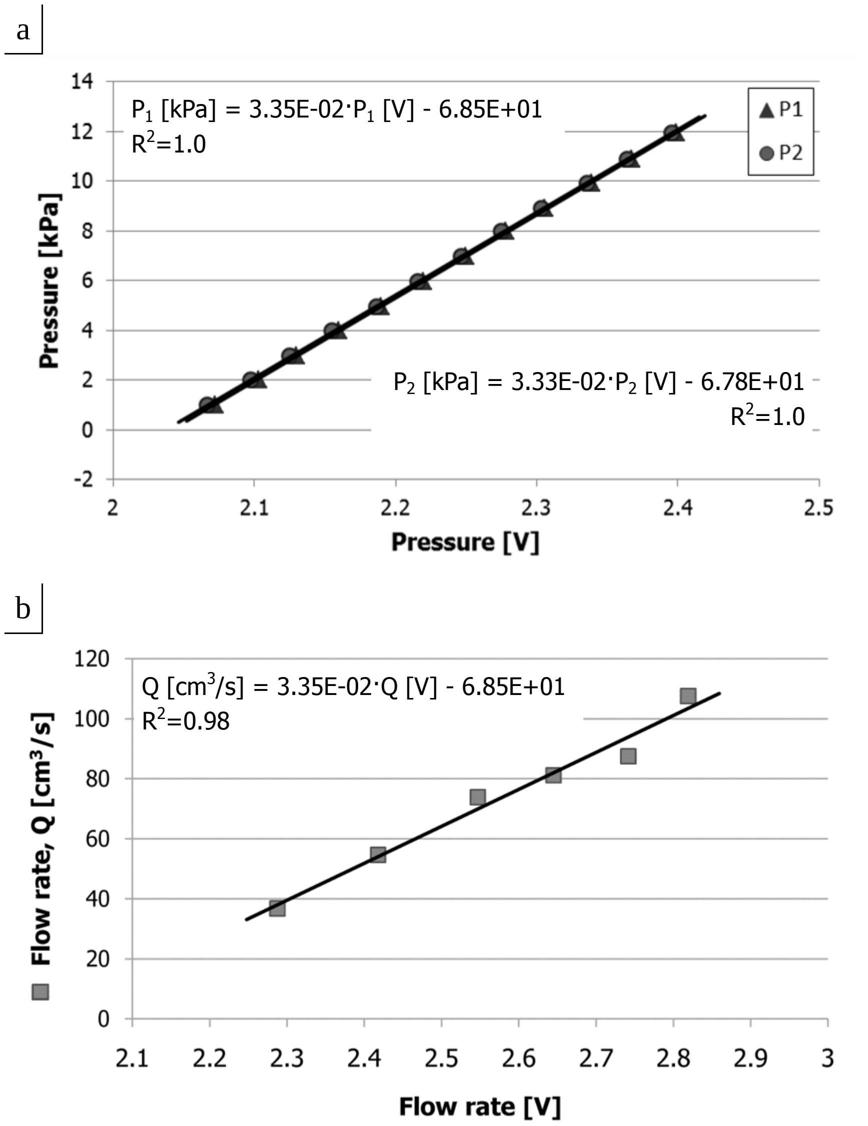

Figure 3.25: Calibration curves of the pressure catheters (a) and the flow probe (b).

3.4.4 Protocol

Steady state

In steps of 1,000 rpm, the design rotational speed of 8,000 rpm was increased and decreased 4 times. Similarly in the backward direction, in steps of the design rotational speed of 2,400 rpm was increased and decreased four times in steps of 200 rpm. This resulted in the pump being characterised for 9 constant rotational speeds in both forward and backward direction, namely in forward direction 4000, 5000, 6000, 7000, 8000, 9000, 10000, 11000 and 12000 rpm and in backward direction 1600, 1800, 2000, 2200, 2400, 2600, 2800, 3000 and 3200 rpm. For each speed, the system was subjected to 7 flow rates. For this the valve at the outlet was controlled and placed fully open, fully shut and 5 positions in between. The pressure and flow signals were acquired at a sampling rate of 500 Hz and at least 10 sec was allowed between the acquisitions of each measurement to allow the system to settle.

The above procedure was repeated twice. For the first set of measurements the pressure transducers were placed near the pump (i_1 in figure 3.20), approximately 12 mm away from the edge of the pump. For the second set the transducers were positioned away from the pump (i_2) and placed at the edge of the aluminium inlet and outlet of the housing. When the catheters are placed at i_2 the catheters' guiding wires will not obstruct the flow path as much as when the catheters are placed at i_1. This change in position of the catheters might subsequently affect the results. For the second set of measurements, in forward and backward direction the rotational speed was increased and decreased with 2,000 and 400 rpm respectively, instead of the 1,000 and 200 rpm that were used previously. This resulted in the pump being rotated at 5 constant rotational speeds in both forward and backward direction, namely in forward direction 4000, 6000, 8000, 10000 and 12000 rpm and in backward direction 1600, 2000, 2400, 2800 and 3200 rpm.

Transient

Transient experiments were performed using the same drive curves as the transient simulations (figure 3.14). The drive curves were loaded into LabView and were set to repeat continuously. The data acquisition was allowed to start 5-10 sec prior to the start of the first transient rotation. Subsequently the first recorded cycle represents the behaviour from stand still and the following thereafter the continuous behaviour. The pressure and flow signals were acquired at a sampling rate of 500 Hz and ±30 sec was allowed between the operations of the different drive curve for the system to settle.

In contrast to the steady state measurements, the pressure signal was only obtained at one location and the pressure catheters remained positioned at i_1 (figure 3.20) throughout all transient measurements.

4 Results I: Numerical Simulations

4.1 Introduction

This chapter details the results of the bi-directional pump design that was developed and subsequently enhanced iteratively using CFD analysis. The results start with the uni-directional blade profile design that is followed by the bi-directional design.

4.2 Uni-directional blade profile

Using the design parameters obtained from the traditional design methods as an initial guess, parametric CFD studies were performed for verification. The effect of changes in blade angle and rotational speed on the predicted pressure rise was modelled and results are shown in figure 4.1. At a blade angle of 75.5° the 2D uni-directional profile at the tip generated a maximum pressure rise of 9.7 kPa at 11,000 rpm and and 16.3 kPa at 13,000 rpm. At a lower rotational speed of 9,000 rpm, maximum pressure rise of 5.0 kPa was generated at a blade angle of 73°. At an even lower rotational speed of 3,000 rpm no pressure rise was generated at any of the modelled blade angles.

Subsequently the uni-directional pump was rotated in the opposite direction to locate areas of the uni-directional profile that reduce the hydraulic performance in the other direction. Figure 2.16 shows the pressure contour (panel a) and velocity streamline (c) when the uni-directional profile is rotated in the direction for which it is designed. The pressure locus at the leading edge and the pressure drop at the pressure side of the blade confirm that a pressure difference is generated between either sides of the blade. When rotated in the opposite direction, panel b and d, the pressure difference drops and velocities have more than doubled, indicating a reduced efficiency.

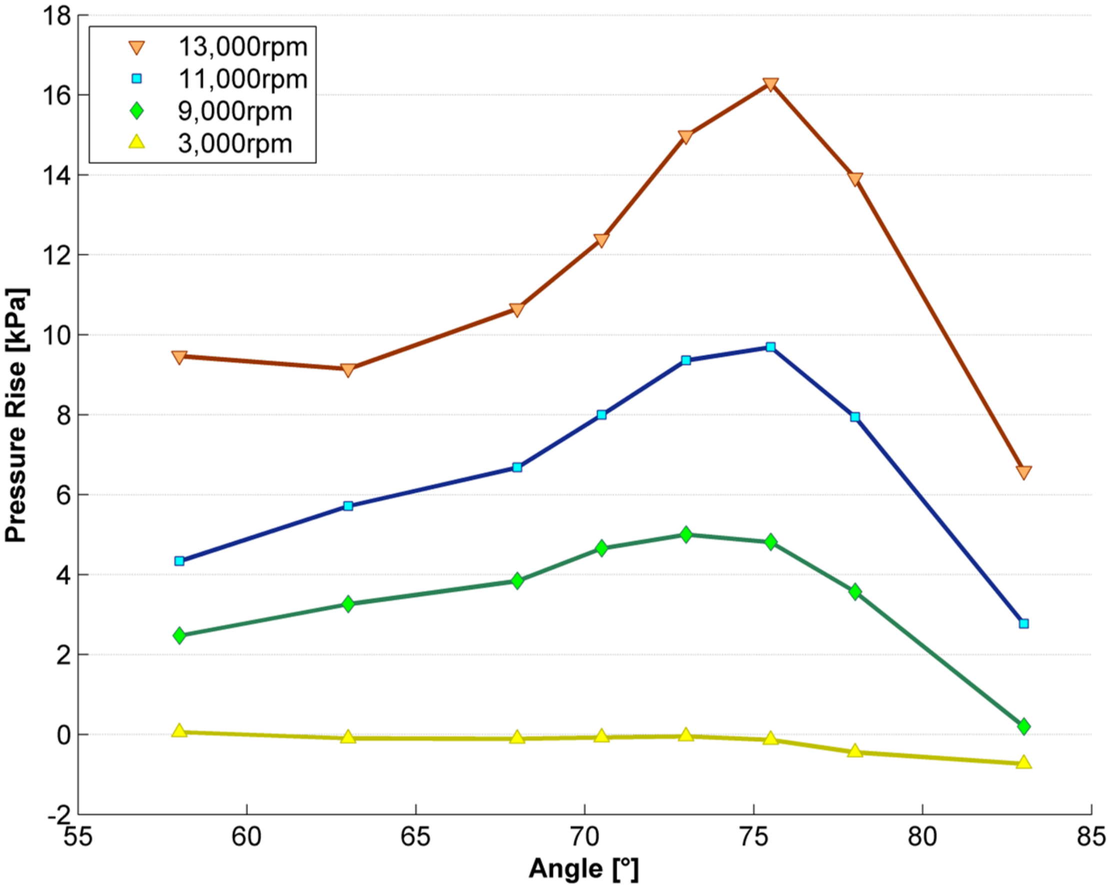

Figure 4.1: Parametric study of the uni-directional NACA 4312 profile at the tip. The effect of changes in blade angle on hydraulic performance, measured by pressure rise, was analysed for a range of rotational speeds. Maximum pressure rise occurred at 75°.

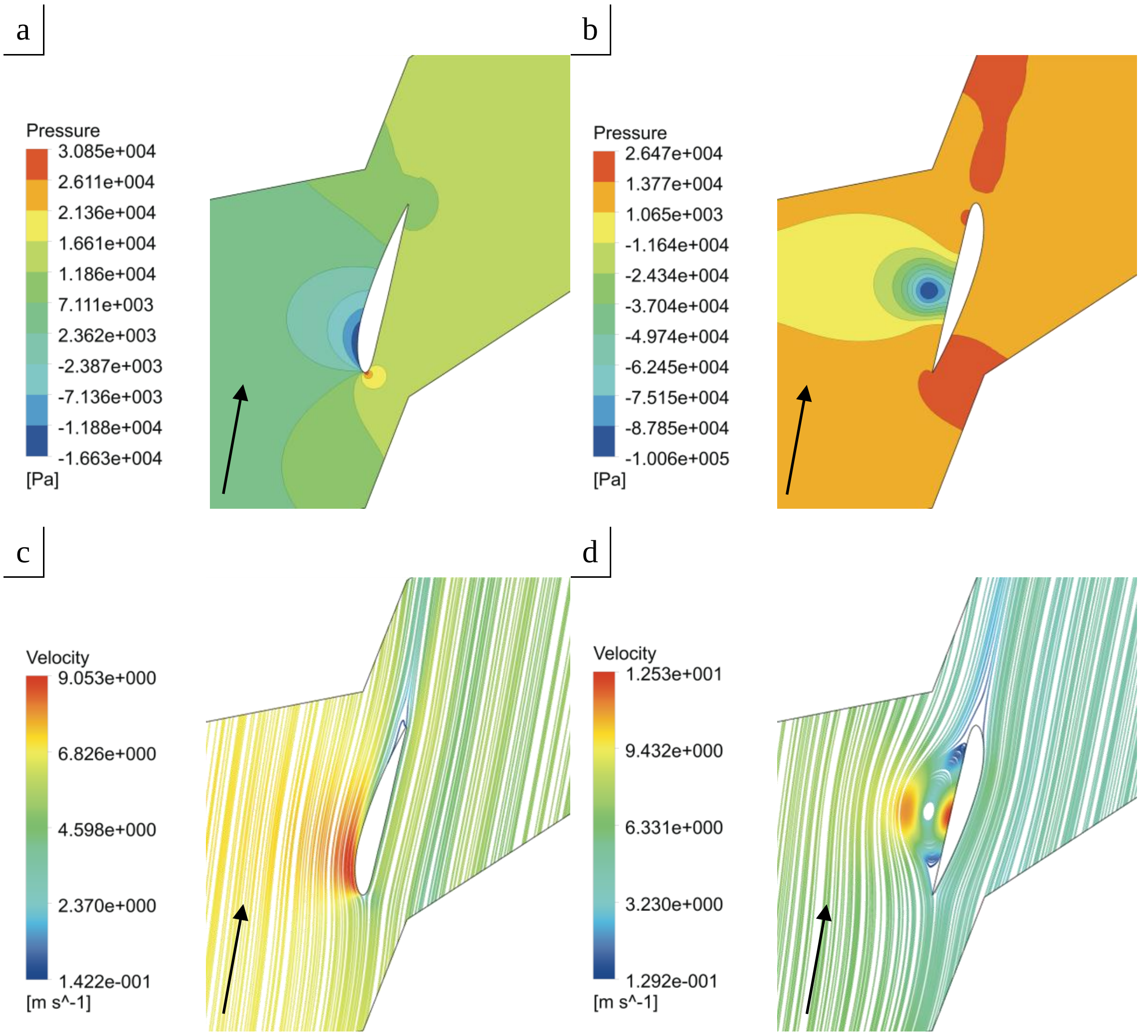

Figure 4.2: Total generated pressure and velocity of the 2D uni-directional model in forward (a,c) and backward (b,d) rotating direction, respectively.

4.3 Bi-directional blade profile

4.3.1 Two-dimensional steady state model

Both the tip and hub hydraulic performance of the symmetric bi-directional blade profile was tested (figure 4.3). It was found that blade performance was highest at the hub when positioned at an angle of 50.5°. At the tip the highest hydraulic performance was found at 73.0°.

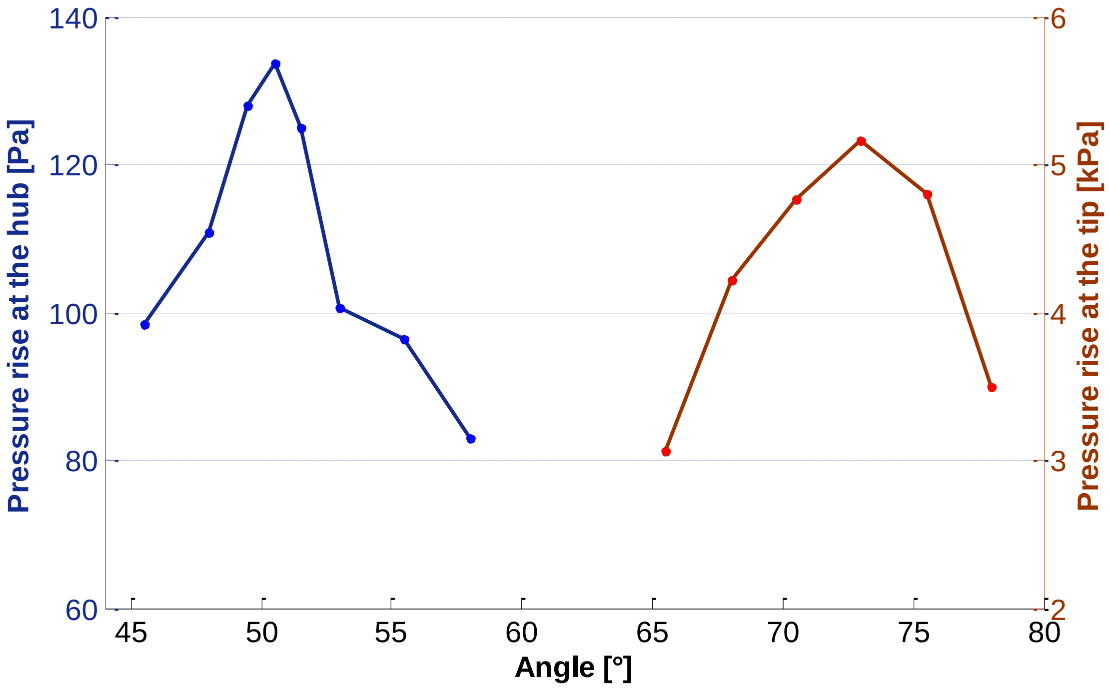

Figure 4.3: Parametric study of the 2D model of the bi-directional profile. The effect of changes in blade angle on hydraulic performance was analysed for hub and tip.

Analysis of the blade loading showed that negative work was done by the trailing edge of the blade (dashed in figure 4.4). The stream wise location, plotted on the x-axis is a ratio that ranges from 0-1 where 0 is at the leading edge and 1 is at the trailing edge of the blade. The blue dashed line in figure 4.4 represents the symmetric bi-directional profile. For this case, at a stream wise location of approximately 0.6, there is a turning point from which onwards to the trailing edge negative work is done. From the total work done, determined by the area of the closed loop, a total of 28% was found negative. This is because the symmetric bi-directional blade no longer has a sharp trailing edge. Although the presence of a sharp trailing edge improves hydraulic performance in the forward rotating direction, it has a negative effect on performance in the backward direction. Incrementally the trailing edge of the blade was flattened (figure 3.8d) to reduce the negative work whilst monitoring the performance in the backward direction. This change was quantified by the change in length in the y-direction (in µm) as the trailing edge was moved down to sharpen the profile (table 4.1). The optimum blade angles of the modified blade profile were established to be 68° and 45° for tip and hub, respectively. Figure 4.4 shows how the blade loading profile changed when applying two levels of modifications to make the trailing edge sharper.

Even after the profile modifications, negative work was still apparent but significantly reduced compared to the symmetric profile. A total power of 2.13x10^{-2} W is required for the rotation of the blade. This seems a very low value, however it is only a 2D slice of a single blade passage that is modelled in this case. From 28% of negative work for the initial profile (blue dashed line in figure 4.4), the corrections resulted in a reduced negative work of 18% (green dashed line) and 11% (solid red line). This behaviour is also seen for the generated pressure difference (table 4.1).

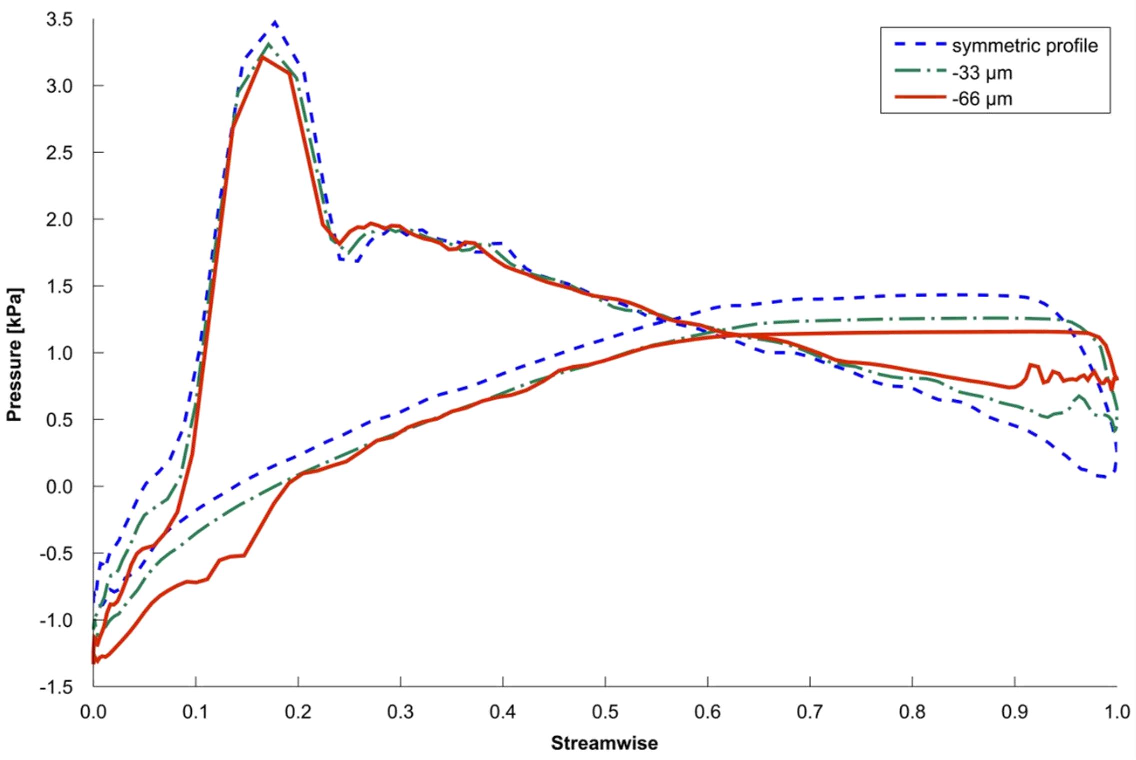

Figure 4.4: Pressure blade loading profiles of the bi-directional blade design obtained from 2D models.

Table 4.1 shows that an increase in generated pressure of approximately 68% (from 5.47 to 9.20 kPa) in the forward direction was observed with the first level of correction (-33 μm) to sharpen the trailing edge of the blade. However, this modification led also to a 38% (from 5.44 to 3.38 kPa) decrease of the generated pressure when the pump was rotated in the backward direction. The second level of correction (-66 μm) to sharpen the blade further increased the pressure rise in the forward direction with 42% (from 9.20 to 13.02 kPa) and decreased it in the backward direction with 80% (3.38 to 0.66 kPa).

Table 4.1: Effect of 2D blade profile design changes on generated pressure difference (in kPa).

	Rot. direction	Forward	Backward
Sharpness [µm]	0	5.47	5.44
	-33	9.20	3.38
	-66	13.02	0.66
Length [mm]	6	13.02	0.66
	8	13.11	0.39
	10	13.59	-0.08
Thickness [mm]	2.0	13.59	-0.08
	1.6	12.32	1.12
	1.2	11.01	2.37

Similarly the blade was increased in length and decreased in thickness to investigate the effect of these changes on the generated pressure rise. Increasing the length of the blade from 6 to 8 and 10 mm, increased the pressure rise in the forward direction with 0.69% (from 13.02 to 13.11 kPa) and 11% (from 13.11 to 13.59 kPa). Whilst in the backward direction, these changes decreased pressure rise with 41% (0.66 to 0.39 kPa) and 121% (0.39 to -0.08 kPa).

Decreasing the thickness of the blade from 2 to 1.6 and 1.2 mm, decreased the pressure rise in the forward direction with 9.3% (from 13.59 to 12.32 kPa) and 3.7% (from 12.32 to 11.01 kPa). Whilst in the backward direction, these changes increased pressure rise with 15% (from -0.08 to 1.12 kPa) and 112% (from 1.12 to 2.37 kPa).

The effects of these changes are not always favourable on other characteristics. Increasing the blade length will reduce the required rotational speed, but it will increase the residence time of the blood inside the pump.

4.3.2 Three-dimensional steady state model

The initial 3D model consisted of an interpolation of a fully symmetric (figure 3.8c) profile between tip and hub. This model yielded pressure rises of 6.38 and 6.18 kPa for systole and diastole respectively (table 4.2). Following the 2D results, the effect of making the trailing edge sharper was studied in more detail. Three additional design modifications (-41, -49 and -58µm) followed between the two levels of design modification (-33 and -66µm) and two additional increased modifications (-75 and -83µm). These modifications were only applied to the upper half (tip) of the blade whilst the hub profile remained fully symmetric. The -33 and -66 µm design modification resulted in 11% (from 6.38 to 7.07 kPa) and 15% (from 6.38 to 7.35 kPa) increases in pressure rise during systole and 4% (from 6.18 to 5.95 kPa) and 2% (from 6.18 to 6.05 kPa) decreases during diastole.

Table 4.2: Effect of 3D blade profile design changes on generated pressure difference (in kPa).

	Rot. direction	Forward	Backward
Sharpness [µm]	0	6.38	6.18
	-33	7.07	5.95
	-41	7.17	6.00
	-49	7.26	6.02
	-58	7.33	6.04
	-66	7.35	6.05
	-75	7.41	5.92
	-83	7.44	5.93
Length [mm]	6	3.69	7.09
	10	4.54	7.98
Thickness [mm]	2.0	3.69	7.09
	1.2	4.04	7.60

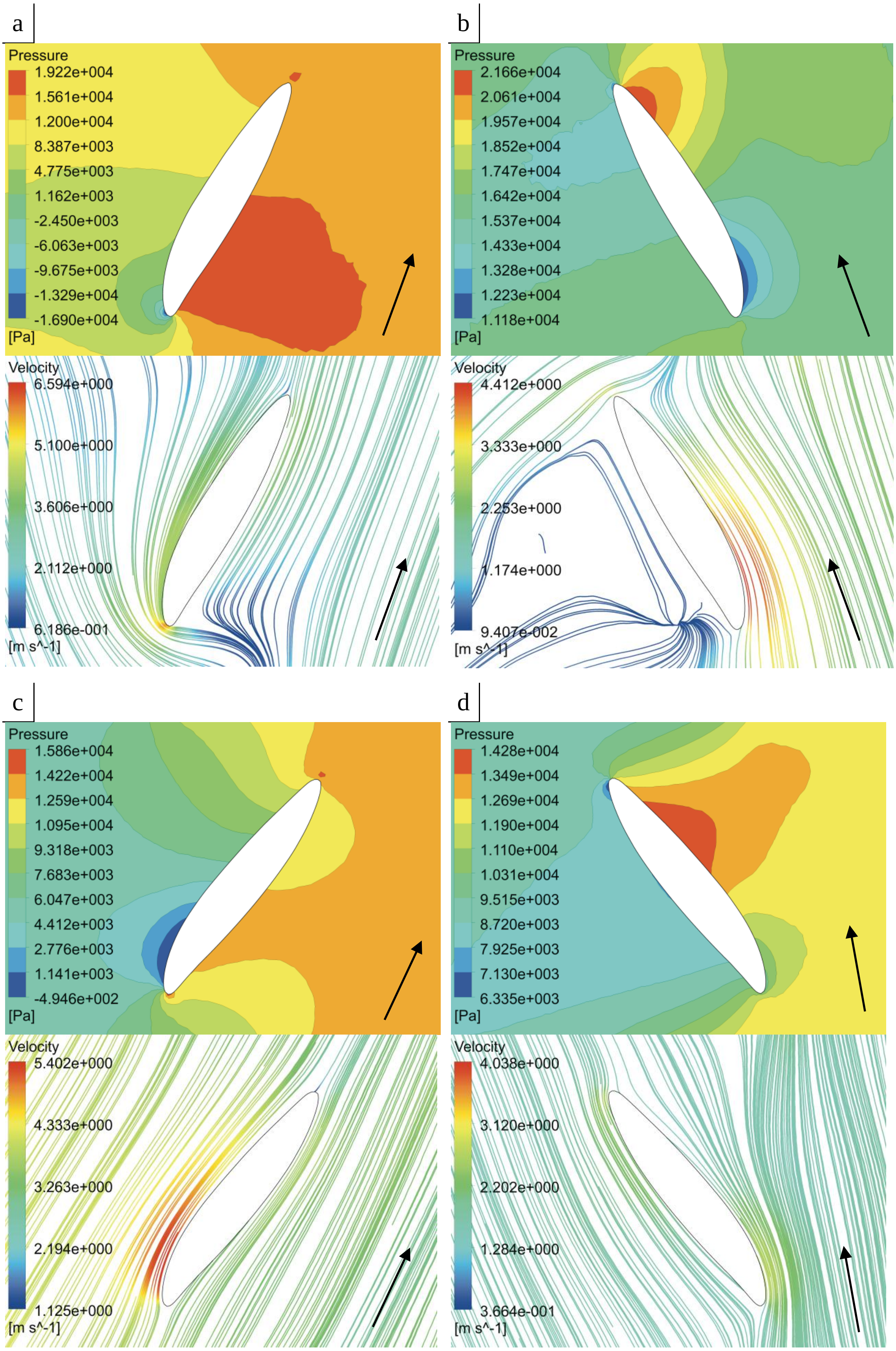

Figure 4.5: Total generated pressure of the 3D model at tip (a,b), hub (e,f) and in between (c,d) sections in forward and backward running direction respectively.

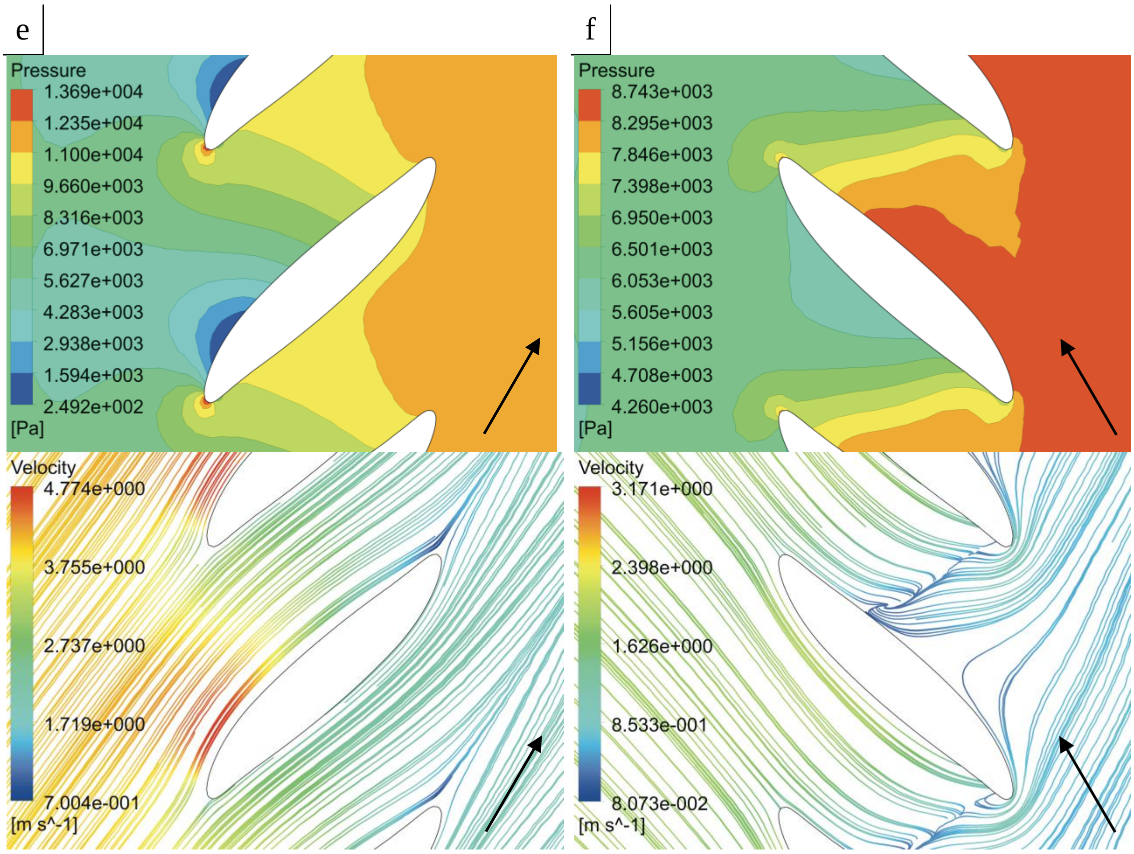

Figure 4.5: (continued)

The levels of modification did not significantly affect the hydraulic performance in the backward direction. In forward direction, however, the -66µm change led to the highest increase in performance (15%), whereas the -33µm change led to a decrease of 11%. Therefore the profile with the -66µm modification at the tip was deemed the most suitable and considered the final blade design of this study.

Figure 4.5 shows the pressure loading of this profile at tip and hub in either rotational direction. The pressure contours show the generation of pressure rise in each direction and in the backward direction this negative work done by the blade at the tip (figure 4.5b) can be noticed.

Of the final design, the profile with the -66µm modification at the tip the characteristic pressure-flow curves were calculated for a range of rotational speeds and flow rates at which the pump is expected to run (figure 4.6).

The model of the final design, with an average systolic pressure rise of 7.35 kPa and diastolic pressure rise of 6.05 kPa, resulted in different pressures rise than in the 2D runs (13.02 and 0.66 kPa, respectively). This could be due to the different level of modelling. The domain for the 2D runs consisted of a section at the hub or the tip whilst the domain of the 3D runs encompasses the entire blade from hub to tip. Another important factor that could explain this difference is the effect of tip clearance.

A set of three steady state simulations was carried out, with a tip clearance of 0, 25 and 50µm (dimension as indicated in figure 3.12a). For each tip clearance the characteristic pressure-flow characteristics at 8,000 rpm were recalculated. It is seen that especially for low flow rates, pressure rise is affected significantly by the tip clearance (figure 4.7). For the lowest flow rate tested (105 cm^3/s) pressure rise decreased by 3% and 16% for a 25 and 50µm clearance respectively. The effect the tip clearance has on pressure rise is visualised by pressure contours in the meridional view (figure 4.8). Furthermore turbulence is seen to increase as the tip clearance is increased (figure 4.9). However, the turbulence kinetic energy seems to get distributed more evenly between hub and tip as the clearance increases and be less localised as was seen with zero clearance.

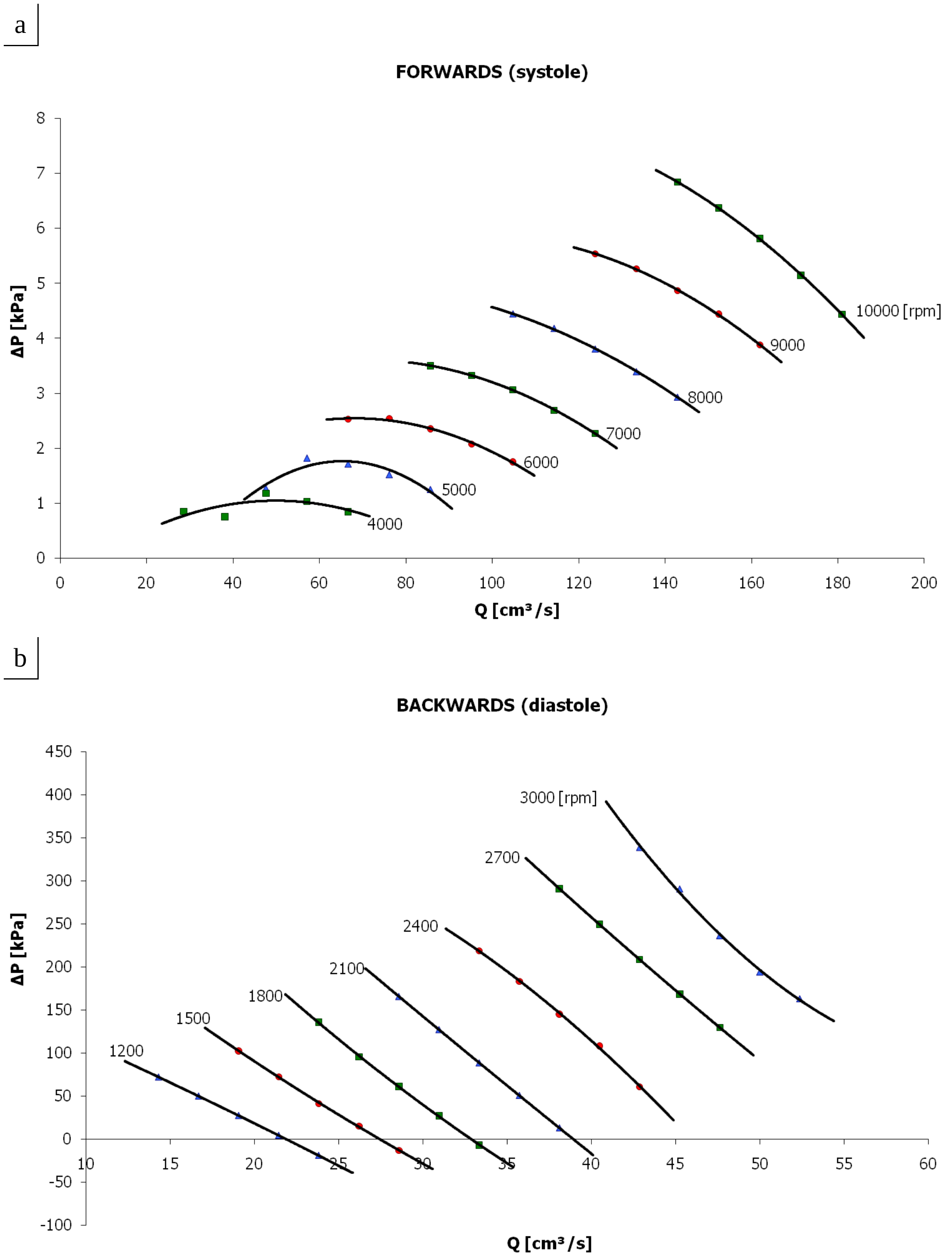

Figure 4.6: The pump's characteristic head-flow curves as obtained from steady state simulations.

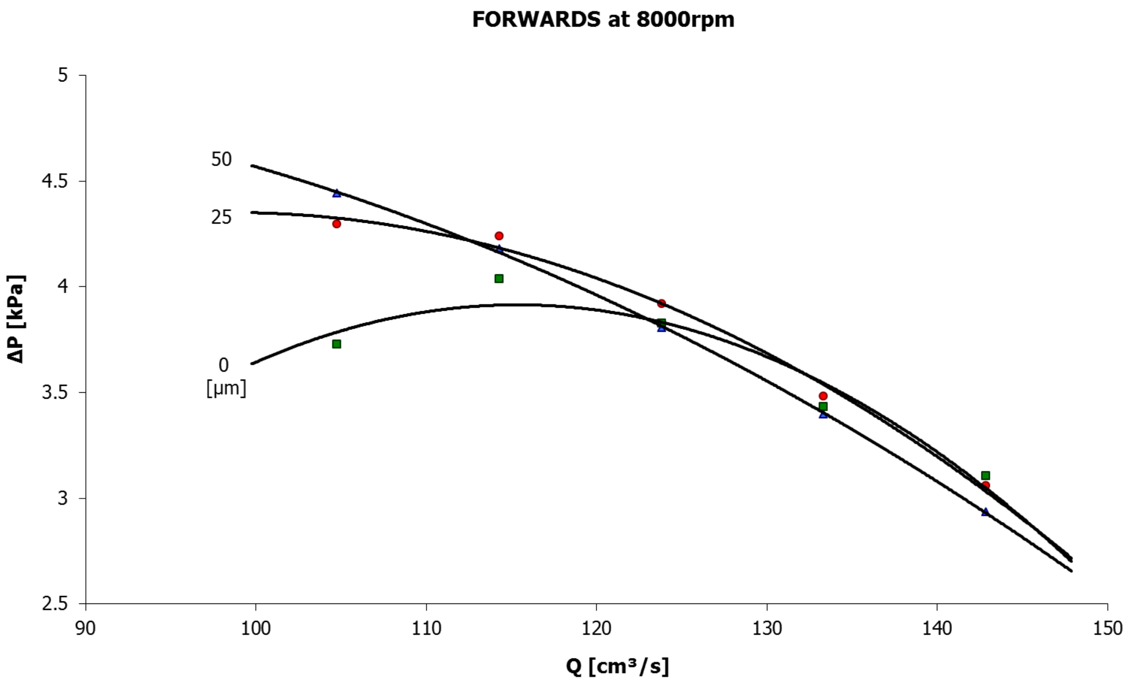

Figure 4.7: The pump's characteristic head-flow curves as obtained from three steady state simulations, respectively with a tip clearance of 0, 25 and 50μm.

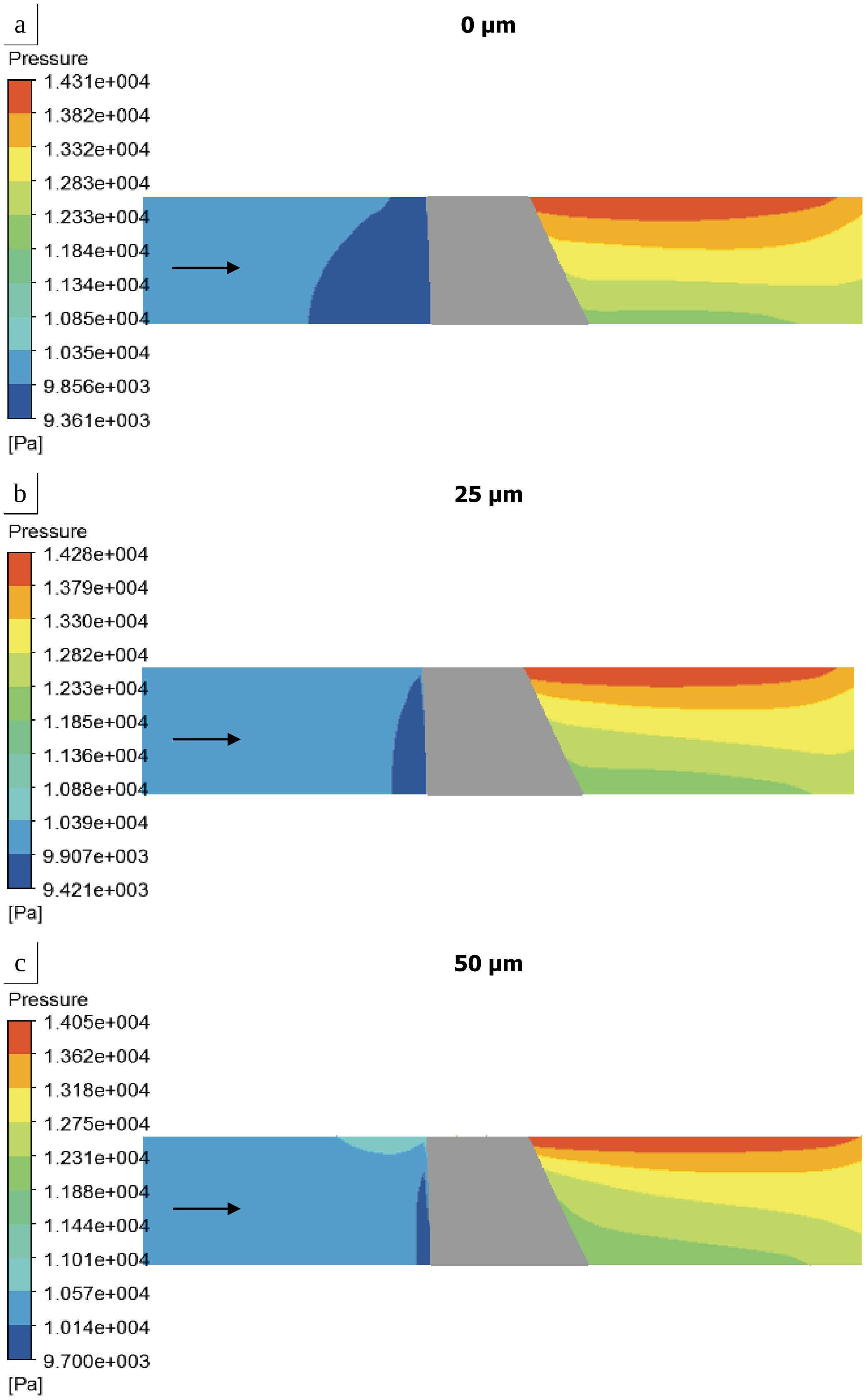

Figure 4.8: The pressure contour, plotted in the meridional view. Three steady state simulations with tip clearances of 0, 25 and 50µm. Each at a constant rotational speed of 8,000 rpm and a constant flow rate of 105 cm^3/s.

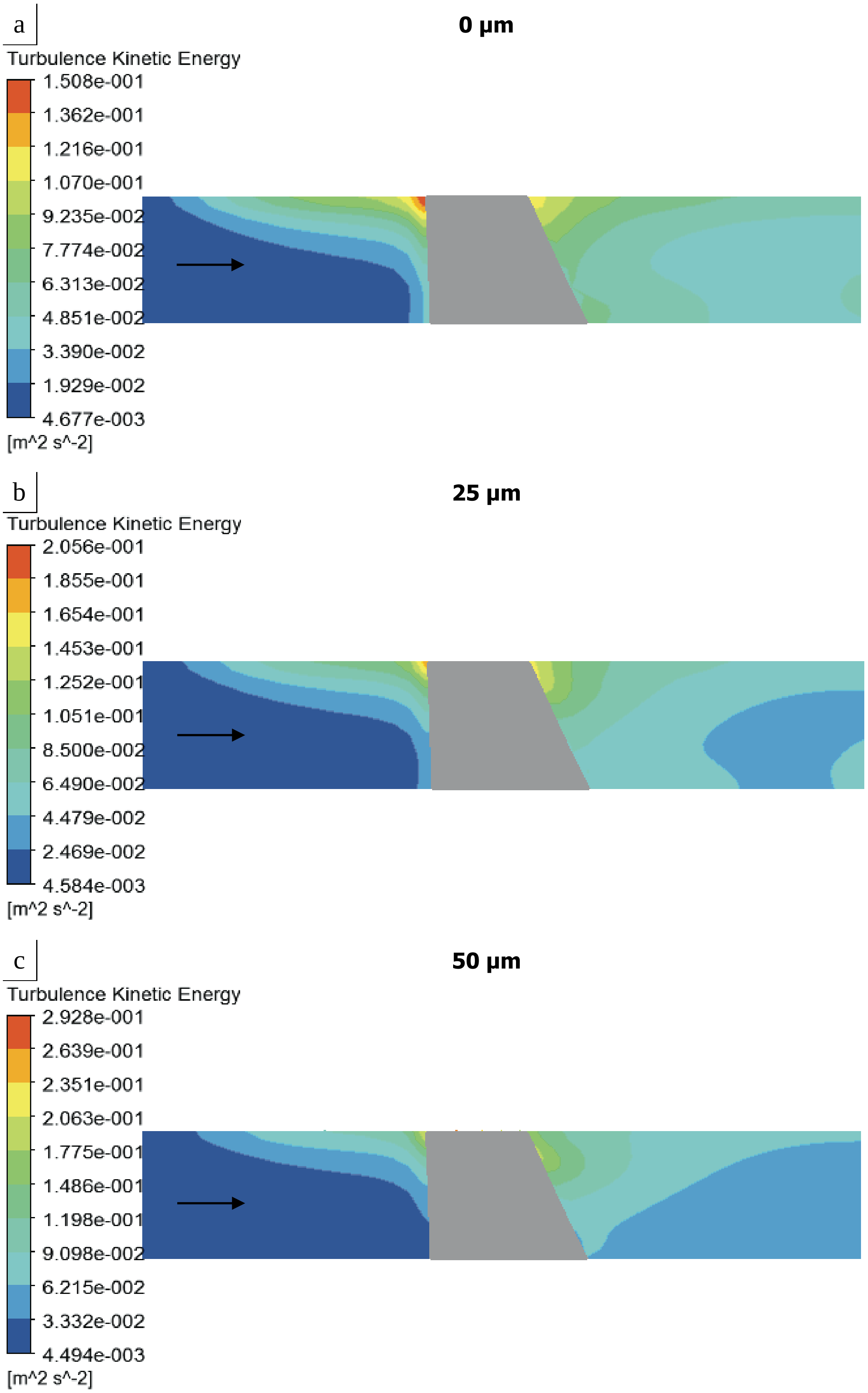

Figure 4.9: The turbulence kinetic energy contour, plotted in the meridional view. Three steady state simulations with tip clearances of 0, 25 and 50µm. Each at a constant rotational speed of 8,000 rpm and a constant flow rate of 105 cm^3/s.

4.3.3 Three-dimensional transient model

Table 4.3 summarises the results of the transient simulations on the “pump only” model. It is seen maximum flow delivery only occurs when the pump is run in one rotational direction only. For the “sys-dia” drive curve (as defined in figure 3.14), the flow delivery during the diastolic phase is decreased by 13%, compared to the “dia only” drive curve (19.4 cm^3 vs. 22.3 cm^3). At a reduced rate, the same behaviour is seen with the “dia-sys” and “sys-only” drive curves that is showing a 4.9% decrease (37.0 cm^3 vs. 38.9 cm^3). For all drive curves, the maximum generated pressure rise during forward and backward directions seems very consistent.

Table 4.3: Results of transient simulations of the “pump only” domain.

	Q_{max} [cm^3/s]		ΔP_{max} [kPa]		Q [cm^3]	
Drive curve	fw	bw	fw	bw	fw	bw
sys only	161.2	-	2.22	-	38.9	-
dia only	-	38.4	-	-0.16	-	22.3
sys-dia	161.2	-36.6	2.22	-0.16	38.6	19.4
dia-sys	160.8	-38.4	2.24	-0.16	37.0	21.4

For the “sys-dia” drive curve, figure 4.11 shows the mass flow rate and generated pressure head for the predefined rotational speed. At a maximum rotational speed of 8,000 rpm during systole, a flow rate of 161 cm^3/s is delivered at a pressure head of 2.22 kPa. During diastole, at a maximum rotational speed of 2,400 rpm, a flow rate of 36.6 cm^3/s is delivered at a pressure head of 0.16 kPa. The total flow delivery is 39 cm^3 and 19 cm^3 for systole and diastole, respectively.

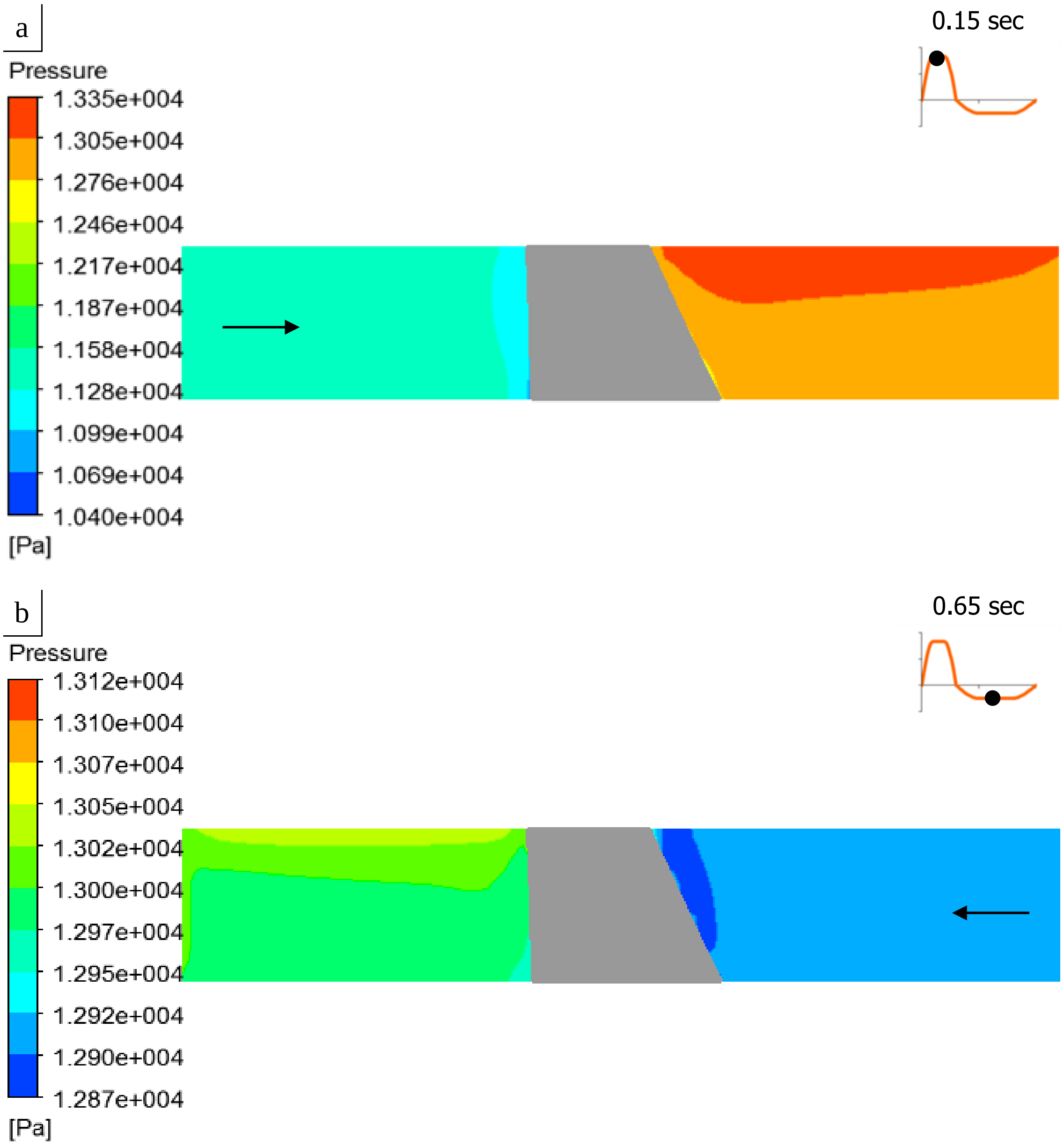

Figure 4.10: The obtained flow rate (a) and pressure rise (b) from the transient “pump only” model.

Theoretical inertia calculations were carried out to obtain an estimate of the pump’s power requirements. A Ø5 mm and 20 mm long titanium (ρ_{tit} = 4,506 kg/m^3) rotating axis was considered for which the standard formula of inertia was used: $I_{\text{axis}}=½mr^2$ (Benson, 1996). The blades were simplified as a thick-walled 5 mm long cylindrical tube, with 20% of the volume consisting of titanium and the remaining 80% of blood (ρ_{bl} = 1,050 kg/m^3). An inner and outer radius of 2.5 and 6 mm respectively were assumed to calculate the inertia of the blades: $I_{\text{blades}}=½m(r_1^2+ r_2^2)$ (Benson, 1996). The total inertia was found to be: $I_{\text{total}}=I_{\text{axis}}+I_{\text{blades}} = 5.53\cdot10^{-9} + 1.72\cdot10^{-8} = 2.27\cdot10^{-8}$ kg·m^2.

A maximum acceleration to 8,000 rpm in 0.1 sec, will subsequently lead to a torque requirement of $T=I\cdot(d\omega/dt)= 1.90\cdot10^{-4}$ N·m resulting in a power requirement of $P=T\cdot\omega$=0.159 W.

In contrast to the above, the CFD calculations (neglecting mechanical friction) are showing a maximum power requirement during systole (between 0.1 and 0.2 sec in figure 4.11a) of approximately 3.7 W and this requirement decreases to 1.3 W during diastole. This is calculated by summing the torque components in the direction of the rotational axis, on all blade surfaces. This total amount of torque is then multiplied by the rotational speed. Power on the fluid by the rotating hub, on which the blades are mounted, is considered negligible. The 3.7 W obtained through CFD is compared with the theoretically estimated 0.159 W. A big discrepancy with a factor of 25x is observed.

The sensitivity was checked of the 20% titanium and 80% blood. These percentages were guessed and might well be 10% greater or smaller. Considering 10% titanium and 90% blood, the required power decreases from 0.159 W to 0.135 W. Considering 30% titanium and 70% blood, the required power decreases to 0.183 W. The theoretically estimated power remains in the same power of magnitude and the big discrepancy cannot be due to the assumed 20% titanium and 80% blood.

In figure 4.12b the CFD results further show that in the forward direction, maximum wall shear around the blades was found to be ~ 140Pa lasting less than 300 ms, whilst in the backward direction this was ~ 23 Pa lasting for less than 700 ms.

Blade loading pressure and velocity streamlines halfway between tip and hub are plotted in figure 4.13 at seven instants. Panel b shows the results at the instant of maximum systolic rotational speed at 0.15 sec into the cycle. A low spread local maximum pressure locus is observed at the trailing edge of the blade indicating negative work is done by this section of the blade. After 0.3 sec, the end of systole, the blades change the direction of rotation, in order to support flow in the opposite direction during diastole (panel d). Flow is stagnating during this short period. Figure 4.11a-b suggests there is a delay for the mass flow rate and the pressure difference to change sign following the change of rotational direction at 0.3 sec. The delay times were found to be approximately 50 ms for the mass flow rate and 100 ms for the pressure difference. Panel f, taken halfway the diastolic phase, shows a mirror image of panel b and confirms flow is now supported in the opposite direction.

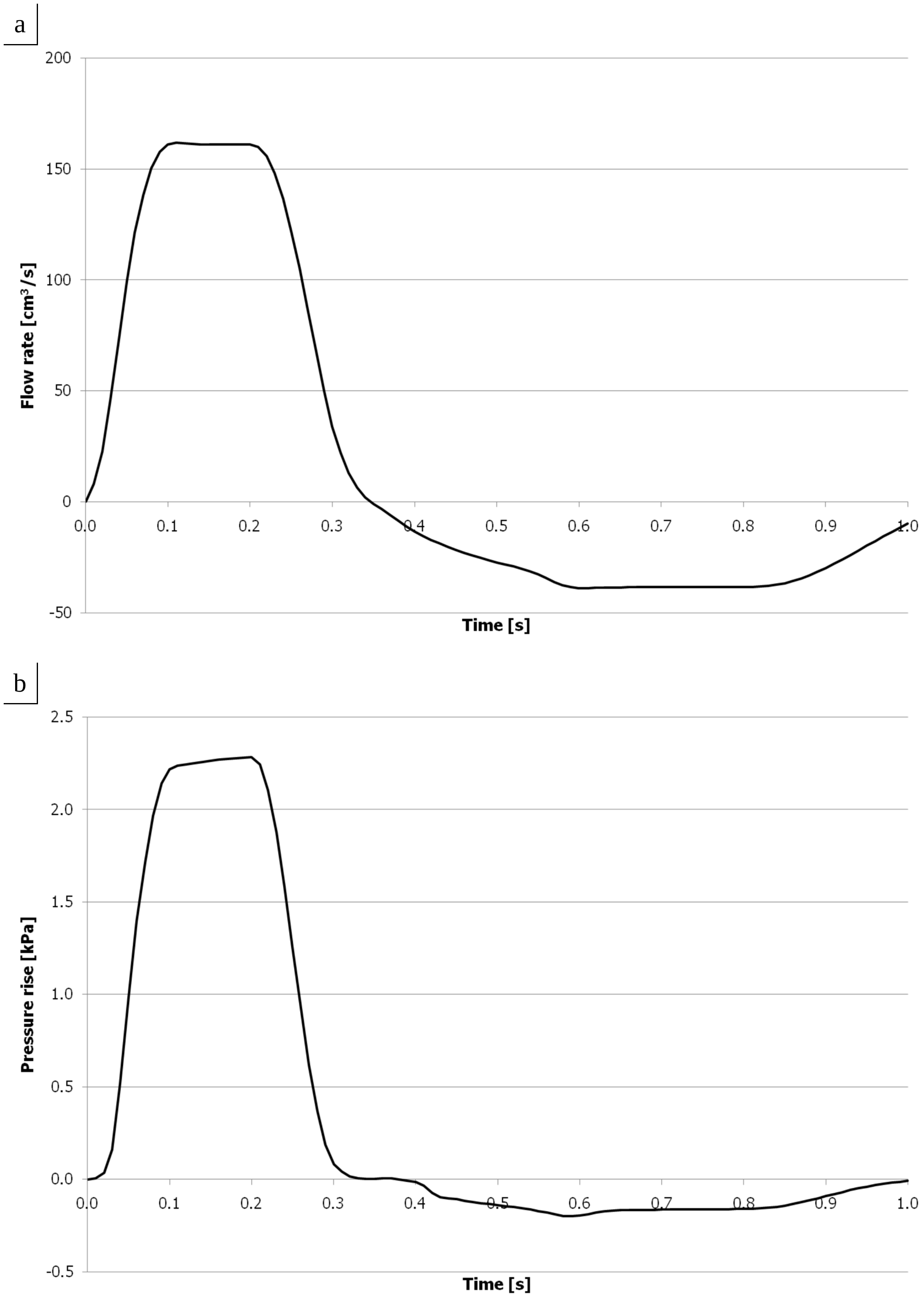

Figure 4.11: The obtained flow rate (a) and pressure rise (b) from the transient “pump only” model.

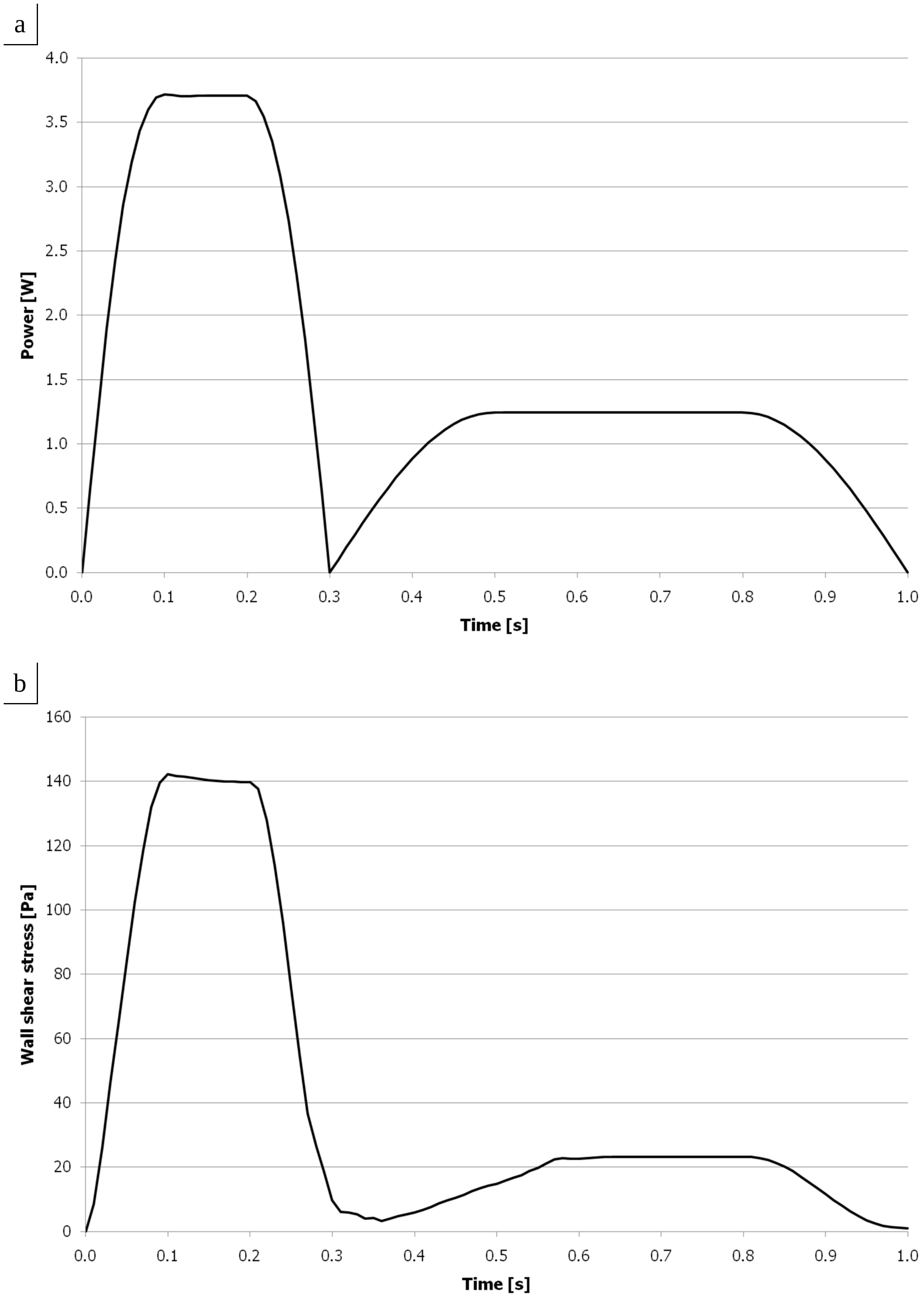

Figure 4.12: The power requirements of the modelled blades domain (a) and wall shear stress around the blades (b) plotted against time.

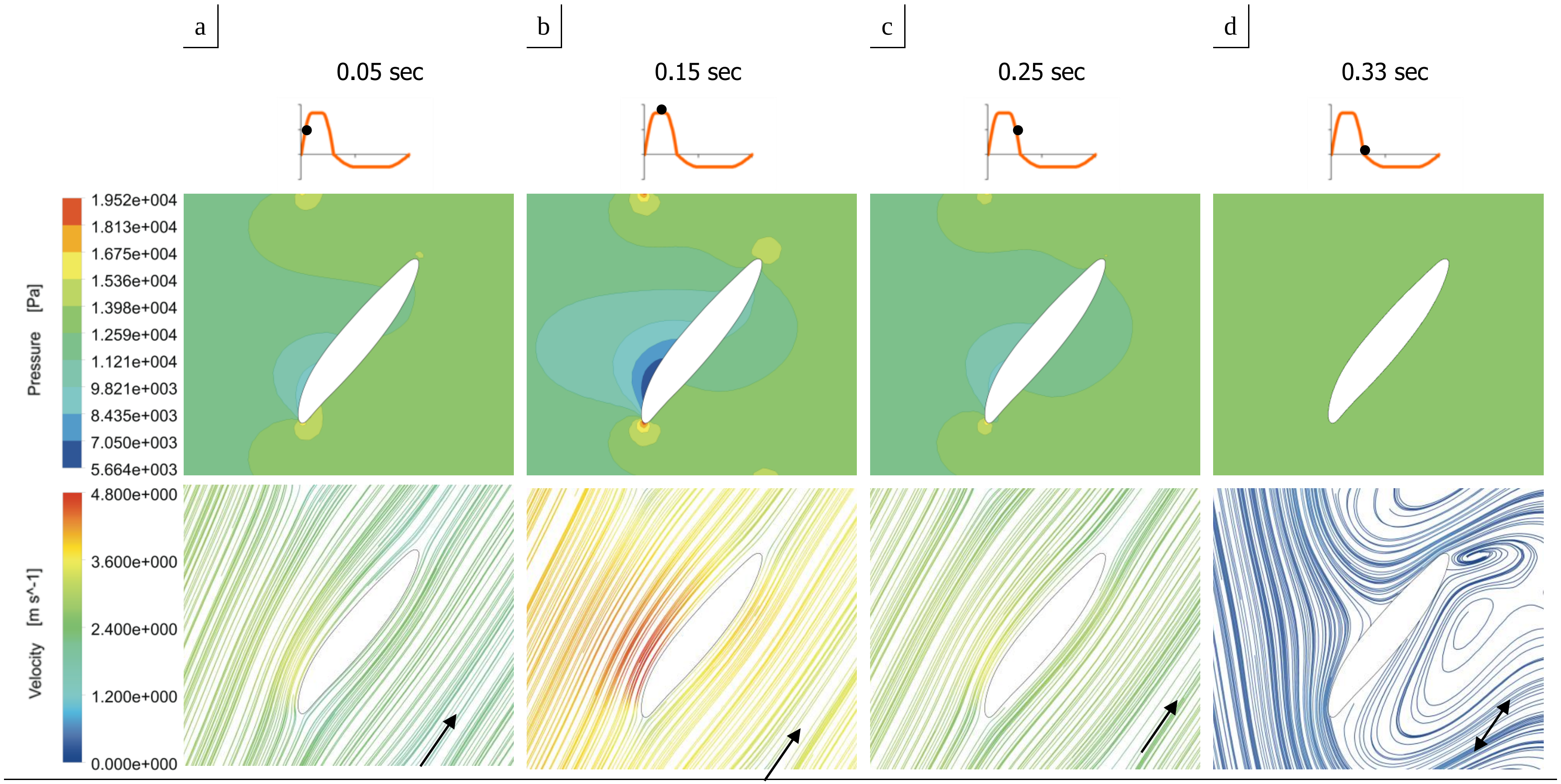

Figure 4.13: Blade loading pressure and velocity streamlines of the 3D transient model at three cycle instants, during systole (a-c), diastole (e-g) and the transition stage (d) in between when the flow is changing direction.

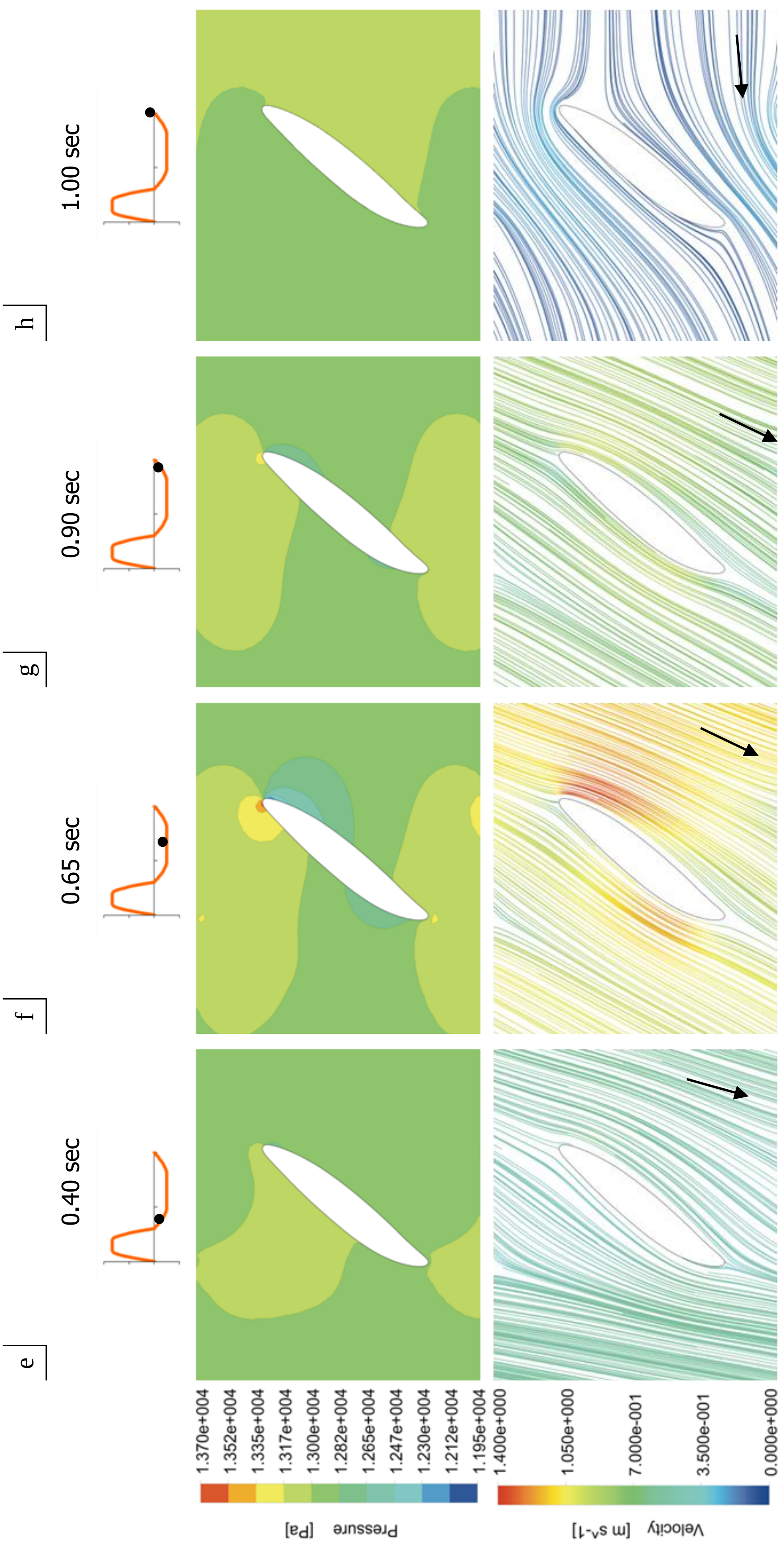

Figure 4.13: (continued)

4.4 Flow phenomena in the transverse of the blade

In figure 4.14, nine velocity streamline plots are presented. Figure 4.14a and figure 4.14i are included as reference for comparison. Figure 4.14b-h show the development of the flow in the period of the driving cycle when the rotational direction is changed. Secondary flows and stagnation areas are developing at this point in time. The colours of the streamlines are indicating the turbulence kinetic energy. Halfway systole (figure 4.14a) a maximum turbulence kinetic energy is seen of 0.28 m^2/s^2. Halfway diastole (figure 4.14i) this maximum is decreased to 0.078 m^2/s^2.

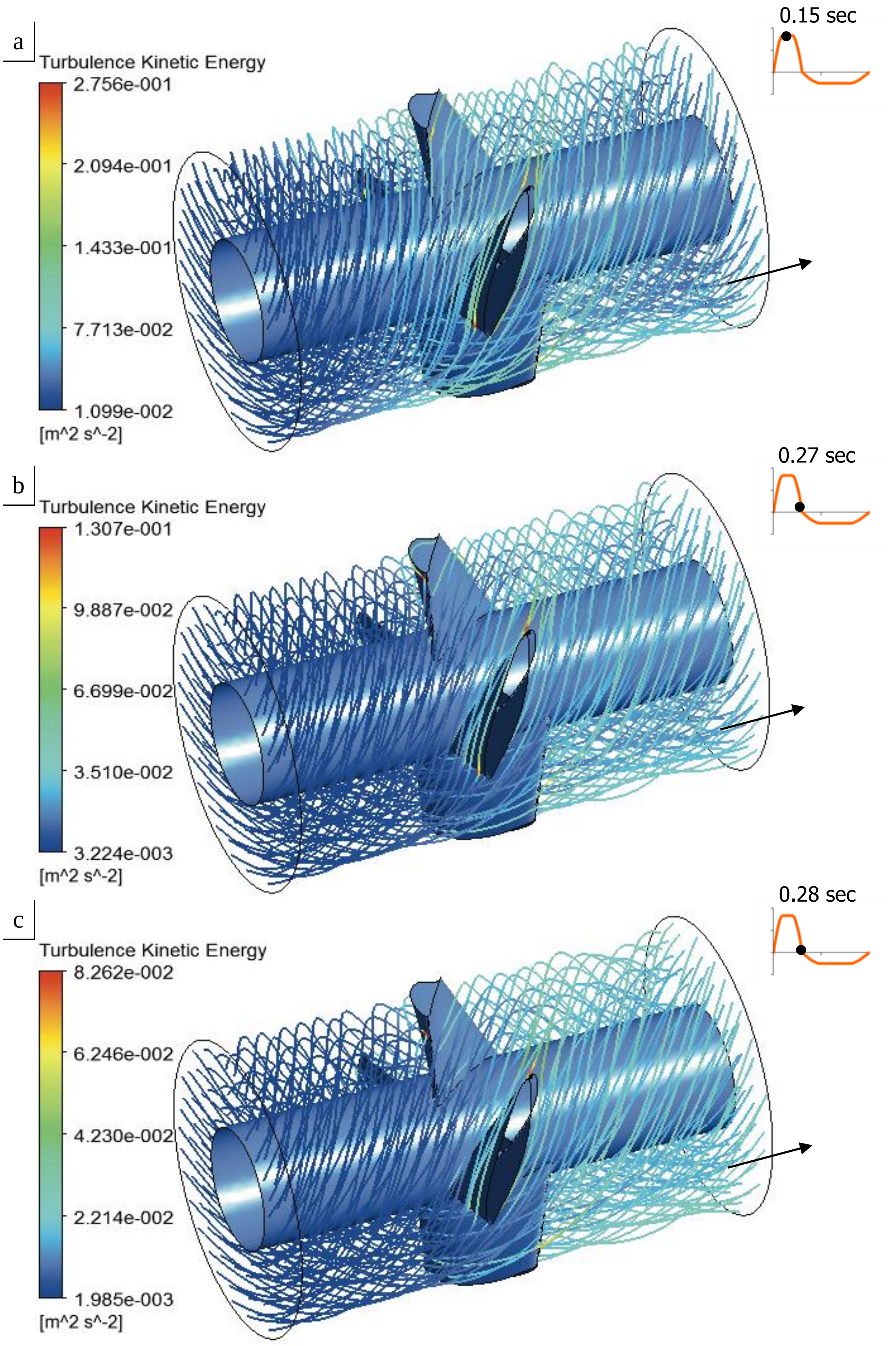

Figure 4.14: Velocity streamlines (massless particle analysis) obtained from the transient "pump only" model, whereby the colour of the streamlines represents the corresponding amount of turbulence kinetic energy.

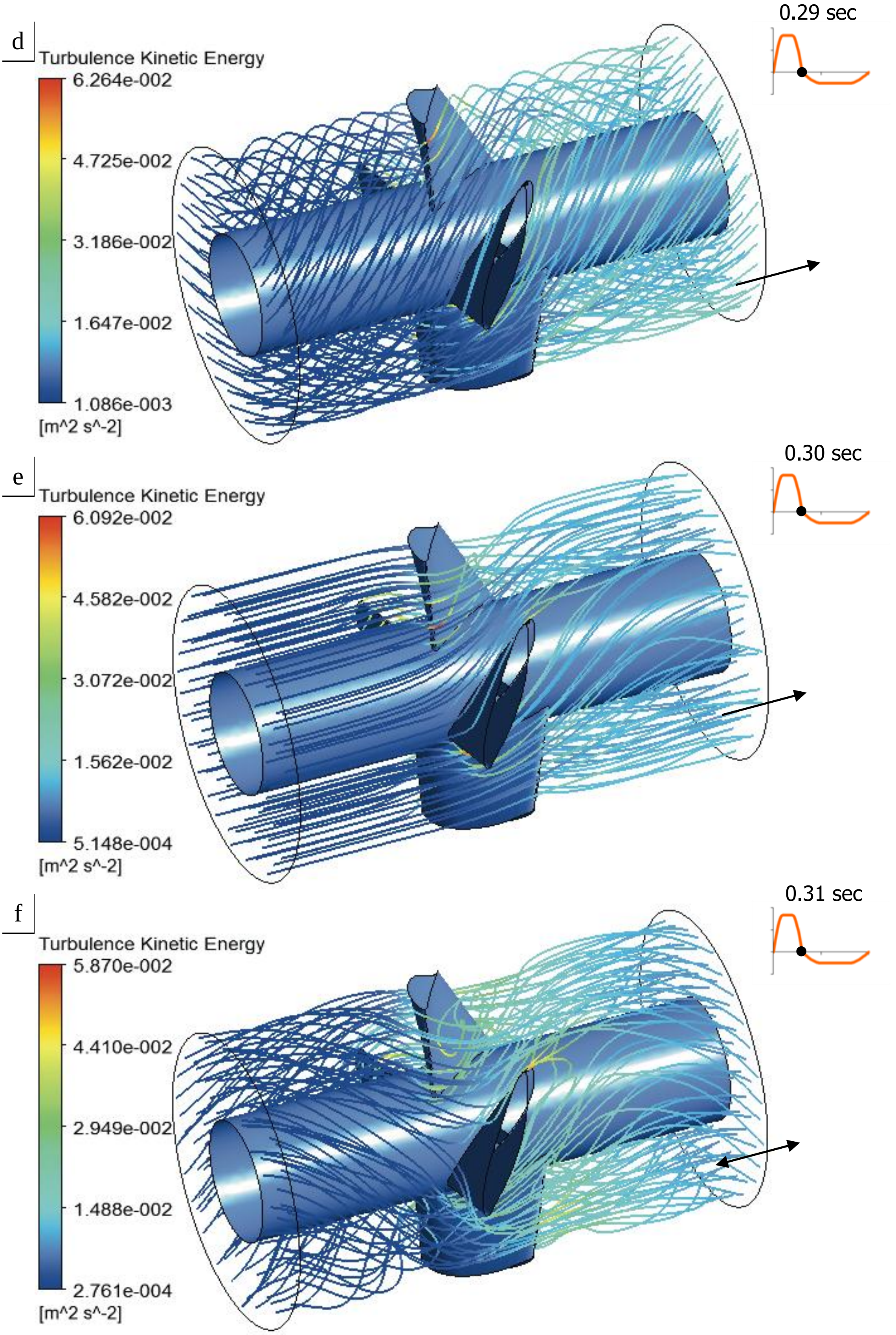

Figure 4.14: (continued)

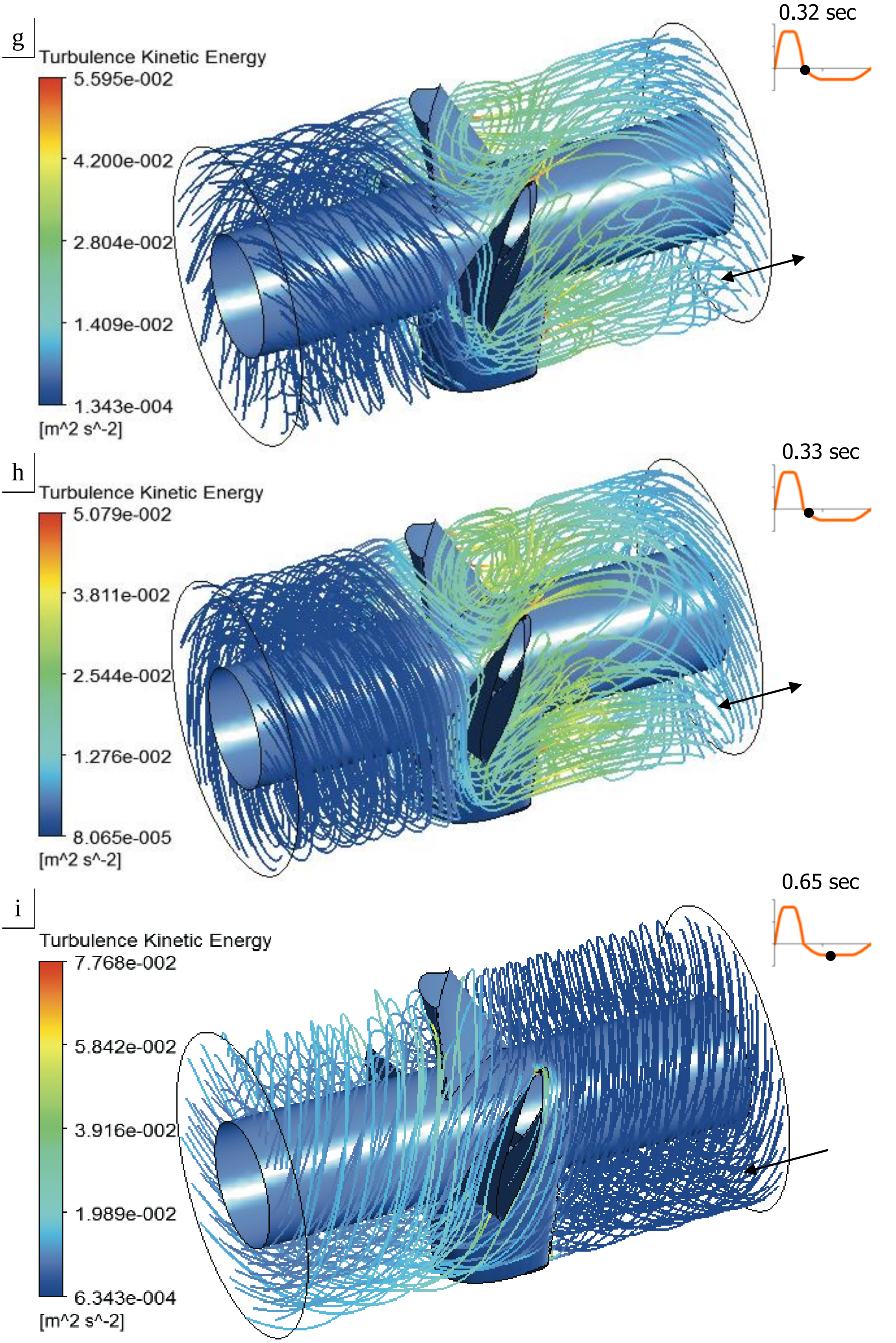

Figure 4.14: (continued)

4.5 Ascending aorta domain

Table 4.4 summarises the results of the transient simulations on the ascending aorta model. When placing the pump in the 25mm tube, a maximum flow rate of 158 cm^3/s is delivered at a pressure head of 2.47 kPa during systole. Whilst during diastole a maximum flow rate of 20.3 cm^3/s is delivered at a pressure head of 0.17 kPa. The total flow delivery is 38 cm^3 and 11 cm^3 for systole and diastole, respectively. The calculations confirm that during both peak systole and diastole pressure difference is generated.

Table 4.4: Results of transient simulations in the ascending aorta domain (for length, L, and diameter, D, as defined in figure 3.13).

		Q_{max} [cm^3/s]		ΔP_{max} [kPa]		Q [cm^3]	
	[mm]	fw	bw	fw	bw	fw	bw
Extending the tube at inlet and outlet (pump placed at wall, D_1 = 25 mm)							
$L_1 – L_2$	20 – 20	157.9	-20.3	2.47	-0.17	37.9	11.0
	20 – 40	159.5	-19.4	2.44	-0.18	38.3	10.3
	20 – 60	157.8	-15.8	2.54	-0.17	38.5	8.1
	20 – 80	153.9	-12.4	2.80	-0.13	38.1	6.0
	40 – 40	158.2	-17.0	2.56	-0.17	38.5	8.8
Pump placed at wall, for different wall diameters							
D_1	20	158.9	-21.0	2.40	-0.17	38.4	11.9
	25	157.9	-20.3	2.47	-0.17	37.9	11.0
	30	156.9	-21.0	2.55	-0.17	37.5	11.2
Pump placed in centre of aorta, for different wall diameters							
D_1	20	156.9	-17.0	2.54	-0.15	37.9	9.0
	25	154.2	-18.7	2.72	-0.16	37.1	9.6
	30	155.5	-19.2	2.70	-0.17	37.3	9.9

Furthermore it is seen that extending the tube length at the outlet (L_2), does not affect the systolic flow delivery. However, increasing L_2 does increase the diastolic flow delivery up to 45% (6.0 vs. 11 cm^3). Whilst having the pump placed at the tube's wall, it is seen that 5 mm increments of the tube diameter D_1, do not affect the systolic or diastolic flow deliveries (maximum change found of 7.6%, 11.0 vs. 11.9 cm^3). This same behaviour is seen when placing the pump in the centre of the tube. When comparing both positions of the pump, it is seen moving the pump from the wall to the centre does not affect the systolic flow delivery (maximum change found of 1.3%). The diastolic flow delivery though decreased by 16.7% as the pump was moved to the centre of the tube.

However, during diastole, velocity vectors (figure 4.15) reveal that the flow is not approaching parallel to the rotational axis. Subsequently the flow is exiting the blades under an increased angle as well. At this instant recirculation areas are observed as the flow is leaving the blades.

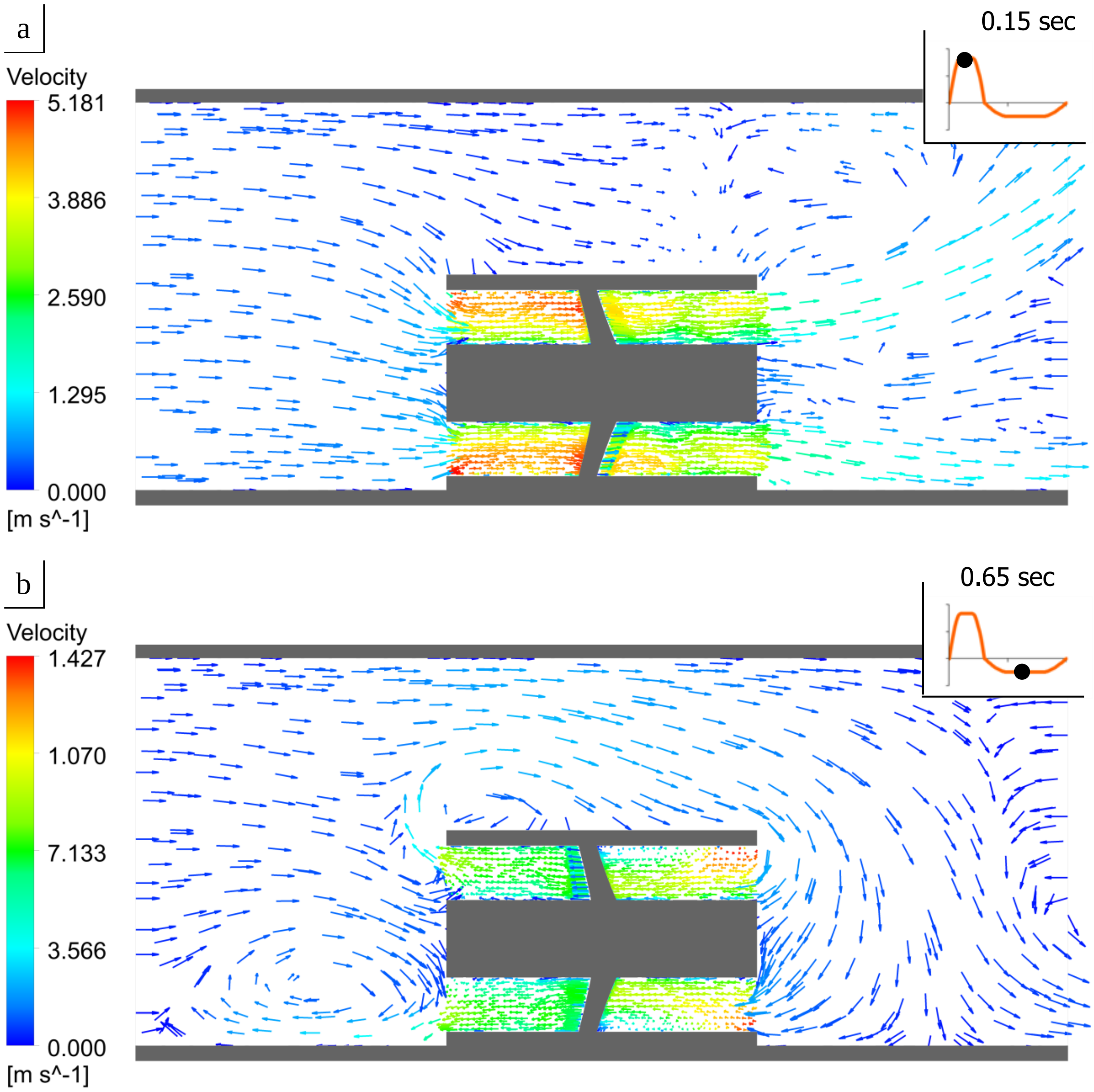

Figure 4.15: The velocity vectors are plotted of a cross sectional cut, halfway the systole (a) and halfway the diastole (b) period.

4.6 Discussion

A blade profile for a bi-directional pump was developed. For systolic conditions the blade was found to operate at maximum hydraulic efficiency when positioned at an angle of 73.0°. For diastolic conditions, best performance was obtained at an angle of 50.5°. However, the symmetric feature of the bi-directional blade resulted in negative work done near the trailing edge of the blade in the forward direction. This behaviour was expected as traditional profiles, designed for maximum performance in one direction, are not symmetric. A more detailed parametric study was used to investigate a compromise between hydraulic efficiency in forward and backward rotational directions. The newly introduced bi-directional design had to feature a high level of symmetry to ensure the required performance in both directions. Therefore symmetry was maintained but reduced by making the trailing edge of the blade sharper. This led to increased performance in the forward direction but decreased performance in the backward direction.

The CFD results further show that in the forward direction, maximum wall shear around the blades was found to be ~ 140Pa lasting less than 300 ms. For shear stresses below 425 Pa and exposure times below 620 ms, blood damage is considered negligible (Paul et al., 2003). The maximum shear stress of ~ 140Pa lasting less than 300 ms is therefore deemed within the accepted limits of haemolysis.

Comparing the results of the “pump only” model and the ascending aorta domain model, a 50% reduction of hydraulic performance was observed in the backward direction during diastole. At 8,000 rpm in forward direction the “pump only” model achieved a maximum flow rate of 36.6 cm^3/s and a total delivery of 19.4 cm^3 (sys-dia drive curve in table 4.3), whilst the aortic model reached a maximum flow rate of 20.3 cm^3/s and a total delivery of 11.0 cm^3 (table 4.4). Further analysis of velocity vectors confirmed that flow is entering and leaving the blades under an increased angle. If the flow does not approach the blades straight, the blades do not perform optimally. During diastole the change of the rotating direction prevents the flow from entering parallel to the rotating axis in the opposite direction. Therefore the discrepancy between the two models is believed to be caused by the occurrence of recirculation areas at the outlet. The placement of inlet vanes to direct the flow to the blades under the ideal angle, might subsequently lead to an increased flow delivery and reduce secondary flows.

The model of the pump domain did not show disturbances in the flow field when the rotating direction was changed. In contrast to the ascending aorta model, the streamlines in diastole (figure 4.13f) are the approximate mirror image of those in systole (figure 4.13b). This confirms the blades design itself is able to deliver bi-directional flow.

5 Results II: Experimental Validation

5.1 Introduction

Steady state and transient experimental work has been carried out in order to validate the numerical work. The objective of the steady state experiments was to obtain the characteristic pressure-flow curve, to be able to compare it with that obtained numerically. The transient measurements were aimed at investigating the dynamic behaviour and the transition period when the rotational direction of the pump is changed.

5.2 Steady state

Figure 5.1 shows the results of the first set of measurements where the pressure catheters were placed near the pump (indicated with i_1 in figure 3.20). For 9 different rotational speeds the pump was rotated forwards (figure 5.1a) and backwards (figure 5.1b) and for each rotational speed 7 flow rates were chosen in the range of what was theoretically calculated (figure 4.6) and pressure rise was measured. By plotting a polynomial fit through the results of each rotational speed, pump's characteristic pressure-flow curves are obtained.

The pressure catheters were moved away from the pump (indicated with i_2 in figure 3.20) and the above measurements were repeated at a reduced variety of rotational speeds. The resulting pressure-flow curves and shown in figure 5.2. It is seen that for all measurements, a lower pressure rise was obtained with the catheters positioned away from the pump. In order to obtain a quantified comparison of the two sets of measurements, the pressure rises obtained with the control valve completely shut ($Q = 0$ cm/s^3) were compared for both cases. These results (table 5.1) show that an average 22% reduction in pressure rise is seen when positioning the pressure catheters away from the pump (from i_1 to i_2 in figure 3.20).

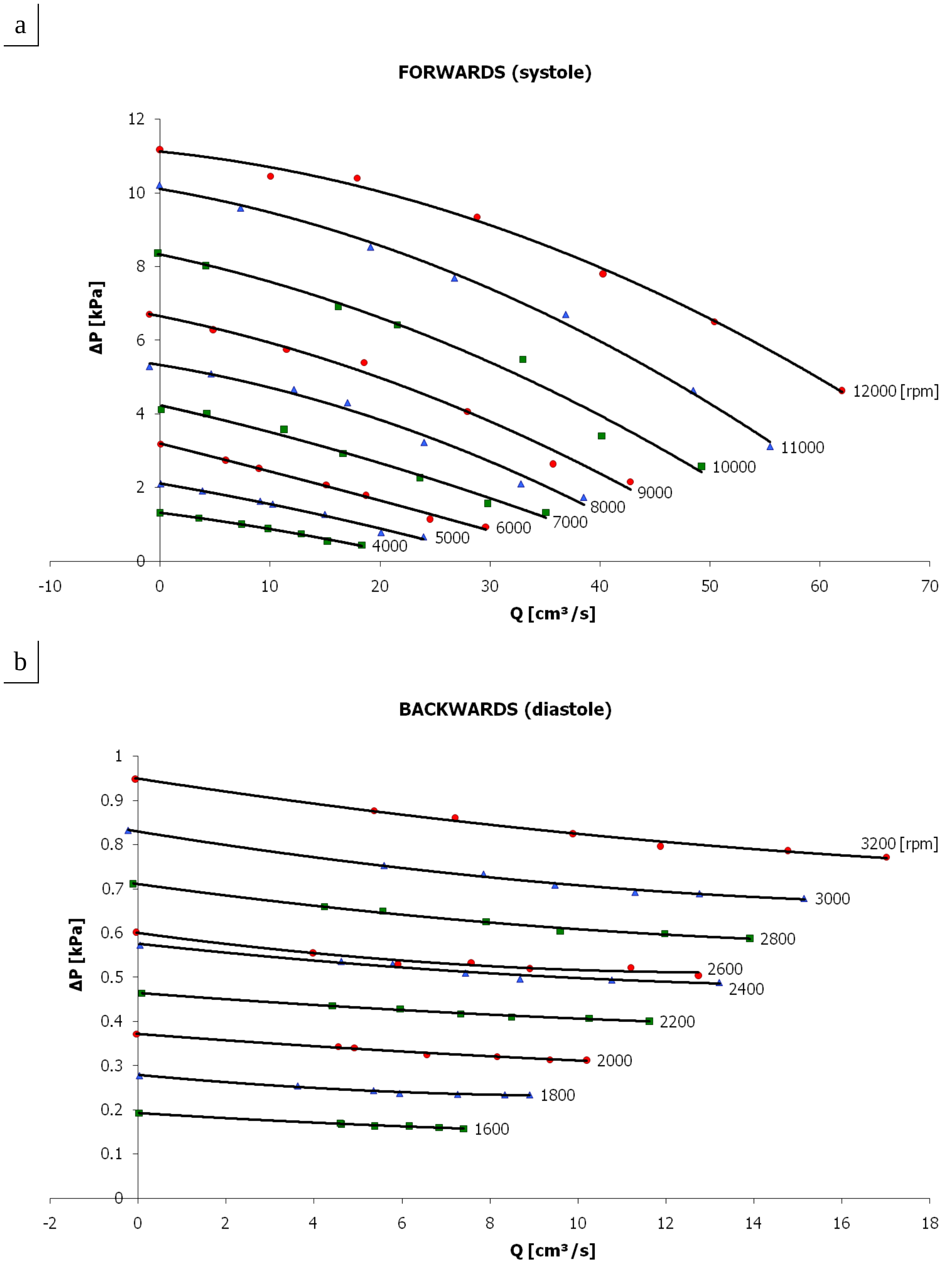

Figure 5.1: Results of steady state experiments, with the pressure transducers placed near the pump.

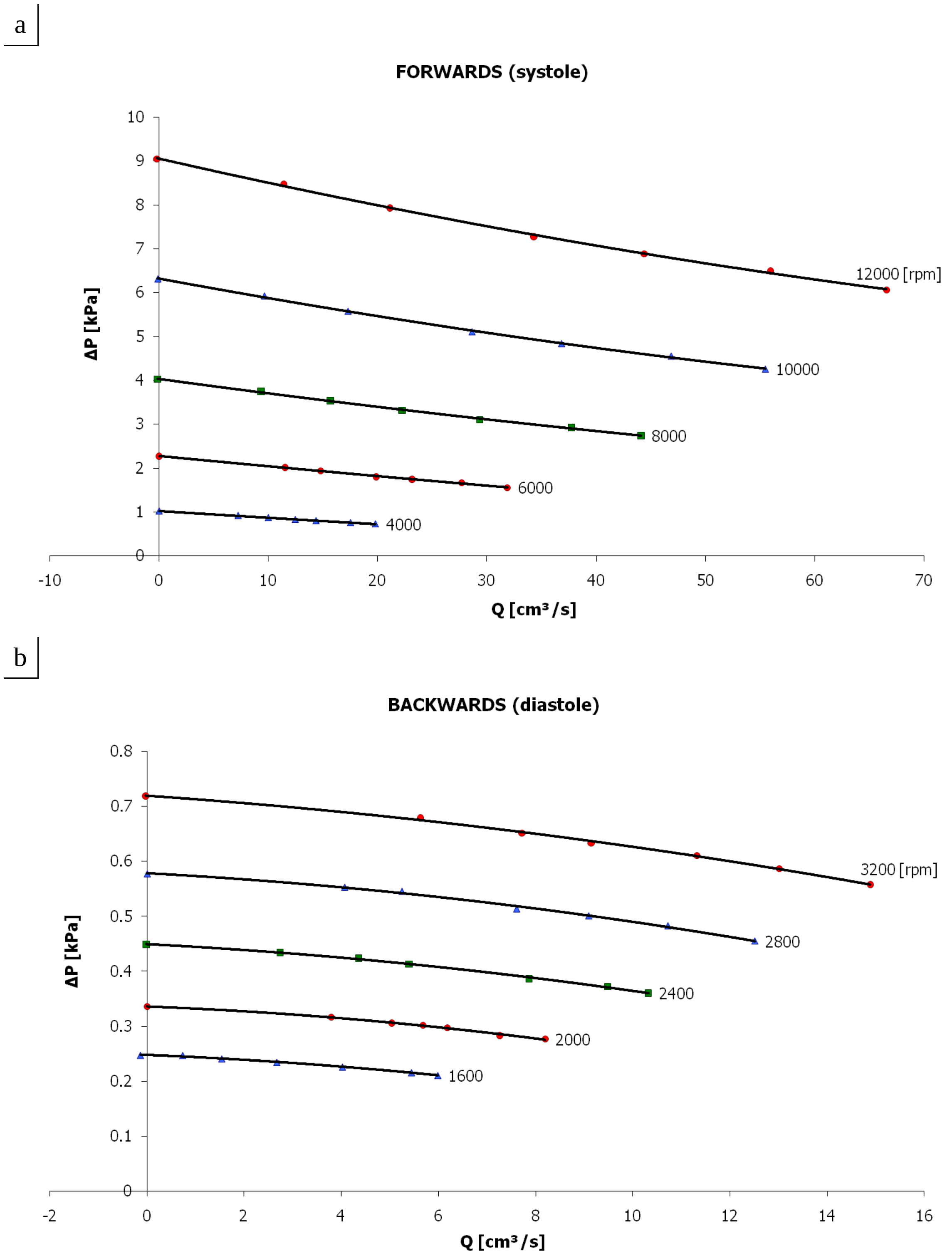

Figure 5.2: Results of steady state experiments, with the pressure transducers placed away from the pump.

Table 5.1: Comparison of placement of the pressure catheters.

	Rot. speed [rpm]	ΔP [kPa] i_1	ΔP [kPa] i_2	Comparison %
Forward	12000	11.18	9.04	-19.1
	10000	8.37	6.31	-24.6
	8000	5.29	4.02	-23.9
	6000	3.18	2.27	-28.5
	4000	1.32	1.02	-22.5
Backward	3200	0.948	0.719	-24.2
	2800	0.711	0.578	-18.8
	2400	0.573	0.449	-21.7
	2000	0.371	0.336	-9.59
	1600	0.193	0.247	28.2

5.3 Transient

The pump was driven at the same drive curves as used with the numerical simulations (Figure 3.14). The sensors of the motor driving the pump allowed for recording of the rotational speed. Figure 5.4 – 5.7 show plots of pressure and flow of the transient results for the “sys-dia”, “dia-sys”, “sys-only” and “dia-only” drive curves respectively. Comparing the systolic pressure rise obtained for the various drive curves, it is seen that both the “sys-dia” and “dia-sys” drive curve generate a systolic pressure rise of 4.0 kPa whilst with the “sys only” drive curve approximately 4.5 kPa is generated. The diastolic pressure rise for all drive curves is found to be 0.55-0.60 kPa. Overall, the pressure rise does not seem significantly affected by the small changes in systolic and diastolic durations.

The flow signals as shown in the figures were processed with a Savitzky-Golay filter, with a filter window of 201 sampling points (100 points on the left and the right) for which the filter used a 2nd order polynomial. The pressure signals were also processed with a Savitzky-Golay filter but as the signals were relatively clean compared to the flow signals, a reduced filter window of 41 sampling points (20 points on the left and the right) and a 3rd order polynomial was found suitable.

The flow signals obtained during the transient experiments appears heavily compromised by an interference signal. The flow signals of the systole only (figure 5.6a) and diastole only (figure 5.7a) drive curves seem to be especially affected. Fast Fourier Transform (FFT) analysis is performed and the frequency of this oscillating signal is found to be approximately 2.5-3.5 Hz (figure 5.6b and figure 5.7b). Initially the flow meter and the motor’s power supply were positioned next to each other. During the experiment, the amplitude of this signal was found to decrease as the distance between the devices was decreased. The results summarised above were obtained whilst a 2 m distance was allowed between the flow meter and the power supply. As can be seen in figure 5.4a – 5.7a, however, this did not make the signal completely disappear.

However, since the frequency of the interference signal does not only occur at a single frequency, the signal might not necessarily originate from electrical equipment. Another possibility is the interia of the fluid in the tubes connecting the experimental housing to the reservoir. It is possible the fluid keeps oscillating between experimental housing and reservoir after the motor is switched off.

The area under the flow curves was integrated to calculate the flow delivery in each direction. For the “sys-dia” drive curve (figure 5.4b), a flow delivery of 2.32 cm^3 in the forward direction and 9.55 cm^3 in the backward direction is found. For the “dia-sys” drive curve (figure 5.5b), a flow delivery of 1.60 cm^3 in the forward direction and 1.61 cm^3 in the backward direction is found.

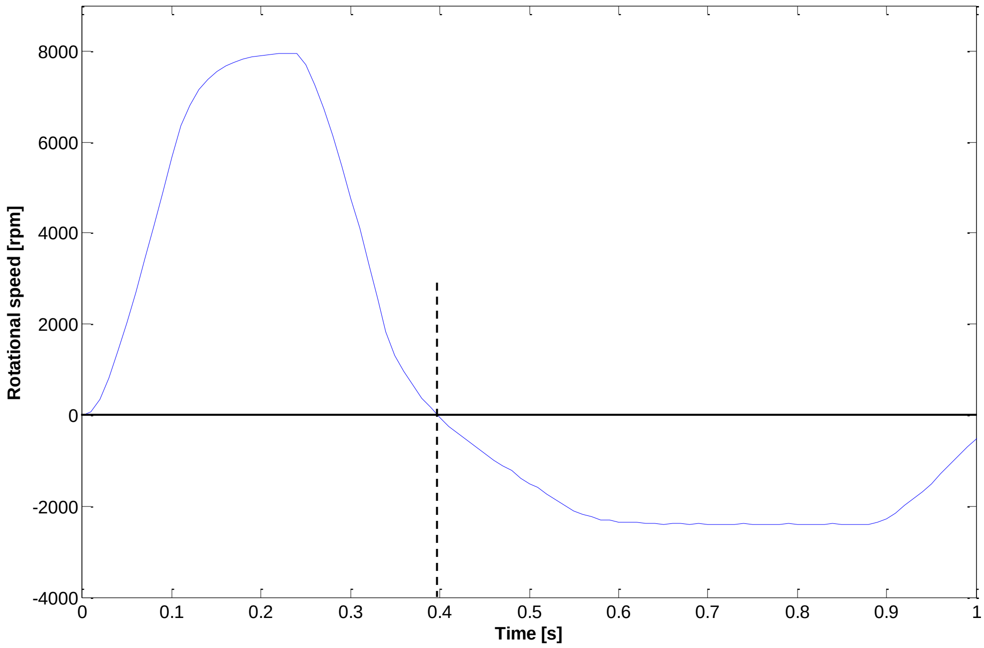

Figure 5.3: Transient drive curve at which the pump was run, as obtained by the motor’s sensors.

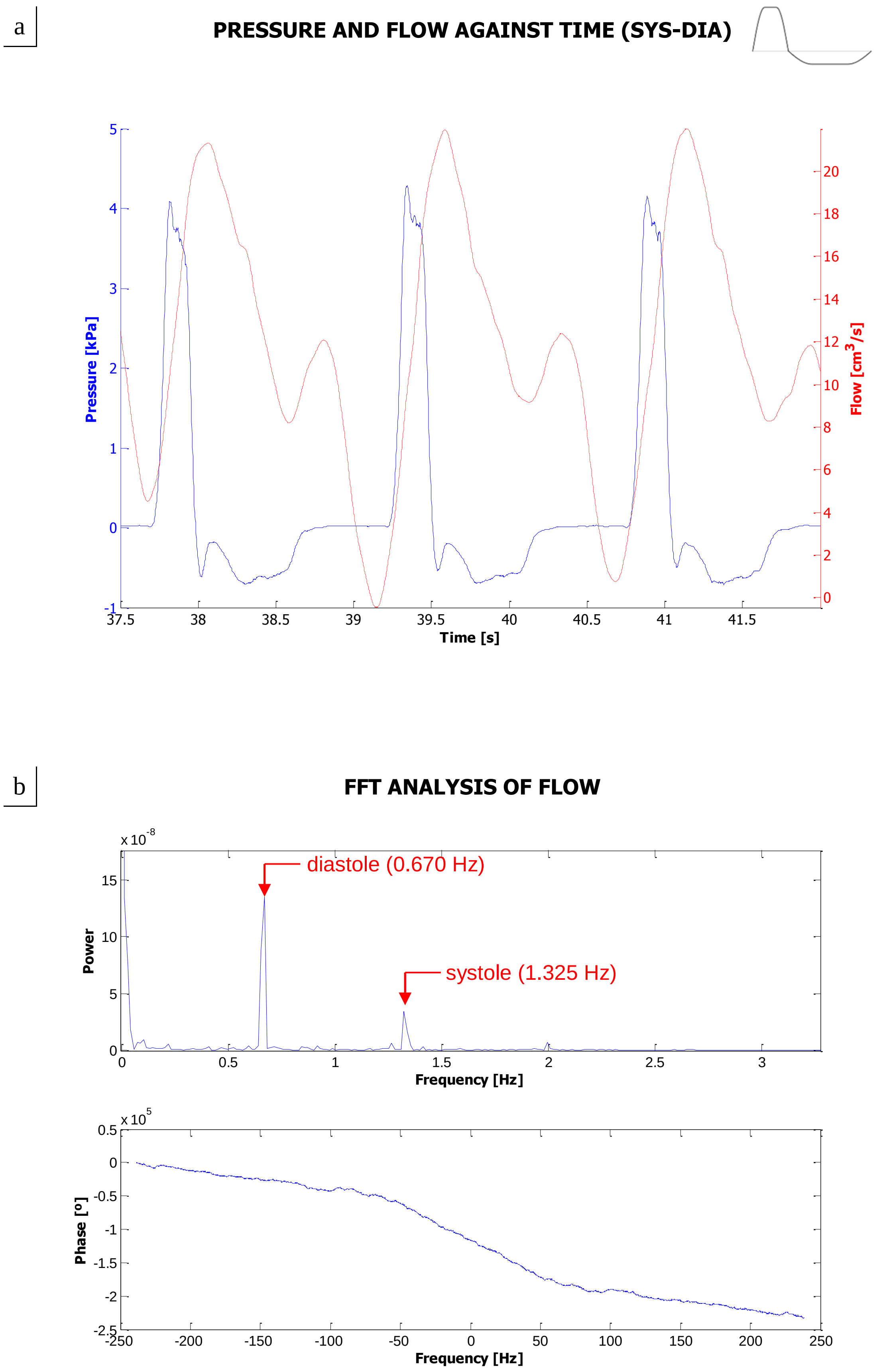

Figure 5.4: Transient experimental pressure (a) and flow (b) results for the “sys-dia” drive curve.

a

PRESSURE AND FLOW AGAINST TIME (DIA-SYS)

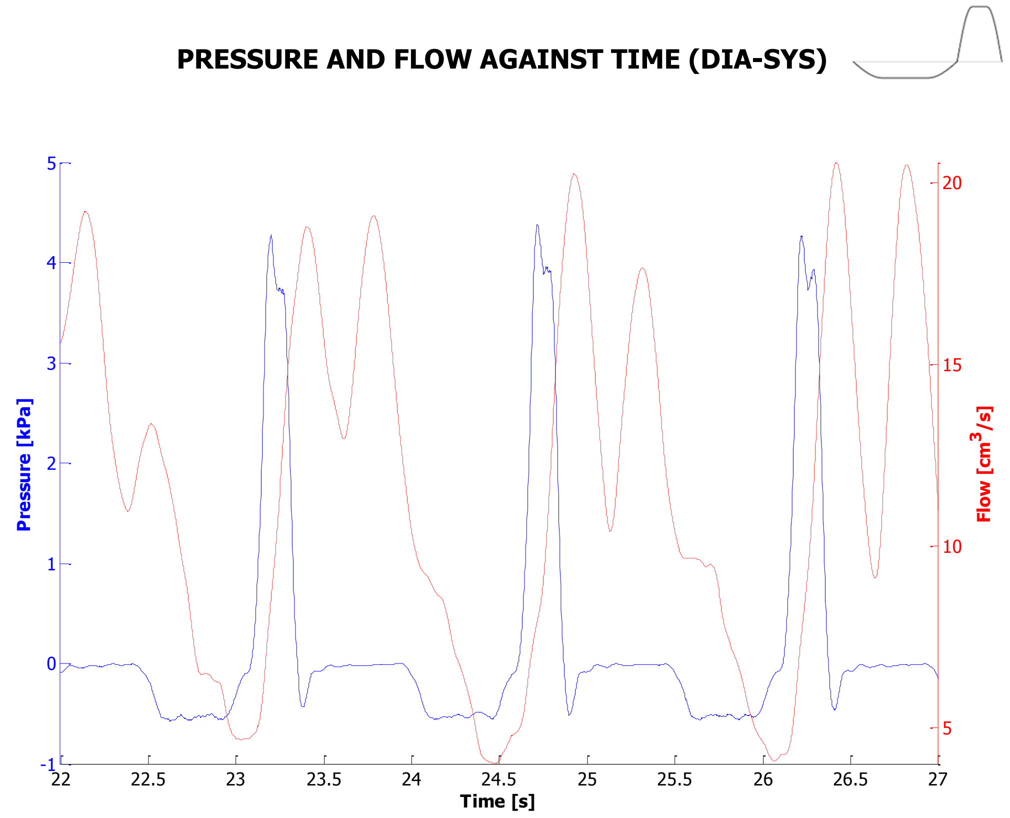

b

FFT ANALYSIS OF FLOW

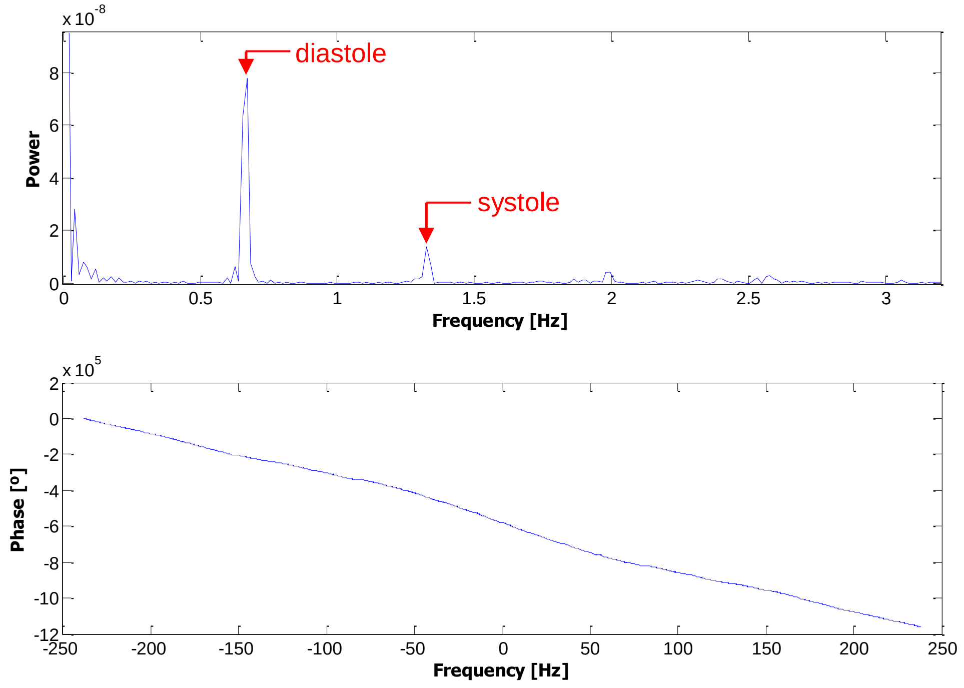

Figure 5.5: Transient experimental pressure (a) and flow (b) results for the “dia-sys” drive curve.

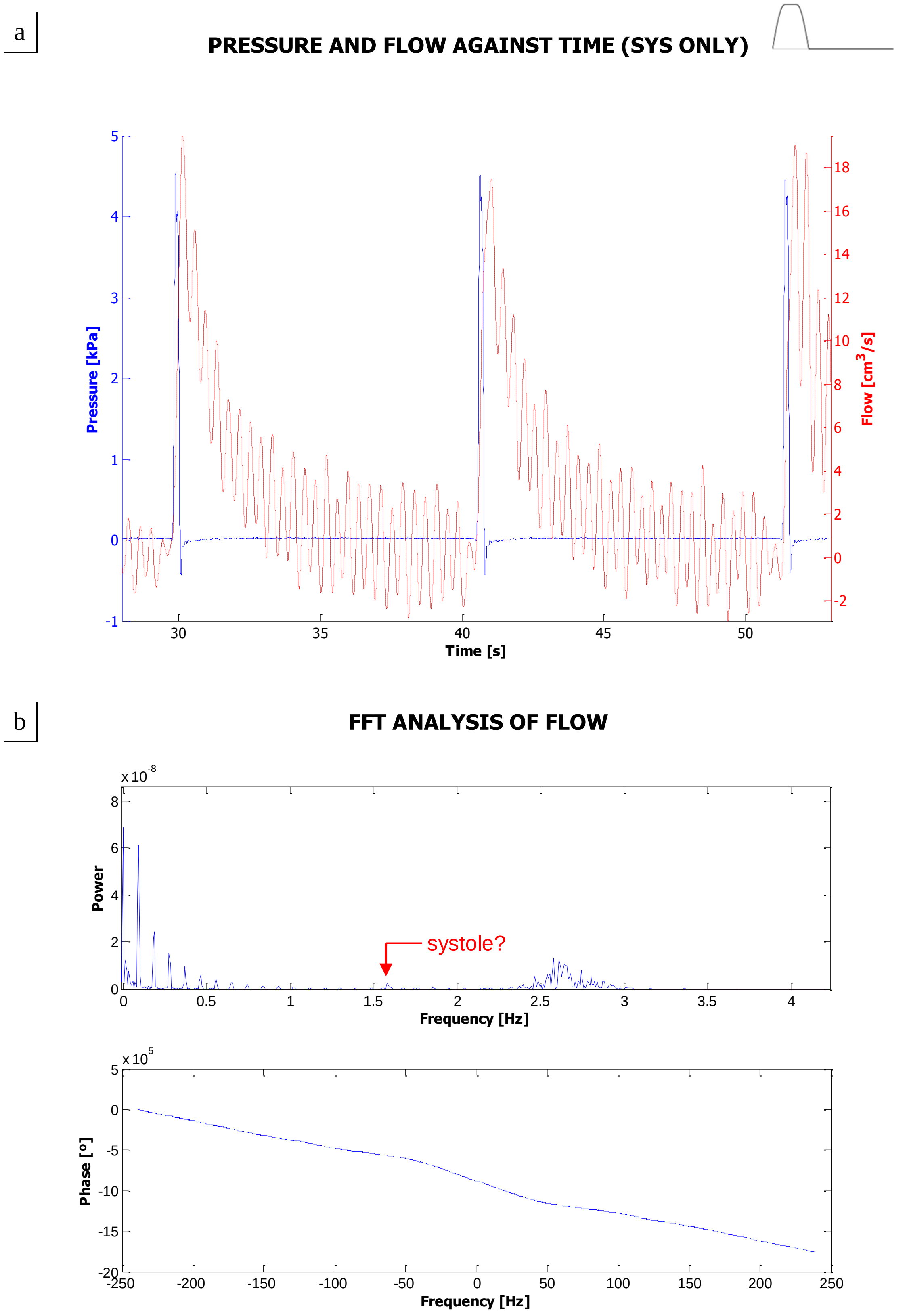

Figure 5.6: Transient experimental pressure (a) and flow (b) results for the “sys-only” drive curve.

a

PRESSURE AND FLOW AGAINST TIME (DIA ONLY)

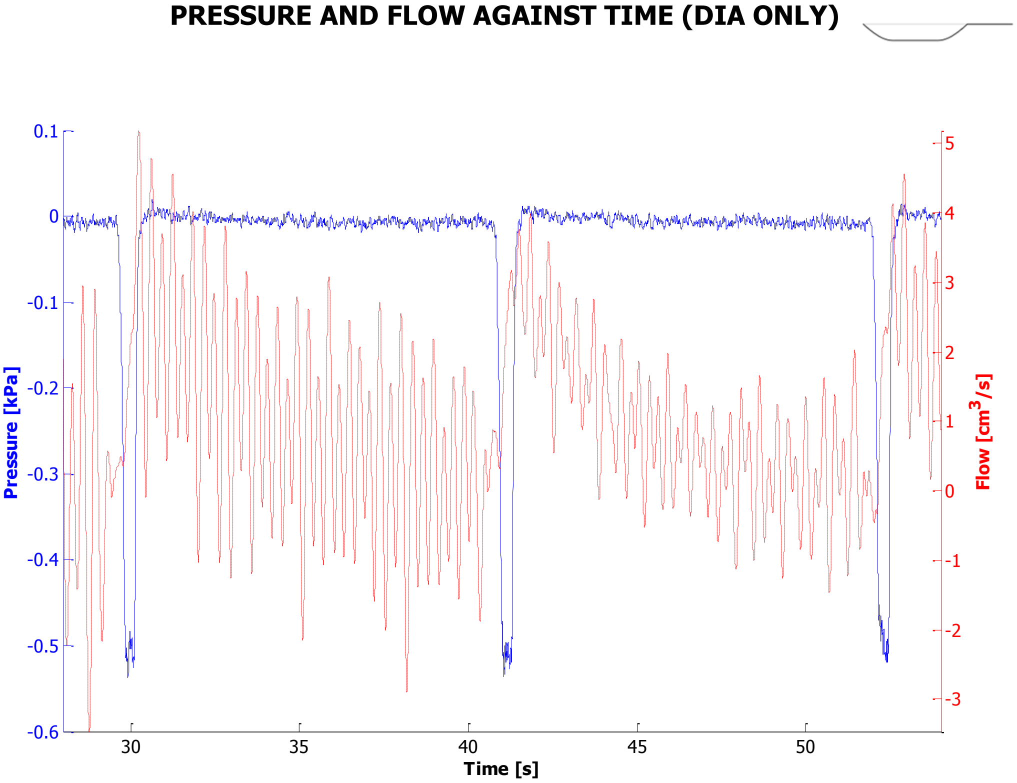

b

FFT ANALYSIS OF FLOW

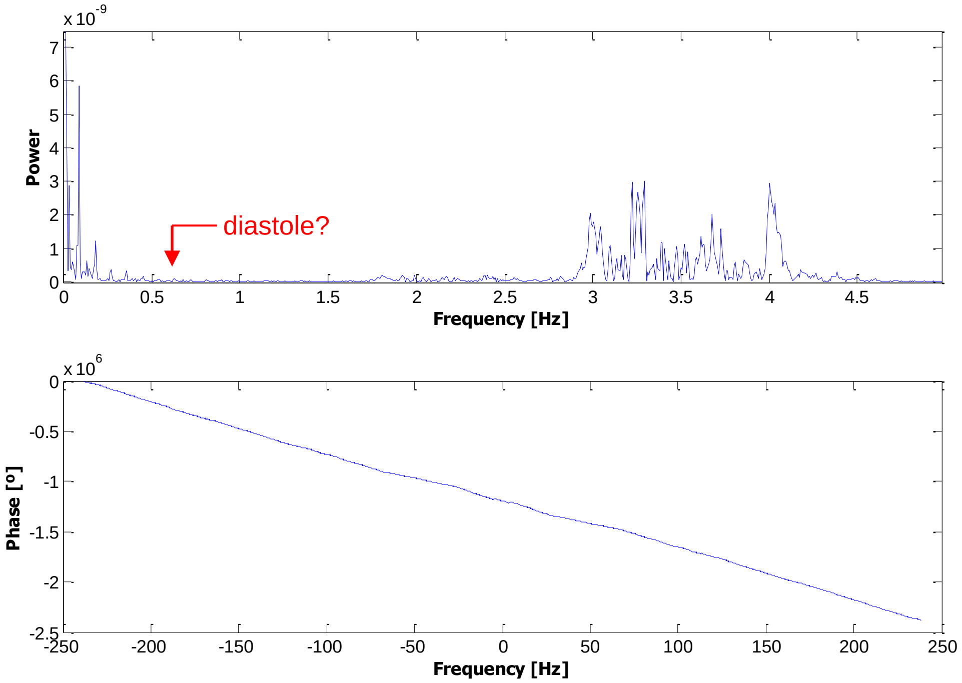

Figure 5.7: Transient experimental pressure (a) and flow (b) results for the “dia-only” drive curve.

5.4 Discussion

Comparing the results in figure 5.1 and figure 5.2, the pressure rise is notably lower when measured away from the pump. This is most likely caused by the pressure catheters that obstruct part of the flow path to a greater degree when positioned near the pump. The catheters occupy $2^2/(12^2-5^2)=3.4\%$ of the cross-sectional area of the flow path. The results show that this lead to a 22% reduction in pressure rise. Possibly whilst positioned close to the pump, the catheters also prevent some fluid from entering the pump parallel to the rotating axis which might have subsequently led to reduced pumping performance.

The flow rates obtained experimentally that were used to plot the characteristic pressure-flow curves (figure 5.1), were approximately 3x smaller than those obtained numerically (figure 4.6). This implies no direct comparison can be made between these results. In order to validate the computational work, the simulations are repeated for the same flow rates as those obtained numerically.

The flow signals got highly compromised by a ~ 2.5-3.5 Hz oscillating signal, of which the amplitude was reduced to approximately half of the original amplitude by allowing distance between the flow meter and the motor’s power supply. Regardless of this, the interference signal was still highly apparent, especially with the “sys only” and “dia only” flow signals. Furthermore these flow signals show that because of inertia and the lack of a mock aortic valve or a mechanically triggered valve, the flow is not changing direction after the rotational direction has changed direction. The pump is shown to deliver in both direction, but the forward flow is still dominating during diastole. In the envisaged physiological setting (figure 2.15) this will most likely not be the case, as the forward flow will be stopped by the closure of the aortic valve. The flow rates were found to range between 0 and 25 cm^3/s and flow deliveries of 1.60-9.55 cm^3. These values are of a very different order of magnitude than in the transient simulations (table 4.3).

6 Discussion

6.1 Comparison of numerical and experimental results

This chapter consists of two sets of data:

1. Figures 6.1 + Table 6.1: Experimental results are compared against computational data whereby zero tip clearance is defined.
2. Figures 6.2 + Table 6.2: Experimental results are compared against computational data whereby tip clearance is defined at 27.5µm (according paragraph 3.4.2).

In the simulations blood was the modelled fluid, while in the experiments water was the working fluid. Therefore, to allow for a direct comparison of the numerical and experimental results, the steady state simulations for the characteristic pressure-flow curve (figure 4.6) were repeated for water. For these simulations the flow rates at the inlet were defined to match exactly with those obtained experimentally (figure 5.1).

Figure 6.1-6.2 shows the pressure-flow curves for forward (a-b) and backward (c-d) rotational speeds. For forward speeds the curves are concave, whilst for the backward speeds the curves are convex. This is expected as the pressure rise and flow are technically both negative, compared to the positive values obtained in the forward direction. However, with plotting the data the pressure and flow in the backward direction were plotted on positive axis. Therefore the curves in the backward direction will show as the mirror image of those obtained in the forward direction.

For the pressure-flow curves, the numerical simulations and the experimental measurements were both taken at the same flow rate, the pressure rises obtained can be directly compared to one another. Table 6.1-6.2 lists the statistics on these results. In the forward direction, it is seen the obtained pressure rises correspond better for lower rotational speeds and higher flow rates. As rotational speeds increases and/or the flow rate goes decreases, big discrepancies occur between the results. In the backward direction, significant discrepancies occur throughout, with measurements taken at 1,600 and 1,800 rpm corresponding the best.

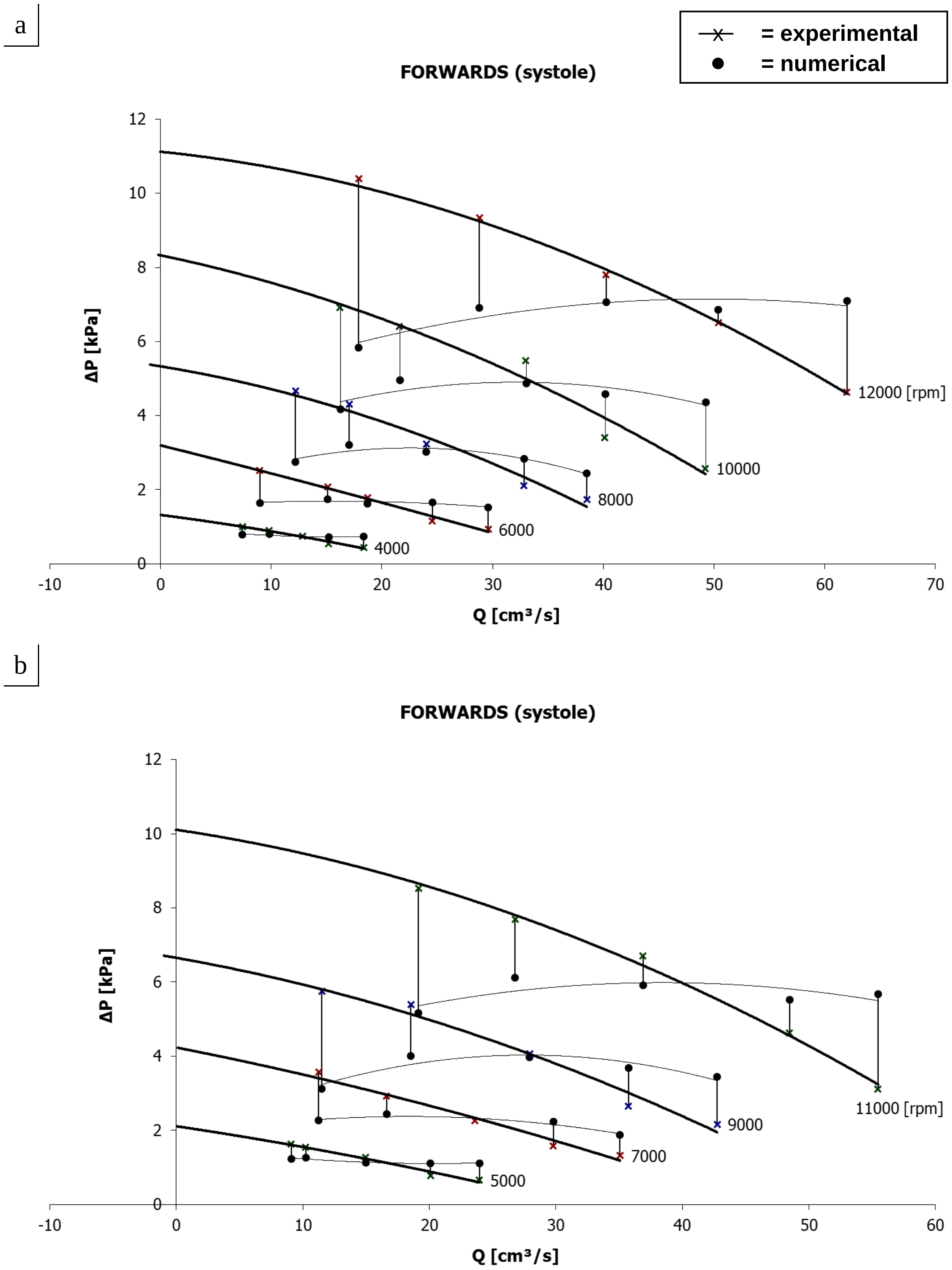

Figure 6.1: Comparison of the numerically (with zero tip clearance defined) and experimentally obtained pressure-flow curves, for forward (a-b) and backward (c-d) rotational speeds. With the pressure catheters positioned near the pump.

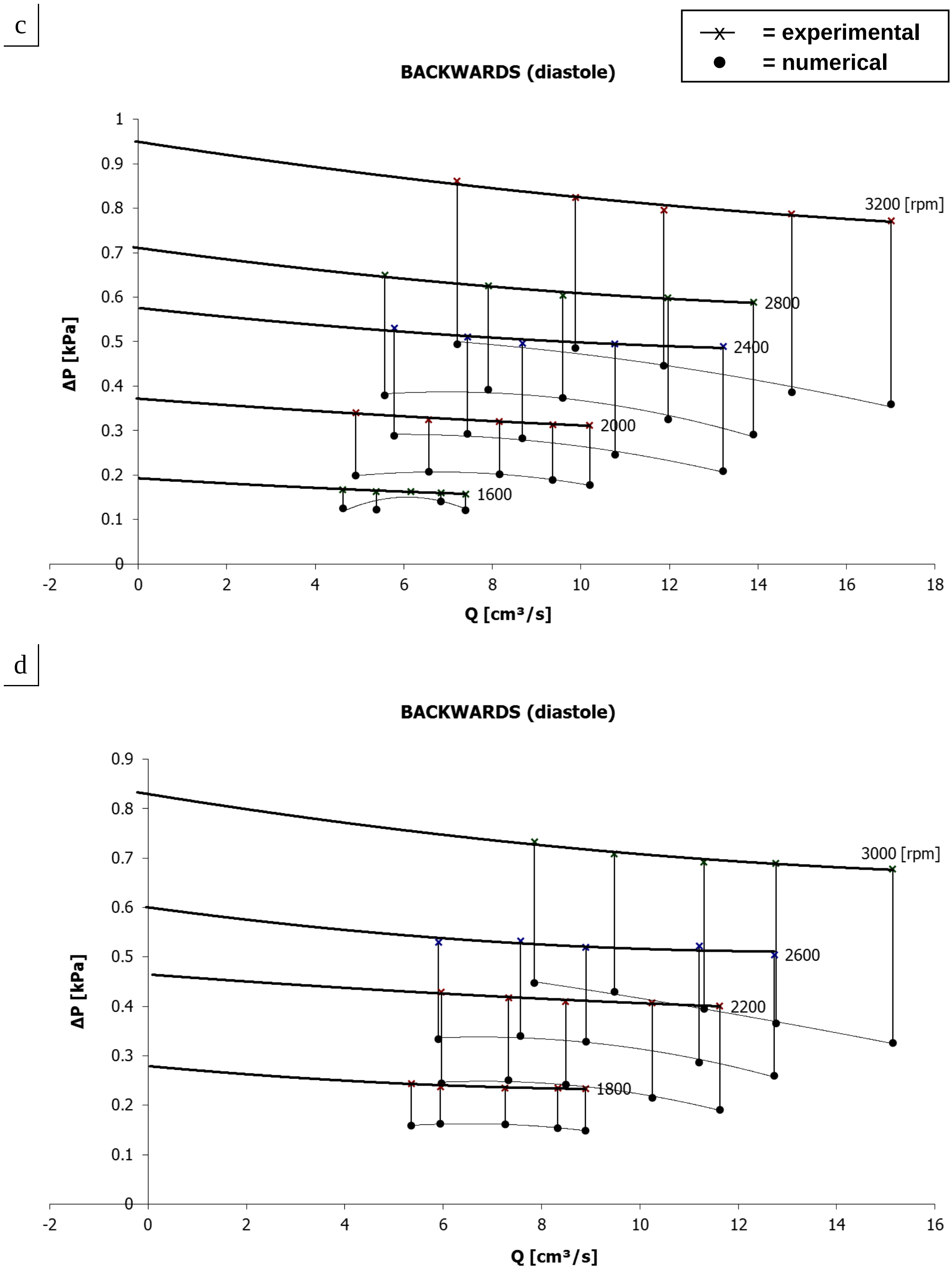

Figure 6.1: (continued)

Table 6.1: Standard deviation (SD) and 95% confidence interval statistics on the comparison of the numerical results (with zero tip clearance defined) and the experimental results.

	Rot. speed [rpm]	Average ΔP [kPa]	
		%-change	95% conf.
Forward	12000	27.6	18.2
	11000	34.7	25.1
	10000	35.6	19.5
	9000	34.4	19.0
	8000	29.6	12.6
	7000	27.9	15.8
	6000	33.6	19.2
	5000	33.6	21.0
	4000	26.9	21.9
	Overall	31.6	5.9
Backward	3200	46.4	4.7
	3000	44.1	4.8
	2800	42.7	4.8
	2600	40.7	5.0
	2400	47.8	5.3
	2200	44.7	4.4
	2000	39.6	2.6
	1800	33.7	1.9
	1600	17.4	9.0
	Overall	39.7	3.0

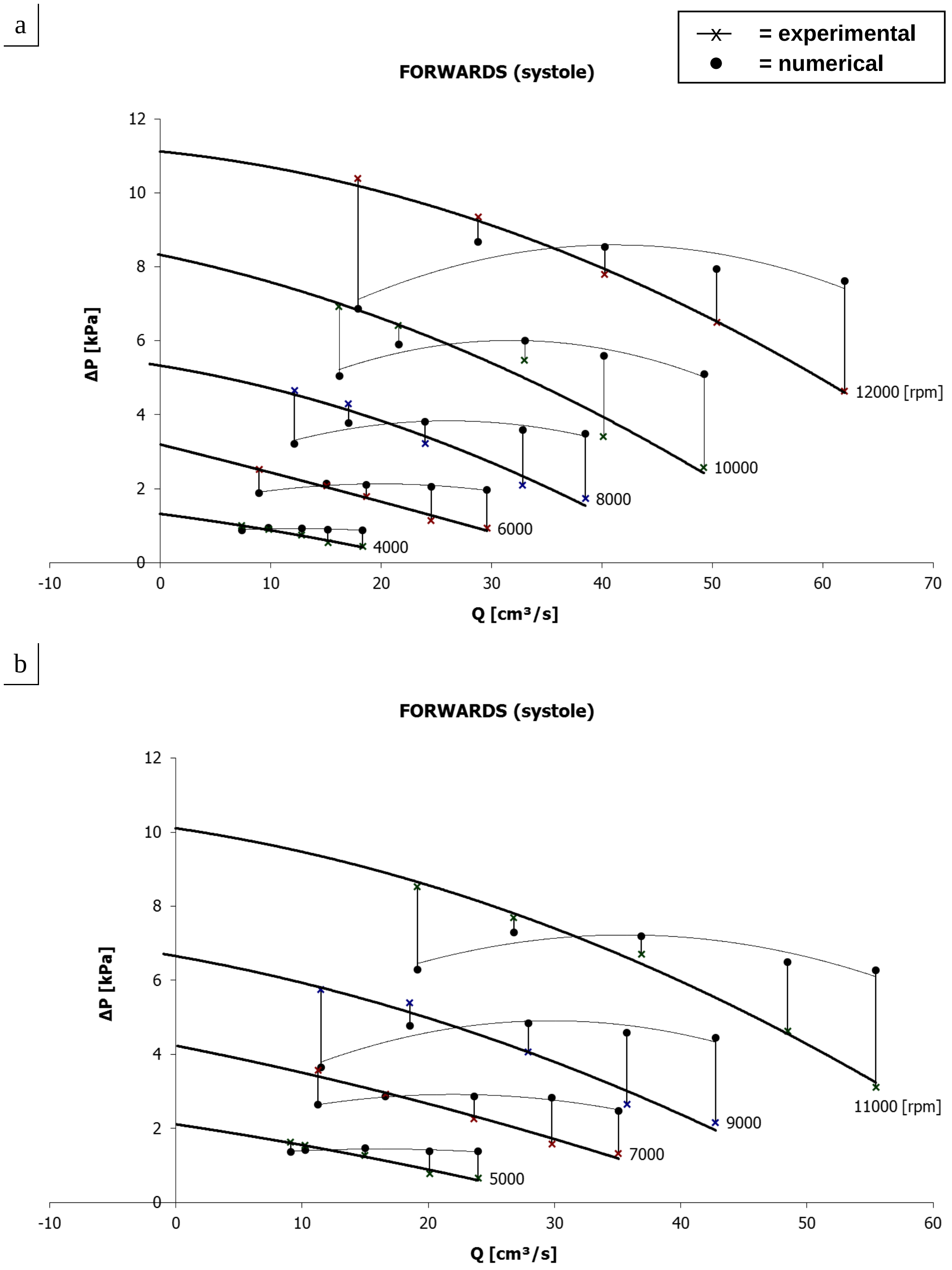

Figure 6.2: Comparison of the numerically (with 27.5µm tip clearance defined) and experimentally obtained pressure-flow curves, for forward (a-b) and backward (c-d) rotational speeds. With the pressure catheters positioned near the pump.

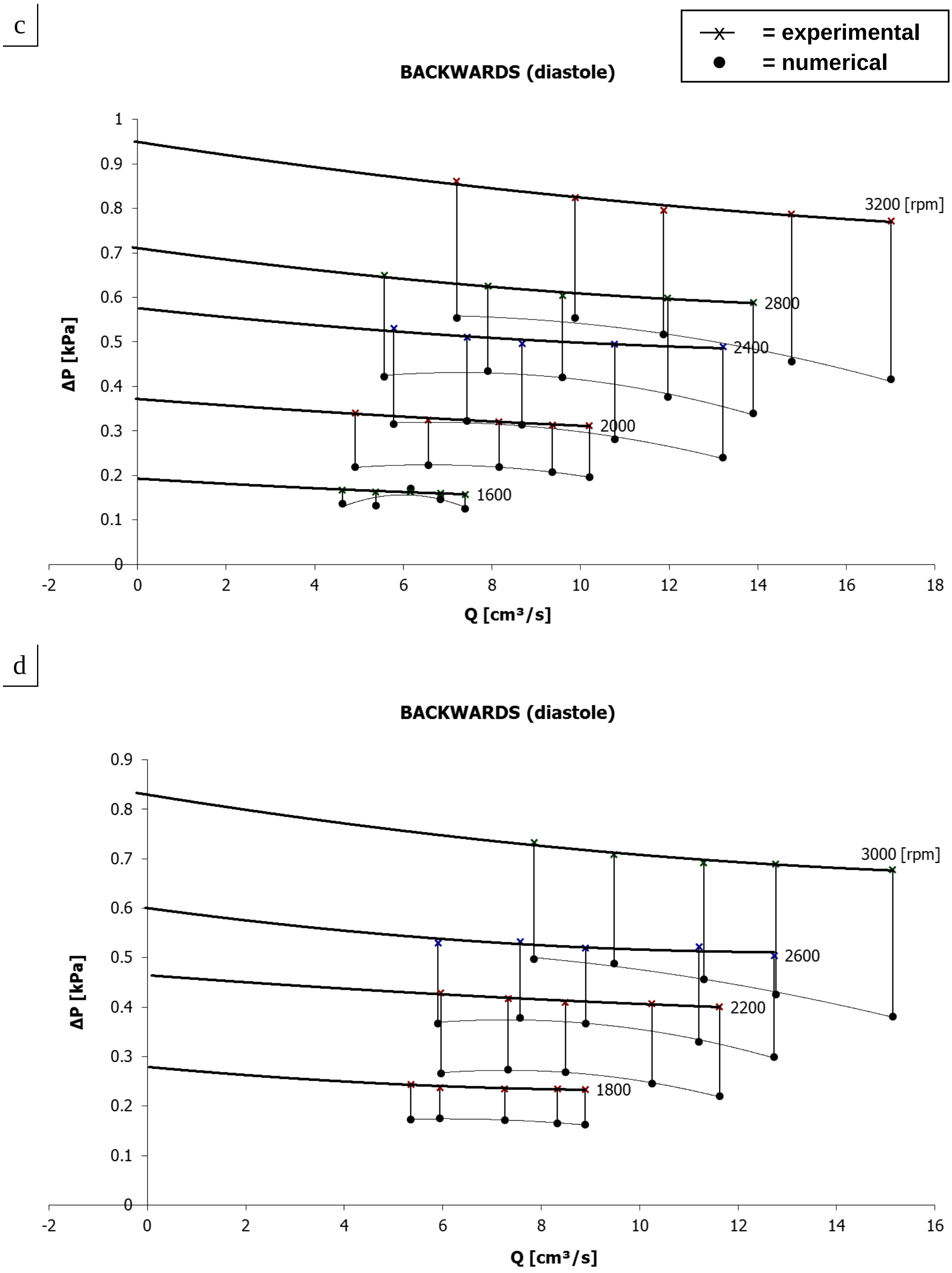

Figure 6.2: (continued)

Table 6.2: Standard deviation (SD) and 95% confidence interval statistics on the comparison of the numerical results (with 27.5μm tip clearance defined) and the experimental results.

	Rot. speed [rpm]	Average ΔP [kPa] %-change	Average ΔP [kPa] 95% conf.
Forward	12000	27.4	20.4
	11000	36.0	34.4
	10000	41.5	34.4
	9000	49.3	34.8
	8000	46.7	33.3
	7000	44.4	32.7
	6000	47.3	40.4
	5000	46.1	40.3
	4000	41.3	35.4
	Overall	42.2	10.6
Backward	3200	38.3	4.8
	3000	35.9	4.5
	2800	35.0	4.4
	2600	33.3	4.5
	2400	41.6	5.1
	2200	38.3	3.9
	2000	34.0	2.3
	1800	28.5	1.6
	1600	14.2	6.3
	Overall	33.2	2.6

The novel bi-directional blades deliver a flow rate of 39 cm^3/s at 2.2 kPa in forward direction whilst rotating at 8,000 rpm requiring a power of 3.7 W. These values are in slightly smaller order of magnitude than those obtained with existing axial flow blood pumps (table 6.3). Existing devices such as the IVAP, Debakey VAD and Heartmate II deliver 85-105 cm^3/s whilst rotating at speeds ranging 7,500 – 120,000 rpm and requiring powers of 6-10 W. It is likely that the increased diameter of the bi-directional blades allows for lower rotational speed. The 3.7 W power requirement calculated for the bi-directional blades does not include the power needed to overcome mechanical friction and other losses. Existing devices, such as the Hemopump and Impella, are designed to deliver a uni-directional continuous flow, whereas the bi-directional pump will run in a pulsatile mode. Therefore the bi-directional pump will produce a maximum flow rate for a smaller period and the blades will need to run efficiently at higher flow rates.

Table 6.3: Comparing characteristics of the bi-directional pump with two existing uni-directional devices.

	Debakey	Impella	Jarvik	Hemopump	Bi-directional pump
Tip diameter [mm]	24	6.4	25	8.1	12
Rotational speed [rpm]	11k	30k	12k	26k	8k
Pressure rise [kPa]	13	13	13	13	2.2
Flow [cm^3/s]	90	117	117	75	39

6.2 Limitations

The domains of the computational model did not include inlet or outlet vanes, or a (partial) model of the circulatory system. The traditional design of an axial flow pump, supplements the blades with static inducer and diffuser vanes. These vanes each have their own function and are geometrically not the same. The inducer vanes' function is to guide the flow and make sure it approaches the blades at the correct angle whilst also reducing secondary flows. The diffuser’s function is to decrease the high tangential velocity of the blood exiting from the blades and transferring this energy into an increase in pressure rise. When applying the bi-directional blades, the static vanes in front of the blades will function as an inducer in one direction but also as a diffuser when the pump is rotating in the opposite direction. Therefore symmetry and geometrical resemblance of inducer and diffuser are important. The traditional design of a diffuser, however, has the static vanes placed under an angle and with a defined curvature. Rotationally these static vanes can therefore not be rotationally symmetric. A specifically designed diffuser, that is rotationally symmetric, will be required to fulfil the functionalities of a diffuser.

This study was limited to investigating the pump’s performance for a fixed heart rate of 60 bpm and a systole and diastole duration of 0.3 and 0.7 sec. In reality both heart rate and the systole/diastole ratio vary, but this was not considered in this work. With the computational work blood was modelled as Newtonian, while in reality it has non-Newtonian characteristics. The experimental work was limited to using water (ρ=1,000 kg/m3, μ=1.0 mPa·s) instead of blood (ρ=1,050 kg/m3, μ=3.6 mPa·s). Using a mixture of water and glycerol would have been an option but was not considered. In light of the objective to prove the concept of bi-directional blades, it was not deemed necessary to match the properties of the blood very accurately. Furthermore, glycerol is known to stick to surfaces and glycerol sticking to the experimental housing and to the blades could have negative effects on the hydraulic efficiency.

7 Conclusions and Future Work

7.1 Conclusions

With reference to the objectives set out in paragraph 2.7, the following conclusions are drawn:

1. Bi-directional blade design: An impeller to support bi-directional flow has been designed. With the blades being 12mm in diameter, this impeller design could be used for a pump that is inserted through the femoral arteries and positioned in the ascending aorta. Such a pump could function as an LVAD and support blood flow in two directions: towards the organs or towards the coronary arteries.
2. Numerical simulations: The impeller design has been optimised and characterised computationally. Analysis of the pressure blade loading profiles confirmed generation of a pressure rise, leading to a good balance in performance between the forward and backward direction. The pump was modelled to accelerate to 8,000 rpm during systole in one rotational direction and to 2,400 rpm during diastole in the other direction. CFD models confirmed pressure rise was generated allowing for a total flow delivery of 39 cm^3 during systole and 19 cm^3 during diastole.
3. Experimental validation: An experimental rig has been designed and the prototype of the bi-directional blades was tested. The numerical and experimental work did not compare well and a discrepancy was found of ~30-40% (table 6.1-6.2). The following root causes, related to the numerical work, were investigated and excluded:

    - Newtonian assumption (§3.3.1)
    - Tip clearance (figure 4.7)
    - Mesh of the model (§3.3.3)

The following root cause was found to be of importance:

- Turbulence model
  For lower rotational speeds, the SST turbulence model compares better with the experimental results, whilst for higher rotational speeds the k-ε turbulence model compares better (figure 3.9). For future work, it will therefore be interesting to consider a combination of the SST and k-ε turbulence models.

7.2 Future work

With regards to the ~30-40% discrepancy between the numerical and experimental work, future work could investigate possible root causes related to the design of the experimental rig:

- gravitational element of ingoing and outgoing flow
  By changing to sealed reservoirs that can be pressurised, it will not be necessary to place the reservoir at the certain height from the housing of the pump to create a static pressure. The length of the flexible tubing between the reservoir and the housing of the pump and the associated fluid mass inside the tubing will be reduced.
- interia of the mass of fluid in front and after the pump
  A mock aortic valve or a mechanically triggered valve will ensure fluid inertia elsewhere in the system cannot comprise the data.

In addition to the above, it is still unclear how placing a bi-directional flow pump will affect the blood distribution in the ascending aorta. This can be further investigated by including an arterial model in the simulations. For these simulations the pump can be modelled as a black box, not considering the flow dynamics inside the pump. The dynamic flow waveform generated by the ventricle and the pressure/flow deliveries of the pump will have to be defined in such a model. This may subsequently yield if and how much flow that is pumped towards the coronary arteries, will actually enter the arteries.

Appendix A: Technical Drawings

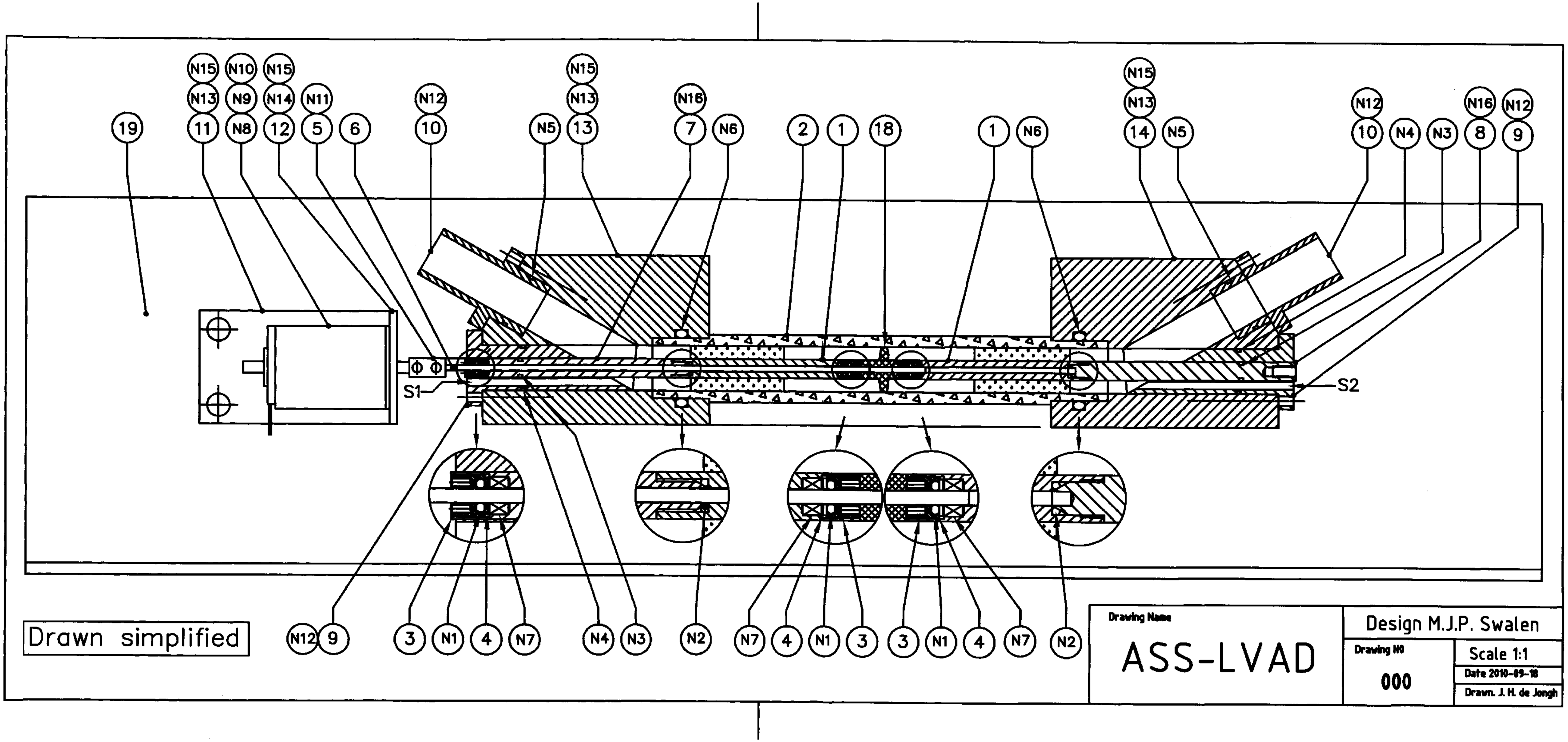

ITEM	PART	QTY
1	GUIDE VANE-01	2x
2	CASING-02	1 SET
3	NUT-03	3x
4	RING-04	3x
5	BUSH-05	1x
6	AXIS-06	1x
7	PEN-L-07	1x
8	PEN-R-08	1x
9	PIPE-R/L-09	1 SET
10	PIPE-R/L-10	2x
11	BLOCK-11	1x
12	PLATE-12	1x
13	HOUSE-L-13	1x
14	HOUSE-R-14	1x
15	ARBOR-15	1x
16	SCREW-16	1x
17	CLAMPBUSH-17 Assembly tool	1x
18	ROTOR-18	1x
19	ASSEMBLYPLATE-19	1x
20	KEY-20 Assembly tool	1x
21	PIN-21 Assembly tool	1x

Part Name	Material	Proces	Quantity
Parts List	–	–	1x

Drawing Name	Drawing NO	Scale
LVAD-PARTS	000-P	Data- Drawn. J. H. de Jongh

ITEM	PART	QTY
N1	0–RING 1.78X1.02ø	3x
N2	0–RING 1.6X1ø	2x
N3	0–RING 3.5X1ø	2x
N4	0–RING 10X1ø	2x
N5	0–RING 13X1ø	2x
N6	0–RING 15.88X2.62ø	2x
N7	BEARING 4X2X1.5ø	3x
N8	MOTOR 283838 MAXON	1x
N9	SCREW M2X3	3x
N10	RING M2	3x
N11	SCREW M2.5X2	2x
N12	SCREW M2.5X10	12x
N13	SCREW M5X16	5x
N14	SCREW M5X18	2x
N15	RING M5	7x
N16	SCREW M2.5X3	2x

Part Name	Material	Proces	Quantity
N–Parts List	–	–	1x

Drawing Name	Drawing N0	Scale
LVAD-PARTS	000-N	Data- Drawn. J. H. de Jongh

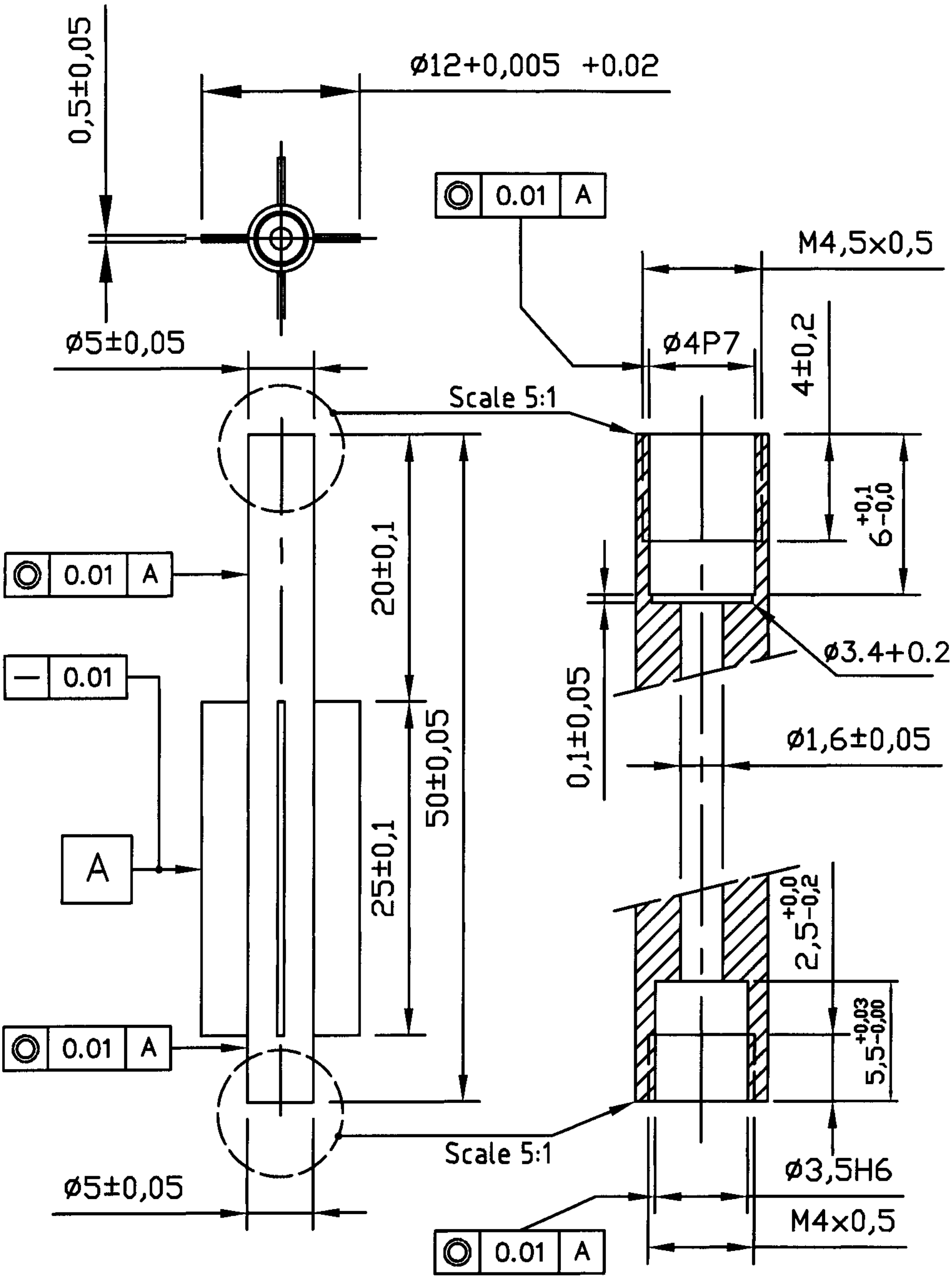

Part Name	Material	Proces	Quantity
GUIDE VANE−01	3.1255	Anodising	2x

Drawing Name	Drawing NO	
LVAD-PARTS	001	Scale 2.5:1 Data- Drawn. J. H. de Jongh

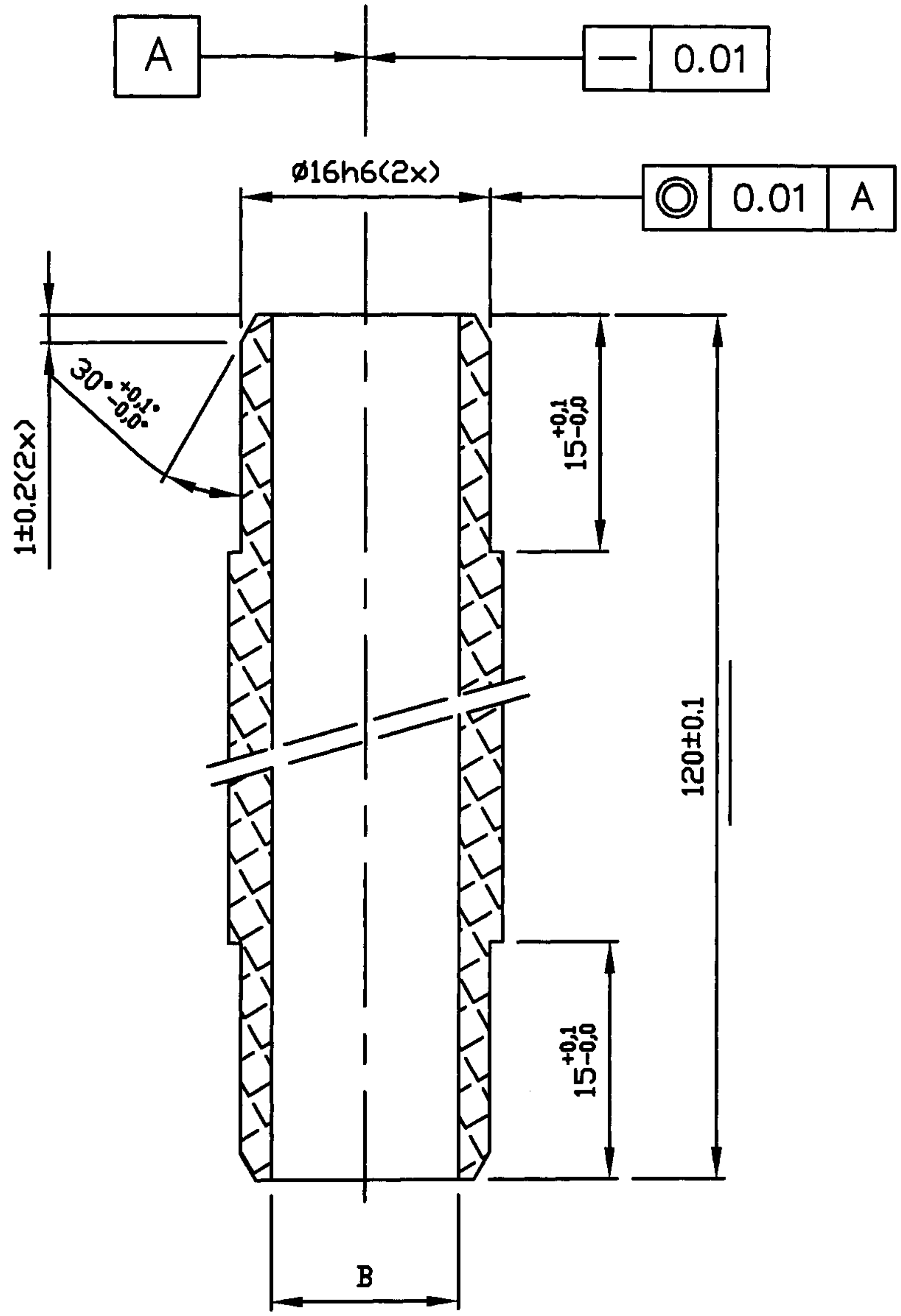

1 Set is a casing of B=Ø12.07±0.01
+ a casing of B=Ø12.12±0.01

Part Name	Material	Proces	Quantity
CASING-02	PMMA	-	1 set

Drawing Name	Drawing NO	Scale 2.5:1
LVAD-PARTS	002	Data- Drawn. J. H. de Jongh

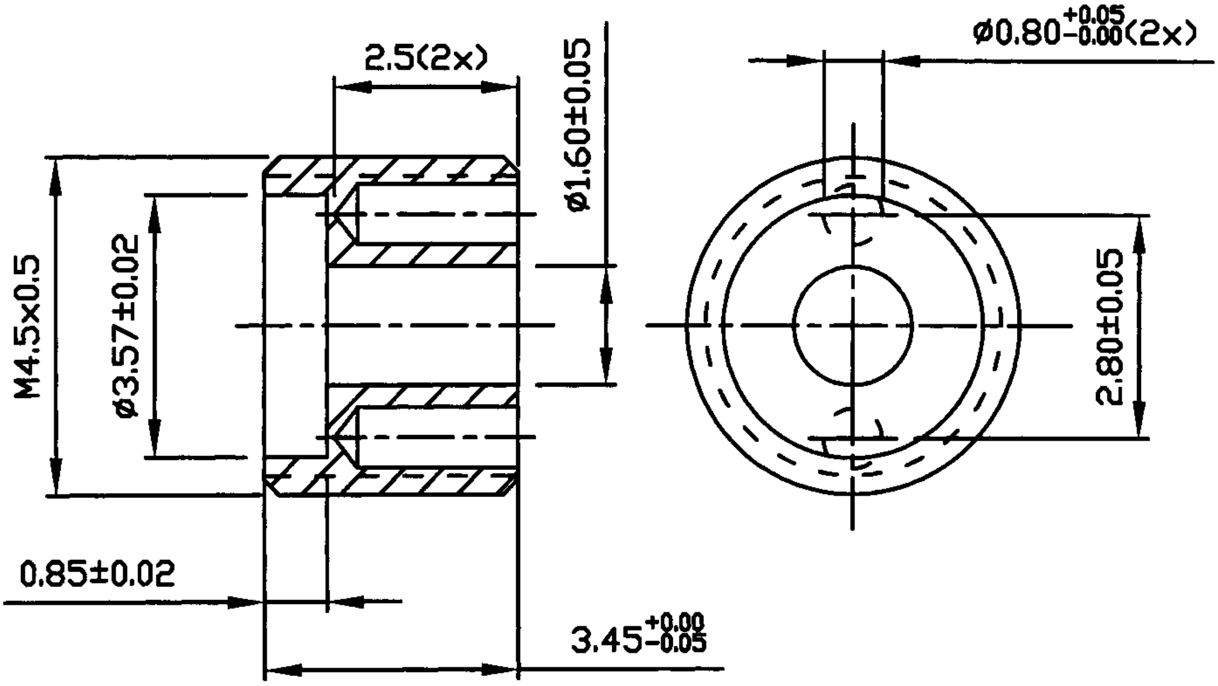

Part Name	Material	Proces	Quantity
NUT-03	1.4305	–	3x

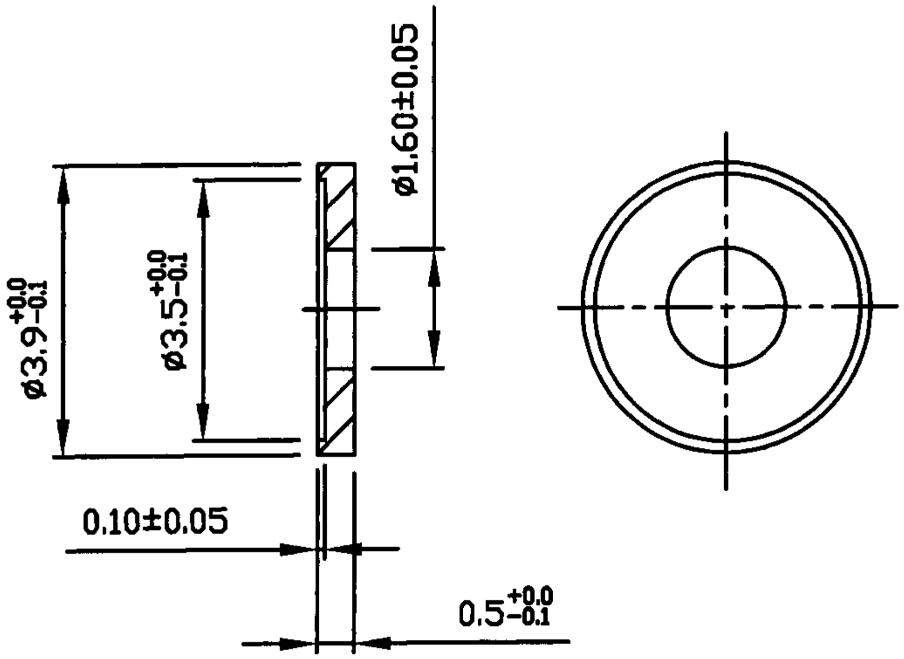

Part Name	Material	Proces	Quantity
RING-04	1.4305	–	3x

Drawing Name LVAD-PARTS	Drawing N0 003/4	Scale 10:1 Data- Drawn. J. H. de Jongh

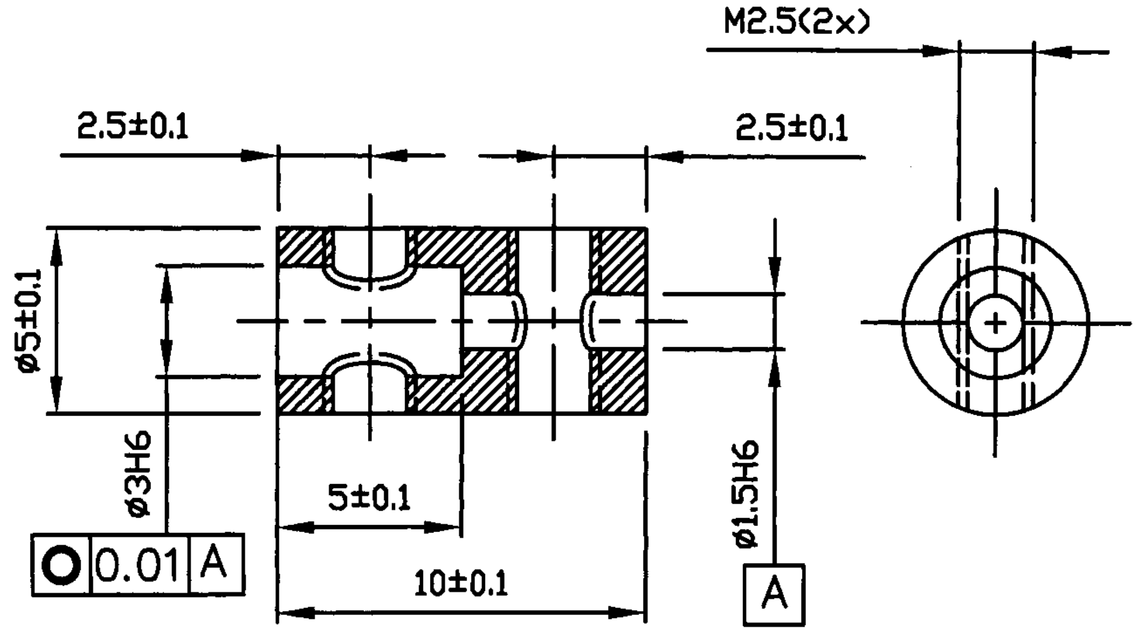

Part Name	Material	Proces	Quantity
BUSH-05	1.4305	–	1x

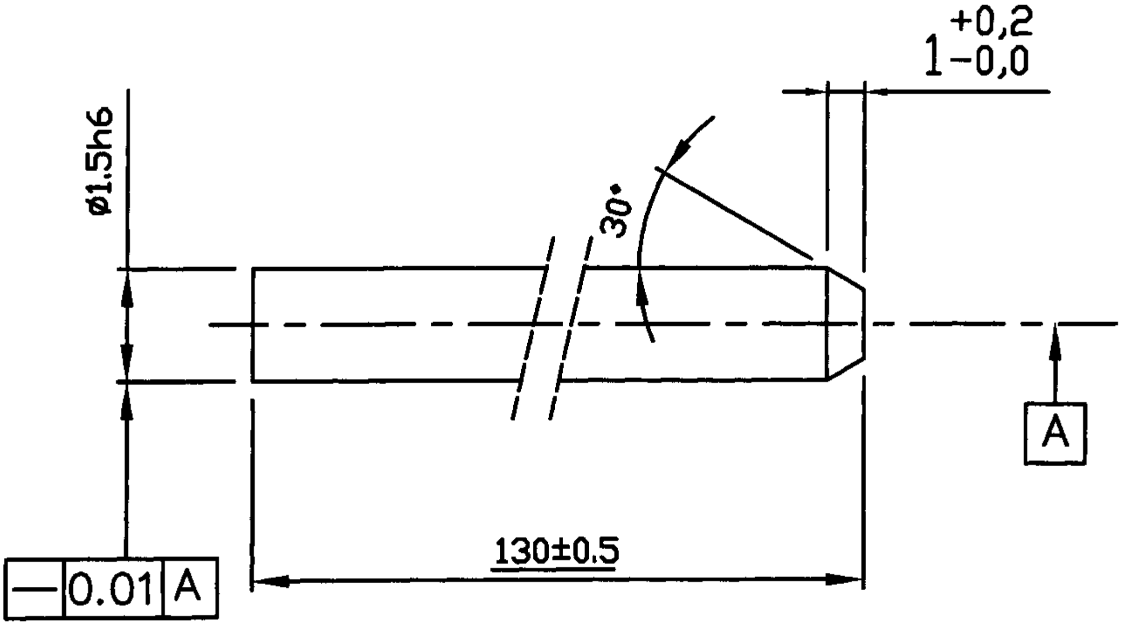

Part Name	Material	Proces	Quantity
AXIS-06	1.1274	–	1x

Drawing Name	Drawing NO	Scale 5:1
LVAD-PARTS	005/6	Data- Drawn. J. H. de Jongh

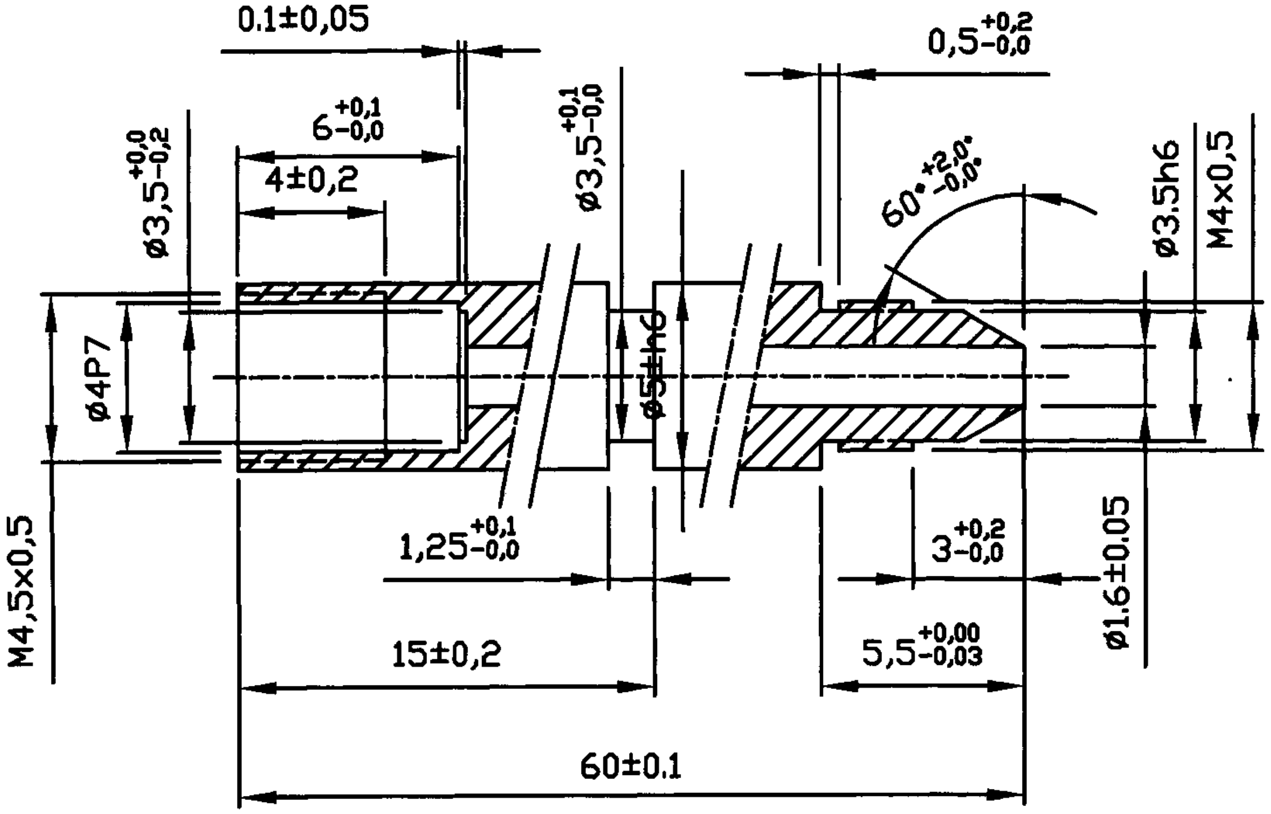

Part Name	Material	Proces	Quantity
PEN–L–07	2.0401	–	1x

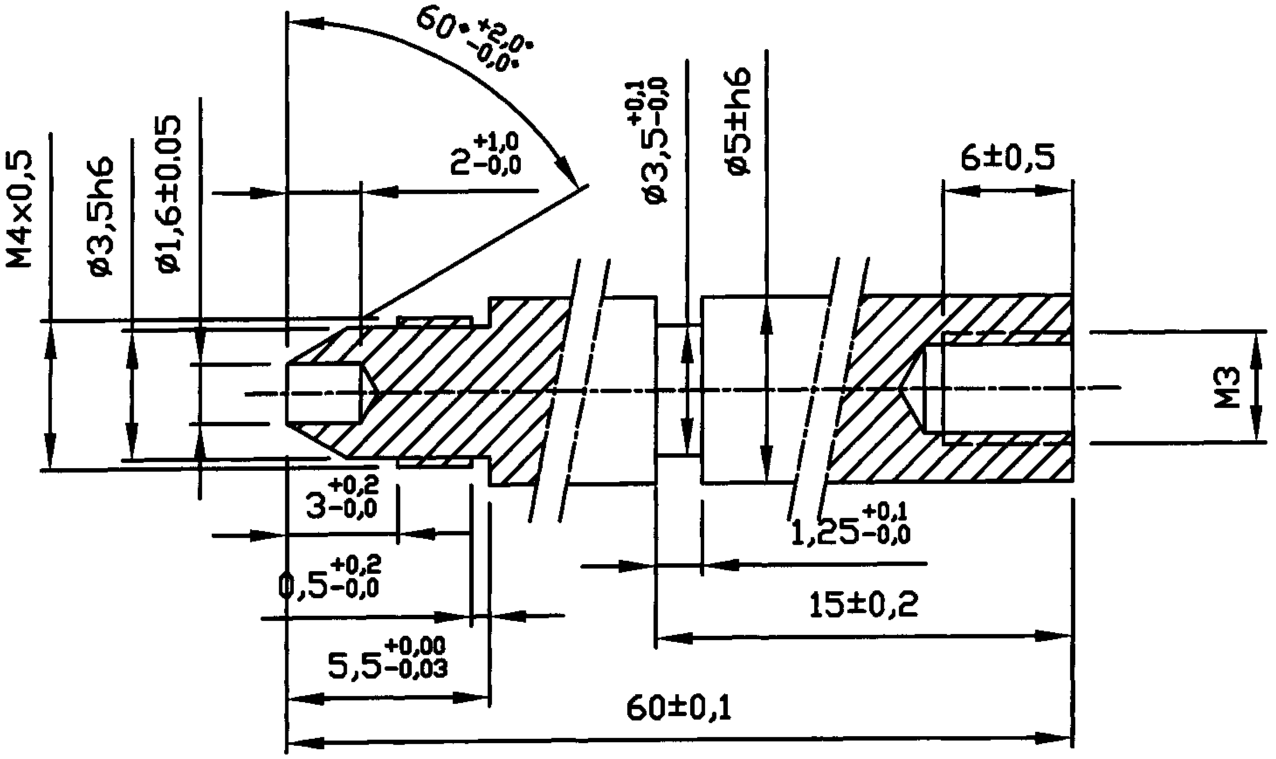

Part Name	Material	Proces	Quantity
PEN–R–08	2.0401	–	1x

Drawing Name LVAD-PARTS	Drawing N0 007/8	Scale 5:1 Data- Drawn. J. H. de Jongh

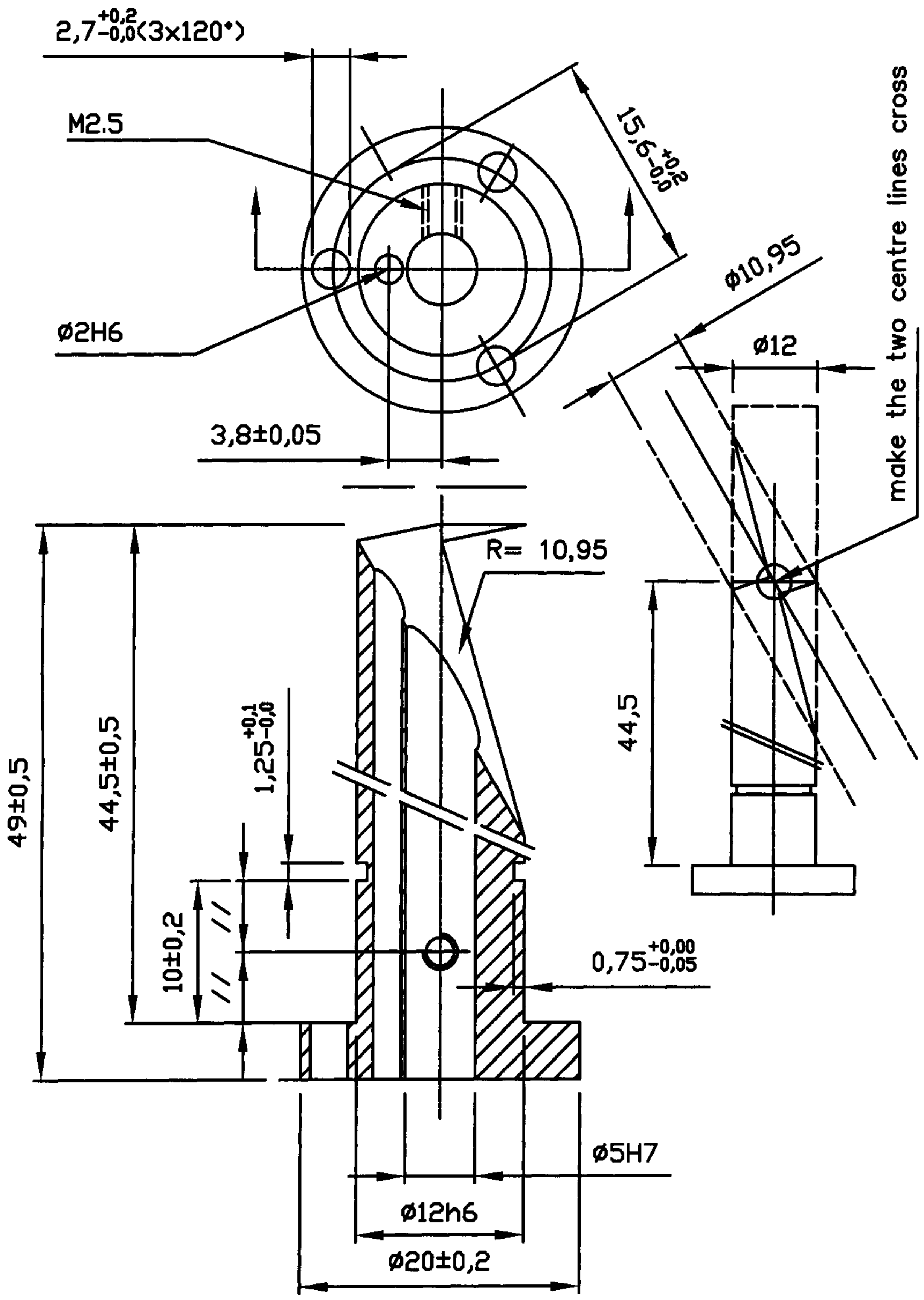

1 set = Tap hole M2,5 Left + 1x Tap hole M2,5 Right in pipe

Part Name PIPE-R/L-09	**Material** 3.1255	**Proces** Anodising	**Quantity** 1 set

Drawing Name LVAD-PARTS	**Drawing NO** 009	Scale 2.5:1 **Data-** **Drawn. J. H. de Jongh**

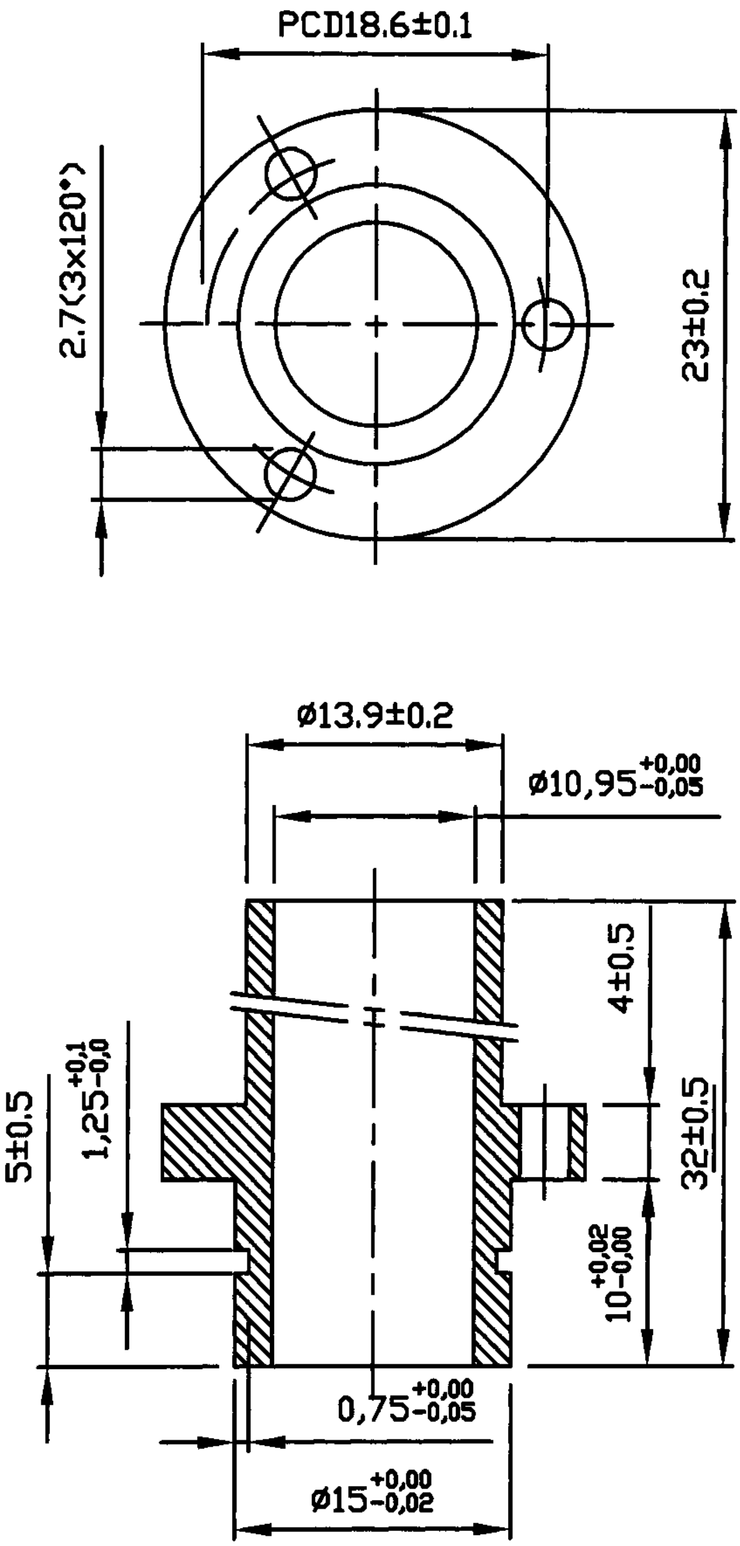

Part Name	Material	Proces	Quantity
PIPE-R/L-10	3.1255	Anodising	2x

Drawing Name	Drawing NO	
LVAD-PARTS	010	Scale 2.5:1 Data- Drawn. J. H. de Jongh

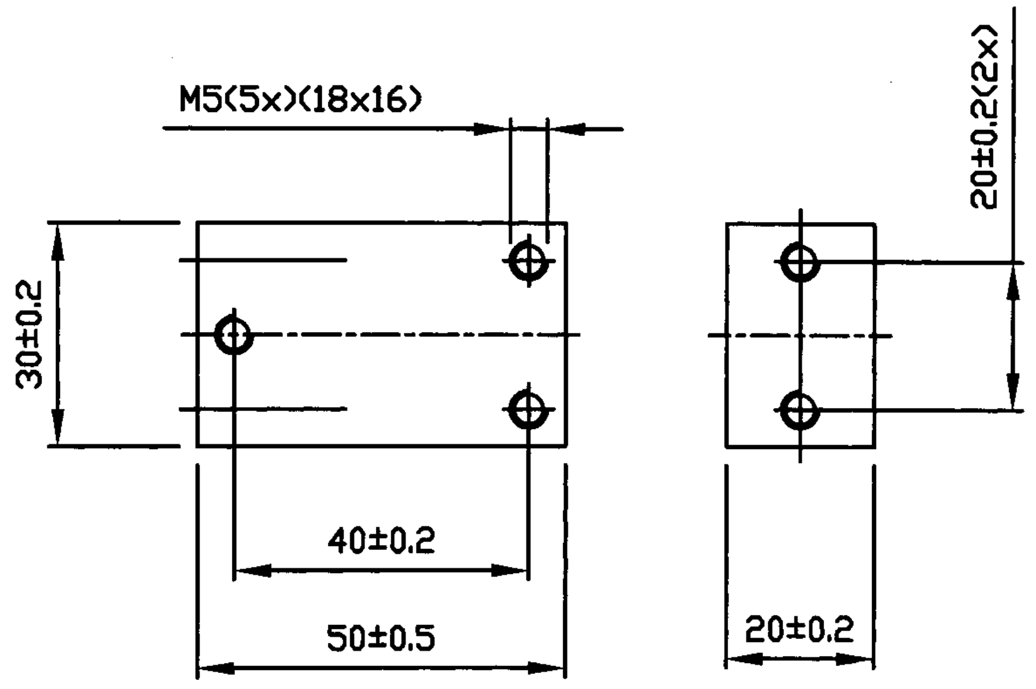

Part name BLOCK–11	Material 3.1255	Proces –	Quantity 1x

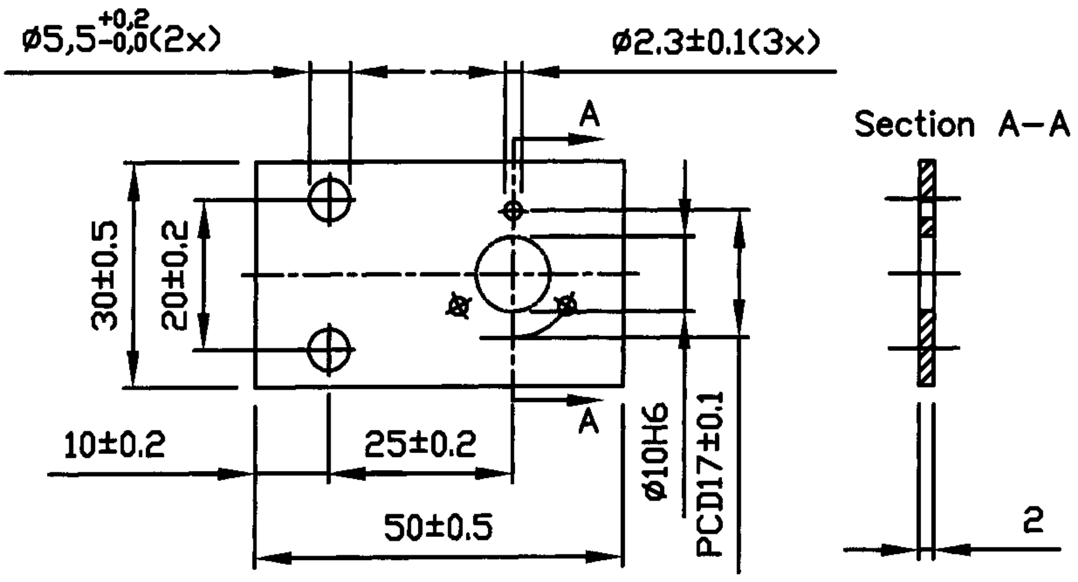

Part Name PLATE–12	Material 1.4541	Proces –	Quantity 1x

Drawing Name LVAD-PARTS	Drawing NO 011/12	Scale 1:1 Data- Drawn. J. H. de Jongh

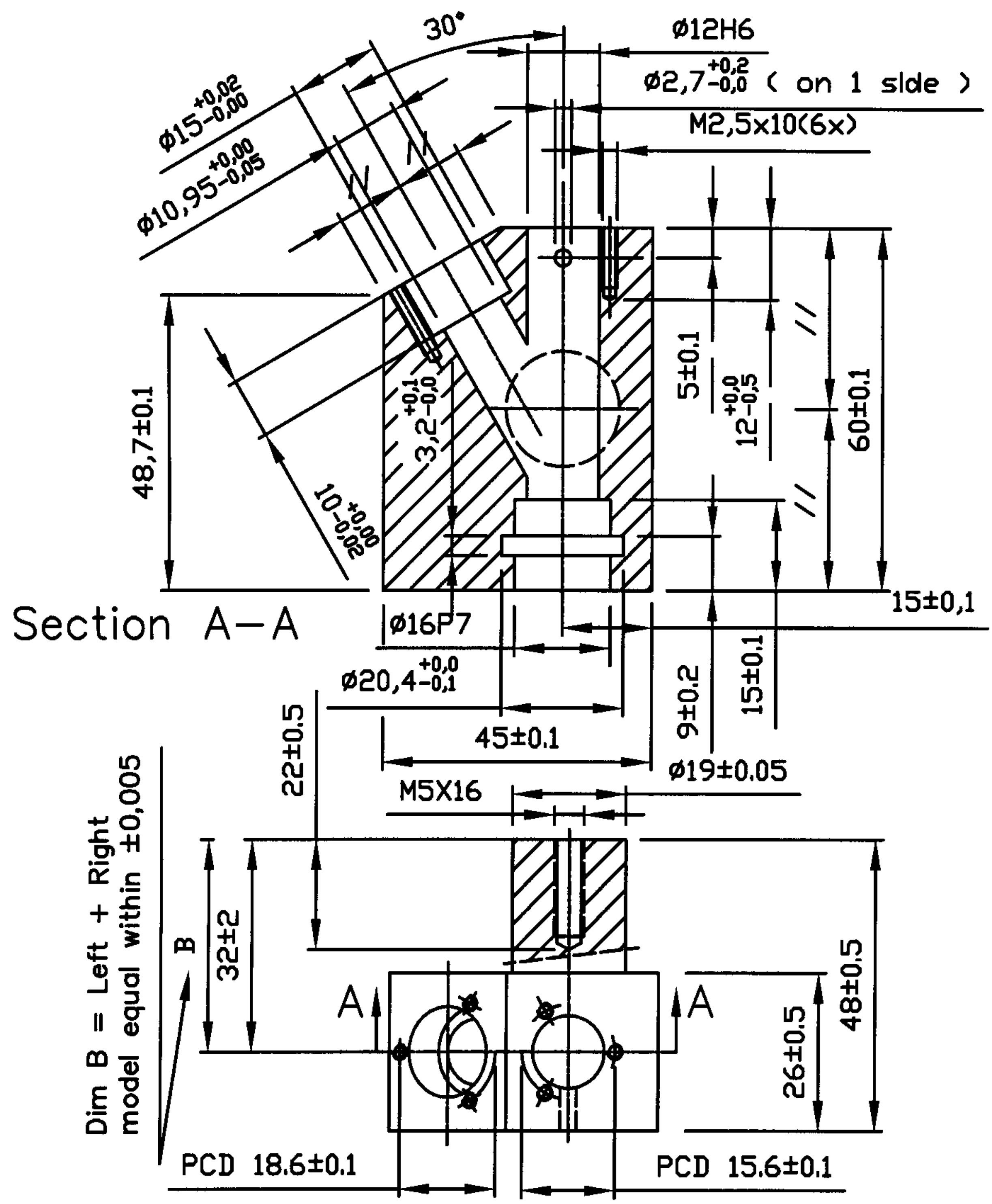

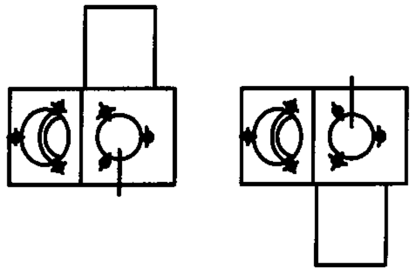

Example

Scale 1:2

1 set = 1x Left + 1x Right model

Part Name	Material	Proces	Quantity
House–13/14–L+R	3.1255	Anodising	1 set

Drawing Name	Drawing NO	
LVAD-PARTS	013/14	Scale 1:1 Data- Drawn. J. H. de Jongh

Mounting arbor for O-ring

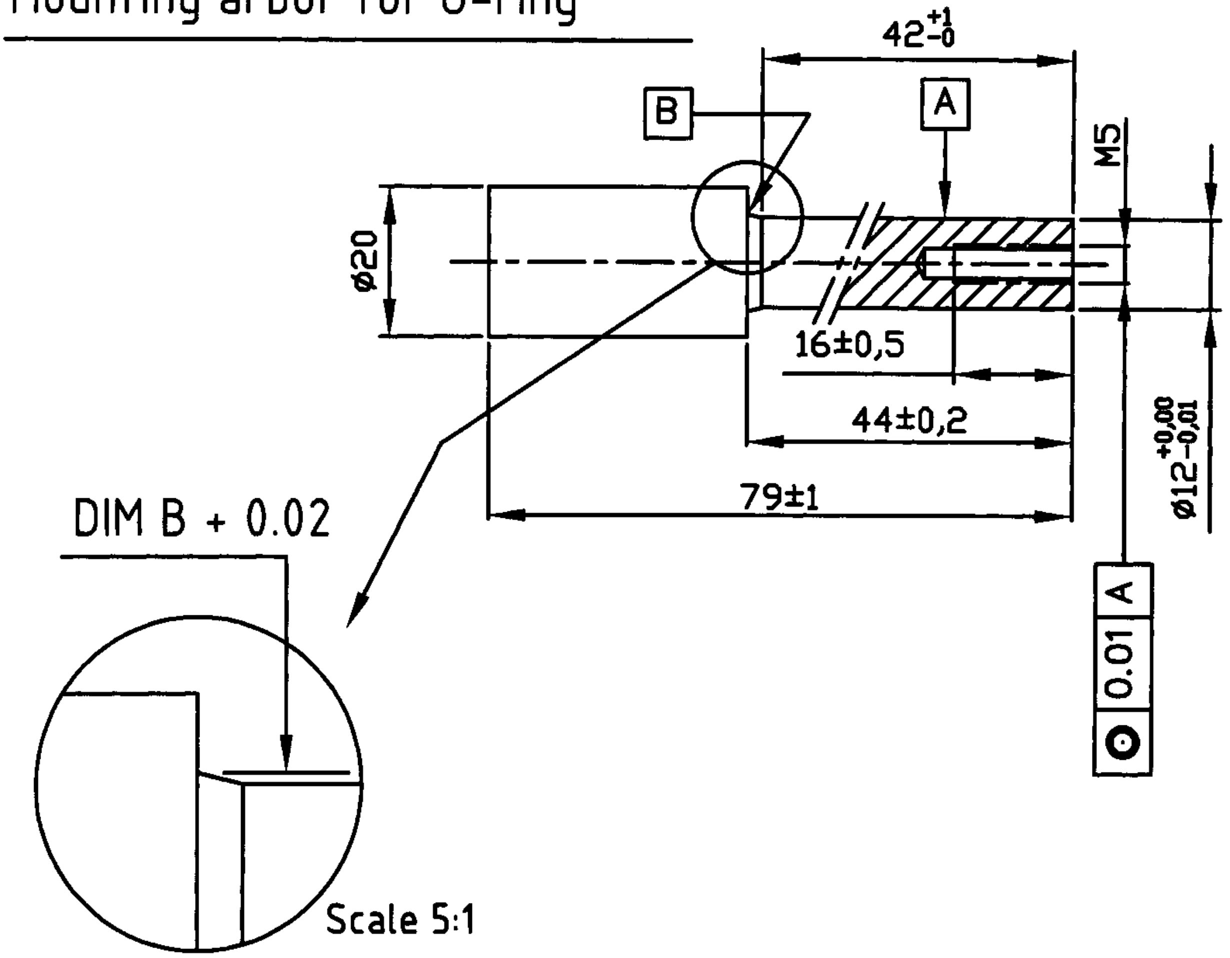

Part Name	Material	Proces	Quantity
ARBOR–15	1.4305	–	1x

Allen screw for mounting arbor O-ring

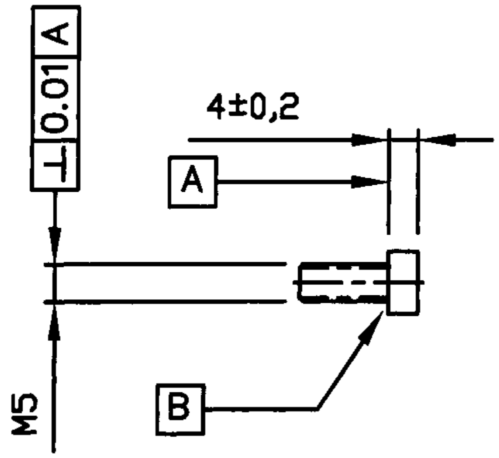

Part Name	Material	Proces	Quantity
SCREW–16	Steel 8.8	–	1x

Drawing Name	Drawing NO	Scale 1:1
LVAD-PARTS	015/16	Data- Drawn. J. H. de Jongh

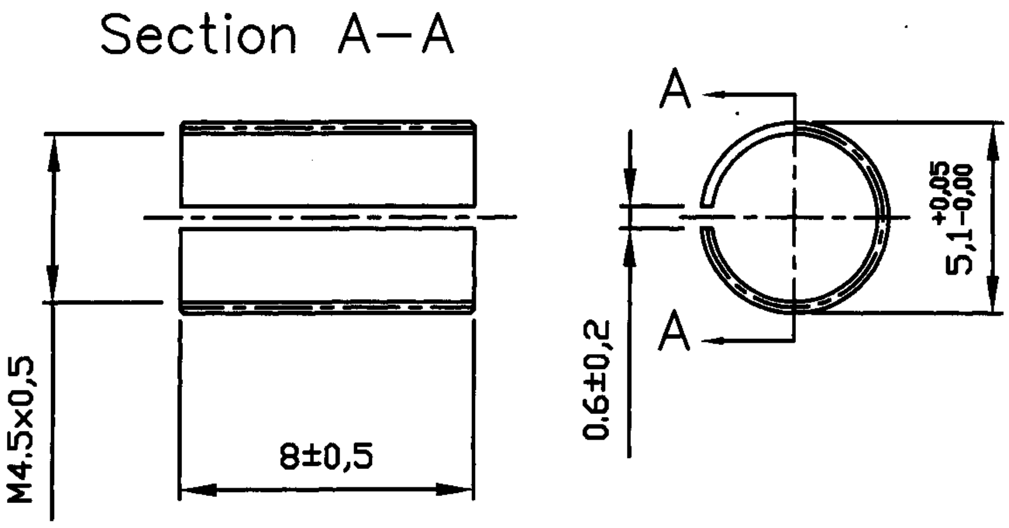

Part Name	Material	Proces	Quantity
CLAMPBUSH–17	1.4305	-	1x

Drawing Name	Drawing NO	Scale 5:1
LVAD-PARTS	017	Data- Drawn. J. H. de Jongh

For machining of pump

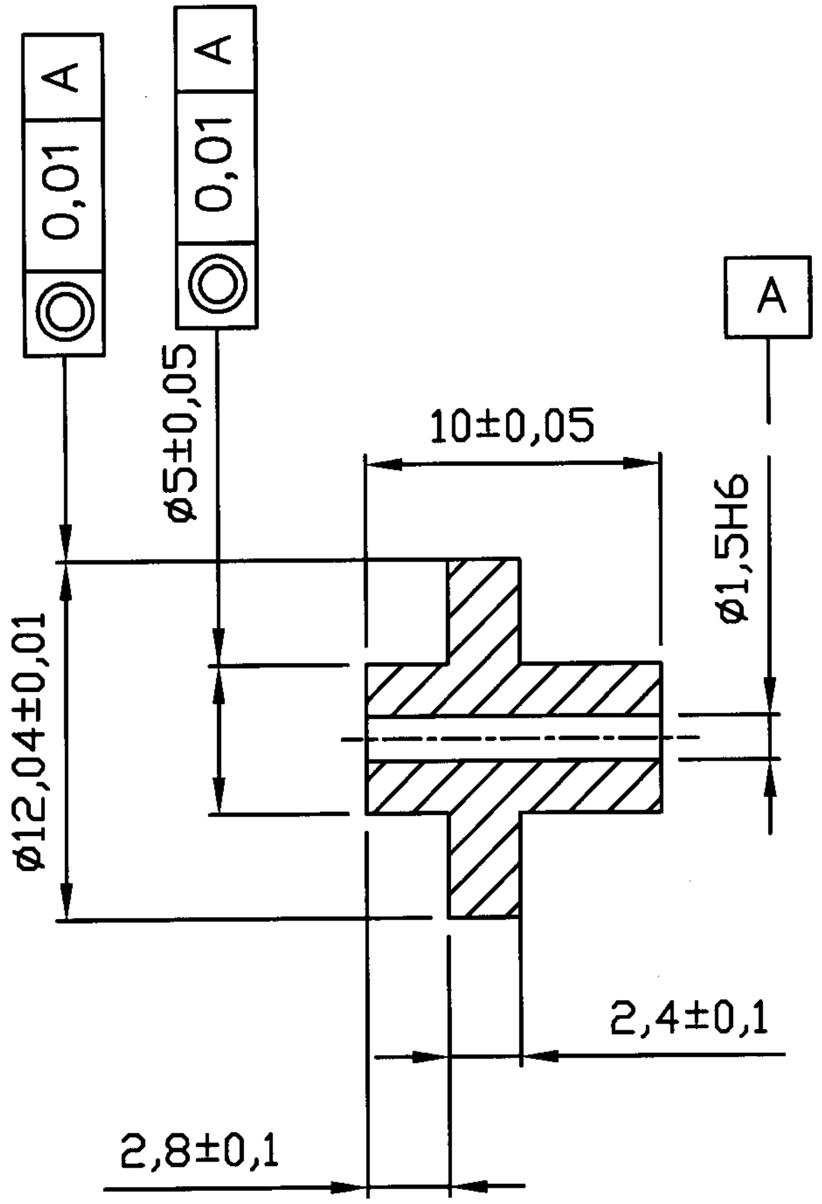

Part Name	Material	Proces	Quantity
ROTOR–18	L 168	–	1x

Drawing Name	Drawing NO	Scale 4:1
LVAD-PARTS	018	Data- Drawn. J. H. de Jongh

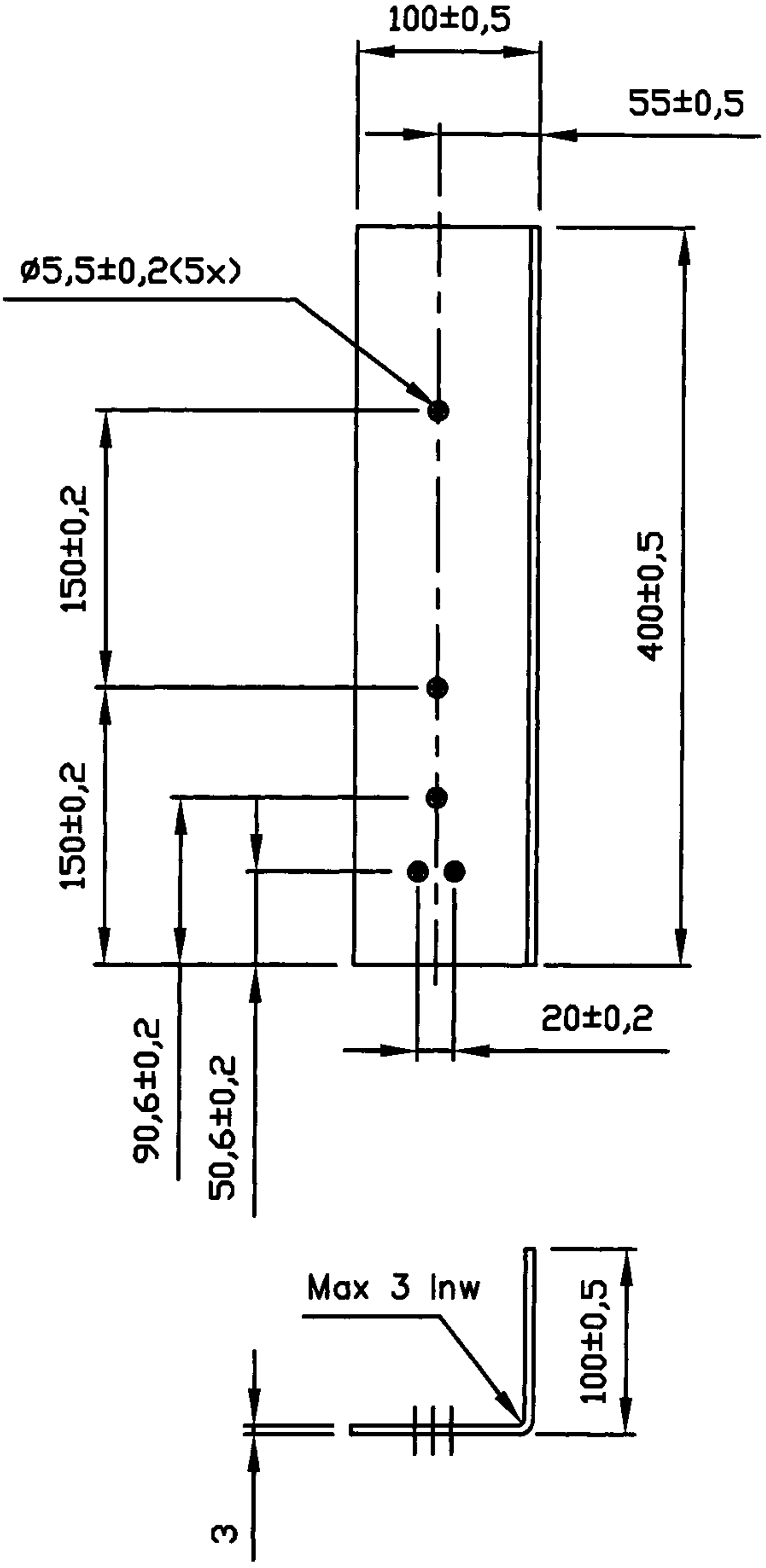

Part Name	Material	Proces	Quantity
ASSEMBLYPLATE-19	3.3545	–	1x

Drawing Name	Drawing NO	
LVAD-PARTS	019	Scale 1:4 Data- Drawn. J. H. de Jongh

Key for NUT–03 (4,5x0,5)

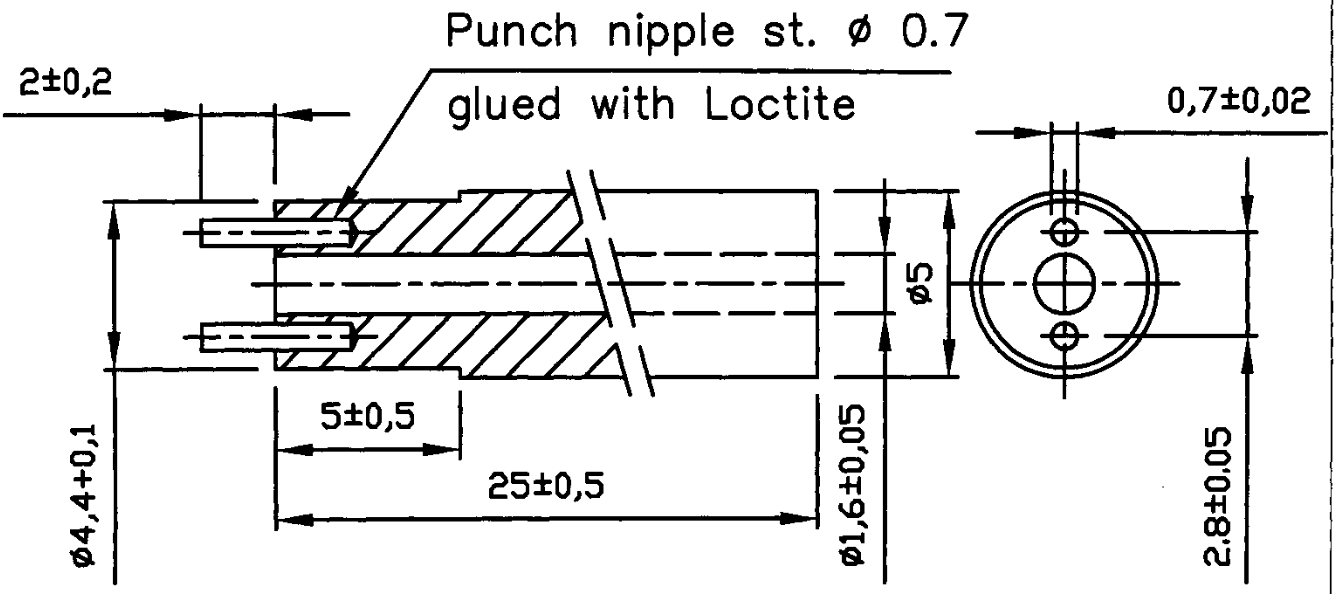

Part Name	Material	Proces	Quantity
KEY–20	1.4305	–	1x

Pin for assembly of bearing (4x1,5x2)

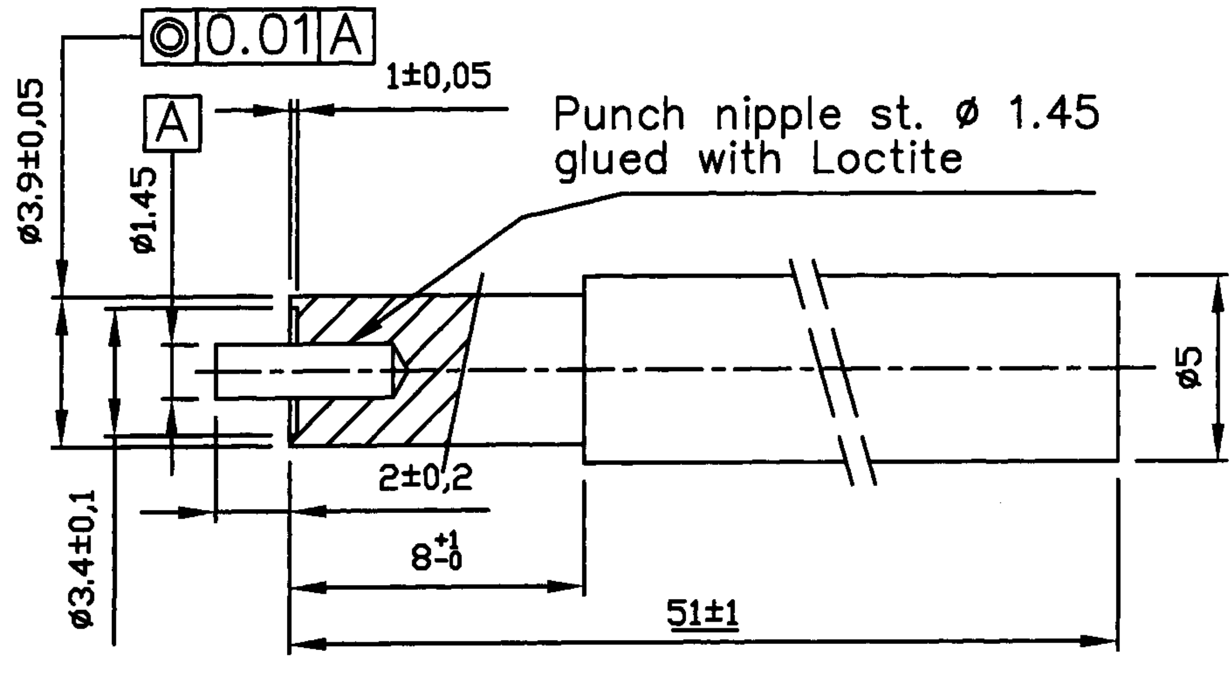

Part Name	Material	Proces	Quantity
PIN–21	1.4305	–	1x

Drawing Name LVAD-PARTS	**Drawing NO** 020/21	Scale 5:1 **Data-** **Drawn. J. H. de Jongh**

List of Publications

Conference Proceedings

SWALEN, M.J.P., KÖNIG, C.S., SAYMA, A.I. and KHIR, A.W., 2010. CFD modelling of a bi-directional axial flow LVAD. Accepted for poster presentation at ESAO 2010.

SWALEN, M.J.P., KÖNIG, C.S., SAYMA, A.I. and KHIR, A.W., 2009. Computational study of a novel axial flow pump as LVAD. Accepted for oral presentation at ESAO 2009. Available from *Artificial Organs*, **32**(7), pp. 401.

SWALEN, M.J.P., KÖNIG, C.S., SAYMA, A.I. and KHIR, A.W., 2008. Development of a novel ventricular assist device (VAD). Accepted for poster presentation at ESAO 2008. Available from *Artificial Organs*, **31**(7), pp. 624.

List of References

ABRAHAM, F., BEHR, M. and HEINKENSCHLOSS, M., 2005. Shape Optimization in Stationary Blood Flow: A Numerical Study of Non-Newtonian Effects. *Computer Methods in Biomechanics and Biomedical Engineering*, **8**, pp. 127–137.

AKIMOTO, T., LITWAK, K.N., YAMAZAKI, K., LITWAK, P., KIHARA, S.I., TAGUSARI, O., YAMAZAKI, S.I., KAMENEVA, M.V., WATACH, M.J., UMEZU, M., TOMIOKA, J., KORMOS, R.L., KOYANAGI, H. and GRIFFITH, B.P., 2001. The Role of Diastolic Pump Flow in Centrifugal Blood Pump Hemodynamics. *Artificial Organs*, **25**(9), pp. 724-727.

ALLAIRE, P.E., WOOD, H.G., AWAD, R.S. and OLSEN, D.B., 1999. Blood Flow in a Continuous Flow Ventricular Assist Device. *Artificial Organs*, **23**(8), pp. 769-773.

ALLEN, G.S., MURRAY, K.D. and OLSEN, D.B., 1997. The importance of pulsatile and nonpulsatile flow in the design of blood pumps. *Artif Organs*, **21**(8), pp. 922-928.

ALLENDER, S., SCARBOROUGH, P., PETO, V. and RAYNER, M., 2008. European Cardiovascular Disease statistics - 2008 edition. Brussels, Belgium: European Heart Network.

ANDERSON, D.W., 2001. Blood pumps: technologies and markets in transformation. *Artificial Organs*, **25**, pp. 406.

ANTAKI, J.F., BURGREEN, G.W., WU, Z.J., BORZELLECA, D., KAMENEVA, M.V., HOLMES, J.A., LITWAK, P., LITWAK, K., WATACH, M., PADEN, B.E., DRAGNES, T., GROOM, N.J. and GRIFFITH, B.P., 2000. Development progress of the University of Pittsburgh Streamliner: a mixed flow blood pump with magnetic bearings. *ASAIO Journal*, **46**, pp. 194.

ANTAKI, J.F., GHATTAS, O., BURGREEN, G.W. and HE, B., 1995. Computational Flow Optimization of Rotary Blood Pump Components. *Artificial Organs*, **19**(7), pp. 608-615.

APEL, J., NEUDEL, F. and REUL, H., 2000. Computational fluid dynamics and experimental validation of a microaxial blood pump. *ASAIO Journal*, **47**, pp. 552-558.

APEL, J., PAUL, R., KLAUS, S., SIESS, T. and REUL, H., 2001. Assessment of hemolysis related quantities in a microaxial blood pump by computational fluid dynamics. *Artificial Organs*, **25**, pp. 341-347.

ARAKI, K., ANAI, H., OSHIKAWA, M., NAKAMURA, K. and ONITSUKA, T., 1998. In Vitro Performance of a Centrifugal, a Mixed Flow, and an Axial Flow Blood Pump. *Artificial Organs*, **22**(5), pp. 366-370.

ARORA, D., BEHR, M. and PASQUALI, M., 2004. A Tensor-based Measure for Estimating Blood Damage. *Artificial Organs*, **28**(11), pp. 1002-1015.

ARORA, D., BEHR, M. and PASQUALI, M., 2006. Hemolysis Estimation in a Centrifugal Blood Pump Using a Tensor-based Measure. *Artificial Organs*, **30**(7), pp. 539-547.

BALLYK, P.D., STEINMAN, D.A., ETHIER, C.R., 1994. Simulation of non-Newtonian blood flow in an end-to-end anastomosis. *Biorheology*, **31**(5), pp. 565–586.

BEHBAHANI, M., BEHR, M., HORMES, M., STEINSEIFER, U., ARORA, D., CORONADO, O. and PASQUALI, M., 2009. A Review of Computational Fluid Dynamics Analysis of Blood Pumps. *European Journal of Applied Mathematics*, **20**, pp. 363–397.

BERGER, S.A., JOU, L.D., 2000. Flows in stenotic vessels. *Annual Reviews of Fluid Mechanics*, **32**, pp. 347–382.

BENNETT, M., HORTON, S., THUYS, C., AUGUSTIN, S., ROSENBERG, M. and BRIZARD, C. 2004. Pump-induced haemolysis: a comparison of short-term ventricular assist devices. *Perfusion*, **19**, pp. 107-111.

BENSON, H., 1996. *University Physics*. New York: John Wiley & Sons.

BHAVSAR, S.S., MOSKOWITZ, W.B. and THROCKMORTON, A.L., 2010. Interaction of an Idealized Cavopulmonary Circulation With Mechanical Circulatory Assist Using an Intravascular Rotary Blood Pump. *Artificial Organs*, **34**(10), pp. 816-827.

BHF coronary heart disease statistics 2009-10Feb/12, 2010-last update [Homepage of British Heart Foundation], [Online]. Available: http://www.bhf.org.uk/plugins/PublicationsSearchResults/idoc.ashx?docid=07a5d384-ac93-4d2b-a84d-918620d7a9f0&version=-1 [June/30, 2010].

BLUDSZUWEIT, C., 1995. Model for general mechanical blood damage prediction. *Artificial Organs*, **19**(7), pp. 583–589.

BLUDSZUWEIT, C., 1995. Three-dimensional numerical prediction of stress loading of blood particles in a centrifugal pump. *Artificial Organs*, **19**(7), pp. 590–596.

BURGREEN, G.W., ANTAKI, J.F. and GRIFFITH, B.P, 1996. A Design Improvement Strategy for Axial Blood Pumps Using Computational Fluid Dynamics. *ASAIO Journal*, **42**, pp. M354-60.

BURGREEN, G.W., ANTAKI, J.F., WU, Z. and HOLMES, A.J., 2001. Computational fluid dynamics as a development tool for rotary blood pump. *Artificial Organs*, **25**(5), pp. 336–340.

CAVAZZUTI, M., ATHERTON, M., COLLINS, M. and BAROZZI, G., 2010. Beyond the Virtual Intracranial Stenting Challenge 2007: Non-Newtonian and flow pulsatility effects. *Journal of Biomechanics*, **43**, pp. 2645-2647.

CHAN, W.K., WONG, Y.W., DING, Y., CHUA, L.P. and YU, S.C.M., 2002. Numerical Investigation of the Effect of Blade Geometry on Blood Trauma in a Centrifugal Blood Pump. *Artificial Organs*, **26**(9), pp. 785-793.

CHAN, W.K. WONG, Y.W., ONG, W., KOH, S.Y., and CHONG, V., 2005. Numerical Investigation of the Effects of the Clearance Gap Between the Inducer and Impeller of an Axial Blood Pump. *Artificial Organs*, **29**(3), pp. 250-258.

CHEN, J., LU, X.Y. and WANG, W, 2006. Non-Newtonian effects of blood flow on hemodynamics in distal vascular graft anastomoses. *Journal of Biomechanics*, **39**, pp. 1983-1995.

CHO, Y.I., KENSEY, K.R., 1991. Effects of the non-Newtonian viscosity of blood on flows in a diseased arterial vessel. Part 1: steady flows. *Biorheology*, **28**, pp. 241–262.

CORBETT, S.C., AJDARI, A., COSKUN, A.U. and HASHEMI, H.N., 2010. In Vitro and Computational Thrombosis on Artificial Surfaces With Shear Stress. Artificial Organs, 34(7), pp. 561-569.

CURTAS, A.R., WOOD, H.G., ALLAIRE, P.E. MCDANIEL, J.C., DAY, S.W. and OLSEN, D.B., 2002. Computational Fluid Dynamics Modeling of Impeller Designs for the HeartQuest Left Ventricular Assist Device. *ASAIO Journal*, **48**, pp. 552-561.

DEBAKEY, M.E., 1997. Development of a Ventricular Assist Device.Article. *Artificial Organs.Tissue Engineering*, **21**(11), pp. 1149-1153.

DEBAKEY, M.E., 2000. The Odyssey of the Artificial Heart. *Artificial Organs*, **24**(6), pp. 405-411.

DEUTSCH, S., TARBELL, J.M., MANNING, K.B., ROSENBERG, G. and FONTAINE, A.A., 2006. Experimental Fluid Mechanics of Pulsatile Artificial Blood Pumps. *Ann. Rev. Fluid Mechanics*, **38**, pp. 65-86.

DIXON, S.L., 1998. *Fluid Mechanics and Thermodynamics of Turbomachinery*. Boston: Butterworth-Heinemann.

DOYLE, M.G., VERGNIAUD, J.B., TAVOULARIS, S. and BOURGAULT, Y., 2008. Numerical Simulations of Blood Flow in Artificial and Natural Hearts With Fluid–Structure Interaction. *Artificial Organs*, **32**(11), pp. 870-879.

DUCAS, J. and GRECH, E.D., 2003. Percutaneous coronary intervention: cardiogenic shock. *BMJ*, **326**, pp. 1450.

FOSSUM, T.W., MORLEY, D., BENKOWSKI, R., TAYAMA, E., OLSEN, D.B., BURNS, G., MILLER, M.W., FRANKS, J., MARTINEZ, E., CARROLL, G., EDWARDS, J., VINNERQVIST, A., LYNCH, B., STEIN, F., NOON, G.P. and DEBAKEY, M.E., 1999. Chronic Survival of Calves Implanted with the DeBakey Ventricular Assist Device. *Artificial Organs*, **23**(8), pp. 802-806.

FOX, R.W., MCDONALD, A.T. and PRITCHARD, P.J., 2011. *Introduction to Fluid Mechanics*. New York: John Wiley & Sons.

FRAZIER, O.H., MYERS, T.J., JARVIK, R.K., et al, 2001. Research and development of an implantable, axial-flow left ventricular assist device: the Jarvik 2000 Heart. *Ann Thorac Surg*, **71**(3 Suppl), pp. S125-S132.

FUMAGALLI, G., 2007. MPhil Thesis. Feasibility Study on the Development of a Novel Type of Cardiac Assist Device. Brunel University, Uxbridge (UK).

GARDINER, J.M., WU, J., NOH, M.D., ANTAKI, J.F., SNYDER, T.A., PADEN, D.B. and PADEN, B.E., 2007. Thermal Analysis of the PediaFlow Pediatric Ventricular Assist Device.Miscellaneous Article. *ASAIO Journal*, **53**(1), pp. 65-73.

GIJSEN, F.J.H., ALLANIC, E., VOSSE, F.N. VAN DE and JANSSEN, J.D., 1999. The influence of the non-Newtonian properties of blood on the flow in large arteries: unsteady flow in a 90° curved tube. *Journal of Biomechanics*, **32**, pp. 705–713.

GIJSEN, F.J.H., VOSSE, F.N. VAN DE and JANSSEN, J.D., 1999. The influence of the non-Newtonian properties of blood on the flow in large arteries: steady flow in a carotid bifurcation model. *Journal of Biomechanics*, **32**, pp. 705–713.

GRUTTOLA, S. DE, BOOMSMA, K. and POULIKAKOS, D., 2005. Computational Simulation of a Non-Newtonian Model of the Blood Separation Process. *Artificial Organs*, **29**(12), pp. 949-959.

GOLDOWSKY, M., 2002. Mini hemoreliable axial flow LVAD with magnetic bearings. I. Historical overview and concept advantages. *ASAIO Journal*, **48**, pp. 96-98.

GOLDOWSKY, M., 2002. Mini hemoreliable axial flow LVAD with magnetic bearings. I. Design description. *ASAIO Journal*, **48**, pp. 98-100.

GOLDSTEIN, D.J. and OZ, M.C., 2000. *Cardiac Assist Devices*. New York: Futura Publishing Company Inc.

GRIFFITH, B.P., KORMOS, R.L., BOROVETZ, H.S., LITWAK, K., ANTAKI, J.F., POIRIER, V.L. and BUTLER, K.C., 2001. HeartMate II left ventricular assist system: from concept to first clinical use. *The Annals of Thoracic Surgery*, **71**(90030), S116-120.

HEUSER, G. and OPTIZ, R.A., 1980. A Couette viscometer for short time shearing of blood. *Biorheology*, **17**(1-2), 17-24.

JACOBS, E.N., WARD, K.E. and PINKERTON, R.M., 1933. The characteristics of 78 related airfoil sections from tests in the variable-density wind tunnel. **460**. Washington: NACA.

JAMES, N.L., WILKINSON, C.M., LINGARD, N.L., VAN DER MEER, A.L. and WOODARD, J.C., 2003. Evaluation of hemolysis in the VentrAssist implantable rotary blood pump. *Artif Organs*, **27**(1), 108-113.

JOHNSTON, B.M., JOHNSTON, P.R., CORNEY, S. and KILPATRICK, D, 2004. Non-Newtonian blood flow in human right coronary arteries: steady state simulations. *Journal of Biomechanics*, **37**, 709–720.

JOHNSTON, B.M., JOHNSTON, P.R., CORNEY, S. and KILPATRICK, D, 2006. Non-Newtonian blood flow in human right coronary arteries: transient simulations. *Journal of Biomechanics*, **39**, 1116–1128.

KARASSIK, I.J., KRUTZSCH, W.C., FRASER, W.H. and MESSINA, J.P., 1986. *Pump handbook*. New York: McGraw-Hill.

KAWAHITO, K. and NOSÉ, Y., 1997. Hemolysis in different centrifugal pumps. *Artif Organs*, **21**(4), 323-326.

KU, D., 1997. Blood Flow in Arteries. *Ann. Rev. Fluid Mechanics*, **29**, pp. 399-434.

LAMBERTI, J.J. and RESNEKOZ, L., 1978. Cardiac Assist Devices. *Ann. Rev. Med*, **29**, pp. 571-82.

LI, X., BAI, J. and HE, P., 2002. Simulation study of the Hemopump as a cardiac assist device. *Med. Biol. Eng. Comput*., **40**, pp. 344-353.

LI, S., NISHI, M. and YOSHIDA, K., 2001. Impeller Geometry Suitable for Mini Turbo-Pump. *Journal of Fluid Engineering*, **123**, pp. 500-506.

LOGAN JR., E., 1993. *Turbomachinery: basic theory and applications*. Second Edition edn. New York: M. Dekker.

MATHERS, C. and LONCAR, D., 2006. Projections of global mortality and burden of disease from 2002 to 2030. *PLoS Medicine*, **3**, 442.

MCDONALD, D.A., 1974. *Blood flow in arteries*. London: Edward Arnold.

MEER, A.L. VAN DER, JAMES, N.L., EDWARDS, G.A., ESMORE, D.S., ROSENFELDT, F.L., BEGG, J.D. and WOODARD, J.C., 2003. Initial In Vivo Experience of the VentrAssist Implantable Rotary Blood Pump in Sheep. *Artificial Organs*, **27**(1), pp. 21-26.

MISRA, J.C., PATRA, M.K. and MISRA, S.C., 1993. A non-Newtonian fluid model for blood flow through arteries under stenotic conditions. *Journal of Biomechanics*, **26**(9), pp. 1129-1141.

MITAMURA, Y., NAKAMURA, H., OKAMOTO, E., YOZU, R., KAWADA, S. and KIM, D., 1999. Development of the Valvo Pump: An Axial Flow Pump Implanted at the Heart Valve Position. *Artificial Organs*, **23**(6), pp. 566-571.

MITOH, A., YANO, T., SEKINE, K., MITAMURA, Y., OKAMOTO, E., KIM, D., YOZU, R. and KAWADA, S., 2003. Computational Fluid Dynamics Analysis of an Intra-Cardiac Axial Flow Pump. *Artificial Organs*, **27**(1), pp. 34-40.

MIYAZOE, Y., SAWAIRI, T., ITO, K., KONISHI, Y., YAMANE, T., NISHIDA, M., MASUZAWA, T., TAKIURA, K. and TAENAKA, Y., 1998. Computational Fluid Dynamic Analyses to Establish Design Process of Centrifugal Blood Pumps. *Artificial Organs*, **22**(5), pp. 381-385.

MUGGLI, F.A. and HOLBEIN, P., 2002. CFD Calculation of a Mixed Flow Pump Characteristic From Shutoff to Maximum Flow. *Journal of Fluids Engineering*, **124**(3), pp. 798-102.

NOSE, Y., YOSHIKAWA, M., MURABAYASHI, S. and TAKANO, T., 2000. Development of Rotary Blood Pump Technology: Past, Present, and Future. *Artificial Organs,* **24**(6), pp. 412-420.

OKADA, Y., MASUZAWA, T., MATSUDA, K.I., OHMORI, K., YAMANE, T., KONISHI, Y., FUKAHORI, S., UENO, S. and KIM, S.J., 2003. Axial Type Self-Bearing Motor for Axial Flow Blood Pump. *Artificial Organs*, **27**(10), pp. 887-891.

OLSEN, D.B., 1999. Rotary blood pumps: a new horizon. *Artificial Organs,* **23**, pp. 695-696.

OLSEN, D.B., 2000. The history of continuous-flow bloodpumps. *Artificial Organs*, **24**, pp. 401.

PAUL, R., APEL, J., KLAUS, S., SCHUGNER, F., SCHWINDKE, P. and REUL, H., 2003. Shear Stress Related Blood Damage in Laminar Couette Flow. *Artificial Organs,* **27**(6), pp. 517-529.

PAUL, R., SCHÜGNER, F., REUL, H. and RAU, G., 1999. Recent findings on flow induced blood damage: Critical shear stresses and exposure times obtained with a high shear couette-system. *Artif Organs*, **23**, 680.

PEDLEY, T.J., 1980. *The Fluid Mechanics of Large Blood Vessels*. Cambridge University Press, Cambridge.

QIAN, K.X., ZENG, P., RU, W.M. and YUAN, H.Y., 2002. Streamlines design of impeller and its effect on pump haemolysis. *Journal of Medical Engineering & Technology*, **26**(2), pp. 79-81.

REUL, H.M. and AKDIS, M., 2000. Blood Pumps for circulatory support. *Perfusion*, **15**, pp. 295-311.

ROBBINS, R.C., KOWN, M.H., PORTNER, P.M. and OVER, P.E., 2001. The totally implantable Novacor Left Ventricular Assist System. *Ann Thorac Surg,* **71**, pp. S162-S165

SAITO, S. and NISHINAKA, T., 2005. Chronic nonpulsatile blood flow is compatible with normal end-organ function: implications for LVAD development. *J. Artif. Organs*, **8**, pp. 143-148.

SATO, K., ORIHASHI, K., KUROSAKI, T., TOKUMINE, A., FUKUNAGA, S., NINOMIYA, S. and SUEDA, T., 2009. Analysis of Flow Patterns in a Ventricular Assist Device: A Comparative Study of Particle Image Velocimetry and Computational Fluid Dynamics. *Artificial Organs*, **33**(4), pp. 352-359.

SAYERS, A.T., 1990. Hydraulic and Compressible Flow Turbomachines. London: McGraw-Hill.

SHI, Y., KORAKIANITIS, T. and BOWLES, C., 2007. Numerical simulation of cardiovascular dynamics with different types of VAD assistance. *Journal of Biomechanics*, **40**, pp. 2919-2933.

SIESS, T., NIX, C. and MENZLER, F., 2001. From a Lab Type to a Product: A Retrospective View on Impella's Assist Technology. *Artificial Organs*, **25**(5), pp. 414-421.

SONG, X., THROCKMORTON, A.L., UNTAROIU, A., PATEL, S., ALLAIRE, P.E., WOOD, H.G. and OLSEN, D.B., 2003. Axial Flow Blood Pumps.Review. *ASAIO Journal,* **49**(4), pp. 355-364.

SONG, X., UNTAROIU, A., WOOD, H.G. PAUL, E., ALLAIRE, P.E., THROCKMORTON, A.L., DAY, S.W. and OLSEN, D.B., 2004. Design and Transient Computational Fluid Dynamics Study of a Continuous Axial Flow Ventricular Assist Device. *ASAIO Journal,* **50**, pp. 215-224.

SONG, X., WOOD, H.G., ALLAIRE, P.E. ANTAKI, J.F. and OLSEN, D.B., 2004. Inlet and Outlet Devices for Rotary Blood Pumps. *Artificial Organs*, **28**(10), pp. 911-915.

SONG, X., WOOD, H.G., DAY, S.W. and OLSEN, D.B., 2003. Studies of Turbulence Models in a Computational Fluid Dynamics Model of a Blood Pump. *Artificial Organs*, **27**(10), pp. 935-937.

SONG, X., WOOD, H.G. and OLSEN, D.B., 2004. Computational Fluid Dynamics (CFD) Study of the 4th Generation Prototype of a Continuous Flow Ventricular Assist Device (VAD). *Journal of Biomechanical Engineering*, **126**, pp. 180-187.

STEPANOFF, A.J., 1957. Centrifugal and Axial Flow Pumps. John Wiley & Sons Inc.

STOIBER, M., GRASL, C., PIRKER, S., RADERER, F., SCHISTEK, R., HUBER, L., GITTLER, P. and SCHIMA, H., 2009. A Passive Magnetically and Hydrodynamically Suspended Rotary Blood Pump. *Artificial Organs*, **33**(3), pp. 250-257.

STRACKEE, J. and WESTERHOF, N., 1993. The Physics of heart and circulation. Philadelphia, PA: Institute of Physics Pub.

SU, B., CHUA, L.P., LIM, T.M. and ZHOU, T., 2010. Evaluation of the Impeller Shroud Performance of an Axial Flow Ventricular Assist Device Using Computational Fluid Dynamics. *Artificial Organs*, **34**(9), pp. 745-759.

TAGUSARI, O., YAMAZAKI, K., LITWAK, P., ANTAKI, J.F., WATACH, M., GORDON, L.M., KONO, K., MORI, T., KOYANAGI, H., GRIFFITH, B.P. and KORMOS, R.L., 1998. Effect of Pressure-Flow Relationship of Centrifugal Pump on In Vivo Hemodynamics: A Consideration for Design. *Artificial Organs*, **22**(5), pp. 399-404.

TAKAMI, Y., MAKINOUCHI, K., NAKAZAWA, T., BENKOWSKI, R., GLUECK, J., OHARA, Y. and NOSÉ, Y., 1996. Hemolytic characteristic of a pivot bearing supported Gyro centrifugal pump (C1E3) simulating various clinical applications. *Artificial Organs*, **20**(9), 1042-1049.

TAKIURA, K., MASUZAWA, T., ENDO, S., WAKISAKA, Y., TATSUMI, E., TAENAKA, Y., TAKANO, H., YAMANE, T., NISHIDA, M., ASZTALOS, B., KONISHI, Y., MIYAZOE, Y. and ITO, K, 1998. Development of Design Methods of a Centrifugal Blood Pump with In Vitro Tests, Flow Visualization and Computational Fluid Dynamics: Results in Hemolysis Tests. *Artificial Organs*, **22**(5), pp. 393-398.

TAYLOR, C.A. and DRANEY, M.T., 2004. Experimental and Computational Methods in Cardiovascular Fluid Mechanics. *Ann. Rev. Fluid Mechanics*, **36**, pp. 197-231.

THROCKMORTON, A.L., BALLMAN, K.K., MYERS, C.D., LITWAK, K.N., FRANKEL, S.H., RODEFELD, M.D., 2007. Mechanical Cavopulmonary Assist for the Univentricular Fontan Circulation Using a Novel Folding Propeller Blood Pump. *ASAIO Journal*, **53**(6), pp. 734-741.

THROCKMORTON, A.L. and KISHORE, R.A., 2009. Design of a Protective Cage for an Intravascular Axial Flow Blood Pump to Mechanically Assist the Failing Fontan. *Artificial Organs*, **33**(8), pp. 611-621.

THROCKMORTON, A.L., UNTAROIU, A., ALLAIRE, P.E., WOOD, H.G., MATHERNE, G.P., LIM, D.S., PEELER, B.B. and OLSEN, D.B., 2004. Computational Analysis of an Axial Flow Pediatric Ventricular Assist Device. *Artificial Organs*, **28**(10), pp. 881-891.

TIMMS, D., HAYNE, M., TAN, A. and PEARCY, M, 2005. Evaluation of Left Ventricular Assist Device Performance and Hydraulic Force in a Complete Mock Circulation Loop. *Artificial Organs*, **29**(7), pp. 573-580.

TRIEP, M., BRUCKER, C., KERKHOFFS, W., SCHUMACHER, O. and MARSEILLE, O., 2008. Investigation of the Washout Effect in a Magnetically Driven Axial Flow Pump. *Artificial Organs*, **32**(10), pp. 778-784.

TRIEP, M., BRUCKER, C., SCHRODER, W. and SIESS, T., 2006. Computational Fluid Dynamics and Digital Particle Image Velocimetry Study of the Flow Through an Optimized Micro-axial Blood Pump. *Artificial Organs*, **30**(5), pp. 384-391.

TURTON, R.K., 1995. Principles of Turbomachinery. London: Chapman & Hall.

UNDAR, A., 2003. Fundamentals of pulsatile versus nonpulsatile flow during chronic support. *ASAIO Journal*, **49**(1), pp. 139-40.

UNTAROIU, A., THROCKMORTON, A.L., PATEL, S.M., WOOD, H.G., ALLAIRE, P.E., and OLSEN, D.B., 2005. Numerical and Experimental Analysis of an Axial Flow Left Ventricular Assist Device: The Influence of the Diffuser on Overall Pump Performance. *ASAIO Journal,* **29**(7), pp. 581-591.

UNTAROIU, A., WOOD, H.G., ALLAIRE, P.E., THROCKMORTON, A.L., DAY, S., PATEL, S.M., ELLMAN, P., TRIBBLE, C. and OLSEN, D.B., 2005. Computational Design and Experimental Testing of a Novel Axial Flow LVAD.Article. *ASAIO Journal,* **51**(6), pp. 702-710.

VERCAEMST, L., VANDEZANDE, E., JANSSENS, P., YVAN, T., PETER, D. and Meyns, B., 2002. Impella: A Miniaturized Cardiac Support System in an Era of Minimal Invasive Cardiac Surgery. *The Journal of Extra-Corporeal Technology,* **34**(2), pp. 92-100.

VERKERKE, G.J., MIHAYLOV, D., GEERTSEMA, A.A., LUBBERS, J. and RAKHORST, G., 1999. Numerical Simulation of the Pulsating Catheter Pump: A Left Ventricular Assist Device. *Artificial Organs,* **23**(10), pp. 924-931.

VOITL, P., VOLLKRON, M., BERGMEISTER, H., WIESELTHALER, G. and SCHIEMA, H., 2009. Coronary Hemodynamics and Myocardial Oxygen Consumption During Support With Rotary Blood Pumps. *Artificial Organs,* **33**, pp. 77-80.

VOLLKRON, M., SCHIMA, H., HUBER, L., BENKOWSKI, R., MORELLO, G. and WIESELTHALER, G., 2006. Advanced Suction Detection for an Axial Flow Pump. *Artificial Organs,* **30**(9), pp. 665-670.

VOSSE, F.N. VAN DE, GIJSEN, F.J.H. and WOLTERS, B.J.B.M., 2001. Numerical analysis of coronary artery flow. Bioengineering Conference, *ASME*, **50**, pp. 17–18.

WALBURN, F.J. and SCHNECK, D.J., 1976. A constitutive equation for whole human blood. *Biorheology*, **13**, pp. 201–210.

WAMPLER and R, K., 2004. THE BIRTH AND EVOLUTION OF THE AXIAL FLOW BLOOD PUMP.Abstract. *ASAIO Journal*, **50**(2), pp. 138.

WESTABY, S., BANNING, A.P., JARVIK, R.K., et al, 2000. First permanent implant of the Jarvik 2000 Heart. *Lancet*, **356**(9233), pp. 900-903.

WHEELDON, D.R., 2003. Mechanical circulatory support: state of the art and future perspectives. *Perfusion*, **18**, pp. 233-243.

WIESELTHALER, G.M., SCHIMA, H., DWORSCHAK, M., QUITTAN, M., NUHR, M., CZERNY, M., SEEBACHER, G., HUBER, L., GRIMM, M. and WOLNER, E., 2001. First Experiences with Outpatient Care of Patients with Implanted Axial Flow Pumps. *Artificial Organs*, **25**(5), pp. 331-335.

WOOD, H.G., THROCKMORTON, A.L., UNTAROIU, A. and SONG, X., 2005. The medical physics of ventricular assist devices. *Reports on Progress in Physics*, **68**, pp. 545-576.

WU, J., PADEN, B.E., BOROVETZ, H.S. and ANTAKI, J.F., 2010. Computational Fluid Dynamics Analysis of Blade Tip Clearances on Hemodynamic Performance and Blood Damage in a Centrifugal Ventricular Assist Device. *Artificial Organs*, **34**(5), 402-411.

WU, Z.J., GOTTLIEB, R.K., BURGREEN, G.W., HOLMES, J.A., BORZELLECA, D.C., KAMENEVA, M.V., GRIFFITH, B.P. and ANTAKI, J.F., 2001. Investigation of fluid dynamics within miniature mixed flow blood pump. *Experiments in Fluids*, 31(6), pp. 651-629.

WURZINGER, L., OPITZ, R. and ECKSTEIN, H., 1986. Mechanical bloodtrauma: an overview. *Angeiologie*, **38**(3), pp. 81–97.

YAMANE, T., 2002. The present and future state of non-pulsatile artificial heart technology. *J. Artif. Organs*, **5**, pp. 149-155.

YAMANE, T., ASZTALOS, B., NISHIDA, M., MASUZAWA, T., TAKIURA, K., TAENAKA, Y., KONISHI, Y., MIYAZOE, Y. and ITO, K., 1998. Flow visualization as a complementary tool to hemolysis testing in the development of centrifugal blood pump. *Artificial Organs*, **22**(5), 375-380.

YANO, T., SEKINE, K., MITOH, A., MITAMURA, Y., OKAMOTO, E., KIM, D.W., NISHIMURA, I., MURABAYASHI, S. and YOZU, R., 2003. An Estimation Method of

Hemolysis within an Axial Flow Blood Pump by Computational Fluid Dynamics Analysis. *Artificial Organs*, **27**(10), pp. 920-925.

YELESWARAPU, K.K., ANTAKI, J.F., KAMENEVA, M.V. and RAJAGOPAL, K.R., 1995. A Mathematical Model for Shear-Induced Hemolysis. *Artificial Organs*, **19**(7), 576-582.

YOKOYAMA, Y., KAWAGUCHI, O., KITAO, T., KIMURA, T., STEINSEIFER, U. and TAKATANI, S., 2010. Prediction of the ExternalWork of the Native Heart From the Dynamic H-Q Curves of the Rotary Blood Pumps During Left Heart Bypass. *Artificial Organs*, **34**(9), pp. 766-777.

ZHANG, Y., XUE, S., GUI, X.M., SUN, H.S., ZHANG, H., ZHU, X.D. and HU, S.S., 2007. A Novel Integrated Rotor of Axial Blood Flow Pump Designed With Computational Fluid Dynamics. *Artificial Organs*, **31**(7), pp. 580-5.

ZHU, X., ZHANG, M., ZHANG, G. and LIU, H., 2006. Numerical Investigation on Hydrodynamics and Biocompatibility of a Magnetically Suspended Axial Blood Pump. *ASAIO Journal*, **52**(6), pp. 624-629.